# Towards Empirically Validated Models of Soft-Rock Landslides' Occurrence, Activity, and Sediment Delivery

A thesis presented in partial fulfilment of the

requirements for the degree of

Doctor of Philosophy

in

Earth Science

at Massey University, Manawatū, New Zealand.

By Forrest F. Williams

2022

[intentionally blank]

# Abstract

Within New Zealand, soft-rock landslides present a severe hazard to infrastructure and contribute to the degradation of river systems by delivering large amounts of sediment to waterways. Updates to New Zealand's national policy statement for freshwater management necessitate accurate accounting of freshwater sediment sources, but current sediment budget models do not account for the sediment inputs from soft-rock, and other large slow-moving landslides. To understand which factors lead to the occurrence and continued activity of these landslides and the role they play in New Zealand's river sediment dynamics, I have completed the following objectives. (i) I have mapped large landslides within the Whanganui-Rangitikei soft-rock hill country in the North Island of New Zealand and conducted a geostatistical analysis to determine which factors control their occurrence. (ii) I have developed a novel remote sensing framework for monitoring large, slow-moving landslides that is based upon time-series Interferometric Synthetic Aperture Radar (InSAR) and time-series sub-Pixel Offset Tracking (sPOT) analyses. Furthermore, I have shown that this framework can identify large landslide activity with an accuracy of 91% and measure the movement of landslides moving with an average velocity of 2.05 m/yr with a mean absolute error of 0.74 m/yr. (iii) I have applied this framework to the landslides of the Whanganui-Rangitikei soft-rock hill country and used its results to perform a geostatistical analysis to determine which factors control a landslide's current activity state and to estimate the total sediment mass delivered by soft-rock landslides to the rivers of this region. In total, I mapped 1057 large landslides in this region and identified 66 of them as currently active. I find that low slopes, river incision, alignment between bedding planes and slopes, and forest cover are predictive of landslide occurrence, but that low slopes and high annual precipitation rates best predict the current activity states of these landslides. I also find that soft-rock landslides contribute a 10±2% of the total sediment mass delivered to the river systems of this region. Overall, this thesis advances our understanding of why soft-rock landslides occur and provides a framework that will allow future studies to monitor these landslides at region to country-wide scales.

# Acknowledgements

It takes a village to take to raise a child… and to get a PhD. Thank you to my committee for supporting and pushing me along the way and to my family for encouraging me. Most of all, thank you to my wife Jessie. Jessie moved across the world to go on this adventure with me, and no one has worked harder, for less thanks, than her.

# Table of Contents

Abstract ....... i
Acknowledgements ....... ii
Table of Contents ....... iii
List of Figures ....... vii
List of Tables ....... xiii
List of Equations ....... xiv
Glossary ....... xv
Chapter 1 Introduction ....... 1
1.1 Background ....... 1
1.2 Aim and Objectives ....... 4
1.3 Thesis Organization ....... 5
Chapter 2 Literature Review ....... 8
2.1 Introduction ....... 8
2.2 Landslide Classification Schema ....... 8
2.3 Landscape Processes Controlling Occurrence and Activity ....... 10
2.3.1 Preconditioning Factors ....... 11
2.3.2 Preparatory Factors ....... 11
2.3.3 Triggering Factors ....... 12
2.3.4 Sustaining Factors ....... 13
2.4 Mapping of Soft-Rock Landslides ....... 14
2.4.1 Mapping via Image Interpretation ....... 14
2.4.2 Mapping via DEMs ....... 15
2.4.3 Landslide Susceptibility Maps ....... 15
2.5 Monitoring of Soft-Rock Landslides ....... 17
2.5.1 Ground-Based Monitoring ....... 17
2.5.2 Image Change Detection ....... 18
2.5.3 Image Feature Tracking ....... 19
2.5.4 InSAR ....... 21
2.6 Landslide Sediment Dynamics ....... 24
Chapter 3 Study Area ....... 27
3.1 Soft-Rock Landslides in New Zealand ....... 27
3.2 The Whanganui Basin ....... 27

3.3 Landslide and Sediment Dynamics Research ........ 29
Chapter 4 Intersection of Fluvial Incision and Weak Geologic Structures Cause a Divergence from a Universal Slope Threshold Model ........ 32
Introduction to Chapter 4 of Thesis ........ 32
4.1 Abstract ........ 33
4.2 Introduction ........ 33
4.3 Study Area ........ 34
4.4 Methods ........ 36
4.4.1 Landslide Mapping ........ 36
4.4.2 Landslide Absence Dataset ........ 37
4.4.3 Susceptibility Factor Datasets ........ 39
4.4.4 Logistic Regression Model ........ 40
4.5 Results ........ 41
4.5.1 Landslide Dataset Characteristics ........ 41
4.5.2 Model Performance ........ 43
4.5.3 Influence of Susceptibility Factors ........ 44
4.6 Discussion ........ 46
4.6.1 Influence of Earthquakes ........ 47
4.6.2 Influence of Rainfall and Land Cover ........ 47
4.6.3 Influence of River Incision ........ 49
4.6.4 Influence of Structural Controls ........ 49
4.6.5 Utility of Landslide Type Classification ........ 50
4.7 Conclusion ........ 50
4.8 Acknowledgements ........ 50
Synthesis of Chapter 4 for Thesis ........ 51
Chapter 5 A Reproducible Framework for Slow-Moving Landslide Activity Detection and Monitoring ........ 52
Introduction to Chapter 5 of Thesis ........ 52
5.1 Abstract ........ 53
5.2 Introduction ........ 53
5.3 Methods ........ 56
5.3.1 Validation Datasets ........ 56
5.3.2 InSAR ........ 59
5.3.3 Sub Pixel-Offset Tracking ........ 63
5.4 Results ........ 64

5.4.1 InSAR ..... 64
5.4.2 Sub-Pixel Offset Tracking ..... 68
5.5 Discussion ..... 73
5.5.1 InSAR ..... 73
5.5.2 Sub-Pixel Offset Tracking ..... 75
5.5.3 A Framework for Landslide Monitoring ..... 75
5.6 Conclusion ..... 76
5.7 Acknowledgements ..... 77
5.8 Code and Workflow Availability ..... 77
Thesis Synthesis of Chapter 5 ..... 77
Chapter 6 The Contributions of Soft-Rock Landslides to Riverine Sediment Budgets ..... 78
Introduction to Chapter 6 of Thesis ..... 78
6.1 Abstract ..... 79
6.2 Introduction ..... 79
6.3 Study Area ..... 81
6.4 Methods ..... 83
6.4.1 Identifying Active Landslides ..... 83
6.4.1.1 Landslide Dataset ..... 83
6.4.1.2 Landslide Activity Screening Using Time-series InSAR ..... 84
6.4.2 Analysis of Landscape Factors Controlling Landslide Activity ..... 86
6.4.3 Estimation of Landslide Sediment Mass Contributions to Catchments ..... 87
6.4.3.1 Time-Series sPOT ..... 88
6.4.3.2 Landslide Metrics ..... 89
6.4.3.3 Sensitivity and Uncertainty Analysis ..... 92
6.4.3.4 Comparison with DoDs ..... 94
6.4.4 Comparison with Modelled Sediment Loads ..... 96
6.5 Results ..... 97
6.5.1 Activity Analysis ..... 97
6.5.2 Landslide Sediment Contributions ..... 99
6.5.2.1 Comparisons with Validation Data ..... 99
6.5.2.2 Regional Sediment Contributions ..... 100
6.6 Discussion ..... 105
6.6.1 Activity Analysis ..... 105
6.6.2 Sources of Uncertainty ..... 107
6.6.3 Role of Deep-seated Landslides Within Catchment Sediment Budgets ..... 108

6.7 Conclusions ........ 110
6.8 Acknowledgements ........ 111
Synthesis of Chapter 6 for Thesis ........ 111
Chapter 7 Synthesis ........ 112
7.1 Thesis Aims and Objectives Revisited ........ 112
7.2 Factors Influencing Soft-Rock Landslide Occurrence ........ 112
7.3 InSAR and sPOT Landslide Monitoring Framework Development ........ 114
7.3.1 InSAR Analysis ........ 114
7.3.2 sPOT Analysis ........ 116
7.4 Factors Influencing Contemporary Soft-Rock Landslide Activity ........ 117
7.5 Estimation of Whanganui Basin Sediment Contribution ........ 119
Chapter 8 Conclusion ........ 121
8.1 Assessment of Objectives ........ 121
8.2 General Findings ........ 122
8.3 Future Research ........ 123
References ........ 125
Appendix A: Open-Source Software Development ........ 147
Appendix B: Statements of Contribution ........ 149

# List of Figures


Figure 2.1 The updated Varnes classification of landslide types as presented in Massey (2010).While not included within this classification, my thesis considers deep-seated soft-rock landslides, typically classified as translational or rotational rock slides, and translational or rotational debris slides. Their classification depends on the geometry of the failure surface and the competency of the landslide material. This figure is based on the classification by Varnes (1978) and the landslide schematics by Highland and Bobrowsky (2008). .................9

Figure 2.2 The relationships between preparatory, triggering, and sustaining landslide susceptibility factors according to Crozier and Glade (2005) ...............................................11

Figure 2.3. Schematic sPOT framework. A match with for the template (second) image patch is searched for within the source (first) image's search area, and the point the maximum similarity (NCC) is identified. This process is then repeated for the entire image to create velocity measurement for each pixel. Modified from (Lei et al., 2021)................................20

Figure 2.4 Schematic of the InSAR principle. By measuring the phase of a microwave signal that travels between a satellite and a ground at two times (R1 and R2), we can compute the change in the phase and the movement of the feature ($\Delta r$). .................................................22

Figure 3.1 A map of the Whanganui Basin with soft-rock landslide extents and major river systems. The bedrock layers shown here include all the soft-rock units of the Whanganui Basin (i.e., it excludes limestone and unconsolidated sediments). The yellow portions of the inset map indicate the parts of New Zealand that are composed of soft-rock Neogene sediments that are similar to those found in the Whanganui Basin.......................................28

Figure 4.1 The Lower Whanganui Basin sediments (shown in colour) are a set of interbedded shallow water mudstones, sandstones, and limestones with a downlapping geometry. Other landslide-prone Neogene sedimentary rocks within New Zealand's North Island are shown in yellow in the inset map. Our study area (black rectangle in inset) contains several major rivers. Soft-rock landslides tend to occur along these river corridors. ..................................35

Figure 4.2 Example landslides from the study area with varying failure geometries. A) Translational rock slide with a prominent long, planar landslide body and low headscarp B) A compound rock slide with characteristics of both a translational and rotational rock slide C) Rotational rock slide with a prominent head scarp, and a relatively short and rotated landslide body. Within the landslide dataset, landslide B was classified as a rotational rock slide due to the concavity of the landslide surface and scar.....................................................................37

Figure 4.3 Landslide size distribution for translational and rotational rock slides. While translational rock slides within our study area do tend to be larger, many landslides larger than 100 ha of both types were identified...................................................................38

Figure 4.4 Methodology for placement of landslide absence objects. A) In order of descending size, landslide absence circles (green) are placed randomly. B) If a landslide absence circle (red) is placed so that it intersects another landslide absence (green) or landslide (white), it is randomly relocated until it is not touching another feature, as in C)...38

Figure 4.5 Susceptibility factor distributions of selected covariates for translational rock slides, rotational rock slides, and landslide absences. Slope and slope and bedding alignment show the largest differences in distribution shape between the landslide absence and landslide presence distributions. All three data sets have nearly identical distance to fault distributions. ..........42

Figure 4.6 Correlation matrix of susceptibility analysis covariates. Each square corresponds to the correlation between the covariates with which the square's sides intersect. Dark blue squares correspond to large positive correlations and dark red squares correspond to large negative correlations. Large correlations exist between non-independent covariate pairs (e.g. rainfall/soil moisture, slope/slope and bedding alignment, and PGA/quaternary sediments) and between slope/forest cover. ..........43

Figure 4.7 Study accuracy expressed as overall accuracy and area under the receiver-operator curve (AUC). In general, our regression analyses' performances are on par with previous studies. ..........44

Figure 4.8 Median regression coefficients for our susceptibility analyses. Standardization of the covariates prior to performing the regression allows for direct comparison of the model coefficients. Based on this data, we identified river incision, slope, forest cover, slope and bedding alignment, and rainfall as the most predictive covariates. ..........45

Figure 4.9 Accuracy of single variable regressions for the five most predictive covariates. When considering regressions that contain a single variable, higher AUCs correspond to greater importance. Slope and bedding alignment is the single best predictor of translational rock slide occurrence, and river incision is the best predictor of rotational rock slide occurrence. ..........46

Figure 4.10 Accuracy of single variable exclusion regressions for the five most predictive covariates. When considering regressions that have excluded a particular covariate, lower AUCs correspond to a greater importance of that variable. Excluding the river incision covariate from the analyses appears to have the largest negative impact on the analyses. .....46

Figure 4.11 Landslide size distribution for forested and non-forested landslides (with a cut-off of 50% forest cover). Both forested and non-forested landslide size distributions conform to the power law distributions typical of landslide inventories (Malamud et al., 2004). The lack of deviation from this distribution for forested landslides suggests that we are accurately mapping soft-rock landslides in forested terrain. ..........48

Figure 5.1 Map of the study area and the validation landslide locations used in this study. A binary assessment of either activity or inactivity was conducted at the green dots (Inactive) and red dots (Active). In addition, a manual feature-tracking analysis using high-resolution imagery was conducted at the Bird Landslide (red triangle), and a dGNSS survey was conducted at the Rangitikei Landslide (red star). ....................................................................57

Figure 5.2 Examples of an active (left) and an inactive (right) landslide from our validation dataset. The active landslide (left) has sharply undulating surface topography, visible fresh scarps at the southern edge of the landslide, and several areas with ponding water which suggests that the drainage network has been disrupted. In contrast, the inactive landslide (right) does not have visible fresh scarps or sharply undulating terrain, and there is no evidence of a recently disrupted drainage network.................................................................58

Figure 5.3 Orientations of the remote sensing velocity measurement vectors used in this study. WE stands for West to East (eastward) movement, SN stands for South to North (northward) movement, and LOS stands for the Line-Of-Sight of the SAR satellite (roughly ENE and WNW with a 30° off-nadir angle). ..........................................................................59

Figure 5.4 The number of valid interferograms (i.e., the average spatial coherence is > 0.4) available for our study area between 2017 and 2021. The top plot shows data availability for the descending orbit data, and the bottom plot shows the availability for the ascending orbit data. The green regions cover the longest continuous interferogram network for each year and represent the epochs used within our study. ...........................................................................61

Figure 5.5 The multi-year combined ascending and descending InSAR velocity-coherence filtered activity dataset overlaid on four landslides from the validation dataset. The top left shows an example of correctly identified inactivity, the top right shows an example of false activity, the bottom left shows an example of false inactivity, and the bottom right shows an example of true activity. .........................................................................................66

Figure 5.6 The average aspect of each active landslide color-coded by the number of years it was identified as active within the combined activity datasets. The LOS of the Sentinel-1 satellites (in the ascending and descending orbits) within the study area are represented by the dotted lines. The distance of the points from the plot's centre represents the surface area of the active region of the landslide in hectares (ha)...................................................................67

Figure 5.7 Examples of InSAR activity false positives that may be related to other geomorphic processes. The left-hand image shows an erroneous zone of activity along the coast of New Zealand that may be related to coastal erosion or applying the double-difference filter near a large incoherent water body. The right-hand image shows another set of erroneous activity zones that may be related to river processes. ............................................68

Figure 5.8 Comparison of the annual movement rates derived from the dGNSS validation data and the sPOT analysis for the Rangitikei Landslide. The left panel shows an image of the Rangitikei Landslide with arrows representing the average annual velocity vector for both datasets at the survey points. In this panel, the length of the velocity vectors has been exaggerated by 33x to improve readability. The centre panel shows the sPOT velocity map in the WE direction (eastward movement is positive), and the right panel shows the sPOT velocity map in the SN northward movement is positive)....................................................69

Figure 5.9 Comparison of the annual movement rates derived from the manual pixel tracking validation data and the sPOT analysis for the Bird landslide. The left panel shows an image of the Bird Landslide with arrows representing the average annual velocity vector for both datasets at the survey points. In this panel, the length of the velocity vectors has been exaggerated by 33x to improve readability. The centre panel shows the sPOT velocity map in the WE direction (eastward movement is positive), and the right panel shows the sPOT velocity map in the SN northward movement is positive)....................................................69

Figure 5.10 Comparison of the sPOT-derived velocity measurements to dGNSS-measured velocities at the Rangitikei and Bird landslides. The left panel shows the two measurements plotted against each other with a 1:1 correspondence line. The CCC metric in the left panel's legend denotes the concordance correlation coefficient (Lin, 1989). The right panel shows the prediction residual of the sPOT measurement when compared to the dGNSS measurement (sPOT - dGNSS). .........................................................................................................71

Figure 5.11 sPOT results for the Rangitikei and Bird landslides in the WE and SN directions (aerial imagery of the landslides can be found in Figure 5.8 and Figure 5.9. There is noise in the stable areas surrounding the landslides. Still, the landslide movement can be seen in all subplots except for the WE Rangitikei Landslide plot since most movement in this location is SN-oriented. ..........................................................................................................72

Figure 5.12 Comparison of the InSAR and sPOT velocity data for the Rangitikei Landslide. The left panel shows an aerial image of the landslide with arrows at the location of dGNSS observations whose colour and length correspond to the measured velocity at that location. The middle panel shows the InSAR WE velocity data, and the right panel shows the sPOT WE velocity data. In all panels, positive values indicate westward motion. Note the much smaller velocity scale for the centre InSAR panel as compared to the two outer panels. It appears that the InSAR analysis identifies movement in the slower-moving central portion of the landslide but fails to identify the faster motion in the bottom portion..............................73

Figure 5.13 Our proposed framework for time-series InSAR and time-series sPOT remote landslide monitoring. First, use time-series InSAR to identify activity within a previously mapped landslide dataset, optionally use the InSAR data to add new active landslides to the landslide dataset, then perform a time-series sPOT analysis within the active landslides to identify faster motion. ..........................................................................................76

Figure 6.1 The Whanganui Basin with deep-seated landslide extents and major river systems. The bedrock layers shown here include all units of the Whanganui Basin that are susceptible to deep-seated landslide occurrence (i.e., it excludes limestone and unconsolidated sediments). The yellow portions of the inset map indicate the parts of New Zealand that are composed of Neogene sediments that are similar to those found in the Whanganui Basin. Specific landslides that are discussed within this study are highlighted within the main portion of the map. ........ 82

Figure 6.2 The number of valid interferograms (with average spatial coherence > 0.4) available for our study area between 2017 and 2021. The top plot shows data availability for the descending orbit data, and the bottom plot shows the availability for the ascending orbit data. The blue regions cover the longest continuous interferogram network for each year and represent the epochs used within our study. ........ 85

Figure 6.3 An example of parasitic landslides within a large landslide complex. The Poroa Landslide Complex contains three active parasitic landslides, the Hautapu, Rangitikei and Lake landslides. While the broader landslide complex is inactive, all three of these parasitic landslides are active and have distinct movement directions. The names for the parasitic landslides are taken from (Thompson, 1982). ........ 88

Figure 6.4 Toe height calculation for the Rangitikei Landslide. The DEM transects for the landslide are shown in the left-hand panels, and the map on the right shows the location of the transects and the associated toe bottom/top locations. While the identification of the toe tops for transects 1 and 2 was relatively straightforward, it was difficult to select an appropriate toe top location for transect 3 ........ 91

Figure 6.5 Comparison between Monte Carlo simulations of landslide depths based on area-volume scaling relationships (V~A) (Equation 6.3) and DEM-based Toe Heights (TH) at the Utiku and Taihape landslides to in-situ depth observations (black bars). Both sites have a large distribution of measured and predicted depth values, but both estimation techniques provide an adequate estimate of landslide depth. ........ 92

Figure 6.6 Dems of Differences (DoDs) for the Rangitikei and Bird landslides. Rangitikei Landslide data was collected in 2016 and 2017, while Bird landslide data was collected in 2016 and 2021. Due to the slow movement rates in the upper portion of the Rangitikei landslide, DoD results are only available for the lower portion of the landslide ........ 95

Figure 6.7 Map of the active landslides identified within our InSAR time-series analysis. The bedrock units indicate the age of the underlying units. More active landslides occur in the Early Pleistocene basin units, but active landslides are scattered throughout the study area. Active landslides are defined here as those showing detectable movement in the timeframe of our analysis ........ 97

Figure 6.8 Logistic regression susceptibility factor importance results for the landslide activity analysis. The top plot shows each factor’s coefficient's standardized value within the model, and the two bottom plots show the jackknife regression results. In the top plot, negative coefficients indicate that landslide activity is more likely when the factor is lower. In the bottom right plot, lower AUCs indicate a drop in performance when a factor is excluded and thus higher variable importance. ........ 98

Figure 6.9 Comparison of sediment volume exports by methodology combination for the Rangitikei and Bird landslides. The bar pattern and colour represent the methodology combination (TH: toe height depth, V~A volume-area scaling depth) used, the bar height represents the median Monte Carlo estimate of sediment export ($m^3$), and the error bars represent the two standard deviation range around the estimates. The horizontal dashed lines represent the DoD sediment export ($m^3$) and the grey area represents the uncertainty of the estimate. ........ 100

Figure 6.10 Sensitivity results for our Monte-Carlo uncertainty analysis. Each subplot shows the results for a different methodology combination. The bar pattern and colour represent the methodology combination (V~A: volume-area scaling depth) used. The width of the bars indicates the difference between the sediment export predicted when a parameter is set to its 0.25 and 0.75 quantile values. (*) the width parameter was assumed to have a negligible error compared to the other parameters and thus is assumed to have no uncertainty. ........ 101

Figure 6.11 Cumulative sediment export of the active landslides within our study area when the landslides are in decreasing order of sediment export. The Poroa Landslide Complex is the single largest contributor of sediment in the study area and contributes 22% of the total sediment. This figure uses the export estimates created using the unaltered velocity and volume-area scaling relationship depth methodologies. ........ 103

Figure 6.12 The catchments within the Whanganui Basin color-coded by the landslide sediment contribution percent of the overall sediment budget. Overlaid on top of the catchments are the major river systems and circles indicating the location of the active landslides. The landslides are color-coded based on the log of their annual sediment contribution (in kilotons per year). This figure uses the export estimates created using the unaltered velocity and volume-area scaling relationship depth methodologies. ........ 105

# List of Tables

Table 4.1 Covariates used within our landslide susceptibility analysis. All covariates have been found to be useful predictors of landslides in previous studies......................................39

Table 5.1 The datasets used in this analysis, their role in the study, the period they were collected, and the velocity vectors along which they measure velocity. WE stands for West to East (eastward) movement, SN stands for South to North (northward) movement, and LOS stands for the Line-Of-Sight of the SAR satellite (roughly ENE and WNW with a 30° off-nadir angle). ..........................................................................................................................59

Table 5.2 InSAR activity accuracy metrics for the various filters considered in this study....65

Table 5.3 Average validation dataset movement rate, average sPOT measurement bias, sPOT bias standard deviation, mean absolute error (MAE), and root mean square error (RMSE) at the Rangitikei Landslide (Rangitikei), the Bird Landslide (Bird), and both landslides combined (Both). The direction column indicates the type of velocity measured (WE, SN, or the magnitude of the combined horizontal movement vector), and the n column shows the number of samples in that group...........................................................................................70

Table 6.1 The collection information for the Sentinel-1 Single Look Complex images (SLCs) and interferograms (Ifgs) available within the study area. ......................................................84

Table 6.2 The susceptibility factor datasets we used within the activity analysis portion of this study. A more in-depth discussion of these datasets can be found in Williams et al. (2021)..87

Table 6.3 Sediment export by methodology combination for all landslides in the study area. The velocity column denotes whether low velocity values were reclassified to zero, or were left unaltered. The Depth column denotes whether the volume-area relationship or the landslide toe height was used to estimate landslide depth. The export column denotes the median total export value for landslides based on the Monte Carlo analysis, and the Proportion of Total column shows what percent of the total sediment input from the study area (based on the NZEEM model) the export value represents. In the last two columns the error values are equal to twice the standard deviation of the Monte Carlo distributions. .....100

Table 6.4 Landslide sediment export and catchment metrics for the Whanganui Basin. The landslide contribution data comes from the export estimates created using the unaltered velocity and volume-area scaling relationship depth methodologies, and the catchment export data comes from the NZeem model of (Dymond et al., 2010). In this table, kT/yr stands for kilotons of sediment per year, and the Landslide Occupied Area column indicates the percent of the catchments' surface area occupied by landslides. ......................................................104

# List of Equations

Equation 4.1 Standardization of a sample member ........................................................ 41

Equation 5.1 The double difference filter ........................................................ 61

Equation 6.1 Standardization of a sample member ........................................................ 86

Equation 6.2 Landslide sediment export ........................................................ 87

Equation 6.3 Volume ~ area scaling relationship ........................................................ 89

# Glossary

**Coherence**: A pixel-wise measure of data quality in InSAR analyses that ranges from 0 to 1, with 0 being very low data quality

**Deep-seated landslide:** A landslide whose failure surface extends into the bedrock and is typically a rock slide in the Varnes landslide classification

**DEM**: Digital Elevation Model

**DoD**: DEM of Difference

**dGNSS**: Differential Global Navigation Satellite Systems. A technique in which repeat GNSS measurements are used to measure landslide motion, or other types of earth-surface motion.

**InSAR**: Interferometric Synthetic Aperture Radar

**Interferogram:** The image formed by combining the phase data of two SAR images that is the fundamental InSAR dataset

**LOS**: Line-of-Sight. The vector along which diplacement is measured in an interferogram. This vector extends from the SAR satellite to the ground surface and an angle of roughly 30°, depending on the SAR satellite. See Figure 5.3 for a graphical depiction.

**NZeem**: New Zealand empirical erosion model

**SAR**: Synthetic Aperture Radar

**SBAS:** Small-BAseline Subsets. A time-series InSAR technique that utilizes pairs of SAR images that have small temporal/perpendicular baselines

**SN**: South to North (in reference to the movement direction of a feature or pixel)

**Soft-rock landslide**: A type of deep-seated landslide that has atypically low internal rock strengths

**sPOT**: sub-Pixel Offset Tracking

**WE**: West to East (in reference to the movement direction of a feature or pixel)

# Chapter 1 Introduction

## 1.1 Background

Landslides are a ubiquitous natural hazard that can threaten infrastructure and the natural environment (Schuster and Fleming, 1986; Schuster and Highland, 2001; Turner, 2018). Within steepland landscapes, landslides are a long-term driver of denudation (Agliardi et al., 2013; Korup et al., 2010; Larsen et al., 2010) and are also a significant source of contemporary sediment generation (Fuller et al., 2016; Mackey and Roering, 2011; Simoni et al., 2013b) that can overwhelm river channels (McGovern et al., 2021; Xu et al., 2009). Thus, monitoring landslides and identifying the factors that lead to the their occurrence and continued activity is an important goal.

Many types of landslides exist, and the hazards they present vary by type. The most widely used classification scheme was first published by Varnes in 1958 (Varnes, 1958), was further developed by him and Cruden in their 1996 publication (Cruden and Varnes, 1996) and was recently updated by Hungr et al. in 2014 (Hungr et al., 2014). This classification scheme divides landslides by movement type (fall, topple, slide, spread, or flow) and by material (rock, debris, or earth). Of particular interest to this thesis, many scientists have also classified landslides by whether they have a deep failure surface that extends into the bedrock (i.e. are deep-seated) (Booth et al., 2013; Fuller et al., 2016; Pánek and Klimeš, 2016; Petley and Allison, 1997), or have shallow failure surfaces that are confined to the soil and regolith (Crozier, 1996; Fuller et al., 2016; Yu et al., 2015). This can be an important distinction in many landscapes, because deep-seated and shallow landslides tend to exhibit different temporal behaviour.

Shallow landslides tend to fail catastrophically in large numbers within multiple occurrence regional landslide events (MORLEs) (Crozier, 2005) and are driven by factors such as slope steepness and soil cohesion (Phillips et al., 2021; Spiekermann et al., 2022; Yu et al., 2015). Conversely, deep-seated landslide have the potential to move slowly through multiple cycles of dormancy and reactivation (Booth et al., 2018; Handwerger et al., 2019a; Pánek and Klimeš, 2016), and are more likely to be influenced by susceptibility factors such as river incision (Holdsworth, 2018), tectonic evolution (Bishop, 2007; Larsen and Montgomery, 2012) and bedrock competency (Holdsworth, 2018; Mountjoy, 2005; Thompson, 1982). In particular, some deep-seated landslides are composed of rock that has low internal strength more akin to soil material (i.e. soft-rock) (Thompson, 1982), and are particularly prone to long-term cycles of dormancy and reactivation (Massey et al., 2016b, 2013). Within the Varnes classification these landslides are typically rock slides, but are often referred to as soft-rock landslides to more accurately convey their typical mechanical properties and movement characteristics.

Soft-rock landslides can be found throughout the world, particularly in uplifting regions (Borgatti et al., 2006; Mountjoy, 2005; Roering et al., 2005), and are known to cause various issues. Due to their typically large size and slow movement rates, it can be challenging to identify and map them, and infrastructure built upon them can be severely damaged if their activity state changes (Massey, 2010; McSaveney and Massey, 2017). In addition, recent research has shown that these landslides can be a large and chronic source of sediment at local and regional scales (Mackey and Roering, 2011; McColl et al., 2022; Simoni et al., 2013a). In particular, Mackey and Roering (2011) estimated these landslides (referred to as earthflows in their study) were capable of producing a regional sediment yield of 1100 t $km^{-2}$ $yr^{-1}$ in the Eel river catchment of California USA, and Simoni et al. (2013b) estimated that similar landslides were producing a regional sediment yield of 1600 t $km^{-2}$ $yr^{-1}$ in the Reno river catchment of the Apennines, Italy.

Due to these concerns, many scientists have worked to determine what factors cause these landslides to occur in many regions of the world, including California, USA (Roering et al., 2015), the Himalayas (Larsen and Montgomery, 2012), the Alps (Jomard et al., 2014) and New Zealand (Parker et al., 2015; Rees et al., 2019). Based on these studies, the primary drivers of soft-rock landslide failure are believed to be weak rock, over-steepened slopes, seismic shaking, river incision, increases in porewater pressure, and the downslope orientation of preferential failure surfaces. In particular, seismic shaking and hydrologic factors (river incision and high porewater pressure) appear to heavily influence the failure of these landslides. However, it is less clear if one of these factors is a more important triggering mechanism for these landslides. Many studies in China (Parker et al., 2011; Yin et al., 2009) and the South Island of New Zealand (Dellow et al., 2017; Parker et al., 2015) have shown that earthquakes are an important trigger, while in California (a similarly tectonically active region) rainfall and river incision appear to be the main drivers (Handwerger et al., 2019b; Roering et al., 2015). Overall, more work needs to be done to determine the relative influence of these factors in more regions of the world.

Many studies have also examined the role that landslides like soft-rock landslides play in terrain regulation. In particular, work in the regions mentioned above has resulted in a formalized slope threshold model of landslide instability (Bennett et al., 2016; Korup and Weidinger, 2011; Roering et al., 2015). This model posits that landslide processes are a primary regulator of hillslope angles in uplifting regions because any factor that would cause a slope to steepen past a threshold angle instead initiates the failure of landslides on that hillslope, limiting any further slope steepening. Further work in central China has also shown that MORLEs associated with earthquakes in the region are capable of removing more material from mountain ranges than is added by co-seismic rock uplift (Parker et al., 2011).

While this is not necessarily the case in all situations, soft-rock landslides tend to be large (2 ha to 500 ha or larger) and move slowly over time (1 mm/yr to 10 m/yr) (Borgatti et al., 2006; Pánek and Klimeš, 2016; Rees et al., 2019). This can make it difficult to monitor these landslides since each landslide needs to be surveyed at numerous sites with precise equipment over long periods in order to acquire informative data. Additionally, soft-rock landslide inventories may contain landslides that are relict, dormant, or active, but this information is not necessarily available for guiding monitoring efforts. For example, New Zealand's national landslide database (Rosser et al., 2017) contains no information on landslide activity state, even though research has shown that a variety of activity states are present in New Zealand (Massey, 2010). Additionally, a regional study of landslides in the

Western United States by Xu et al. (2021b) revealed that many landslides in existing inventories were dormant, and many active landslides that they discovered were not included in those same inventories. However, deploying field surveys accurate enough to determine the landslide activity state at regional (1,000 – 100,000 $km^2$) scales is typically cost-prohibitive.

Due to these limitations, considerable work has been done to develop remote sensing monitoring strategies for these landslides. Two of the most significant methodological developments within the past twenty years are the use of interferometric synthetic aperture radar (InSAR) (Even and Schulz, 2018) and sub-pixel offset tracking (sPOT) (Bickel et al., 2018; Sun and Muller, 2016) for landslide monitoring. InSAR is capable of directly observing centimetre-scale landslide movement (Bayer et al., 2017; Bozzano et al., 2017; Shi et al., 2019a; Villi et al., 2016; Yan et al., 2018), greatly reducing the need to conduct ground observation campaigns. In addition, the creation and distribution of the freely-available synthetic aperture radar (SAR) datasets from the Sentinel-1 (Torres et al., 2012) and ALOS-1 (Rosenqvist et al., 2007) missions has allowed scientists to extend InSAR analyses to regional scales (Bonì et al., 2018; Haghighi and Motagh, 2017; Xu et al., 2021b). sPOT techniques have also been used to track the motion of landslides, particularly in cases where the landslide movement is faster than  the upper detectable limit of InSAR analyses (Amitrano et al., 2019; Dille et al., 2021). However, little work has been done to apply sPOT analyses on regional scales. The technical details for both techniques are discussed further in the literature review section of this thesis.

While both techniques show promise, they are both relatively new and more work needs to be done to adapt them to a wider variety of environments. For example, InSAR analyses are sensitive to centimetre scale movement which can cause them to identify many types of movement that are not related to landslide activity, such as the swelling of soil due to increasing pore water pressures and movement related to vegetation growth (Ahmed et al., 2011; Bayer et al., 2018; Plank et al., 2012). Additionally, more work needs to be done to explore how movement above the range of InSAR-detectable movement is represented within these datasets. Similarly, more work needs to be done to determine the lower limit of sPOT-detectable movement (Bickel et al., 2018) and to expand this technique to broader areas. In addition, both methods are computationally intensive, and require an extensive background in remote sensing and computer programming to conduct effectively. Both techniques would greatly benefit from being paired with high-performance computing environments, for example those afforded by cloud computing providers, and standardized workflows so that others without this background can use these techniques.

More governments and conservation organizations have begun to view suspended sediment as a significant environmental pollutant. In particular, the New Zealand government recently released their 2020 National Policy Statement on Freshwater Management (Ministry for the Environment, 2020), which introduces maximum allowable limits for suspended sediment in many of New Zealand's waterways. This is in part due to increasing evidence that high suspended sediment loads are decreasing water clarity (Davies-Colley and Hughes, 2020; Davies-Colley and Smith, 2001), and eliminating habitat for riverine invertebrates (Jones et al., 2012; Suren et al., 2005). Site investigations of soft-rock landslides have shown that they can deliver significant amounts of sediment over long periods (Dille et al., 2019; McColl et al., 2022), and we know that they are an important erosional process in the sediment dynamics of uplifting regions over geologic timescales (Agliardi et al., 2013; Kuehl et al., 2016; Larsen et al., 2010). However, more work needs to be done to quantify their contemporary sediment contributions at regional scales in a wider variety of settings. In particular, many sediment budgets that are used to assess the impacts of various erosional process do not include location specific sediment contribution data for soft-rock and other deep-seated landslides (Dymond et al., 2016, 2010). Thus, they are often excluded from suspended sediment reduction discussions, even though they have the potential to be a major source of suspended sediment (Dille et al., 2021; Mackey and Roering, 2011; McColl et al., 2022; Simoni et al., 2013b).

## 1.2 Aim and Objectives

The aim of this thesis is to analyse the factors that lead to the occurrence and contemporary activity of soft-rock landslides within the Whanganui Basin of New Zealand, create remote sensing methodologies that can be used to monitor these landslides effectively, and quantify the sediment input of these landslides to the catchments in which they occur. I hope that this work will broaden our understanding of soft-rock landslides generally and provide a new set of examples that future studies can compare to their own results. Additionally, I hope that the InSAR and sPOT methodologies that I developed for this work will make it easier for others to undertake these types of analyses in the future. I then hope to build on this methodology to estimate the sediment input from soft-rock landslides to the catchments within the Whanganui Basin of New Zealand. Finally, I argue that information on soft-rock landslides should be included in the sediment budgets of the regions where they exist and provide a methodology for doing so.

The aim of this thesis is met by five objectives:

1. Create an updated map of the soft-rock landslides in the Whanganui Basin region of New Zealand that is more accurate than existing inventories and includes information on landslide age, and type

2. Determine the susceptibility factors that have led to the occurrence of these landslides using a logistic regression analysis of landslide occurrence

3. Develop a remote sensing framework to identify the activity state and measure the movement rates of soft-rock landslides

4. Identify the active soft-rock landslides in the Whanganui Basin region and determine what factors have led to their activity using a logistic regression analysis

5. Estimate the annual average sediment contributions of these active landslides and determine their proportional contribution to the annual average sediment load within the Whanganui Basin

## 1.3 Thesis Organization

This thesis comprises eight chapters. These include: this introductory chapter; a literature review of the factors that lead to soft-rock landslide occurrence as well as the techniques used to map and monitor them; a description and literature review of the Whanganui Basin region; three original research chapters intended for publication; and a synthesis chapter, and a concluding chapter. The structure of the original research chapters have not been altered from the form in which they have or will be submitted for publication. This has led to a degree of repetition in these chapters, particularly in the introduction and study area subsections, and slightly altered terminology is sometimes used as well. While the content and figures have not been altered, the formatting of these chapters has been modified to match the style of this thesis. Each research chapter also has an introduction and summary separate from the manuscript that describes how the chapter fits into the overarching thesis.

Chapter 1 gives a high-level introduction to this thesis. It provides a short description of the knowledge and methodological gaps this thesis addresses, lays out the specific objective this thesis attempts to address, and describes its organization. Chapter 1 is not intended for publication and instead seeks to introduce the thesis as a complete body of work.

Chapter 2 reviews the relevant scientific literature and explores the causes of soft-rock landslide failure, the techniques used to map and monitor these landslides, and the evolution of sediment budget models. The discussion in Chapter 2 serves to identify critical gaps in the current body of knowledge and provides in-depth descriptions of the remote sensing techniques that will be utilized throughout this thesis. This chapter is not intended for independent publication but provides the scientific context for the work conducted in Chapters 4, 5, & 6.

Chapter 3 provides an in-depth description of the Whanganui Basin region of New Zealand, where the analyses in this thesis are conducted. This includes a description of the basin's geologic setting and history, a review of the soft-rock landslide site investigations that have been conducted there, and a review of scientific research undertaken in the basin more broadly. As opposed to Chapter 2, which provides a global summary of relevant studies, the literature reviewed in this chapter is focused on country and region-specific landslide and sediment budget studies. This chapter is not intended for independent publication but describes the landscape where the analyses in Chapters 4, 5, & 6 are conducted.

Chapter 4 describes the mapping of the soft-rock landslides in the Whanganui Basin (Objective 1) and the creation of a landslide susceptibility model. I use this model to assess the relative influence of a suite of landslide susceptibility factors on the likelihood of soft-rock landslide occurrence (Objective 2). I then evaluate the relative importance of seismic and hydrologic factors in this region and explore the validity of the slope threshold model of landslide generation in a structurally controlled landscape. This chapter has been published in the journal *Geomorphology* as: Williams, F., McColl, S., Fuller, I., Massey, C., Smith, H., Neverman, A., 2021. Intersection of fluvial incision and weak geologic structures cause divergence from a universal threshold slope model of landslide occurrence. *Geomorphology* 389, 107795. https://doi.org/10.1016/j.geomorph.2021.107795.

Chapter 5 describes the development and testing of a remote sensing monitoring framework for soft-rock landslides (Objective 3). This framework relies on time-series interferometric synthetic aperture radar (InSAR) to detect landslide activity and time-series sub-pixel offset tracking (sPOT) to measure movement rates. While this framework was designed for soft-rock landslides, it can generally be used to monitor multiple types of large, slow-moving features. We compare the results of this framework to a suite of validation sites within the Whanganui Basin to determine if the framework provides accurate results. This framework is then utilized in Chapter 6 to meet Objectives 4 and 5. This chapter will soon be submitted for publication to *Remote Sensing of Environment* as: Williams, F., McColl, S., Fuller, I., Neverman, A., Smith, H., 2022. A reproducible framework for slow-moving landslide activity detection and monitoring.

Chapter 6 utilizes the framework developed in Chapter 5 to identify active soft-rock landslides in the Whanganui Basin, create an active landslide susceptibility model. It also describes the development and use of a soft-rock landslide component for a sediment budget model. This landslide activity information and the activity susceptibility model are used to determine which of the susceptibility factors assessed in Chapter 4 are predictive of current landslide activity (Objective 4). An estimation of the sediment export from each active landslide is then made using the landslide velocity estimates created using the framework from Chapter 5. The total sediment export from these landslides is then compared to an external estimate of the sediment export for the entire region to determine the proportional sediment contribution from soft-rock landslides (Objective 5). Due to the dependency of this chapter on the methods of Chapter 5, this Chapter will not be submitted for publication until Chapter 5 has been accepted. Consequently, this chapter is in preparation for publication in *Earth Surface Processes and Landforms* as: Williams, F., McColl, S., Fuller, I., Neverman, A., Smith, H., 2022. The contributions of soft-rock landslides to riverine sediment budgets.

Chapter 7 provides an overall synthesis of the thesis. This chapter ties together the findings from Chapters 4, 5, & 6, then discusses how these findings have helped to fill the knowledge gaps discussed in Chapters 1 & 2, and how the methodologies used in this thesis could be improved in the future. This chapter is not intended for individual publication but serves to present the overall findings and challenges of thesis within a single discussion.

Chapter 8 concludes the thesis, describes how Objectives 1-5 were met, and suggests opportunities for future research. It describes the specific ways in which each goal was met and details the opportunities for future research that this thesis has exposed. This chapter is not intended for individual publication.

In addition to these chapters, this thesis contains two appendices. Appendix A details the contributions I have made to several open-source scientific software development projects.

While these contributions are difficult to highlight within the context of a scientific publication, they still represent an important contribution I have made to the scientific community. Appendix B contains “Statement of Contribution” forms, which are required by Massey University for the three scientific manuscript chapters (4, 5, & 6) within this thesis. These forms are akin to “Authors’ Contributions” sections, which can be found in some scientific journal articles.

# Chapter 2 Literature Review

## 2.1 Introduction

In this chapter, I review the core concepts that are discussed in Chapters 4, 5, and 6 and highlights gaps in the research that I believe my thesis helps to address. I start with a discussion of the factors that control the stability of soft-rock deep-seated landslides, then discuss various strategies that have been used to map and monitor them. Due to my theses' focus on soft-rock deep-seated landslides within the Whanganui Basin, I constrain my discussion of landslide susceptibility factors to those that affect landslides of this type. Still, I want to acknowledge that any discussion of landslide susceptibility factors is tied to the types of landslides being considered. A discussion of landslide susceptibility for an alternate landslide type would emphasize factors differently and address a modified set. A similar line of reasoning also holds for my discussion of mapping and monitoring techniques. I discuss interferometric synthetic aperture radar and sub-pixel offset tracking in greater depth than other landslide monitoring techniques because they are the methods best suited for studying soft-rock deep-seated landslides at a regional scale. These techniques excel at monitoring large landslides that move slowly over time, but different techniques would need to be used to study landslides that experience rapid and complete failure. This chapter focuses on a broad view of these topics, and I recommend you refer to Chapter 3 if you want to gain a better understanding of the state of soft-rock deep-seated landslide research within New Zealand and the Whanganui Basin.

## 2.2 Landslide Classification Schema

Landslides have harmed both the built and natural environment throughout the world. While many examples exist (Guzzetti, 2000; Massey et al., 2018; Petley and Rosser, 2005) a recent poignant example is the loss of life associated with landslides after the Wenchuan earthquake in 2008. In this case, landslides triggered by the earthquake and the failure of landslide dams led to the deaths of roughly 20,000 people (Xu et al., 2009; Yin et al., 2009). Landslides also play a significant role in terrain regulation and the long-term evolution of landscapes (Korup et al., 2010; Larsen and Montgomery, 2012). Thus, understanding the factors that influence their occurrence and activity is an important goal.

The factors controlling the occurrence and activity of landslides are directly related to the type of landslide being discussed. The Cruden and Varnes (1996) landslide classification scheme and its 2014 update (Hungr et al., 2014) are widely used for classifying and describing different types of landslides. This classification divides landslides by material (rock, debris, and earth) and failure mechanics (fall, topple, slide, spread, and flow) (Figure 2.1). While not included within the classification scheme, the term "deep-seated landslides" is also commonly used (Crosta et al., 2013; Korup, 2006; Roering et al., 2005) to refer to all landslides that have failure surfaces that occur within bedrock. This corresponds to rock planar slides, rotational slides, compound slides, and slope spreads within the Hungr et al. (2014) classification.

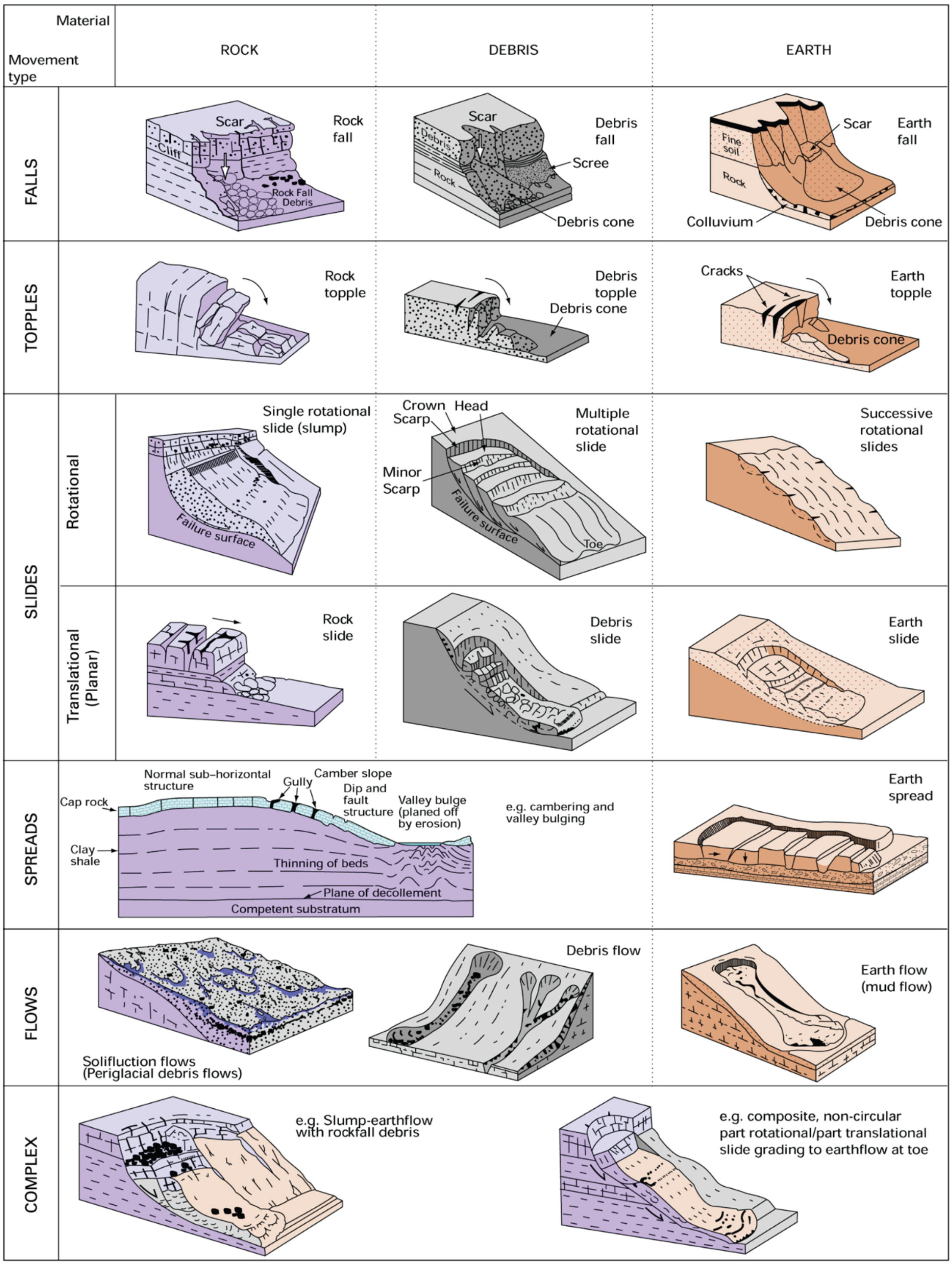


**Falls** mass detached from steep slope/cliff along surface with little or no shear displacement, descends mostly through the air by free fall, bouncing or rolling.
**Topples** forward rotation about a pivot point.
**Rotational slides** sliding outwards and downwards on one or more concave-upward failure surfaces.
**Translational (planar) slides** sliding on a planar failure surface running more-or less parallel to the slope.
**Spreads** fracturing and lateral extension of coherent rock or soil materials due to liquefaction or plastic flow of subjacent material.

**Flows** slow to rapid mass movements in saturated materials which advance by viscous flow, usually following initial sliding movement. Some flows may be bounded by basal and marginal shear surfaces but the dominan movement of the displaced mass is by flowage.
**Complex slides** slides involving two or more of the main movement types in combination.

*Figure 2.1 The updated Varnes classification of landslide types as presented in Massey (2010).While not included within this classification, my thesis considers deep-seated soft-rock landslides, typically classified as translational or rotational rock slides, and translational or rotational debris slides. Their classification depends on the geometry of the failure surface and the competency of the landslide material. This figure is based on the classification by Varnes (1978) and the landslide schematics by Highland and Bobrowsky (2008).*

Some deep-seated landslides occur within "soft rock". This term describes rock that has low internal shear strengths due to a stunted diagenesis (Massey et al., 2013), intense weathering (Roering et al., 2005), or extensive metamorphism (Crosta et al., 2013). Work on soft-rock landslides was pioneered in England by Skempton (Skempton and De Lory, 1957; Skempton et al., 1989), Petley and Alison (Petley and Allison, 1997) and Hutchinson (Hutchinson, 1969), who described the large sizes, slow movement rates, and deep-seated nature of these landslides. They also described how these landslides' weak internal structures and interactions with groundwater formed slope failures that could sustain seasonal slow movement over long periods of time. Since their early work, soft-rock landslides have been studied in Italy (Borgatti et al., 2006; Villi et al., 2016), North America (Finnegan et al., 2019; Hu et al., 2020b), New Zealand (Massey et al., 2016a, 2016b; Rees et al., 2019) as well many other places across the globe. These landslides are also the focus of this thesis. Deep-seated landslides that form in these conditions may be referred to as "soft-rock deep-seated landslides". For brevity's sake however, I will use the term "soft-rock landslides" to refer to these landslides.

## 2.3 Landscape Processes Controlling Occurrence and Activity

The term 'stability' is often used as a relative term for describing the likelihood of slope failure, but many authors have used the Factor of Safety (FoS) approach (Crozier, 1986) to provide a quantitative aspect to discussions of stability. FoS is defined as the ratio between shear strength (resisting forces) and shear stress (driving forces) of a slope and is used as a numerical representation of the balance between forces resisting the failure of a slope and the forces driving that failure. When resisting forces are greater than driving forces, the FoS will be greater than one, and the slope will be stable under the modelled conditions. If any factor reduces resisting forces or increases driving forces so that the FoS is less than one (unity), the slope has failed (in theory). Thus, describing how different factors influence a slope's FoS provides a useful framework for quantifying the multitude of factors that influence landslide failure.

Many factors contribute to the instability of landslides, such as slope steepness, landslide material, and rainfall (Crozier, 1986; Korup et al., 2007), and these factors are typically classified as either preconditioning, preparatory, triggering, or sustaining factors (Crozier and Glade, 2005) (Figure 2.2). Preconditioning factors are factors that are inherent and static (over human timescales), and influence the margin of stability (e.g. rock strength) or the effectiveness of other destabilising forces (e.g. rock permeability). Preparatory factors shift slopes from a stable to marginally stable state, either slowly (e.g. weathering), or more rapidly (e.g. deforestation), and make slopes sensitive to potential triggers. Triggering factors are the instantaneous events such as earthquakes and precipitation events that move a slope into an actively unstable state. Some landslides move just once, fully vacating their source area and coming to rest, while others are longer-lived. For many deep-seated landslides in soft rock, the initial failure does not fully evacuate the landslide material (Booth et al., 2018; Massey, 2010; Pánek and Klimeš, 2016). Instead, a persistent landslide body develops that can undergo sustained or episodic movement, controlled by sustaining factors (e.g. groundwater fluctuations). Due to this behaviour, understanding how sustaining factors influence landslide movement over time is a key factor in understanding the evolution of soft-rock landslides (Carey et al., 2019; Massey et al., 2013; Pánek and Klimeš, 2016)

*Figure 2.2 The relationships between preparatory, triggering, and sustaining landslide susceptibility factors according to Crozier and Glade (2005)*

### *2.3.1 Preconditioning Factors*

Preconditioning factors tend to develop over geologic (>$10^6$ yr) timescales and tend to not vary significantly over short (< 10 yr) timescales. Some examples include bedrock strength, and bedrock discontinuity geometry. Since soft-rock landslides typically have failure planes that are within bedrock, the inherent material strength of the bedrock is an essential component of their stability (Borgatti et al., 2006; Crosta et al., 2013; Korup et al., 2007; Massey et al., 2016b). Similarly, the orientation of discontinuities within the bedrock and their relationship with topography influence the likelihood of failure (Chittenden et al., 2014; Stead and Wolter, 2015). In several cases, soft rock landscapes have shown preferential landslide development where bedding dips toward valley bottoms (i.e. dip slopes) (Chen et al., 2019; Chittenden et al., 2014; Rees et al., 2019; Thompson, 1982). On the opposite side of the valley, where bedding dips away from the valley (i.e. scarp slopes), these hillslopes are comparatively stable, with erosion taking place as either small-scale rock falls (spalling) or shallow landslides.

### *2.3.2 Preparatory Factors*

In addition to preconditioning factors, preparatory factors can develop over long timescales, but this is not always the case. For instance, uplift (an important landslide preparatory factor) can occur either slowly or rapidly, as can the development of material strength degradation factors. While uplift itself does not directly cause landslides, it is a precursor for the generation of steep, dip slopes, which does affect stability. The steepening of slopes leads to increases in the proportion of the gravitational force that contributes to shear stresses and reduces normal stresses, destabilizing slopes (Bennett et al., 2016; Korup and Weidinger, 2011). However, the strength equilibrium hillslope model suggests that this relationship is not linear. Larsen and Montgomery's (2012) analysis of Himalayan landslides showed that above a certain slope angle, increased uplift was accommodated via increased landsliding, not by increased slope angle. They suggested that since slopes tend to equilibrate at an angle where the stresses and strengths of a hillslope are at unity (FoS = 1), increases in slope beyond a given threshold led to increased landsliding and not to steeper slopes. It is important to remember that the steepness of this threshold depends on how other susceptibility factors within the landscape are acting upon the slope. Consequently, steeper slopes within a landscape where equilibrium slopes exist may represent areas with a higher threshold slope (and likely a more stable bedrock), and not necessarily an area with an increased risk of landslide occurrence (Korup and Weidinger, 2011). In addition, uplift can lead to the exhumation of sedimentary layers that have not fully undergone diagenesis, exposing relatively weak rock, which promotes unstable conditions (Pulford and Stern, 2004; Roering et al., 2005).

Material strength degradation factors are also important preparatory factors. This term refers to all factors that deteriorate the strength of slope material over time, such as physical weathering, chemical weathering, and fracture formation (Calcaterra and Parise, 2010; Korup et al., 2010). However, the impacts of these factors are often poorly understood (Wieczorek and Jäger, 1996). This is due to the difficulty inherent in observing processes that occur over thousands of years or 'hidden' within the bedrock (Petley, 2011). Strength degradation can also be achieved through stress-induced fatigue, which is defined as any stress-caused weakening of the slope material that occurs at sub-critical stresses (Cruden, 1974). In many cases, stress-induced fatigue can also take the form of a heterogeneous distribution of stress within the landslide body that results in accelerated fracture propagation.

### *2.3.3 Triggering Factors*

Earthquakes and heavy rainfall are often cited as the most common triggering factors for soft-rock landslides. For earthquakes, the sudden reorientation and increase/decrease of the driving/resisting forces is the primary cause of induced failure, and is often exacerbated by topographic amplification of seismic shaking at ridge crests where co-seismic landslides typically initiate (Meunier et al., 2008; Sepúlveda et al., 2005). When earthquakes are strong enough to trigger deep-seated landslides, they tend to generate clusters of multiple landslides that are both deep-seated and shallow. Some prominent examples include the landslides following the $M_w$ 7.8 Kaikoura, New Zealand earthquake (Massey et al., 2018), the $M_w$ 8.0 Wenchuan earthquake (Parker et al., 2011; Yin et al., 2009), and the $M_w$ 8.8 Chile megathrust earthquake (Serey et al., 2019). The generation of landslide swarms can also lead to additional hazards since mass landslide generation is more likely to overwhelm and block river channels. This can lead to the generation and failure of dangerous landslides dams (Xu et al., 2009; Yin et al., 2009).

While heavy rainfall is an important triggering factor for most landslides, shallow landslides tend to respond to rainfall differently than soft-rock (and other deep-seated) landslides. Shallow landslides tend to be triggered by losses in soil cohesion at a shallow depth, but soft-rock landslides tend to be triggered by increases in pore-water pressure due to changes in groundwater levels (Miao et al., 2014; Van Asch et al., 1999). This also affects the temporal response of the landslides to storm events. Shallow landslides tend to fail during or immediately after the storm event when the loss of near-surface soil cohesion is greatest (Fuller et al., 2016), but the response of soft-rock landslides is more gradual. Since rising groundwater levels are the pathway through which these landslides are triggered, the initiation of a soft-rock landslide can occur sometime after the storm event occurs. Additionally, research has shown that these landslides respond more strongly to increases in average monthly rainfall than to isolated storm events (Prokešová et al., 2013; Zêzere et al., 2005).

In addition to earthquakes and rainfall, other factors can trigger soft-rock landslides. In several cases, river incision and erosion following major rainfall events and coastal erosion have been found to lead to the failure or reactivation of landslides (Doi et al., 2020; Massey et al., 2016b; Young, 2015). Due to their slow movement rates, a single erosion event can also destabilize a landslide for several years. Massey et al. (2016b) noted that increased movement rates of a soft-rock landslide following a flood lasted two years after the event. However, a river's ability to destabilize a landslide's toe requires that the river is proximal to the landslide, and that the landslide is inherently unstable. Thus, river meandering and other changes in alignment can disconnect landslide toes from the erosive power of rivers and, given sufficient incision, leave them stabilized on floodplains (Bilderback et al., 2015). In a similar vein, sea-level rise can also lead to increased coastal toe erosion and destabilization (Della Seta et al., 2013).

Additionally, anthropogenic interventions such as, tunnel construction (Bayer et al., 2017; Ruggeri et al., 2016), and land use changes (Villaseñor-Reyes et al., 2018) have been shown to lead to failure. Finally, there are some cases where none of these factors seem to play an important role. For example, a recent investigation of a soft-rock landslide in the Democratic Republic of Congo by Dille et al., (2019) found that gradual weathering of the landslide's material, and not a distinct triggering factor, led to its failure. Also, due to the longevity of soft-rock landslides (Korup et al., 2007; Pánek and Klimeš, 2016), it can be difficult to determine which factor led to their initial failure. Thus, whether earthquakes, increasing pore-water pressure, or some other trigger, is a more important for soft-rock landslides is still an ongoing debate (Crozier et al., 1995; Johnson et al., 2017; LaHusen et al., 2020; Lo et al., 2016). Overall, the influence of these triggering factors likely varies by landscape and more work needs to be done to determine the roles of these factors worldwide.

#### *2.3.4 Sustaining Factors*

The fourth class of stability factors are sustaining factors, which influence the motion of landslides that are already in an unstable state. Examples include processes such as the rate of sustained removal of buttressing support by fluvial or coastal erosion, or seasonal pore-water pressure fluctuations. In partnership with uplift, fluvial incision has been shown to steepen slopes (Bilderback et al., 2015; Roering et al., 2015) and erode landslide toes (McColl et al., 2022; McSaveney and Massey, 2017), which can both destabilize soft-rock landslides. Toe erosion can also be brought on by coastal erosion processes (Doi et al., 2020; Hutchinson, 1969; Young, 2015). Toe erosion can also be an important sustaining factor for soft-rock landslides since continual removal of toe material by rivers or coastal erosion can lead to a continuous "conveyor-belt" system of landslide movement, such as the patterns of movement that resulted from river-bed gravel mining in the Rangitikei River of New Zealand (McSaveney and Massey, 2017).

Studies have also shown that seasonal loading of slopes via increased water content and increased porewater pressure can lead to annual cycles of instability (Carey et al., 2019; Handwerger et al., 2019a; Iverson, 2000; McColl and McCabe, 2016; Van Asch et al., 2009, 1999). While their mechanisms differ, the severity of river erosion, coastal erosion, and increases in porewater pressure all tend to vary within glacial precipitation cycles. Studies within New Zealand (Bilderback et al., 2015) and the western United States (Johnson et al., 2017) have shown that deep-seated landslide activity rates increase during inter-glacial periods. This is likely due to the increased rates of fluvial incision, wetter climates and reduced rates of hillslope sediment delivery that occur during inter-glacial periods.

## 2.4 Mapping of Soft-Rock Landslides

### *2.4.1 Mapping via Image Interpretation*

Landslide maps are created for a variety of purposes, including (i) to document the size and extent of landslides (Guzzetti et al., 1999; Trigila et al., 2010) (ii) as a preliminary dataset for hazard analyses (Bălteanu et al., 2010; Guzzetti et al., 2005) and (iii) to investigate the relationship between landslide occurrence/movement and landscape characteristics (Larsen and Montgomery, 2012; Parker et al., 2011). As described by Guzzetti et al. (2012), landslide maps can range from small scale (<1:200,000), to medium scale (1:25,000 to 1:200,000), to large scale (>1:25,000) and, based on the identification protocol, can be grouped into one of three types. Maps derived from historical accounts of landslide failure are called archival maps, maps derived from geomorphological evidence of past or present movement are called historical maps (Bălteanu et al., 2010; Trigila et al., 2010), and maps that catalogue landslides caused by a single event are called event maps (Dellow et al., 2017; Parker et al., 2011). Since soft-rock landslides are typically large and long-lived, medium to large-scale historical maps are typically used to catalogue their presence. The remainder of this review will focus on these maps and will use the term "landslide map" to refer to these maps exclusively.

Before the advent of remote sensing, defined here as the analysis of objects without physical contact, landslide maps were compiled through direct in-field interpretation of landslide features such as scarps, hummocky terrain, and evidence of displacement (Cruden and Varnes, 1996; Guzzetti et al., 2012). However, these techniques are poorly suited for cataloguing soft-rock landslides because of the limited perspective of ground observations. These observations often miss the large, subtle features of soft-rock landslides that are easier to observe from a birds-eye view. Following the Second World War, aerial imagery became available for civilian use and it became an integral dataset for creating landslide maps (Campbell, J.b, Wynne, 2011).

Stereoscopic interpretation was the predominant technique used to identify landslides in aerial imagery until the 21st century (Guzzetti et al., 1999). The stereoscopic illusion of terrain provides a valuable source of terrain information that aids in identifying landslides quickly over large regions. New Zealand's GNS Science still maintains a nation-wide landslide map (Rosser et al., 2017) created largely using this method. Within the 21st century, stereoscopic imagery analysis has been extended to satellite images (Nichol et al., 2009), offering a new tool for landslide mapping. While satellite data has lower spatial resolutions than the concurrent aerial imagery, satellite images offer a higher temporal resolution, with many satellites offering monthly revisit times. This increased the frequency with which landslide mapping surveys could be conducted (Guzzetti et al., 2012).

### *2.4.2 Mapping via DEMs*

In addition to visible-spectrum remote sensing, advancements in digital elevation model (DEM) creation have led to significant improvements in landslide mapping (Derron and Jaboyedoff, 2010; Gorsevski et al., 2016; Li et al., 2015; Ren et al., 2017; Van Den Eeckhaut et al., 2005). Unlike stereoscopic methods, which rely on multiple perspectives to create an illusion of terrain relief in imagery, DEMs directly describe the variations in elevation found within the landscape. Early remote sensing based DEMs used a technique called photogrammetry, to combine data from aerial photographs taken at multiple angles to create estimates of surface elevations (Chandler, 1999; Westoby et al., 2012). Soon after this, DEMs based on active remote sensing, such as the global DEM derived from the Shuttle Radar Topography Mission (SRTM), were introduced.

While these datasets were useful, significant advancements in mapping capability were also introduced via the creation of high-resolution (sub-meter) DEMs by techniques such as Light Detection and Ranging (LiDAR) and Unmanned Aerial Vehicle (UAV) structure-from-motion SfM photogrammetry. As opposed to previous DEMs, LiDAR DEMs offer much higher resolutions and collect multiple returns at each sample location, which allows for the removal of the vegetation signature from DEMs. This increases the likelihood of identifying landslides in heavily vegetated areas where landslides are generally harder to identify (Guzzetti et al., 2012; Li et al., 2015; Roering et al., 2015). Using UAVs that fly close to the ground surface to conduct SfM surveys is another way to produce high-resolution DEMs (Westoby et al., 2012). However, removal of the vegetation height signature from SfM-derived DEMs usually results in a highly erroneous interpolation in vegetated areas, which is less of an issue for LiDAR. Typically, a distinction is made between a DEM, which does not include the vegetation signature (sometimes referred to as a Digital Terrain Model), and a Digital Surface Model (DSM), which does include the vegetation signature. The inclusion of the vegetation signature makes SfM DSMs less useful than LiDAR DEMs for identifying landslides. Still, SfM DSMs are useful in places devoid of dense or wooded vegetative cover and are much cheaper to obtain. DEMs and visible spectrum remote sensing imagery can also be combined within a GIS platform to produce the type of data used in stereoscopic surveys (Peruccacci et al., 2012). This allows for a stereoscopic-like survey to be conducted within a digital platform, which significantly increases the efficiency of the analysis.

### *2.4.3 Landslide Susceptibility Maps*

As an alternative to visually inspecting either imagery or DEMs to identify landslides, scientists have also developed maps that contain information on the where landslides are likely to occur. These maps are called landslide susceptibility maps. While predicting where landslides are likely to occur is distinctly different than identifying where landslides exist, both strategies seek to provide information that can be used to avoid landslide hazards. Early susceptibility models used heuristic-based methodologies that relied on the experience of experts to determine the likelihood of a landslide occurring in an area based on that area's geomorphological characteristics (Nilsen and Brabb, 1977). Today however, these models use either a traditional statistical approach or machine learning techniques to assign a probability of landslide occurrence to points within a landscape based upon data from a variety of sources (Micheletti et al., 2014; Reichenbach et al., 2018). These data sources typically include information regarding the landslide susceptibility factors discussed in the previous sections along with geomorphometric information (i.e., slope, curvature, and surface roughness) but vary depending on the setting of the study (Bălteanu et al., 2010; Smith et al., 2021; Xiao et al., 2018). In addition to providing information on the likelihood of future landslide occurrence (i.e. prediction), the importance of each susceptibility factor within the model can be used to determine which factors best explain the occurrence of past landslides (i.e. postdiction) (Lombardo and Mai, 2018). This information can then be used to infer which combination of factors and processes most typically lead to the generation of landslides within the study area.

Traditional statistical models typically use a form of multivariate regression to create a susceptibility model and primarily use a multivariate logistic regression model (Budimir et al., 2015; Reichenbach et al., 2018). This model is designed to predict the likelihood of a given phenomenon to be either absent or present, which aligns well with the goals of a landslide susceptibility study. Machine learning models use a wider range of methodologies, including random forest (Belgiu and Drăgu, 2016), standard neural-network (Gorsevski et al., 2016; Hua et al., 2020), and convolution neural-network models (Fang et al., 2020), but there is no clear consensus regarding which model framework is best-suited for landslide susceptibility models (Merghadi et al., 2020; Yuan et al., 2020). Overall, machine learning models are considered to be better at modelling non-linear relationships in the data and thus tend to be more accurate when well designed (Merghadi et al., 2020). However, these models create more complex relationships between the input data sources, making it more difficult to assess the importance of the individual factors within the model (Reichenbach et al., 2018).

Both statistical and machine learning models can use pixel-based or object-based methodologies to identify landslides. This distinction describes whether the model generates a continuous (i.e., pixel-based) measure of landslide likelihood or estimates landslide likelihood within discrete objects (e.g. a hillslope). Pixel-based methodologies predate object-based techniques and are best suited for areas that experience widespread generation of small (i.e., shallow) landslides (Dymond et al., 2006; Shahabi and Hashim, 2015; Smith et al., 2021). Many researchers have argued, however, that pixel-based approaches perform poorly when used to predict the occurrence of larger soft-rock landslides (Hölbling et al., 2016, 2012; Van Den Eeckhaut et al., 2005). Object-based methods, on the other hand, first segment the landscape into homogenous zones then perform the analysis using summarized values of the susceptibility factors within each zone (Alvioli et al., 2016; Hölbling et al., 2012; Hua et al., 2020). This approach allows landslides to be classified as discrete objects and is generally considered the best method for predicting the occurrence of large landslides (Alvioli et al., 2016; Hölbling et al., 2016, 2012; Van Den Eeckhaut et al., 2005).

However, current object-based methodologies do not always work well when used to identify soft-rock landslides (Zhong et al., 2020). Object-based methodologies typically rely on algorithms to divide landscapes into zones that are internally homogenous, and different from the zones that surround them. For example, the algorithm described in Alvioli et al., (2016) creates zones that correspond to hillslopes by creating object zones that have an internally homogenous hillslope aspect. Large soft-rock landslides can be composed of many areas that have distinct aspects (e.g. a toe vs a head scarp vs a side lobe) which means that a single landslide would be composed of multiple objects when using this algorithm. Thus, object-based classifications are likely to identify portions of each landslide separately, which may complicate classification efforts. New techniques, such as combining objects based on their spatial relationships (Prabhu and Babu, 2015; Weaver, 2010) are being developed to solve these issues. Alternatively, when the goal of the analysis is to understand the factors that contribute to landslide occurrence, previously mapped landslides can be used as the classification zones (Williams et al., 2021), which alleviates the need to divide the entire landscape into discrete zones.

## 2.5 Monitoring of Soft-Rock Landslides

While landslide maps provide useful information on landslide presence, or likelihood of occurrence, they do not contain information on landslide activity state or movement rates. While this information may not be important within some use cases, it is needed to assess the hazards and impacts (e.g. sediment delivery) associated with landslides. Monitoring regional landslide activity and movement rates is difficult to do well, and soft-rock landslides are particularly difficult to monitor. This is due to some of the unique characteristics that soft rock landslides possess. First, the geomorphic evidence of a soft-rock landslide failure can persist within the landscape for thousands of years after landslide failure occurs. This means that soft-rock landslide maps often contain many relict or dormant landslides (Loche et al., 2022). Second, these landslides tend to experience cyclic periods of dormancy and reactivation (Booth et al., 2018; Handwerger et al., 2019a; Massey et al., 2013), which means that monitoring must be consistently performed to obtain accurate activity information. Third, soft-rock landslides typically move slowly and monitoring their movement rates requires sensitive measurement techniques. Due to these complexities, a variety of techniques are used to monitor soft-rock landslides, each of which has its own advantages and disadvantages.

### *2.5.1 Ground-Based Monitoring*

To track the slow movement rates of soft-rock landslides, precise techniques are often needed. Many ground-based geodesic survey techniques can acquire data at high levels of precision and have been used to monitor these landslides. The first set of techniques are those that utilize precise geodetic survey equipment to track landslide motion. This includes repeat manual global navigation satellite systems (GNSS) measurements of a set of survey points (McColl et al., 2022), the use of a robotic total station to automatically measure survey points at a set interval (Massey et al., 2013), and continuously operating GNSS receivers that record their position at set intervals (Šegina et al., 2020). Additionally, inclinometer measurements are often used to measure the local displacements of landslides, but lack information regarding their exact global position (Massey et al., 2013; Simoni et al., 2013a).

Other studies have used ground and UAV based LiDAR and SfM systems (Bitelli et al., 2004) to monitor landslides via repeat DEM analyses. These surveys operate similarly to those discussed in the mapping section, but their proximity to the ground surface allows them to collect significantly higher resolution data. Today's surveys are capable of creating DEMs that have resolutions of 10 cm or less (McColl et al., 2022) and have sub-centimetre levels of precision. By combining DEMs from multiple survey dates it is possible to create DEMs of Difference (DoDs) that allow you to measure elevation gains and losses due to landslide activity (Williams, 2012).

While these techniques have been used effectively in many studies, they are not well suited for monitoring landslides at regional scales. The main limitation of these techniques is their time and monetary costs, which limit the size and number of landslides that can be surveyed. Consequently, it is rare to find studies that present data using these techniques for more than a few landslides. Additionally, the high cost of instrumenting a landslide using these techniques frequently leads researchers to conduct monitoring only within landslides that are already known to be active (Simoni et al., 2013a). Thus, these techniques are seldom used to identify previously unreported active landslides. However, remote sensing techniques have been developed that make it easier to monitor soft-rock landslides on regional scales (Zhong et al., 2020).

### *2.5.2 Image Change Detection*

In the last twenty years, numerous Earth observation satellite missions have begun to provide remote sensing data at little or no cost. Researchers have used these data to find signs of landslide activity at regional scales by identifying changes in the landscape between successive images (i.e., change detection) (Huang et al., 2019; Mondini, 2017; Parker et al., 2011). In addition, satellite images frequently measure electromagnetic radiation outside of the visible spectrum, allowing different aspects of the landscape, such as temporal variations in the normalized difference vegetation index, to be analysed (Behling et al., 2014; Huang et al., 2019).

The amount of data available to perform this type of analysis is staggering. Terabytes of new remote sensing data are produced daily, which is much faster than visual interpretation methods can utilize it. Instead, many researchers rely on automated change detection techniques, which can be used to automatically identify changes in images (Huang et al., 2019; James et al., 2012; Lu et al., 2011). These models use the same types of statistical techniques used within landslide susceptibility studies, but use them to identify changes in remote sensing images that are related to landslide failure (Huang et al., 2019; Lu et al., 2011).

The changes detected by these models are often related to the removal of vegetative cover and the generation of landslide scars (Handwerger et al., 2022), which makes them the preferred method for creating event-based landslide maps for shallow landslides. However, since soft-rock landslides tend to move more slowly and do not fully vacate their scars, changes related to their movement can be more difficult to detect. Still, soft rock landslide movement can produce new scarps or tension cracks which can be observed using these techniques (Hervás et al., 2003). Additionally, performing change-detection analyses using time-separated DEMs (James et al., 2012) provide another way to detect soft-rock landslide activity since their movement is more apparent within these datasets.

### *2.5.3 Image Feature Tracking*

While change detection can identify signs of activity, another technique called image feature tracking can track the movement of features between successive images. The first studies to perform image feature tracking did so by manually identifying features within remote sensing images, then calculating their displacement between successive geolocated images (Lucchitta and Ferguson, 1986; Mackey and Roering, 2011). Soon, it became clear that manual feature tracking could not keep pace with the rates of remote sensing data production and automated processes were developed to perform the feature tracking. These algorithms are collectively known as digital image correlation (DIC), or pixel offset tracking (POT) algorithms and use statistical measures of pixel similarity to track the movement of features within successive images (Bickel et al., 2018; Heid and Kääb, 2012). While a variety of algorithms exist, two prominent implementations include the autonomous repeat image feature tracking (AutoRIFT) (Lei et al., 2021) and Co-Registration of Optically Sensed Images and Correlation (COSI-Corr) (Leprince et al., 2007) algorithms. In addition, many of these POT algorithms employ super-sampling (i.e., interpolating between pixel values in an image to synthesize a higher resolution image) to identify features at the sub-pixel level (Amitrano et al., 2019; Sun and Muller, 2016). POT algorithms that employ super-sampling are called sub-pixel offset tracking (sPOT) algorithms and are currently considered to be the most effective image feature tracking approach (Bickel et al., 2018; Heid and Kääb, 2012).

There are a variety of sPOT algorithms, but the majority rely on a process similar to the one described below (Figure 2.3) (Bickel et al., 2018). First, a small square of the second image (called the template chip), typically 4 to 32 pixels wide, is selected surrounding a given pixel, and the similarity of this small square is compared to the area surrounding the given pixel in the first image (called the source image patch). The similarity between the template chip and all locations within the source image path are then calculated using a statistical measure. The location with the highest similarity to the template chip is deemed to be the template pixel’s original location. Often, the template chip and source image patch are oversampled to create higher resolution imagery, allowing you to identify the best match at the sub-pixel level. Finally, the displacement of the template pixel is measured by calculating the distance between the template pixel and its original location. This process is repeated for each pixel within the second image, which results in a map of the displacement between the two images.

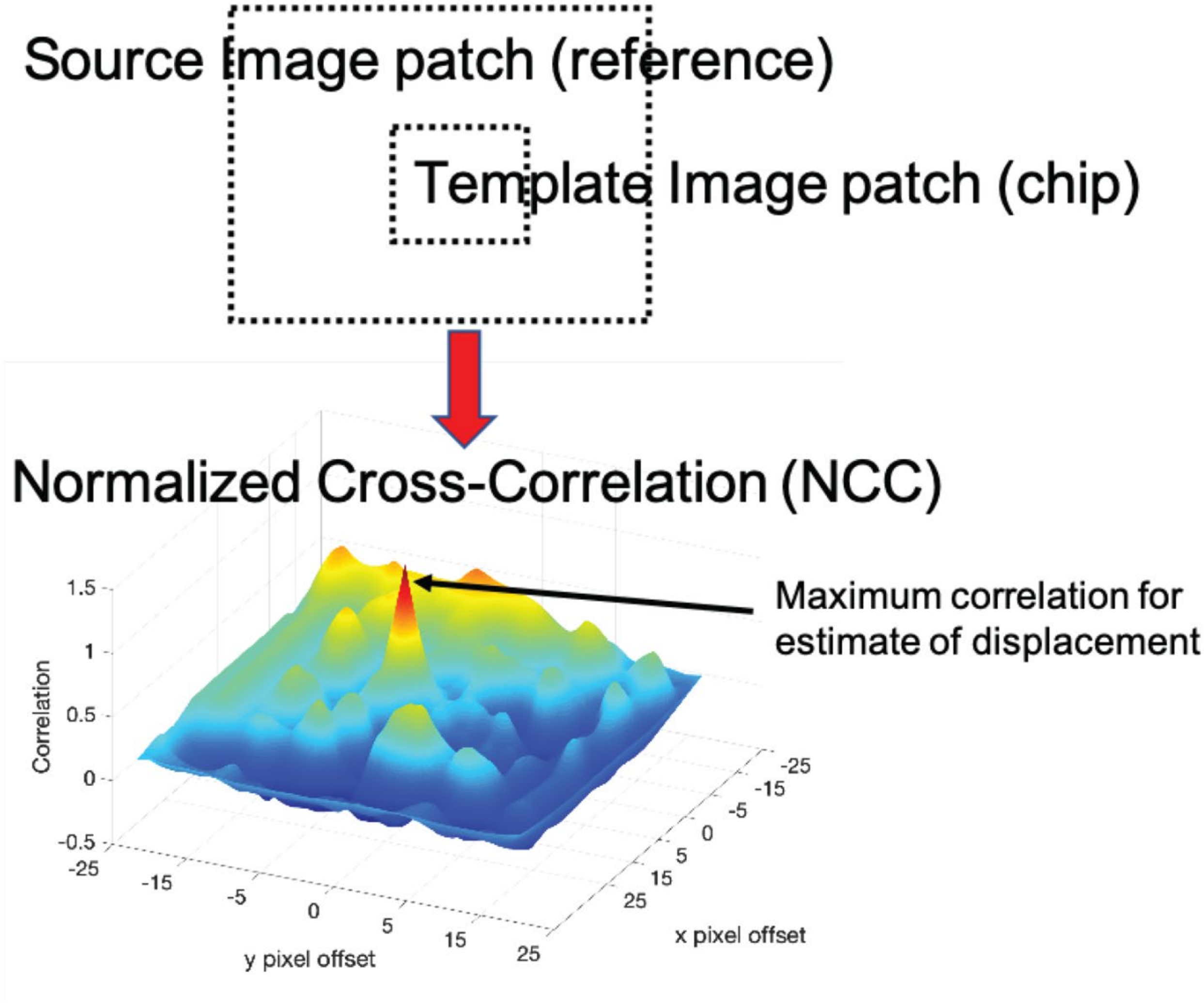


*Figure 2.3. Schematic sPOT framework. A match with for the template (second) image patch is searched for within the source (first) image's search area, and the point the maximum similarity (NCC) is identified. This process is then repeated for the entire image to create velocity measurement for each pixel. Modified from Lei et al., (2021).*

The main difference between sPOT algorithms is how they search for the location of the reference chip in the second image and what similarity measure they use. To measure similarity, most algorithms either use the normalized cross-correlation coefficient of the base imagery (Lei et al., 2021) or of the data's fast Fourier transform (FFT) (Leprince et al., 2007). Some studies have shown that transforming the data into the frequency domain can improve the number of pixels where sPOT can identify matches between the two images, but both options tend to produce data of comparable accuracies (Bickel et al., 2018). Several studies have also attempted to improve accuracy by pre-filtering the imagery, but this has had limited success (Cai et al., 2017; Dille et al., 2021; Sun and Muller, 2016).

In addition to these techniques, researchers have also tried to improve the accuracy and temporal span of sPOT analyses by combining data from multiple image pairs (Casu et al., 2011; Dai et al., 2020; Sun et al., 2017). This technique is called time-series sPOT. Time-series sPOT uses a methodology similar to SBAS InSAR (described below) to combine data from multiple time-spans into a single deformation time-series and velocity estimate. This technique has been shown to improve accuracies, and the final velocity estimates tend to have an average error between 1/20th to 1/10th of the imagery pixel size (Bickel et al., 2018; Lei et al., 2021; Leprince et al., 2007). Imagery from the Sentinel-1, Sentinel-2, and Landsat constellations are commonly used to perform sPOT and have pixel sizes of roughly 10 – 15 m, which corresponds to likely errors of 0.5 to 1.5 m. Notably, sPOT analyses conducted with current publicly available satellite data have a lower velocity observation limit similar to the upper-velocity observation limit of InSAR analyses. Consequently, researchers have demonstrated that InSAR and sPOT are complementary tools (Amitrano et al., 2019; Hu et al., 2020b), but to date no regional landslide studies have combined these techniques within a single monitoring framework.

#### *2.5.4 InSAR*

While the remote sensing techniques previously discussed rely on identifying signatures and structures that are characteristic of landslides, a process called Interferometric Synthetic Aperture Radar (InSAR) is capable of directly observing landslide movement (Bayer et al., 2018; Bozzano et al., 2017; Shi et al., 2019b; Villi et al., 2016; Yan et al., 2018). This ability offers a new way to approach landslide mapping and can be used to monitor landslide activity on a regional scale (Bonì et al., 2018; Haghighi and Motagh, 2017). InSAR utilizes data from Synthetic Aperture RADAR (SAR) satellites. SAR satellites use RADAR systems that direct pulses of microwave electromagnetic radiation toward the ground surface, then observe both the amplitude and phase of the returned signal (i.e., echo) (Rosen et al., 2000). By combining data from multiple pulses broadcast at different locations along the satellite's orbit, these satellites can create images at a much higher resolution (i.e., synthesize a larger aperture) than standard RADAR systems.

SAR systems have several unique characteristics that make them useful in a variety of applications (Massonnet and Feigl, 1998; Osmanoğlu et al., 2016). SAR systems generate their own source of electromagnetic radiation. Thus, unlike visual spectrum passive remote sensing satellites that observe the reflection of electromagnetic radiation from outside sources, SAR satellites can make observations at night. Second, microwaves do not interact strongly with water vapor in the atmosphere, which means they can observe the ground surface when there is cloud cover. This is a significant advantage since roughly 75% of Earth's surface is covered by clouds at any given time (Wylie et al., 2005). Thus, SAR is well suited for applications requiring consistent repeat measurements and applications requiring data immediately, regardless of cloud coverage or time of day. These scenarios include military applications, flood tracking (Martinis et al., 2015; Tellman et al., 2021), and other forms of natural disaster response (Handwerger et al., 2022; Joyce et al., 2009).

These repeat measurement applications all utilize SAR amplitude data, but SAR data also includes a phase component. The phase component of SAR data records the phase of the microwave signal that is returned from each location on the ground. The returned phase is a function of the distance between the satellite and the ground, but because only the final phase of the wave, and not the number of completed wave cycles, is observable, a single SAR phase acquisition appears to be random noise. However, by comparing phase data from two acquisitions taken at the same location but at different times, it is possible to measure the relative change in the distance between the ground surface and satellite on millimetre to centimetre scales (Rosen et al., 2000)  (Figure 2.4). This analysis is called interferometry and allows users to measure small ground movements with high accuracy. InSAR is used in various applications, including landslide, earthquake, volcano, and infrastructure monitoring (Anantrasirichai et al., 2021; Bürgmann et al., 2000; Hooper et al., 2012; Schaefer et al., 2019; Wasowski and Bovenga, 2014).

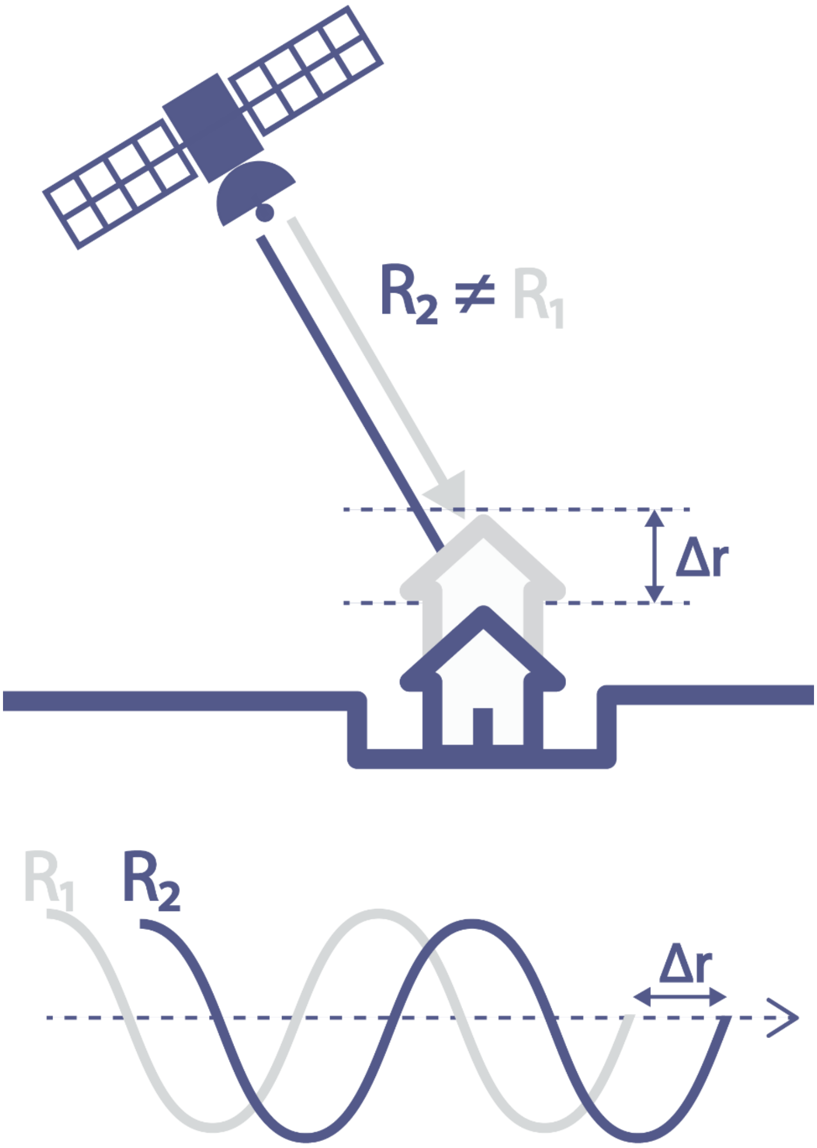


*Figure 2.4 Schematic of the InSAR principle. By measuring the phase of a microwave signal that travels between a satellite and a ground at two times (R1 and R2), we can compute the change in the phase and the movement of the feature (Δr).*

Landslide InSAR monitoring has not yet become highly utilized, largely due to the difficulty in acquiring high-quality landslide InSAR data. The main issue that prevents the collection of these data is that InSAR images must be highly coherent to produce high-quality data (Wasowski and Bovenga, 2014). In this context, coherence is defined as the strength of the correlation between the phase and amplitude signal returned by the first observation and the phase and amplitude of the following observation. High coherence is particularly difficult to achieve in the natural settings where landslides occur because factors such as interference with the ionosphere and troposphere, movement of the satellite, movement of vegetation, and fast ground movement are all capable of decorrelating the signal. Loss of coherence due to ground movement theoretically occurs when movement in the satellite's line-of-sight exceeds half the wavelength of the signal emitted by the satellite. For Sentinel-1, the most commonly used SAR satellite (Mantovani et al., 2019), the maximum displacement that can be observed between two capture dates is roughly 2.5 cm. This means that landslides moving faster than this can be challenging to measure. This is a persistent issue in landslide InSAR research that limits the types of landslides observable with the technique.

To combat these issues, researchers have developed techniques that combine data from many highly coherent InSAR images of a single location across multiple years (Wasowski and Bovenga, 2014). This approach includes a variety of techniques that are collectively referred to as time-series InSAR. The method was pioneered by Ferreti et al. (2001), who used a careful selection of pixels that represent highly coherent objects (persistent scatterers (PSs)), such as the sides of buildings and rock outcrops, to solve for deformation over time. While this was a major advancement, many researchers noted that this technique performed poorly in natural areas where few PSs are present (Berardino et al., 2002). To address this issue, the small baseline subset (SBAS) technique, which relies on distributed scatters (DSs) instead of PSs, was developed by Berardino et al. (2002). Unlike PSs, which have a coherent signal created by a single source, DSs are composed of many distributed scatterers that, on average produce a coherent signal, such as bare earth or short grass (Even and Schulz, 2018). While PS and DS methods remain the foundation of time-series InSAR, many new techniques have been developed that extend or modify their capabilities. A notable advancement was made with SqueeSAR (Ferretti et al., 2011), which treats internally homogenous groups of DSs as PSs, thus enabling the processing of both PSs and DSs within a PS workflow. However, software to conduct SqueeSAR-type analyses is not yet publicly available, and most research still relies on either a PS or DS methodology.

Since time-series InSAR is sensitive to movement on the order of millimetres to centimetres and is challenging to conduct in natural areas, the ground deformation maps produced by time-series InSAR often contains high levels of noise and deformation signals related to other processes. This can make it challenging to identify landslide movement within these datasets. Consequently, researchers have employed various techniques to identify the InSAR signal produced by landslides. One method is to visually inspect the full deformation dataset to identify zones of activity that mimic the movement expected of landslides (Handwerger et al., 2019b; Xu et al., 2021b). While this technique can work, it is difficult to perform consistently and efficiently across large regions. Other studies have filtered time-series InSAR data to enhance the strength of landslide movement signals by either projecting the InSAR-measured velocities in the downslope direction (the expected path of landslide movement) (Notti et al., 2014; Solari et al., 2019) or by applying filters that emphasize local deformation at the expense of obscuring regional trends (Bekaert et al., 2020). In many cases, statistical thresholds are then applied to the datasets (i.e., the velocity of the landslide must be greater than the standard deviation of the entire velocity dataset) to identify local zones of activity (Bekaert et al., 2020; Bonì et al., 2018; Plank et al., 2012; Solari et al., 2020).

Overall, considerable progress has been made towards improving the quality of landslide time-series InSAR analyses, but more work needs to be. The existence of a relatively low maximum movement detection limit (2.5 cm between image pairs of Sentinel-1 images), the reductions in coherence related to vegetative cover, and the numerous types of movement present within the sensitivity range of time-series InSAR all diminish the utility of this technique. Additionally, it is often difficult to assess the quality of InSAR landslide activity identification analyses because studies often do not include a robust statistical comparison to external validation data (Bekaert et al., 2020; Solari et al., 2020). Assessing the quality of InSAR activity monitoring is another important step we need to take to determine if this technique is suitable for landslide monitoring. As discussed above, many techniques have been developed to address these issues individually. Still, if we want InSAR activity monitoring to be widely usable, we need to develop holistic frameworks that address all of these issues.

## 2.6 Landslide Sediment Dynamics

Studies from across the world have documented the high sediment production rates of soft-rock landslides, and the important role they play in the sediment delivery dynamics of uplifting regions. Work by Korup and colleagues (Korup et al., 2010; Korup and Weidinger, 2011) highlighted that landslides play an important role in the denudation and evolution of mountain ranges. Also, work on the threshold slope model of terrain evolution has demonstrated that landslide activity directly regulates terrain slope angles (Agliardi et al., 2013; Bennett et al., 2016; Korup and Weidinger, 2011; Roering et al., 2015).

While these studies demonstrate the long-term importance of landslides in regional sediment dynamics, other studies have also noted the contemporary impacts of landslides have on river sediment systems. Work in the China by Parker et al., (2011) showed that landslide-related denudation caused by the 2008 $M_w$ 7.9 M Wenchuan earthquake was greater than the amount of volume gained during the associated uplift. Also, work by Mackey and Roering (2011) in California, and Simoni et al., (2013b) in Italy showed that large landslides in these regions contributed 1.1 Kt/km$^2$/yr and 1.3 Kt/km$^2$/yr of sediment to their respective catchments. Additionally, work in our study area (the Central North Island of New Zealand) has measured the sediment contribution from a single landslide and found that it contributes at least 40 Kt/yr of sediment (McColl et al., 2022).

Understanding the sediment delivery dynamics of soft-rock landslides in particular has become more important as our understanding of river water quality has evolved. Fine-grained sediment is now known to be a significant biological impairment that decreases water clarity and increases the cost of water treatment (Collins et al., 2011; Davies-Colley and Hughes, 2020, p.; Davies-Colley and Smith, 2001; Owens, 2020). Excess sedimentation can also lead to the embedding of coarse substrate in rivers and a consequent loss of habitat for riverine invertebrates (Bilotta and Brazier, 2008; Jones et al., 2012). Due to these issues, many governments have started to recognize excessive fine-grained sediment as a pollutant and have begun to regulate its occurrence (Bilotta and Brazier, 2008; MacDonald et al., 2000). In New Zealand and other countries, maximum sediment standards based on either turbidity or sediment concentrations have been set that river managers must now meet.

The primary tools that managers use to understand sediment dynamics are erosion, sediment load and budget models (Hinderer, 2012). These models use a combination of direct observations, statistical relationships, and physical models to identify sediment sources within a catchment and quantify the sediment contributions from each source. Early erosion models such as the universal soil loss equation (USLE) (Renard and service, 1997) and the Water Erosion Prediction Project (WEPP) (Bălteanu et al., 2010; Guzzetti et al., 2005) focused on a single erosion process, but more recent models such as SedNet (Wilkinson et al., 2009) and SedNetNZ (Dymond et al., 2016) use frameworks that include a wider variety of erosion processes. While most early models focused on overland flow processes, newer models such as SedNetNZ include information on channel, gully and shallow landslide erosion processes (Betts et al., 2017; Dymond et al., 2016; Williams et al., 2020). However, no major sediment budget models include information on large, slow-moving landslides (e.g. soft-rock landslides), even though previous research has shown that these landslides are likely an important component of sediment budgets (Mackey and Roering, 2011; Simoni et al., 2013a).

Large, slow-moving landslides have likely not been included within sediment budget models for three reasons: 1) the rapid influx of sediment but long dispersal times of catastrophic large landslide failures can provide chronic sediment delivery at a single source and irreversibly alter river configurations (Booth et al., 2013; Finnegan et al., 2019; Xu et al., 2009) 2) there has been an absence of data on landslide sediment loads, because measuring movement rates is challenging over large regions, and 3) for simplicity many previous sediment budget models treat  sediment as a non-point source pollutant (Dymond et al., 2016; Renard and service, 1997; Wilkinson et al., 2009), and thus point-sources of sediment like large landslides do not fit into their frameworks. However, the advances made in remote sensing and sediment budget analyses over the last twenty years may offer ways to incorporate large landslides into sediment budget models (Mackey and Roering, 2011; Simoni et al., 2013a). Early sediment budget models relied on broad physical and statistical models partly because it was infeasible to measure all of the erosion processes within a catchment. However, remote sensing analyses such as repeat LiDAR-DEM surveys (Day et al., 2013a, 2013b), automated tracking of river migration (Williams et al., 2020), and techniques such as InSAR and sPOT now provide ways to monitor erosional process on regional scales with comparatively low costs.

Sediment budget model frameworks that represent erosion within discrete features are also being developed (Dymond et al., 2016; Wilkinson et al., 2014), but none of these models currently incorporate a soft-rock landslide component, although Dymond et al (2016) include an earthflow erosion component in SedNetNZ. Yet, two studies from the early 2010s (Mackey and Roering, 2011; Simoni et al., 2013a) demonstrated that regional sediment budget models of soft-rock landslides could be created using landslide movement and terrain data. However, both studies rely on manual or non-remote sensing monitoring strategies (manual feature tracking, and inclinometer measurements) that are difficult to scale efficiently. Still, with the recent advances in remote sensing techniques, I believe it is now possible to combine time-series InSAR and time-series sPOT landslide techniques with the methodologies of these studies to create a remote sensing based soft-rock landslide component for sediment budget models.

# Chapter 3 Study Area

## 3.1 Soft-Rock Landslides in New Zealand

Soft-rock landslides are common within much of New Zealand. Large portions of New Zealand are composed of weak Neogene sedimentary rocks that are susceptible to slope failure (Figure 3.1). Soft-rock landslides have caused issues such as  damage to houses in the towns of Abbotsford (Hancox, 2008) and Taihape (Massey et al., 2013), undermining of the country's major highway and railroad line near Utiku (McSaveney and Massey, 2017), and damage to agricultural land and operations at a number of farms (Dellow et al., 2017; McColl and McCabe, 2016). Sediment delivery is also emerging as an important issue. New Zealand's national government is working to reduce in-stream sediment concentrations, and the National Policy Statement for Freshwater 2020 requires an accurate accounting of all sediment sources. A recent study of one soft-rock landslide in the region has shown that these landslides are capable of contributing sizeable volumes of sediment to rivers (i.e. 40 Kt/yr of sediment for a single landslide) (McColl et al., 2022). Thus there is clearly a need to understand the factors their lead to their occurrence and continued activity as well as the overall role these landslides play in the sediment budgets of the country.

## 3.2 The Whanganui Basin

An important hotspot of soft-rock landslides within New Zealand is the Lower Whanganui Basin (Figure 3.1), which I will refer to as the Whanganui Basin for the remainder of this thesis. The basin is in the southwest portion of the North Island and is bounded by the Ruahine axial ranges composed of greywacke to the east and the Taupo Volcanic Zone to the north. It is a back-arc basin associated with subduction along the Australian-Pacific plate boundary off the east coast of the North Island (Walcott, 1978). Migration of the Taupo Volcanic Zone to the south-southwest within the past 5 Ma has caused a migration of the basin centre and a 2°–15° rotation of the basin's bedrock in the same direction (Pulford and Stern, 2004).

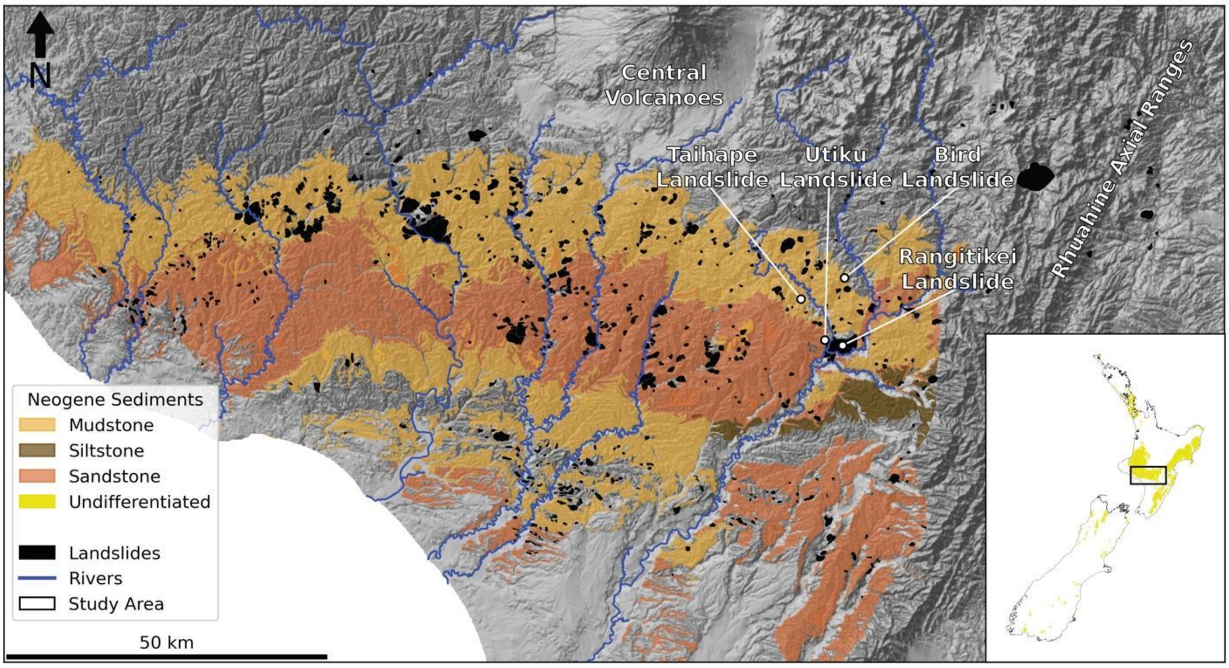


*Figure 3.1 A map of the Whanganui Basin with soft-rock landslide extents and major river systems. The bedrock layers shown here include all the soft-rock units of the Whanganui Basin (i.e., it excludes limestone and unconsolidated sediments). The yellow portions of the inset map indicate the parts of New Zealand that are composed of soft-rock Neogene sediments that are similar to those found in the Whanganui Basin.*

The sediments of the Whanganui Basin reach a maximum thickness of 4 km and range in age from 0-5 Ma (Anderton, 1981). Similar rates of uplift and aggradation during basin formation and the migration of the basin centre has led to the deposition of shallow water limestones, mudstones, and sandstones with a downlapping geometry. Cyclothems are well preserved, resulting in alternating layers of sandstone, mudstone and shell beds within the broader sandstone and mudstone units (Carter and Naish, 1998). Within the sandstone and mudstone units of the basin, thin syndepositional clay layers that are rich in smectite (Reyes, 2007), thought to be formed from volcanic ash sourcing from nearby rhyolitic volcanoes, also occur and have been shown to be preferential failure surfaces for soft-rock landslides (Massey et al., 2016b). The matching rates of deposition and uplift have led to stunted diagenesis of the basin sediments, which has resulted in bedrock with relatively low internal strengths. Continued regional uplift and current geomorphic processes have resulted in deeply incised rivers with rectilinear slopes and sharp drainage divides.

Prior to human habitation, the basin was vegetated by native forest cover (McGlone, 1989). When Polynesians arrived in New Zealand in the late 13$^{th}$ or 14$^{th}$ centuries AD they burned portions of the lowland forest to make room for farmland (Ewers et al., 2006), though forest cover in Whanganui Basin was left largely intact (McGlone, 1989). When early European settlers arrived in the late 19$^{th}$ century however, they proceeded to clear the forest rapidly, and by the mid-20$^{th}$ century, most of the land surface had been converted to cropland and pasture. Widespread increases in shallow landsliding, gully erosion, and earthflows (Glade, 2003; Marden et al., 2012) led to conservation programs in the 1960s that resulted in the establishment of exotic forest plantations (Michelsen et al., 2014; Richardson, 2011). It is not known what influence, if any, deforestation and afforestation have had on the activity and development of large, soft-rock landslides. According to the Ministry of Environment's land use dataset, the basin is now composed of 19% Native Forest, 8% Exotic Forest and 73% Pastureland.

Previous mapping efforts in the region (Rees et al., 2019; Rosser et al., 2017) have identified several hundred soft-rock landslides that cover roughly 8% of the basin's total surface area. While a portion of the landslides in the regions have been mapped, the current maps contain many errors that could be corrected, and information on the activity state or movement rates of these landslides exists for only 4 landslides within a small area towards the east of the region (Figure 3.1).

## 3.3 Landslide and Sediment Dynamics Research

Within the soft rocks of the Whanganui Basin, recent research has focused on determining which factors influence the occurrence of soft-rock landslides. Earlier work by Crozier et al. (1995) as well as Mountjoy and Pettinga (2006), in the western portion of the basin used several methods, including proximity to known faults and a limit equilibrium analysis to support the hypothesis that soft-rock landslides in the region are triggered by earthquakes. In addition, Rees et al.'s (Rees et al., 2019) study found similar results in the eastern portion of the basin. In particular, they found that most landslides in their study area occurred proximal to known faults and incising rivers. They therefore suggested that earthquakes and river incision were the main drivers of landslide failure within the weak rocks.

The more general assertion that earthquakes are an important triggering factor for large landslides in New Zealand is also supported by several studies conducted on the deep-seated landslides found in the South Island of New Zealand. Massey et al. (2018) documented the generation of numerous deep-seated landslides during the 2008 $M_w$ 7.8 Kaikoura earthquake, and a numerical stability analysis of the Ella Landslide in North Canterbury demonstrated that strong ground motion was likely required to initiate its failure (Mountjoy and Pettinga, 2006). Also, work in the northwest of the South Island (Parker et al., 2015) documented many large landslides coincident with two large (> $M_w$ 7) 1929 and 1968 earthquakes. However, the landslides discussed in these studies were generally composed of more competent rock (e.g. greywacke or stronger sedimentary units) than the soft-rocks found within the Whanganui Basin, so these findings may not be transferrable.

While previous work suggests that earthquakes may initiate failures of soft-rock landslides, field investigations in the Whanganui Basin have suggest that, relative to other drivers, seismic shaking may play a small role in driving movement of active landslides (Massey et al., 2016a). Multi-year monitoring programs at the Taihape and Utiku landslides (Massey et al., 2013; McSaveney and Massey, 2017), have instead suggested that movement is driven by increases in porewater pressure, the presence of weak clay layers that act as preferential sliding surfaces (Massey et al., 2016a), the exposure of these clay layers by river incision, and slope steepening by fluvial toe erosion. However, these factors interact and vary in their importance, as shown by differences  between the two landslides and changes over time. At the Taihape landslide, monitoring between 1985 and 2011 showed that basal sliding was relatively insensitive to changes in porewater pressure for much of the monitoring period.

When a 2004 flood led to fluvial erosion at the toe of the landslide however, movement rates dramatically increased for several years (Massey et al., 2016b), indicating that toe erosion is driving landslide activity. Conversely, at the Utiku landslide, where toe erosion is more persistent (McSaveney and Massey, 2017), monitoring between 2008 and 2015 revealed that seasonally high porewater pressure did lead to a seasonal fluctuation in movement rates (Carey et al., 2019), but the response of the landslide to pore water pressure changes also depended on the internal mechanics and stress state of the landslide (Massey et al., 2013). In both cases, river erosion that led to the exposure of weak clay layers was an important factor facilitating the activation and reactivation of these landslides. The importance that toe erosion plays in the reactivation of these landslides is supported by research at other North Island soft-rock landslides. At the nearby Rangitikei Landslide, fluvial undercutting of the landslide toe, particularly during high flow events, plays a major role in the movement pattern of the landslide, at times producing a more detectable signal of movement than localized rainfall (McColl et al., 2022). Also, the rapid (aseismic) failure of the 2019 Te Ore landslide in Whanganui Basin and the 2018 Mangapoike landslide in the adjacent Hawke's Bay region, suggest that seismic triggers are not required to initiate soft-rock landslides. For the Mangapoike landslide, river incision is suggested to have led to its initiation (McGovern et al., 2021), and saturated ground and daylighting of the failure plane by river incision are likely responsible for the Te Ore landslide (Horrey et al., n.d.).

The roles of fluvial incision and weak dip slopes have been identified as important for several individual cases, but at a regional scale their importance in priming landslides has not been thoroughly investigated. As mentioned above, Rees et al. (2019) have posited that river incision, bedrock orientation and seismic ground motion are the main causes of landslide occurrence, but their study only covered a portion of the basin, they did not perform an inferential statistical analysis to defend this hypothesis, and no activity related to seismic ground motion has been detected during recent field monitoring projects in the region. Consequently, more work can  be done to determine which factors control the occurrence and activity of soft-rock landslides at the basin scale. This in turn will help us better understand the role these landslides play in the broader sediment dynamics of the region.

The catchments within and surrounding the Whanganui Basin have played essential roles in the development and testing New Zealand's sediment budget models. The NZEEM (Dymond et al., 2010) and SedNetNZ (Dymond et al., 2016) sediment budget models were developed around and within the basin. The SetNetNZ model is the preferred sediment budget model within New Zealand and is used for a wide array of conservation purposes (Basher et al., 2020, 2018; Kuehl et al., 2016). This model is based on Wilkinson et al.'s (2014, 2009) SedNet model, which estimates the sediment contribution of surficial erosion, and gully erosion within small watersheds then compounds these results to generate yearly sediment fluxes for large watersheds. SedNetNZ (Dymond et al., 2016) follows a similar approach for compounding results but instead focuses on the sediment sources that are believed to dominate New Zealand catchments. Namely, shallow landslides, earthflows, and massive gullies, but with a notable absence of large, soft-rock landslides. The shallow landslides found within the Whanganui basin have also been used to assess the validity of the landslide components for several of these models (Betts et al., 2017; Dymond et al., 2006), as well as the more general techniques used to conduct shallow landslide susceptibility analyses (Smith et al., 2021).

In recent years, efforts have been made to create an improved sediment budget model for New Zealand that offers increased spatial and temporal resolution and incorporates erosion data from individual features. Due to the long history of sediment budget studies in the area, the validation work for this model is primarily occurring within the Whanganui Basin and the surrounding regions. This effort is led by the Smarter Targeting of Erosion Control (STEC) program within Manaaki Whenua - a New Zealand environmental science organization. As opposed to SedNetNZ, which delivers mean annual suspended sediment load estimates, the STEC program seeks to create a new event-based sediment budget model that predicts and measures sediment inputs from discrete features. In part, this thesis aims to develop a remote sensing based soft-rock landslide sediment export model that can be utilized within the STEC program.

# Chapter 4 Intersection of Fluvial Incision and Weak Geologic Structures Cause a Divergence from a Universal Slope Threshold Model

## Introduction to Chapter 4 of Thesis

Chapter 4 addresses Objective 1 (create an updated map of soft-rock landslides in the Whanganui Basin) and Objective 2 (determine the landslide susceptibility factors that lead to the occurrence of soft-rock landslides in the basin). The creation of an up-to-date map of landslides in the basin was a foundational step in the development of this thesis and all three research chapters (4, 5, and 6) rely on this dataset. The landslide occurrence factor analysis helps to explain why soft-rock landslides are prevalent in the basin, and demonstrates that landslides in this structurally controlled landscape diverge from a uniform slope threshold model. Also, a note on terminology. At the time this paper was published I referred to the soft-rock deep-seated landslides in the basin as "deep-seated" landslides, but I now prefer to refer to them as "soft-rock" landslides. To maintain consistency within my thesis, I have changed the terminology used from the published version of this paper. Aside from this change and some format alterations, this chapter is identical to the version in Issue 389 of Geomorphology.

*This chapter has been published in Geomorphology as:*

Williams, F., McColl, S., Fuller, I., Massey, C., Smith, H., Neverman, A., 2021. Intersection of fluvial incision and weak geologic structures cause divergence from a universal threshold slope model of landslide occurrence. Geomorphology 389, 107795. https://doi.org/10.1016/j.geomorph.2021.107795

## 4.1 Abstract

In some rapidly uplifting regions, soft-rock landslides are a prominent natural hazard that influence landscape evolution and are an important source of sediment. They pose a threat to infrastructure, and their failure can deliver sediment that overwhelms or blocks river channels. Consequently, a better understanding of why and where soft-rock landslides occur would help us reduce hillslope erosion, improve water quality, and allow us to better understand how landscapes evolve. Although the slope threshold model provides a framework for understanding how these landslides form, it has several shortcomings. Specifically, it fails to predict the spatial organization of landslides within a region, and it does not explain why landslide-prone portions of a region can exhibit relatively low slopes. To explore these issues, we have used a landslide susceptibility analysis within the Whanganui Basin of the North Island of New Zealand to explore the role that multiple susceptibility factors play in the occurrence of both translational and rotational soft-rock rock slides. Our findings contribute to a growing view of the relative importance of fluvial incision and the more subordinate role that earthquakes play in the development of large, soft-rock landslides. Additionally, our analyses identify the potential influence that widespread deforestation may have had on promoting instability, despite the deep-seated nature of the landslides studied. Most importantly however, we find that where slopes and weak geological structures align, a universal threshold slope does not exist, and many landslides develop on hillsides with below-average slope angles. This suggests that the presence of structural controls on landslide occurrence create a more complex landscape, where hillsides structurally predisposed to landslide occurrence have a much lower threshold slope angle.

## 4.2 Introduction

Landslides are a pervasive natural hazard that threaten the built and natural environment (McSaveney and Massey, 2017; Xu et al., 2009) and enhance the denudation of uplifting regions (Korup, 2008, 2006). Soft-rock landslides, mass movements whose failure surfaces occur below the regolith and typically range in size from one to several hundred hectares (Hungr et al., 2014; Pánek and Klimeš, 2016), have an outsized influence on the evolution of landscapes, particularly when compared to shallow, soil-stripping landslides (Crosta et al., 2013; Korup et al., 2010; Roering et al., 2015). Additionally, their ability to transport large amounts of material can overwhelm or block river channels (Korup, 2006, 2005, 2004; Xu et al., 2009). Infrastructure that is built upon these landslides can also be severely damaged when they occur (Bertolini and Pizziolo, 2008; Massey et al., 2013). Consequently, obtaining a better understanding of where and why soft-rock landslides occur would help reduce landslide-associated hazards, and help us better understand how landscapes evolve.

In mountain regions, uplift is often accompanied by a resulting period of denudation as rivers incise and slopes steepen (Korup and Weidinger, 2011; Roering et al., 2015). This steepening typically increases until a threshold slope steepness is reached, at which point landsliding is far more likely to occur (Larsen and Montgomery, 2012). In regions where the bedrock is structurally weak, due to intense metamorphism (Roering et al., 2015), or shortened diagenesis (Bilderback et al., 2015; Crozier and Pillans, 1991) this process can occur particularly rapidly. Although this threshold slope model (Korup et al., 2010) is foundational to our understanding of landslide processes, it leaves many aspects of landslide formation unexplained. Many authors have noted that the slope threshold model fails to explain the spatial organization of landslides (Roering et al., 2015), and the shallower slopes found within landsliding areas when compared to stable areas (Agliardi et al., 2013). Additionally, many studies that analyse soft-rock landslides fail to inspect the differences that exist between landslides with differing failure geometries (e.g. translational versus rotational failure surfaces) which may respond differently to changes in slope or fluvial incision (Bilderback et al., 2015; Pánek and Klimeš, 2016; Rees et al., 2019).

In this work, we seek to provide a better understanding of how, where, and why soft-rock landslides form in response to uplift and fluvial incision in rapidly uplifting landscapes. This is achieved using a landslide susceptibility model (Reichenbach et al., 2018) to determine the relative importance of terrain characteristics and slope stability factors within the Lower Whanganui Basin of New Zealand, which has a high density of large translational and rotational rock slides. We also perform separate susceptibility analyses for translational and rotational rock slides to determine if they are controlled by differing susceptibility factors. Based on previous work, we hypothesize that at a regional scale, the presence and distribution of translational rock slides is strongly controlled by the alignment between slopes and preferential failure surfaces (Massey et al., 2016a; McSaveney and Massey, 2017), which causes them to deviate from the slope threshold model. Conversely, we hypothesize that non-structurally controlled rotational failures will be more strongly related to topography (i.e. the slope threshold model). Our findings support and extend previous studies of regional controls on soft-rock landslides in the region (Rees et al., 2019; Thompson, 1982) and provide wider context for detailed engineering geological investigations of single landslides (Massey et al., 2016b, 2013).

## 4.3 Study Area

The Lower Whanganui Basin (hereafter referred to as the Whanganui Basin) of the southwest North Island, New Zealand is bounded by axial ranges (greywacke basement rock) to the east and the Taupo Volcanic Zone to the north (Figure 4.1). It is a back arc basin that is associated with subduction along the Australian-Pacific plate boundary off the east coast of the North Island (Walcott, 1978). Migration of the Taupo Volcanic Zone to the south-southwest within the past 5 Ma has caused a commensurate migration of the basin centre and rotation (of 2º-15º) of the basin sediments in the same direction (Pulford and Stern, 2004). At present day, the basin centre lies offshore and is actively aggrading.-

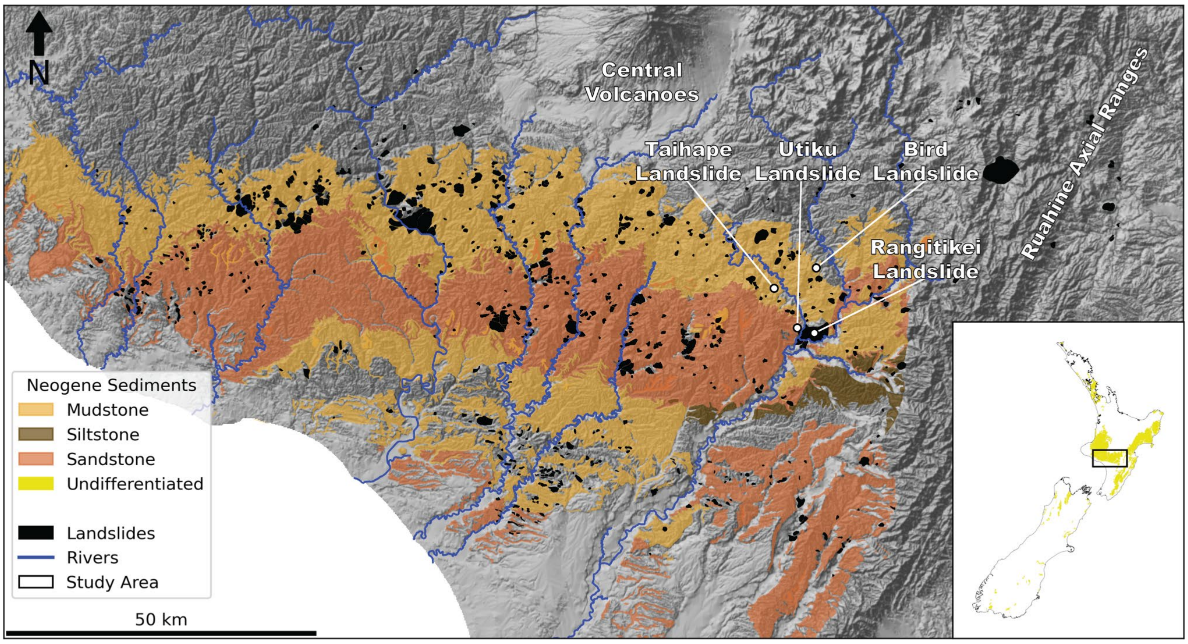


*Figure 4.1 The Lower Whanganui Basin sediments (shown in colour) are a set of interbedded shallow water mudstones, sandstones, and limestones with a downlapping geometry. Other landslide-prone Neogene sedimentary rocks within New Zealand's North Island are shown in yellow in the inset map. Our study area (black rectangle in inset) contains several major rivers. Soft-rock landslides tend to occur along these river corridors.*

The sediments of the Whanganui Basin reach a maximum thickness of 4 km and range in age from 0-5 Ma (Anderton, 1981). Similar rates of uplift and aggradation during basin formation and the migration of the basin centre has led to the deposition of shallow water limestones, mudstones, and sandstones with a downlapping geometry. Cyclothems are well preserved, resulting in alternating layers of sandstone, mudstone and shell beds within the broader sandstone and mudstone units (Carter and Naish, 1998). Within the sandstone and mudstone units of the basin, thin syndepositional clay layers that are rich in smectite (Reyes, 2007) – thought to be formed from volcanic ash sourcing from nearby rhyolitic volcanoes – also occur and have been shown to be preferential failure surfaces for soft-rock landslides (Massey et al., 2016b). The matching rates of deposition and uplift have led to stunted diagenesis of the basin sediments, which has resulted in relatively low internal strengths. Current geomorphic processes have resulted in deeply incised rivers with rectilinear slopes and sharp drainage divides. Soft-rock landslides cover roughly 8% of the study area.

Prior to human habitation, the basin was vegetated by native forest cover (McGlone, 1989). When Polynesians arrived in New Zealand in the late 13th or 14th centuries AD they burned portions of the lowland forest to make room for farmland (Ewers et al., 2006), although forest cover in Whanganui Basin was left largely intact (McGlone, 1989). When early European settlers arrived in the late 19th century however, they proceeded to clear the forest rapidly, and by the mid-20th century, most of the land surface had been converted to cropland and pasture. Widespread increases in shallow landsliding, gully erosion, and earthflows (Glade, 2003; Marden et al., 2012) led to conservation programs in the 1960s that resulted in the establishment of exotic forest plantations (Michelsen et al., 2014; Richardson, 2011). It is not known what influence, if any, deforestation and afforestation have had on the activity and development of large, soft-rock landslides. According to the Ministry of Environment's land use dataset, the basin is composed of 19% Native Forest, 8% Exotic Forest and 73% Pastureland.

Previous investigation of soft-rock landslides within the Whanganui Basin includes in-situ monitoring studies of the Utiku and Taihape landslides (Massey et al., 2016b, 2013), and regional studies in portions of the Whanganui Basin (Crozier and Pillans, 1991; Rees et al., 2019; Thompson, 1982). These studies all conclude that low internal rock strength, presence of low shear-strength clay layers and high rates of uplift contribute to the occurrence of soft-rock landslides in the region, but they disagree on whether earthquakes exert a first-order control on landslide generation. Crozier and Pillans (1991) and Rees et al. (2019) in our study area, and Massey et al. (2018) at the nearby Kaikoura Peninsula, interpret the proximity of many landslides to major faults as evidence of the influence of earthquakes on landslide failure. However, recent monitoring, modelling and lab work by Massey et al. (2016a) at a landslide in our study area has shown that earthquake-induced displacement was negligible when compared to inter-seismic displacements driven by seasonal changes in pore water pressure.

## 4.4 Methods

To determine which susceptibility factors contribute to the occurrence of soft-rock landslides within the Whanganui Basin sediments, we used a logistic regression susceptibility model (Budimir et al., 2015). While advances in machine learning models have provided performance increases within susceptibility analyses (Smith et al., 2021), we chose to use a logistic regression model because interpretation of covariate performance within the model is well defined, and it is arguably the standard against which other models are compared (Reichenbach et al., 2018).

### *4.4.1 Landslide Mapping*

To revise and improve upon previous landslide mapping in our study area, we used imagery and terrain data available within the Google Earth platform in conjunction with aerial imagery and a photogrammetry-derived digital surface model (DSM) provided by Horizons Regional Council. The imagery ranged in resolution from 0.3 m to 1 m and the elevation data ranged in resolution from 1 m to 15 m. We excluded all landslides that were less than 2 ha in size from our mapping to limit our dataset to large landslides, consistent with the GNS Science Large Landslide Database (Rosser et al., 2017). In addition to mapping landslide area, we classified each landslide according to the updated Cruden and Varnes classification (Hungr et al., 2014). Since landslides of differing types are known to be triggered by different factors (Hungr et al., 2014), we conducted our susceptibility analysis separately for each landslide type. Overall, translational and rotational rock slides (Figure 4.2) dominated the dataset, with a total count of 738 and 233 respectively. All other landslide types did not occur in sufficient quantities to perform regression analyses. Roughly thirty rock slides were identified as compound rock slides, involving a combination of translational and rotational movement, which was too few to treat as a separate landslide type in our analyses. To make use of these data we instead assigned them to either the translational or rotational rock slides type, based on their dominant style of failure, with concavity of the landslide surface and scar used for discrimination (Figure 4.2).

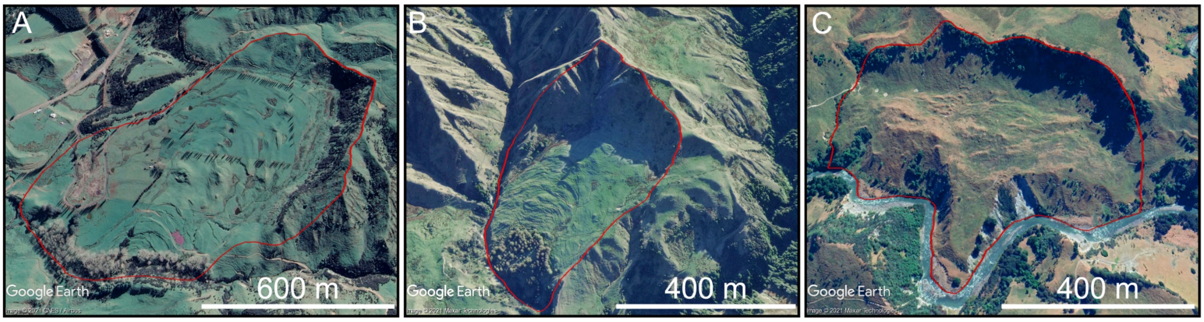


*Figure 4.2 Example landslides from the study area with varying failure geometries. A) Translational rock slide with a prominent long, planar landslide body and low headscarp B) A compound rock slide with characteristics of both a translational and rotational rock slide C) Rotational rock slide with a prominent head scarp, and a relatively short and rotated landslide body. Within the landslide dataset, landslide B was classified as a rotational rock slide due to the concavity of the landslide surface and scar.*

### *4.4.2 Landslide Absence Dataset*

In addition to a dataset of landslides, landslide susceptibility models also require a control group of landslide absences that the landslide dataset can be compared to. We created an absence dataset whose size distribution matched the size distribution of our landslide dataset to ensure that the large distribution in landslide size was reflected in our absence dataset (Figure 4.3). We accomplished this by using the Python *statsmodel (Version 0.12.0)* package to calculate the empirical distribution of landslide size within our landslide dataset, from which we randomly sampled the required number of data points. Since we are attempting to investigate the differences that exist between landslide areas and stable areas, not to maximize the accuracy of a susceptibility map, we chose to use a 1:1 ratio of landslide absences to landslide occurrences. However, to ensure that a 1:1 sampling ratio was not biasing our results (Heckmann et al., 2014), we also ran the analysis with a 5:1 sampling scheme. We found that using a 5:1 sampling scheme did not produce a significant change in the results and so chose to only report the 1:1 sampling scheme results. Once we had calculated the sizes of the landslide absences, we created the samples by randomly placing circles with the desired sizes within the study area (Figure 4.4). We placed the absence circles in order of descending size, and if a sample intersected another absence circle or a landslide, we randomly relocated it until the issue was resolved. We repeated this process ten times, creating ten separate absence datasets to ensure that our selection of absences did not bias our results.

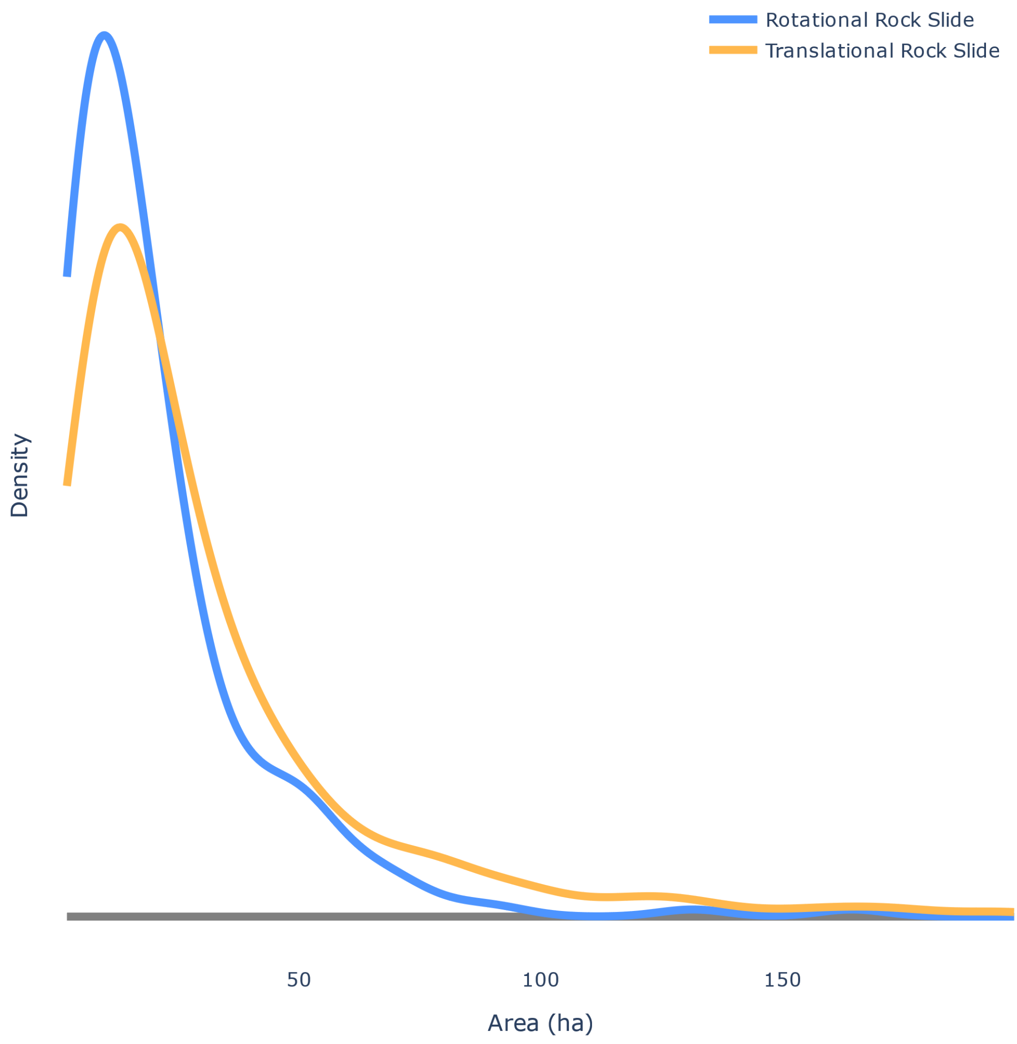


*Figure 4.3 Landslide size distribution for translational and rotational rock slides. While translational rock slides within our study area do tend to be larger, many landslides larger than 100 ha of both types were identified.*

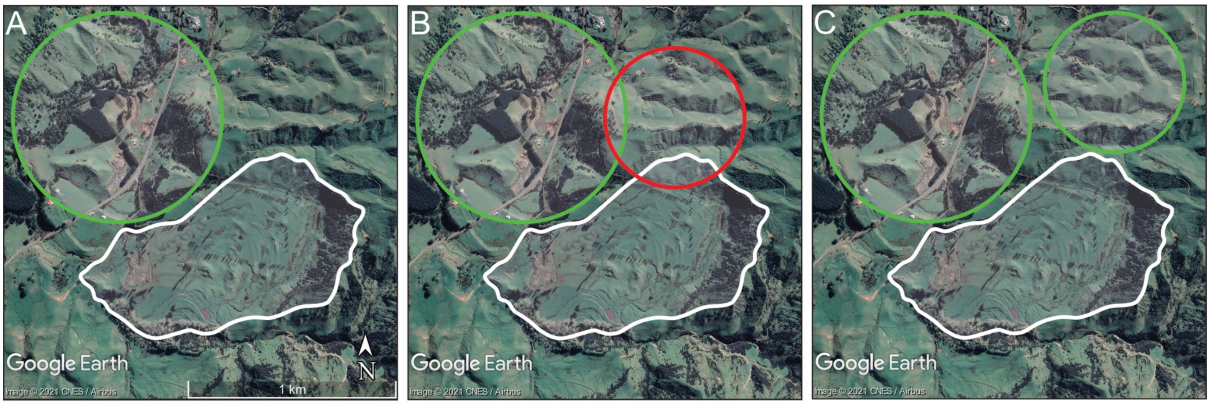


*Figure 4.4 Methodology for placement of landslide absence objects. A) In order of descending size, landslide absence circles (green) are placed randomly. B) If a landslide absence circle (red) is placed so that it intersects another landslide absence (green) or landslide (white), it is randomly relocated until it is not touching another feature, as in C).*

### *4.4.3 Susceptibility Factor Datasets*

Within our model, we included 17 susceptibility factors (covariates) that have been found to influence soft-rock landslide occurrence in previous studies (Table 4.1). Broadly, these datasets can be grouped within four categories of susceptibility factors: geologic and tectonic factors, geomorphic factors, climatic factors, and land use factors. Three of these covariates are categorical factors that correspond to the age of geological units within our study area.

| Susceptibility Factor | Category | Source |
|---:|---:|---:|
| Rainfall | Climatic | NZ Ministry of Environment |
| Soil Moisture | Climatic | NZ Ministry of Environment |
| Uplift | Geologic | Pulford and Stern 2004 |
| Dip Angle | Geologic | Rattenbury and Isaac 2012 |
| Distance to Active Fault | Geologic | Rattenbury and Isaac 2012 |
| Distance to Fault | Geologic | Rattenbury and Isaac 2012 |
| Early Pleistocene Sediments | Geologic | Rattenbury and Isaac 2012 |
| Quaternary Sediments | Geologic | Rattenbury and Isaac 2012 |
| Predicted Peak Ground Acceleration (2475 yr return) | Geologic | Stirling et al 2012 |
| Stream Power Index | Geomorphic | GRASS GIS r.watersheds tool |
| River Incision | Geomorphic | Litchfield and Berryman 2006 |
| Maximum Elevation | Geomorphic | NZSoSDEM |
| Eastness | Geomorphic | NZSoSDEM, Horn 1981 |
| Northness | Geomorphic | NZSoSDEM, Horn 1981 |
| Slope | Geomorphic | NZSoSDEM, Horn 1981 |
| Slope and Bedding Alignment | Geomorphic | Santangelo et al 2015 |
| Forest Cover | Land Use | NZ Ministry of Environment |

*Table 4.1 Covariates used within our landslide susceptibility analysis. All covariates have been found to be useful predictors of landslides in previous studies.*

We obtained geologic information for the study area from New Zealand's national 1:250,000 resolution geologic map (Rattenbury and Isaac, 2012). We broadly grouped geologic units by geologic age, which reduced the number of lithologic covariates while also preserving key differences in rock strength. We believe this simplification is justified because the strength of the Whanganui Basin sediments is broadly controlled by the degree of burial and diagenesis they underwent, which is well correlated with age (Pulford and Stern, 2004). Areas with limestone deposits or syndepositional clay units clearly deviate from this assumption but because they do not occur broadly enough (limestones) and are not mapped with adequate accuracy (clay units), it was not feasible to include them as separate variables. In keeping with our desire to limit the number of categorical variables within our analysis, the percent forest cover (both native and plantation forests) of each feature is the only land use covariate we included in our analysis.

We used the national geological map to produce the distance to faults (relict and active) and distance to active faults (active only) covariates. We created an interpolated map of bedding and slope alignment using structural data from the national geologic map and the GRASS GIS r.surf.ba tool (Santangelo et al., 2015). Uplift data was provided by Pulford and Stern (2004). We also included probabilistic peak ground acceleration data for a 2475 year return period earthquake as predicted by the corrected 2010 New Zealand National Seismic Hazard Model (Stirling et al., 2012) as another way to assess the role of earthquakes in landslide generation.

Geomorphic covariates were derived from the NZSoSDEM v1.0 (Columbus et al., 2011) digital elevation model (DEM). The NZSoSDEM is based on an interpolation of a 20 m elevation contour map, has a horizontal resolution of 15 m and a vertical accuracy of ± 5 m. Slope, slope aspect (northness and eastness) were calculated using the GRASS GIS r.slope.aspect tool, which uses the equations found in Horn (1981) to calculate these metrics. Northness and eastness are defined as the cosine and sine transformations of a circular, 360-degree representation of aspect (Harshburger et al., 2010) because circular variables cannot be used within our chosen model. While others have found measures of terrain curvature and roughness to be useful for predicting the occurrence of landslides (Budimir et al., 2015), we chose to exclude them from our analysis because they better represent the results of landslide occurrence (i.e. effect), instead of landslide susceptibility factors (i.e. cause), for the size of landslide investigated here. We also included the maximum elevation of each feature as a covariate, as well as an index for river incision.

Our index for river incision is based on the work of Litchfield and Berryman (2006), but it has been fully automated within the GRASS GIS environment. We created our incision index by first using the r.geomorphons tool (Brown, 2016) to identify summits within our study area. We then masked our DEM using our summit dataset and used the regularized spline method to interpolate a raster of filled-valley elevation from the summit elevation dataset. The actual DEM was then subtracted from our filled-valley DEM to derive a raster that represents the depth of expected river incision. The stream power index was calculated using the GRASS GIS r.watersheds tool by multiplying the upslope contributing area by the tangent slope at each pixel. We used the $A^T$ least-cost path multiple flow direction algorithm to calculate the upslope contributing area (Holmgren, 1994). Finally, from New Zealand's Ministry for the Environment, we obtained maps of yearly average rainfall and soil moisture for the years 1972 to 2013, which we used to represent average rainfall and soil moisture.

#### *4.4.4 Logistic Regression Model*

By summarizing the raster covariate datasets at each landslide and absence feature, we created data matrices for the ten absence sample sets and the landslide sample set. We conducted the regression analysis separately for translational and rotational rock slides to determine if differing susceptibility factors contributed to their occurrence. We then combined each of the ten absence datasets with the landslide dataset to create the datasets we use in our binary logistic regression models. To limit covariance within our datasets, we calculated the variance inflation factor (VIF) for all covariates within our dataset and removed covariates with a VIF score of ten or more in keeping with Heckman et al. (2014).

Via this process, the range and standard deviation of the landslides' elevation values were removed from the analysis. Finally, before the regressions were conducted, covariate values were converted to their standard score using the formula:

*Equation 4.1 Standardization of a sample member*

$$z = \frac{x - \mu}{\sigma}$$

Where $z$ is the standard score, $x$ is the data value, $\mu$ is the covariate's mean and $\sigma$ is the covariate's standard deviation. This conversion normalizes the distribution of the covariate values, which in turn allows the model coefficients of each covariate to be interpreted as a measure of covariate importance (Lombardo and Mai, 2018).

Once these covariates were standardized, we used a five-fold cross-validation approach to perform five regressions within each of the ten landslide and absence dataset combinations. This resulted in fifty total regressions for each landslide type. Similarly to Lombardo and Mai (2018) we used a LASSO regularization within our model to penalize model complexity. We selected a scaling parameter of 5 for all model iterations because it was found to be the largest value that did not compromise model accuracy.

In keeping with the work of Lombardo and Mai (2018), we used standardized model coefficients and jackknife regression analyses to assess the importance of model covariates. Jackknife regression analysis highlights the importance of covariates in univariate and multivariate contexts by first performing regressions that use only one covariate at a time, and then performing regressions that exclude one variable at a time. The single variable regressions highlight the univariate predictive power of covariates, while the single variable exclusion regressions highlight the contribution of covariates in a multivariate setting. In the latter case, larger drops in performance correspond to higher variable importance. Since we standardized covariate values prior to use within the regressions, all resulting coefficient values are in the same unitless scale and can be directly compared.

## 4.5 Results

### *4.5.1 Landslide Dataset Characteristics*

In total, we mapped 638 translational rock slides and 233 rotational rock slides for a total of 871. The translational rock slides tended to be larger than the rotational rock slides, with average sizes of 36.4 ha and 24.1 ha respectively (Figure 4.3). Both landslide types had a wide distribution of sizes and many landslides larger than 100 ha were mapped. The size distributions of both translational and rotational rock slides (Figure 4.3) displayed power law distributions that are typical for landslides (Malamud et al., 2004), but the translational rock slide distribution did include more landslides that were larger than 50 ha. Additionally, while both types of landslides occurred on relatively shallow slopes, rotational landslides tended to occur on steeper terrain (average slopes of 18.2° versus 16°) (Figure 4.5).

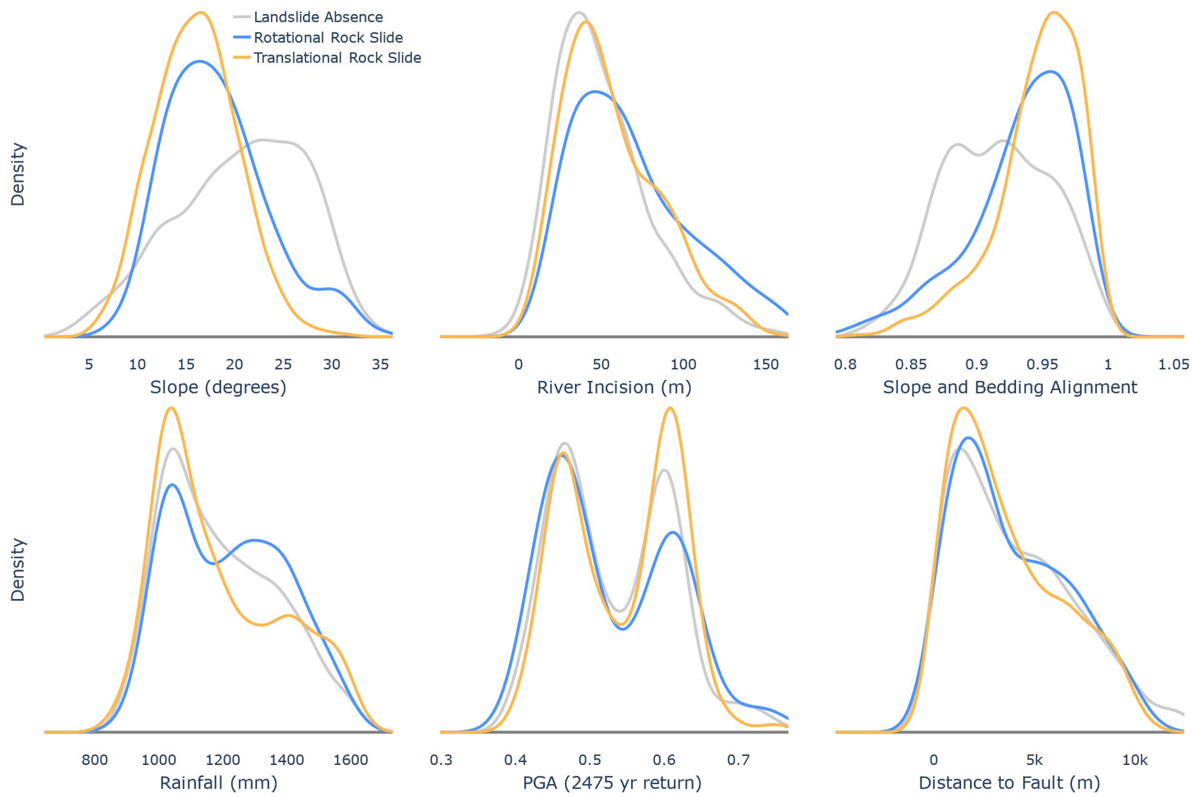


*Figure 4.5 Susceptibility factor distributions of selected covariates for translational rock slides, rotational rock slides, and landslide absences. Slope and slope and bedding alignment show the largest differences in distribution shape between the landslide absence and landslide presence distributions. All three data sets have nearly identical distance to fault distributions.*

The correlation between each of the seventeen susceptibility factors included in our analysis can be found in Figure 4.6. While slope and bedding alignment had a variance inflation factor (VIF) of less than ten, it was still highly correlated with slope. This is likely because slope is a component of the calculation used to derive slope and bedding alignment. Slope and bedding alignment also appears to have higher than average correlation with many other covariates. Forest cover also shows a moderate correlation with slope, suggesting that steeper slopes have preferentially not been deforested or have been preferentially converted to exotic tree plantations.

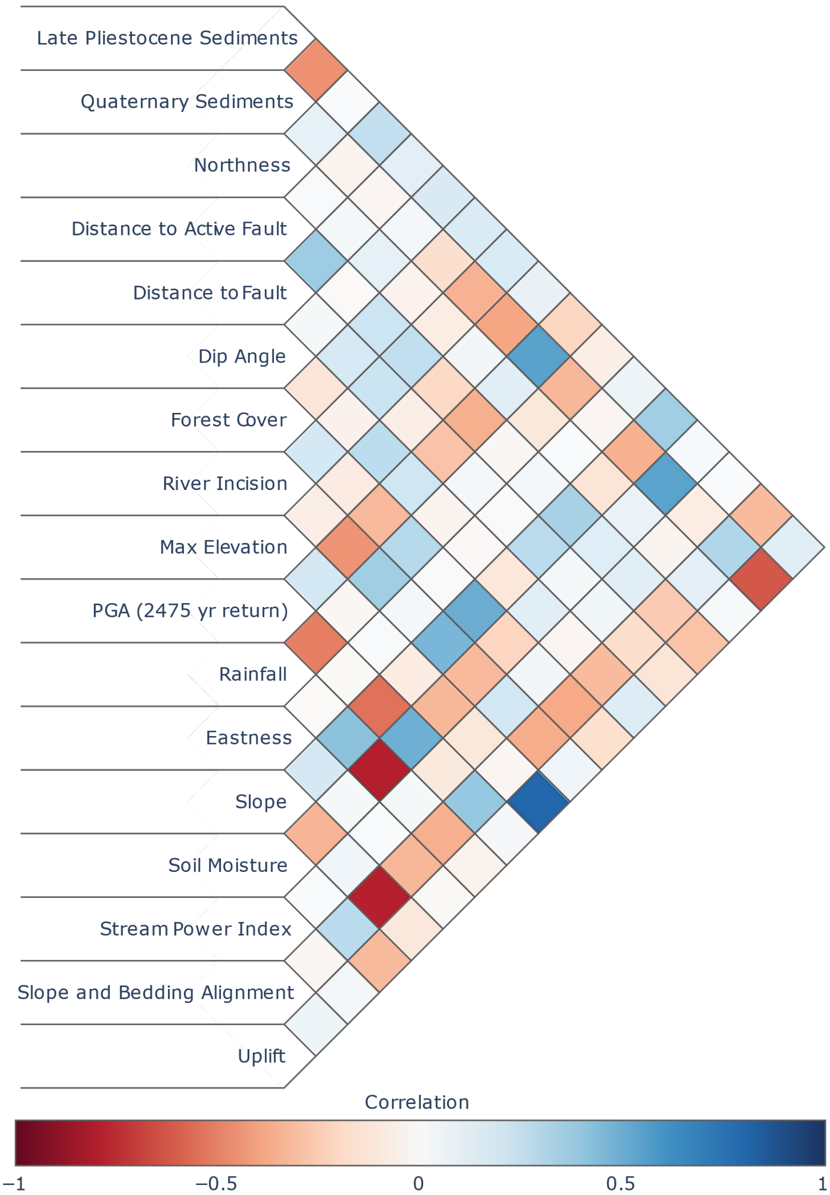


*Figure 4.6 Correlation matrix of susceptibility analysis covariates. Each square corresponds to the correlation between the covariates with which the square's sides intersect. Dark blue squares correspond to large positive correlations and dark red squares correspond to large negative correlations. Large correlations exist between non-independent covariate pairs (e.g. rainfall/soil moisture, slope/slope and bedding alignment, and PGA/quaternary sediments) and between slope/forest cover.*

### *4.5.2 Model Performance*

The median accuracy for the translational rock slide regressions was 0.74 and the median area under the receiver-operator curve (AUC) was 0.82, while for rotational rock slide regressions, the median accuracy was 0.72 and the median AUC was 0.79. While these values are similar, value distributions of accuracy and AUC were larger for the rotational rock slides (Figure 4.7). This is likely attributable to the smaller number of landslides present within the rotational rock slide dataset (233 versus 638). The accuracy of our models is on par with previous landslide susceptibility studies (Budimir et al., 2015; Reichenbach et al., 2018; Smith et al., 2021) and thus we feel confident interpreting the influence of model covariates as a measure of their impact on landslide susceptibility.

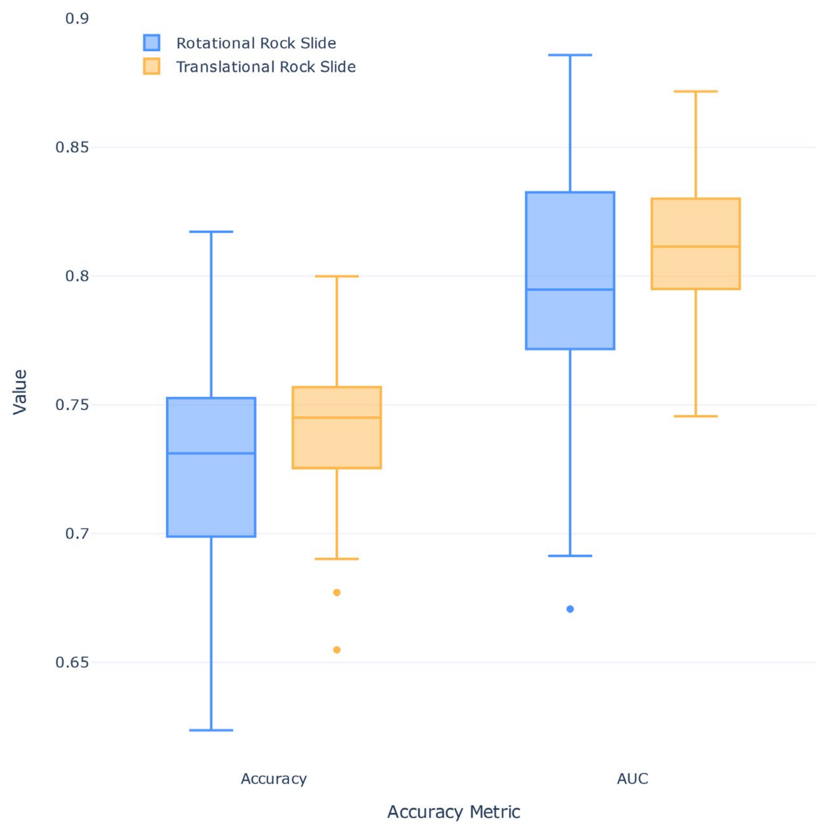


*Figure 4.7 Study accuracy expressed as overall accuracy and area under the receiver-operator curve (AUC). In general, our regression analyses' performances are on par with previous studies.*

### 4.5.3 Influence of Susceptibility Factors

Figure 4.8 summarizes the model coefficients for each of the fifty translational and rotational rock slide regressions. In descending order of coefficient magnitude, river incision, slope, forest cover, slope and bedding alignment, and rainfall had the largest average coefficient magnitudes. In the case of slope and forest cover, negative coefficients indicate that increases in the given covariate are associated with a decrease in the likelihood of a landslide occurring. Also, while coefficient values are similar for the two landslide types, coefficients for slope and forest cover had larger coefficient magnitudes in translational rock slide regressions, while river incision and the stream power index had larger coefficient magnitudes in rotational rock slide regressions. The predicted peak ground acceleration from New Zealand's seismic hazard model, distance to faults, and distance to active faults did not have large coefficient values for either landslide type.


*Figure 4.8 Median regression coefficients for our susceptibility analyses. Standardization of the covariates prior to performing the regression allows for direct comparison of the model coefficients. Based on this data, we identified river incision, slope, forest cover, slope and bedding alignment, and rainfall as the most predictive covariates.*

For the jackknife single variable regressions, slope and bedding alignment was the most predictive covariate for translational rock slides and the second-most powerful predictor for rotational rock slides (Figure 4.9). River incision was the most predictive covariate for rotational slides, but it had a noticeably smaller AUC when used to predict translational rock slides. Slope was also a powerful predictor of both translational and rotational rock slides, but contrary to the slope threshold model, lower slope values were associated with landslide occurrence. Overall, single variable regressions had higher AUCs when used to predict translational rock slides than when used to predict rotational rock slides.

The jackknife single variable exclusion regressions displayed far fewer differences between translational and rotational rock slides (Figure 4.10). In both cases, excluding forest cover or river incision from the analysis had a large impact on model performance. Removing slope and bedding alignment and slope however did not appear to decrease model AUC. In part, the strong correlation between slope, slope and bedding alignment, and many other covariates likely resulted in lower impacts to model performance even though they are two of the strongest predictors of landslide occurrence in the univariate case.

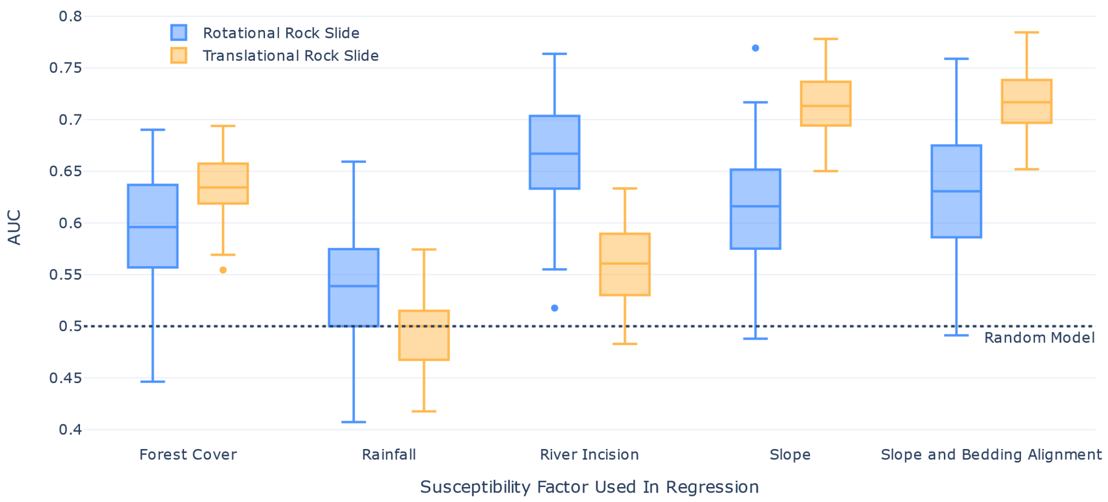


*Figure 4.9 Accuracy of single variable regressions for the five most predictive covariates. When considering regressions that contain a single variable, higher AUCs correspond to greater importance. Slope and bedding alignment is the single best predictor of translational rock slide occurrence, and river incision is the best predictor of rotational rock slide occurrence.*

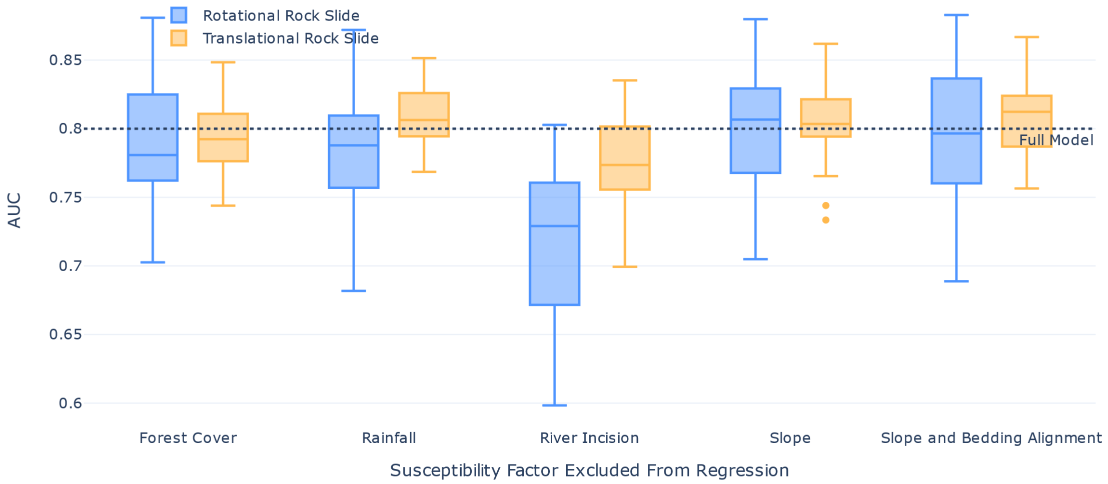


*Figure 4.10 Accuracy of single variable exclusion regressions for the five most predictive covariates. When considering regressions that have excluded a particular covariate, lower AUCs correspond to a greater importance of that variable. Excluding the river incision covariate from the analyses appears to have the largest negative impact on the analyses.*

## 4.6 Discussion

Overall, our results indicate that the occurrence of soft-rock landslides within our study area correlated with river incision, slope and bedding alignment, forest cover, and rainfall. The rapid uplift and weak structure of the Whanganui Basin sediments make them particularly prone to soft-rock landslides, but failure does not occur uniformly across the region. Our analysis suggests that river incision and slope and bedding alignment are the key factors that control long-term patterns of failure, but that the relative influence of these factors differs for translational and rotational rock slides.

#### *4.6.1 Influence of Earthquakes*

Notably, distance to faults and active faults were two of the least predictive covariates within this study, and in many cases their coefficients were set to zero during the LASSO regularization (Figure 4.8). This finding, along with the low importance of the peak ground acceleration (PGA), suggests that earthquakes are not an important cause of these landslides or that co-seismic triggering is highly dependent on priming by other factors. This finding contradicts the earlier work of Rees et al. (2019), who argued that a high number of soft-rock landslides proximal to faults within a subset of the Whanganui Basin suggested that earthquakes are an important triggering mechanism. However, because there are many faults within the study area, our approach shows that randomly placed landslide absences have the same tendency to occur next to faults (Figure 4.5). Our findings are consistent with a field investigation by Massey et al. (2016a) which showed that moderate earthquake ground accelerations (0.94 $m/s^2$) induced no movement of a critically-stable landslide in our study area. Modelling by Massey et al. (2016a) further suggested that earthquakes have contributed little to the longer-term movement of the landslide, with greater contributions from river incision and changes in pore water pressure. Earthquakes may still have an important role in triggering slope failures once other factors have sufficiently prepared slopes for failure, but the reasons for earthquakes playing a seemingly minor role in both landslide distributions and movement at our study site remains an area of active investigation.

#### *4.6.2 Influence of Rainfall and Land Cover*

In contrast to fault proximity, we found that mean annual rainfall and forest cover were both useful predictors of soft-rock landslide occurrence. The increased likelihood of landslide occurrence in areas with higher rainfall is supported by the previous results from the long-term monitoring of the Utiku and Taihape landslides (Massey et al., 2013). In this work, increases in pore-water pressure were found to accelerate the movement of these landslides when the landslides were in marginally unstable states (i.e. following toe erosion), and it is likely that areas with higher rainfall experience high pore-water pressure for longer periods of time. Additionally, high rainfall may contribute to river incision when sediment flux and tectonic controls allow.

While the failure surfaces of these landslides are too deep to benefit from the increased cohesivity afforded by tree root systems (e.g. failure surfaces for the Taihape and Utiku landslides are up to 30 and 70 m deep, respectively) (Massey, 2010), our analyses show that forest cover appears to decrease the likelihood of soft-rock landslide occurrence. While this finding could be due to the increased difficulty in identifying landslides in forested imagery, a separate landslide survey that used circa 1950s pre-plantation imagery did not find a higher number of landslides in the now forested areas. Additionally, if landslides are difficult to identify under forest cover we might expect that we would only be able to identify the largest landslides in these areas. However, when we compare the size distributions of forested and non-forest landslides in our dataset, we do not see this trend (Figure 4.11).

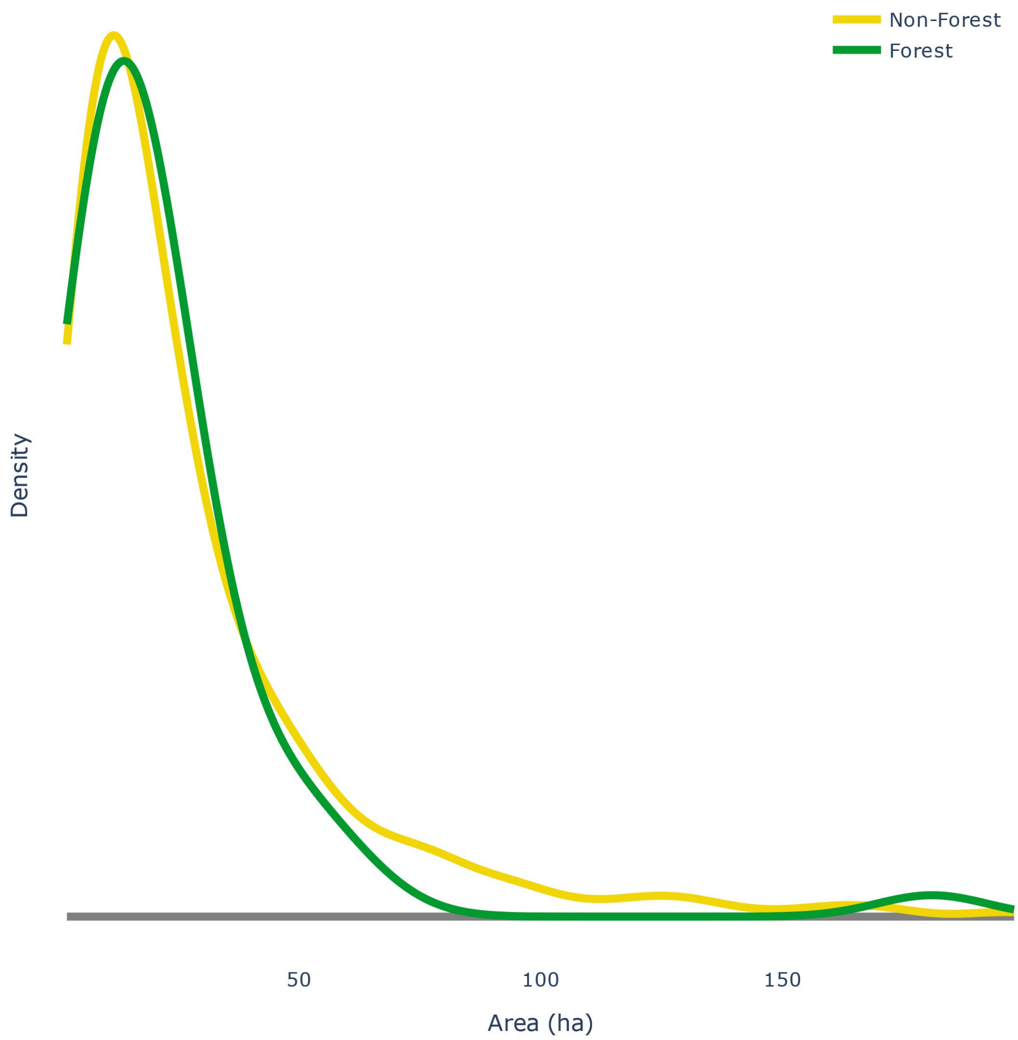


*Figure 4.11 Landslide size distribution for forested and non-forested landslides (with a cut-off of 50% forest cover). Both forested and non-forested landslide size distributions conform to the power law distributions typical of landslide inventories (Malamud et al., 2004). The lack of deviation from this distribution for forested landslides suggests that we are accurately mapping soft-rock landslides in forested terrain.*

Another possibility is that forests have been preferentially preserved in steep areas that were difficult or unsuitable for pasture conversion, as evidenced by the relatively strong correlation between forest cover and slope (Figure 4.6). Thus, the lack of landslides in forested regions may be better explained by the factors that allow the landscape to maintain steep slopes, than by the presence of forest. If however forest cover is directly reducing the likelihood of soft-rock landslide occurrence, this is likely because the evapotranspiration of the forest cover is leading to a reduction of pore water pressure at the failure surface. An interesting consequence of this hypothesis is that many of these landslides could have formed in response to native forest removal in the 19$^{th}$ century, which would make them much younger than they are typically believed to be (e.g. the postglacial landslide initiation in the Waipaoa) (Bilderback et al., 2015).

### *4.6.3 Influence of River Incision*

In agreement with previous research, our analysis also identified river incision as a key predictor of landslide occurrence. Research at the Utiku and Taihape landslides (Massey et al., 2013; McSaveney and Massey, 2017) and in the nearby Waipaoa catchment (Bilderback et al., 2015), indicate that river incision can promote failure in two ways. Local incision can lead to the removal of material at the base of slopes which can destabilize toe material and promote movement along exposed clay layers that act as preferential failure surfaces (Massey et al., 2016a). Work in the Waipaoa catchment has shown that uplift and climatic cycles can induce catchment-wide river incision which can cause these processes to occur throughout a catchment. The regional scale influence of river incision on landslide occurrence is also well established by the slope threshold model. While this result is unsurprising, river incision is one of the few influential factors identified that operates on human timescales. Thus, monitoring where incision occurs may help us better predict where new landslide movement is likely to occur.

### *4.6.4 Influence of Structural Controls*

The influence of bedrock structure on landslide occurrence has been previously documented (Santangelo et al., 2015), but our inclusion of slope and bedding alignment within a regional-scale susceptibility model is a novel approach. Furthermore, its predictive power within our model and its differing relationship with translational and rotational rock slides suggests that variations in slope and bedding alignment could explain some aspects of landslide behaviour unexplained by a universal slope threshold model. Within the Whanganui Basin, where slope and bedding are not aligned, the slopes are generally stable. Landslides are less likely to occur here and the average slope attained in these settings is much steeper than in failure-prone areas. Conversely, in areas where slope and bedding are aligned, even gentle slopes are prone to failure along weak bedding planes. For instance, within our study, stable areas had an average slope of 20.6°, while translational and rotational rock slides had lower average slopes (16° and 18.2° respectively) (Figure 4.5).

Since at least moderate slope and bedding alignment appears to be needed to create rotational failures in this setting, some portion of rotational failure surfaces are likely occurring along bedding planes, contrary to our initial hypothesis. It may be that in cases where there is only oblique slope and bedding alignment, translational failures do not occur, but increased river incision can induce rotational failures that partially occur along bedding planes. In either the moderate or strong slope and bedding alignment case, this alignment appears to reduce the threshold slope angle of the landscape. Thus, the tendency of landslide failures to occur along weak bedding planes has led to a system in which there is no universal slope threshold. Instead, the threshold slope for a given hillside decreases as the degree of alignment between the landscape's orientation and bedrock's orientation increases. It should be noted however that this relationship only holds for soft-rock landslides that are structurally controlled, with the traditional slope threshold model holding true for other locations and landslide types in our study area. Studies of shallow landslides in this area (Dymond et al., 2006) show that increasing slope is directly related to an increase in shallow landslide occurrence, in agreement with the traditional slope threshold model. Similarly, our finding likely does not apply to all soft-rock landslides, (Roering et al., 2015), but it is likely to be applicable to many other areas where preferential failure surfaces align with bedrock orientation (Chittenden et al., 2014; Nunes et al., 2015; Santangelo et al., 2015).

#### *4.6.5 Utility of Landslide Type Classification*

Our decision to analyse the occurrence for translational and rotational rock slides separately, allowed us to better understand the dynamics of landslide occurrence. For instance, while river incision and slope and bedding alignment were useful predictors of both landslide types, our analysis showed that river incision was more influential in rotational rock slide models. Conversely, slope and bedding alignment was more influential in translational rock slide models. These findings were key to our interpretation of the results and suggest that performing separate susceptibility analyses for landslides with differing failure geometries can improve the accuracy of landslide susceptibility models.

## 4.7 Conclusion

In this study, we performed landslide susceptibility analyses for translational and rotational rock slides within the Whanganui Basin region of New Zealand. We utilised seventeen covariates that corresponded to geologic, geomorphic, climatic, and land use factors that have been previously shown to impact landslide occurrence. Overall, river incision, slope, slope and bedding alignment, forest cover, and rainfall were found to be the most predictive of landslide occurrence. Notably, no earthquake-related covariates were found to be predictive of landslide occurrence, suggesting that earthquakes are not an important primary causative factor for these landslides.

These results provide us two key insights. First, there are measurable differences in how landslides with differing failure geometries form and accounting for these differences can improve the utility of susceptibility analyses. Second, the alignment of slopes and the underlying bedding is a key predictor of landslides that helps to explain the spatial organization of landslides and provides a rationale for why landslide-prone sections of our study area have lower slopes. Within other soft-rock landslide prone landscapes, a structurally-dependent slope threshold model may be able to explain patterns in landslide occurrence and local slope gradients that a universal slope threshold model alone cannot.

## 4.8 Acknowledgements

Thank you to our colleagues at GNS Science who provided early guidance in the development of this study, and to Anna Pulford and Tim Stern of Victoria University of Wellington for the use of their data on uplift rates of the Whanganui Basin. Additionally, thank you to Horizons Regional Council for the use of their digital surface model. This research was supported by the New Zealand Ministry of Business, Innovation and Employment research program “Smarter Targeting of Erosion Control (STEC)” [Grant Number C09X1804] and by the MBIE Strategic Science Investment Funded Hazards Programme at GNS Science.

## Synthesis of Chapter 4 for Thesis

In this chapter I described the mapping of soft-rock landslides in the Whanganui Basin (Objective 1). In total, I mapped 871 landslides in the basin, and classified each according to Varnes's landslide classification schema. Developing an accurate map of soft-rock landslides was a necessary first step towards evaluating landslide activity across the region, and this map is used throughout Chapters 5 and 6 to meet objectives 4-5. While this dataset does not yet contain activity state information (Objective 4) this will be added to the dataset via the InSAR analysis described in Chapter 5 and conducted in Chapter 6. I also used this dataset to conduct my landslide occurrence factor analysis (Objective 2), which assessed why the soft-rock landslides of the region occur in particular locations. This analysis showed that slope, slope and bedding alignment, and river incision were the most important preparatory factors, and that seismic forces were not an influential factor. In Chapter 6 the findings of this analysis are compared to the key factors identified for the landslide activity factor analysis conducted using the InSAR activity state information.

# Chapter 5 A Reproducible Framework for Slow-Moving Landslide Activity Detection and Monitoring

## Introduction to Chapter 5 of Thesis

Chapter 5 addresses Objective 3 (develop a remote sensing framework for identifying the activity state and estimating the movement rates of soft-rock landslides). This objective was necessitated by the large number of landslides in the basin (871), which made it impossible to complete Objective 4 and Objective 5 within the constraints (budgetary and time) of my PhD project without utilizing remote sensing techniques. While other studies have used InSAR and sPOT to study landslides, this chapter demonstrates how on-demand processing services can be utilized to decrease the analysis time for these methodologies without sacrificing reliability. Additionally, it highlights and discusses the implications of some of the key methodological choices made, namely image network selection, that are often excluded from discussions of InSAR and sPOT analyses.

*This chapter will soon be submitted to Remote Sensing of Environment as:*

Williams, F., McColl, S., Fuller, I., Smith, H., Neverman, A., 2022. A reproducible framework for slow-moving landslide activity detection and monitoring. Remote Sensing of Environment.

## 5.1 Abstract

Landslides are a widespread natural hazard that can significantly impact society and the environment. Quantitative landslide hazard assessments require information on the frequency and movement of landslides, but this information is usually difficult and costly to produce. Remote sensing analyses such as time-series interferometric synthetic aperture radar (InSAR) and time-series sub-pixel offset tracking (sPOT) offer ways to identify landslide activity and measure movement efficiently. However, these techniques must be combined into a widely available and computationally efficient framework if they are to be adopted by practitioners. This study presents a workflow for remote landslide monitoring that combines InSAR and sPOT analyses and relies on cloud-computing services, open-source Python libraries, and Jupyter notebooks to create an efficient and reproducible framework. By comparing our results to independent validation datasets, we find that our framework can accurately identify large slow-moving landslide activity with an accuracy of 91% (Cohen's kappa of 0.76) and can measure the movement of landslides which have average annual speeds of 2.05 m/yr with a mean absolute error of 0.74 m/yr. Because of this framework's reliability, accessibility, and ease of use, we believe that it represents a cost-effective, reproducible, and reliable framework for the remote monitoring of active landslides.

## 5.2 Introduction

Landslides are a well-known natural hazard that can affect both the built and natural environment (Schuster and Highland, 2001; Turner, 2018), and large slow-moving landslides present a unique hazard (Agliardi et al., 2013; Crosta et al., 2013; Korup and Weidinger, 2011; Roering et al., 2015). For example, due to their large size these landslides, they can transport considerable amounts of material that can overwhelm or block river channels (McColl et al., 2022; Xu et al., 2009). Additionally, they can be long-lived and remain active for long periods (Larsen and Montgomery, 2012), but their slow movement rates (~1 cm/yr – 10 m/yr) can make it difficult to discern their current activity states. This, in turn, can lead to infrastructure issues when structures are built on top of or across a landslide's surface (e.g. (McSaveney and Massey, 2017)).

Governmental and research institutions are aware of these concerns and often work together to obtain up-to-date information on landslide presence and activity (Rosser et al., 2017; Schmitt et al., 2017). Due to their relative ease of collection and utility, data on the location and size of landslides is usually available, and is commonly organized within static landslide inventories (Guzzetti et al., 2012) collected using historical or geomorphological evidence. These datasets may include information on landslide age or timing (Massey et al., 2018; Pánek, 2019; Pánek and Klimeš, 2016), which can be useful for quantifying landslide frequency or assessing trigger thresholds. They can also be used to assess which landscape factors are predictive of landslide failure (Massey et al., 2018; Williams et al., 2021). However, they typically do not include information on a landslide's activity state or its movement rate, which, along with location and frequency, are important for quantitative hazard assessment.

Since most static landslide datasets rely on historical and geomorphological information to identify landslide extents, it is common to include landslides within these datasets that may no longer be active and are unlikely to become active in the future (Williams et al., 2021). Thus, while inactive (relict) landslides are useful for evaluating landslide frequency and magnitude relationships, they say little about which landslides pose the most significant risk to infrastructure and the natural environment. This can make it challenging to prioritize engineering and conservation efforts effectively. In-field geodetic surveys can be used to obtain information on landslide activity (Massey et al., 2013), but these types of surveys are often too costly to conduct for more than a few landslides. Recent advances in remote sensing technology do, however, offer alternatives to field-based monitoring. In particular, researchers have started to explore using interferometric synthetic aperture radar (InSAR) (Antonielli et al., 2019; Shi et al., 2020; Xu et al., 2021a) and feature tracking methodologies such as sub-pixel offset tracking (sPOT) (Amitrano et al., 2019; Dai et al., 2020; Dille et al., 2021) to monitor landslides without requiring in-field instrumentation.

InSAR is a remote sensing technique that can be used to measure Earth surface displacements and has been employed to monitor tectonic (Hooper et al., 2012), volcanic (Schaefer et al., 2019), and landslide processes (Wasowski and Bovenga, 2014). Recently, the consistent and high-quality data produced by the European Space Administration's Sentinel-1 C-band (5.55 cm wavelength) synthetic aperture radar (SAR) mission has led to an explosion of InSAR research across these fields. Despite the broad utility of InSAR, some fundamental limitations make InSAR landslide monitoring challenging.

Most of these limitations relate to the introduction of decorrelation noise by factors such as vegetation, landslide movement, and propagation delays in the atmosphere (Ahmed et al., 2011; Dille et al., 2021; Wang et al., 2019). The first factor is particularly acute in natural settings where no artificial structures exist. SAR sensors with longer wavelengths, such as the upcoming NASA-ISRO SAR (NISAR) mission, which uses an L-band (24 cm wavelength) sensor, will likely be less sensitive to some of these effects, but these data are not yet available. Others have tried to overcome these limitations using existing SAR data by installing corner reflectors that increase the strength of the returned SAR signal at their location (Bovenga et al., 2012; Crosetto et al., 2013). However, like geodetic ground surveys, this technique works best when the landslides of interest are accessible and are known to be active a priori. Alternatively, new filtering techniques such as Bekaert et al.'s (2020) double-difference filter have been shown to increase the strength of the local deformation signal while also reducing the negative impacts of atmospheric propagation delays and other sources of decorrelation.

InSAR is also insensitive to deformation that exceeds the half-wavelength distance (2.78 cm for Sentinel-1) between the image capture dates of the InSAR pair and can only measure movement in the satellite's line-of-sight (LOS) direction. In cases where this threshold is exceeded or the satellite's LOS measurements are inadequate, the tracking of pixels in subsequent images of the ground surface (SAR or reflectance-based) can provide an alternative solution for monitoring landslides (Amitrano et al., 2019; Dille et al., 2021). As opposed to InSAR, which measures changes in distance between an antenna and the ground surface, feature tracking approaches track the horizontal movement of features between two temporally-separated images using a statistical approach (Bickel et al., 2018). Early feature tracking approaches relied on manual tracking of features between two images, for instance the tracking of human-identifiable objects such as fence posts or isolated trees (Mackey and Roering, 2011). However, new feature tracking techniques such as sPOT use statistical measures of pixel similarity to autonomously track feature motion at the sub-pixel scale (Dille et al., 2021; Leprince et al., 2007). Because sPOT does not rely on any of the unique characteristics of SAR data, sPOT analyses can be conducted using either SAR or reflectance-based imagery.

Although sPOT can monitor landslide movement that exceeds the movement speeds identifiable by InSAR, it is less sensitive to slow movements. The sPOT technique should theoretically be able to detect movement that is greater than $1/20^{th}$ the pixel size (Leprince et al., 2007) of the images used to perform the sPOT analysis, but this limit may be closer to $1/10^{th}$ of the pixel size in practice (Bickel et al., 2018; Mulas et al., 2020). Attempts to increase sPOT accuracy have involved the use of multiple sPOT observations within a time-series analysis similar to an InSAR small baseline subset (SBAS) approach (Dai et al., 2020; Li et al., 2020; Stumpf et al., 2017) and they have had some success. However, these techniques and developments have mostly been applied to single landslides, so their applicability and ease of application to large regions with multiple landslides remains under-developed. Furthermore, no studies have attempted to leverage the benefits of both InSAR and sPOT techniques together within a study area exceeding 1000 $km^2$.

In addition to the technical challenges of remote landslide monitoring, these techniques suffer from computational and utilitarian deficiencies that severely limit their adoption and reproducibility, especially at regional scales. Fragmentation of scientific software across multiple software platforms and programming languages makes it difficult to combine methodologies into a coherent framework. Additionally, most scientific code used to perform analyses are still not publicly available and instead must be requested from the author by each interested scientist (Nosek et al., 2015; Stodden et al., 2016). Unfortunately, this system limits the rate at which new techniques can be adopted and iterated upon (Lees, 2012). Luckily, the scientists that make up the geoscience community has begun to recognize and grapple with these issues (Gil et al., 2016). In particular, they have started to coalesce around the Python programming language and tools found therein for their scientific analyses (Harris et al., 2020). Today, many essential software packages for InSAR and sPOT processing are available in Python, including the Miami InSAR Time-series in Python (MintPy) (Yunjun et al., 2019) and the Autonomous Repeat Image Feature Tracking (AutoRIFT) (Lei et al., 2021) packages. Additionally, scientific programming notebooks such as Jupyter IPython notebooks now provide a platform for describing and running scientific analyses simultaneously (Kluyver et al., 2016), aiding reproducibility.

Acquiring the images for and computing InSAR/sPOT pairs requires more computational resources than are typically available to the average scientist. To address this, cloud-computing platforms, such as Google Earth Engine (Gorelick et al., 2017), the Alaska Satellite Facility's Hybrid Plugin Processing Pipeline (HyP3) (Hogenson et al., 2016), and Microsoft's Planetary Computer have begun to provide cloud-based InSAR pair generation and imagery preparation services to scientists at no cost. Using these services drastically reduces the computer infrastructure needed to perform these analyses, allowing more scientists to apply these remote sensing tools to their research. In addition to these logistical factors, InSAR and sPOT analyses to date have typically lacked rigorous comparison to external data for validation. A more significant effort needs to be made to compare these analyses to external data to assess their validity, applicability, and to evaluate uncertainties.

With the co-advent of the creation of open-source InSAR and sPOT utilities within a single programming language and low-cost cloud computing services for scientists, we believe that it is now possible to produce an efficient and unified InSAR and sPOT framework that enables scientists to conduct remote landslide monitoring within natural terrain. This paper describes and tests an InSAR and sPOT-based framework that utilizes cloud computing platforms and open-source principles to create a reliable and reproducible remote large landslide monitoring system. Furthermore, this framework is entirely contained within Jupyter notebooks that are available online and can be freely downloaded at any time (see the Code and Data Availability section for details).

## 5.3 Methods

### *5.3.1 Validation Datasets*

To assess the accuracy of the time-series InSAR and time-series sPOT results, we compared the output of these analyses to independent data collected within the south-central portion of the North Island of New Zealand (Figure 5.1). This area is part of a back-arc basin complex associated with subduction along the Australian-Pacific plate boundary. It is composed of young (0-5 Ma) down lapping sandstones, mudstones, and shales that dip gently to the southwest. Uplift in this region has led to stunted diagenesis and low internal strengths of the rocks, resulting in high rates of landsliding within the area. In particular, our recent study (Williams et al., 2021) identified a suite of large slow-moving landslides in this region that range from 10 ha to greater than 500 ha in size that cover roughly 8% of the region's surface area. Due to these landslides' slow movement rates, it is difficult to determine which of these landslides are active and which are inactive without expensive field campaigns.

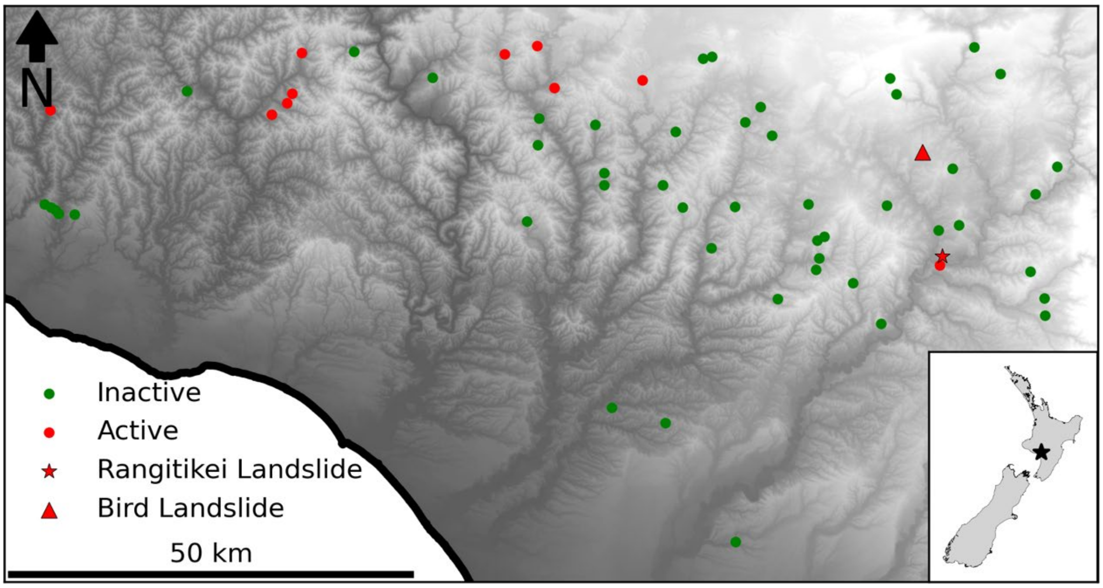


*Figure 5.1 Map of the study area and the validation landslide locations used in this study. A binary assessment of either activity or inactivity was conducted at the green dots (Inactive) and red dots (Active). In addition, a manual feature-tracking analysis using high-resolution imagery was conducted at the Bird Landslide (red triangle), and a dGNSS survey was conducted at the Rangitikei Landslide (red star).*

To determine whether our InSAR analysis can reliably predict whether a given landslide is active or inactive, we have selected a subset of landslides in this region that will act as a validation dataset for our InSAR activity analysis. Using recent aerial and satellite imagery, we visually assessed landslides in the area to identify a set of landslides whose geomorphic features clearly indicated recent movement (e.g., fresh scarps, visible ground undulations, and interrupted drainage patterns) as well as another set of landslides whose geomorphic features clearly indicate inactivity (e.g., lack of visible scarps, smooth, unbroken terrain, and established drainage networks) (Figure 5.2). Of the 544 large slow-moving landslides in the study area, we could reliably identify 12 that are likely to be active and 48 that are likely to be inactive. The active landslides had a median size of 56.5 ha and, in total covered 819 ha, while the inactive landslides had an average area of 23.5 ha and in total covered 1775 ha. We acknowledge that the presence or absence of geomorphic features does not necessarily indicate landslide activity or inactivity, and visual inspection from imagery is subjective. Still, with very few landslides with field monitoring in place, we believe that this approach is the best source of validation data that we have available for regional assessments. For two landslides, we were however able to make use of field monitoring data to validate the methods and we use this data validate our sPOT analysis.


*Figure 5.2 Examples of an active (left) and an inactive (right) landslide from our validation dataset. The active landslide (left) has sharply undulating surface topography, visible fresh scarps at the southern edge of the landslide, and several areas with ponding water which suggests that the drainage network has been disrupted. In contrast, the inactive landslide (right) does not have visible fresh scarps or sharply undulating terrain, and there is no evidence of a recently disrupted drainage network.*

To investigate the quality of our sPOT velocity analysis, we compared the sPOT results to the known movements of two landslides in our study area, the Rangitikei and Bird landslides, for which we had existing or collected new movement data (Figure 5.1). We used 30 survey pegs on and around the Rangitikei Landslide to measure landslide displacements at 3-6 month intervals from 2015-2019 using differential GNSS (dGNSS). Repeat measurements of stable survey pegs between surveys showed that the dGNSS surveys had a mean horizontal error of 0.027 m (s.d. 0.014 m) and a mean vertical error of 0.050 m (s.d. 0.057 m), which were generally several orders of magnitude smaller than the annual movements. At the Bird Landslide we used photogrammetrically-derived orthophoto mosaics from an existing 2016 high-resolution aerial survey and a drone survey we undertook in 2021, to perform a manual feature-tracking analysis at 18 locations across the landslide's surface. We measured the offsets of 15 stable features (control locations) outside of the landslide boundary, which suggest our feature-tracking analysis had an average horizontal error of 0.30 m (s.d. 0.13 m), and were of a smaller magnitude than most features tracked on the landslide. For both landslides, we used the field data to create estimates of the annual velocities in both the West-East (WE) and South-North (SN) directions that could be directly compared to the sPOT velocity maps. Table 1 describes the validation (field) and prediction (remote sensing) datasets, their collection periods, and the vector(s) in which they can measure landslide velocities. Figure 5.3 illustrates the velocity vectors displayed in Table 5.1.

*Table 5.1 The datasets used in this analysis, their role in the study, the period they were collected, and the velocity vectors along which they measure velocity. WE stands for West to East (eastward) movement, SN stands for South to North (northward) movement, and LOS stands for the Line-Of-Sight of the SAR satellite (roughly ENE and WNW with a 30° off-nadir angle).*

| Dataset | Role | Time Period | Measurement Vectors |
|---|---|---|---|
| dGNSS | Validation | 2015 - 2019 | WE, SN, Vertical |
| Manual Feature Tracking | Validation | 2016 - 2021 | WE, SN |
| Timeseries InSAR | Prediction | 2018 - 2021 | LOS, WE*, Vertical* |
| Timeseries sPOT | Prediction | 2016 - 2021 | WE, SN |

*InSAR can only measure WE and Vertical velocities via reprojection of LOS datasets

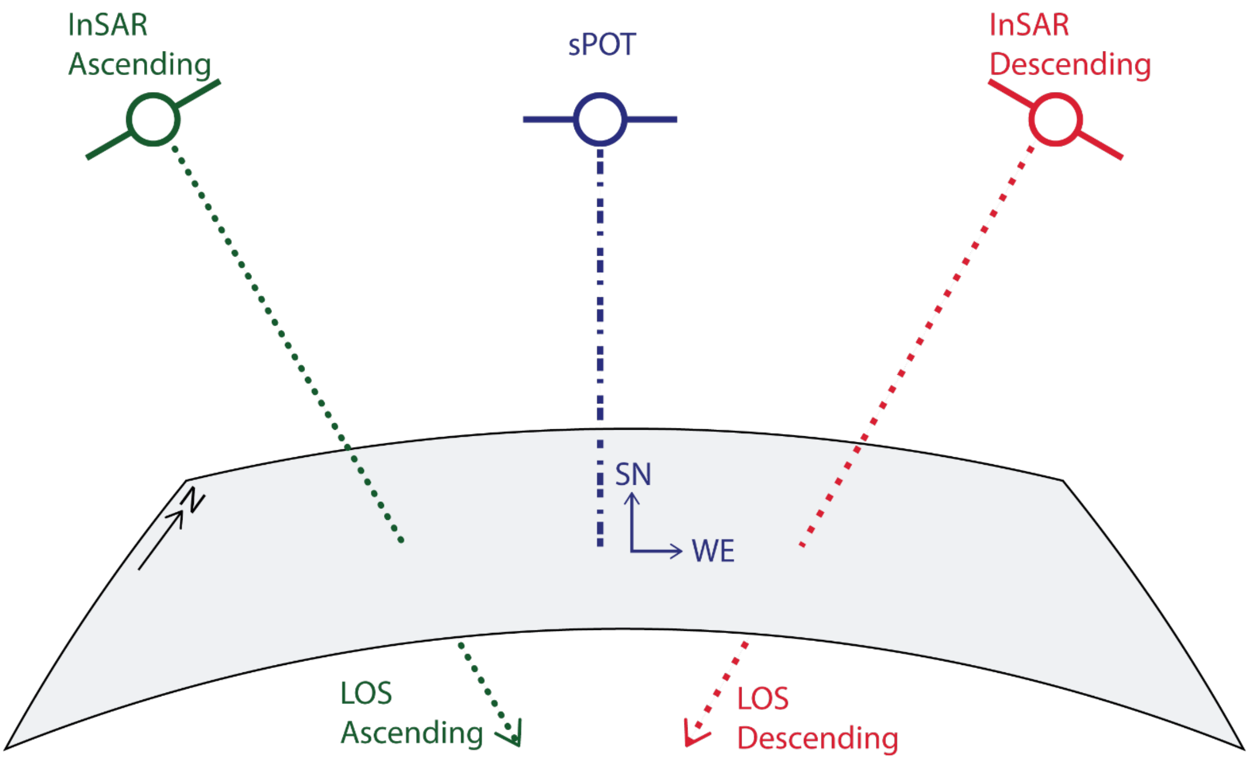


*Figure 5.3 Orientations of the remote sensing velocity measurement vectors used in this study. WE stands for West to East (eastward) movement, SN stands for South to North (northward) movement, and LOS stands for the Line-Of-Sight of the SAR satellite (roughly ENE and WNW with a 30° off-nadir angle).*

### *5.3.2 InSAR*

To generate the interferograms used in this study, we utilized the on-demand interferogram processing capabilities provided by the Alaska Satellite Facility's Hybrid Pluggable Processing Pipeline (HyP3) (Hogenson et al., 2016). This service allows users to request the generation of Sentinel-1 interferograms created using GAMMA InSAR software from an on-demand service that sits within the Amazon Web Services cloud computing environment. We chose to use the two-pixel range and ten-pixel azimuth multi-looked version of interferograms provided by HyP3, which have a 40 m pixel size.

While this service provides fewer customization options than other InSAR software packages such as the InSAR scientific computing environment (ISCE2) (Rosen et al., 2015), using HyP3 dramatically reduced the computational resources and data storage needed to perform our InSAR analyses while still producing quality interferograms. For example, our study used data from 2017 to 2021 and four frames (2 for each orbit direction), which resulted in a total of 228 individual SAR images and 1355 interferograms. If creating each interferogram resulted in 10 Gb of data and took 2 hours to create and unwrap (reasonable assumptions for Sentinel-1 data on a standard desktop computer), these interferograms would take roughly 113 days to create and require 12 TB of storage. In contrast, the HyP3 generated interferograms were created and downloaded within 48 hours and required 2 TB of storage.

Due to inconsistencies in the timing of Sentinel-1 observations over New Zealand and the low coherence within the natural terrain of our study area, InSAR pairs suitable for an InSAR time-series analysis were only available sporadically within the past five years (Figure 5.4). While it is possible to perform an InSAR time-series analysis using a disconnected interferogram network (Yunjun et al., 2019), we found that doing so created a large amount of bias in the resulting time-series products. Consequently, we chose to perform our analysis using a subset of connected networks. For the years between 2017 and 2021, we downloaded HyP3 interferograms formed between each SAR image and the previous three SAR images, then excluded all interferograms that had an average spatial coherence of less than 0.4. We identified the largest connected network that was available for each year and orbit direction (Figure 5.4) and performed our time-series analysis for each of these epochs separately. Sentinel-1 descending orbit data were not available for our study area during 2017, so we excluded this year from our analysis. In addition to maintaining connected networks, splitting our analysis into yearly epochs allowed us to better measure sporadic landslide movement (i.e., landslides that may move one year but not the next).

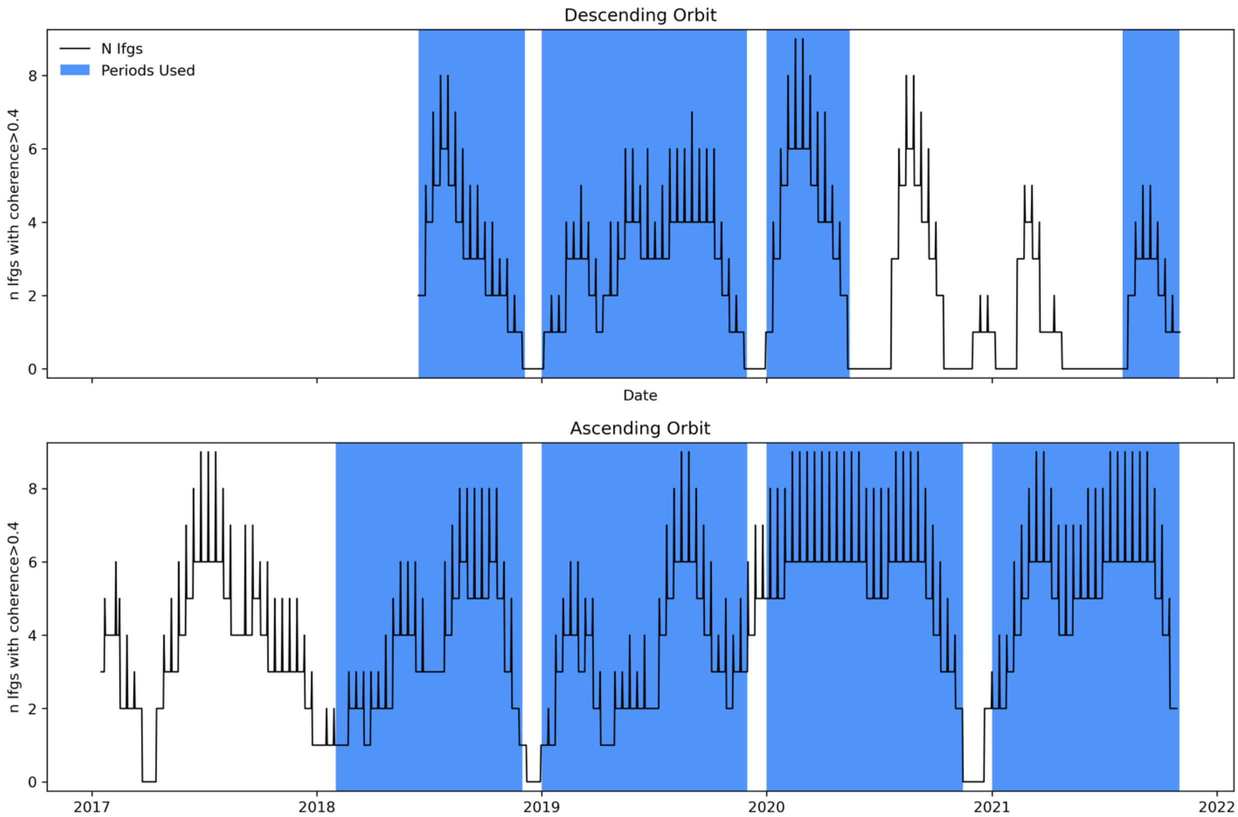


*Figure 5.4 The number of valid interferograms (i.e., the average spatial coherence is > 0.4) available for our study area between 2017 and 2021. The top plot shows data availability for the descending orbit data, and the bottom plot shows the availability for the ascending orbit data. The blue regions cover the longest continuous interferogram network for each year and represent the epochs used within our study.*

Once we had requested and downloaded the interferogram pairs, we ingested the data into the Miami InSAR Timeseries software in Python (MintPy) (Yunjun et al., 2019), where we conducted the remainder of our InSAR analysis. MintPy is an open-source Python library that uses a SBAS approach to perform InSAR time-series analyses and has many valuable utilities. After removing interferograms with average spatial coherences less than 0.4, and prior to the SBAS time-series inversion, we applied the double-difference filter that Bekaert et al. (2020) proposed to each time epoch. This filter is designed to amplify the strength of local deformation signals at the expense of obscuring regional trends. The filter is applied by first calculating a regional average for unwrapped InSAR data using a large averaging kernel of the unwrapped InSAR data, then subtracting that from a local averaging kernel according to the formula:

*Equation 5.1 The double difference filter*

$$Filtered\ Data = Local\ Average - Regional\ Average$$

For our study, we used a local kernel diameter of 200 m and a regional kernel diameter of 2000 m. We found these kernel sizes to provide an adequate balance between noise-reduction and over-smoothing. More information on selecting an appropriate filter size can be found in Bekaert et al. (2020). Once we had applied the double-difference filter, we performed an SBAS time-series inversion to estimate a line-of-sight (ENE for the ascending orbit data and

WNW for the descending orbit data) deformation time-series using a least-squares approach (Yunjun et al., 2019). In both ascending and descending orbit cases, these time-series represent movement along a 3D vector with horizontal and vertical components (Figure 5.3). We used a set of 100 bootstrapped subsamples of the deformation time-series to create a suite of estimated linear velocities for each pixel, then averaged these estimates to determine a final velocity at each pixel. Since tropospheric delay tends to be spatially correlated at the scale of the double-difference filter, applying this filter removes much of the atmospheric noise, and no additional tropospheric correction was needed. We performed this workflow separately for both the ascending and descending orbit data.

We then used the ascending and descending velocity datasets to perform our landslide activity analysis. We trialled filtering these datasets using two different methodologies to isolate velocity zones that represented areas of activity. The first filter we applied was the original standard-deviation filter used by Bekaert et al. (2020). This filter removes all pixels whose velocity is less than two times the standard deviation of the velocity estimation set produced for each pixel during the bootstrapped velocity estimation process, then additionally removes pixel clusters that contain fewer than a given number of pixels.

Our second filter was a velocity and coherence filter that removes all pixels with a temporal coherence less than the mean temporal coherence of the dataset (0.905 in our case) and all pixels with an estimated velocity two standard deviations or more from the average velocity of the dataset. Then, in keeping with Bekaert et al.'s (2020) filter, we removed all pixel clusters below a given size threshold. Bekaert et al. (2020) initially removed all pixel clusters that included fewer than 3 pixels, but we found that a higher threshold of 19 pixels (3 ha for our dataset) led to better results, and this threshold value was used for both filters.

We applied both filters to the ascending and descending orbit data separately for each year. We also combined the data from various orbits and years to determine if these combinations improved activity classification. For each filter, we combined the ascending and descending activity datasets (using a logical OR operation) to determine if combining data from both LOS geometries improved performance. Additionally, we used the combined datasets from each year to determine how many years each landslide was identified as active. We then used this metric to determine overall activity (i.e., was a given landslide active in at least two years? At least three years?). When combining data from multiple years, we did not impose an area limit, so it is possible to have zones of activity that are below the previously discussed 19 pixel (3 ha) area threshold because only a sub-section was active during multiple years.

We deemed a landslide to be active wherever an area of activity fell within a landslide's mapped extent (buffered inward by 40 m to remove edge effects). We assessed the quality of our method, and all filter combinations, by intersecting the activity datasets with the 'likely active' and 'likely inactive' visual validation dataset. We quantified the accuracy using the true positive rate, true negative rate, overall accuracy, and Kohen's kappa. While there is an ongoing debate concerning the utility of the kappa statistic (Cicchetti and Feinstien, 1990; Flight and Julious, 2015), we report it here because it is a widely used metric, and including it allows past and future studies to more easily compare our results to theirs. Due to the roughly East-West orientation of the Sentinel-1 LOS vectors, Sentinel-1 InSAR measurements are typically insensitive to purely North-South movement. To determine if this biased our measurements of landslide activity, we also investigated whether there was a relationship between our classification accuracy and landslide orientation by comparing the landslides' aspect to how often it was correctly classified.

To allow us to also compare our InSAR velocity data to our movement datasets for the Bird and Rangitikei landslides, we also reprojected the ascending and descending orbit data into the WE horizontal movement direction (Samsonov et al., 2020) for the areas surrounding the Rangitikei Landslide and the Bird Landslide. This reprojection allows us to directly compare our InSAR velocity data to our movement validation data and our sPOT velocity data, since both of these datasets measured movement in the WE direction.

#### *5.3.3 Sub Pixel-Offset Tracking*

We performed times-series sub-pixel offset tracking (sPOT) analyses at the Bird and Rangitikei landslides, to evaluate the utility and accuracy of this method. We used Sentinel-2 near-infrared imagery (band 8) sourced from a consistent path and orbit. Image selection and sub-setting were done within Microsoft's Planetary Computer Hub environment, and sPOT tracking was performed using the Auto-Repeat Image Feature Tracking (AutoRIFT) python library (Lei et al., 2021). The time-series analysis was conducted using the same MintPy SBAS and time-series utilities used for our InSAR analyses.

A Sentinel-2 path and orbit, that optimized coverage, was selected for each landslide. Then we created an initial dataset containing all Sentinel-2 ground reflectance images (Level-2C) corresponding to this path\orbit. We filtered out images with cloud cover at the landslide then selected a network of annual images that fell closest to a single calendar day (i.e., all the images were in the same month or close to it). In contrast to the InSAR analysis, where short temporal baselines are needed to form coherent interferograms, this network of images produced the best results for the sPOT analysis because 1) the temporal baselines of at least one year allowed for there to be sufficient landslide movement to produce a strong signal in the sPOT analysis and 2) selecting images from the same period during the year reduced noise related to seasonal variations in vegetation and shadows.

For the AutoRIFT analysis, we used a minimum template window size of 32, a maximum template window size of 128, and an 8-pixel step. We ran AutoRIFT using all possible pair-wise combinations of the images to produce a stack of offset datasets in the WE and SN direction. We then loaded these offset datasets into MintPy, where we corrected bias in the images by subtracting the median offset value within the stable regions (i.e., the regions not known to contain a large landslide) from each image. While it could be argued that it would be more appropriate to define the stable regions as any location without an active landslide, we chose to exclude all landslide areas from the stable regions to ensure that we were not including any active areas within the stable regions regardless of the accuracy of our InSAR activity analysis. We then used MintPy's SBAS time-series inversion utility and linear velocity estimation utility to estimate the average movement velocity for the offset image stacks. This produced WE and SN velocity datasets with a resolution of 80 m.

To assess the accuracy of these sPOT datasets, we compared their predicted velocities with those measured using dGNSS and manual feature-tracking at the Rangitikei Landslide and the Bird Landslide. For each dGNSS and manual feature-tracking location, we determined their annual WE and SN velocities by fitting a linear time-series regression, then compared these results to those of our sPOT analysis. We assessed the accuracy of our sPOT velocity predictions using the mean, the standard deviation, the mean absolute error (MAE), and the root mean square error (RMSE) error of the offset estimates. For each of these metrics, we calculated them separately using the WE and SN datasets, as well as in combination via the magnitude of the combined horizontal movement vector.

## 5.4 Results

### *5.4.1 InSAR*

Overall, the velocity-coherence filter more reliably identified active landslides than the standard deviation filter of Bekaert et al. (2020). In both the ascending and descending orbit data, applying the double-difference filter led to a significant increase in the temporal stability of the phase signal (the average temporal coherence increased from 0.66 to 0.905). This increase in the temporal stability of the data led to very similar velocity estimates regardless of which bootstrapped date sample was used, which led to minimal standard deviations of these estimates. Since the standard deviation filter uses this standard deviation product to remove low-quality data, the low values within our study area led to a large portion of the region (60%) being classified as active. Consequently, most of the inactive and active landslides within the validation data were identified as active using this filter. This led to classification accuracies of 23% and 29% and kappas of 0.05 and 0.02 for the ascending and descending data, respectively (Table 5.2). Due to the low quality of the classification for the ascending and descending datasets when using the standard deviation filter, combining data from multiple orbits and years did not increase the performance of the classification.

*Table 5.2 InSAR activity accuracy metrics for the various filters considered in this study.*

| Filter | Orbit | True Negative Rate (n=48) | True Positive Rate (n=12) | Accuracy | Kappa |
|---|---|---|---|---|---|
| Standard Deviation | Ascending | 4% | 100% | 23% | 0.02 |
| Standard Deviation | Descending | 11% | 100% | 29% | 0.06 |
| Standard Deviation | Combination (OR) | 2% | 100% | 22% | 0.01 |
| Velocity Coherence | Ascending | 91% | 66% | 86% | 0.57 |
| Velocity Coherence | Descending | 94% | 64% | 88% | 0.61 |
| Velocity Coherence | Combination (OR) | 88% | 77% | 85% | 0.59 |
| Velocity Coherence | Active at least 1 year | 70% | 100% | 76% | 0.49 |
| Velocity Coherence | Active at least 2 years | 91% | 91% | 91% | 0.76 |
| Velocity Coherence | Active at least 3 years | 95% | 58% | 88% | 0.60 |

In contrast, we found that the velocity-coherence filter accurately predicted the activity state of landslides within the dataset (Table 5.2). Using this filter, the ascending and descending orbit activity datasets had accuracies of 86% and 88% and kappas of 0.57 and 0.61, respectively. Combining these datasets using a logical OR operation did not improve the classification, but it did result in more balanced true positive and true negative rates. Overall, the best classification result was achieved by combining the logical OR combination datasets across multiple years. In particular, defining activity as being active in two out of the four combination datasets resulted in an overall classification accuracy of 91%, balanced true positive and true negative rates, and a kappa of 0.76. This classification resulted in the misclassification of only one active landslide and three inactive landslides (Figure 5.5). While there is geomorphic evidence supporting recent landslide activity at the landslide that was misidentified as inactive, it is also possible that it was not active for the majority of the study period and thus was not identified as active when using the two-year activity cut-off.

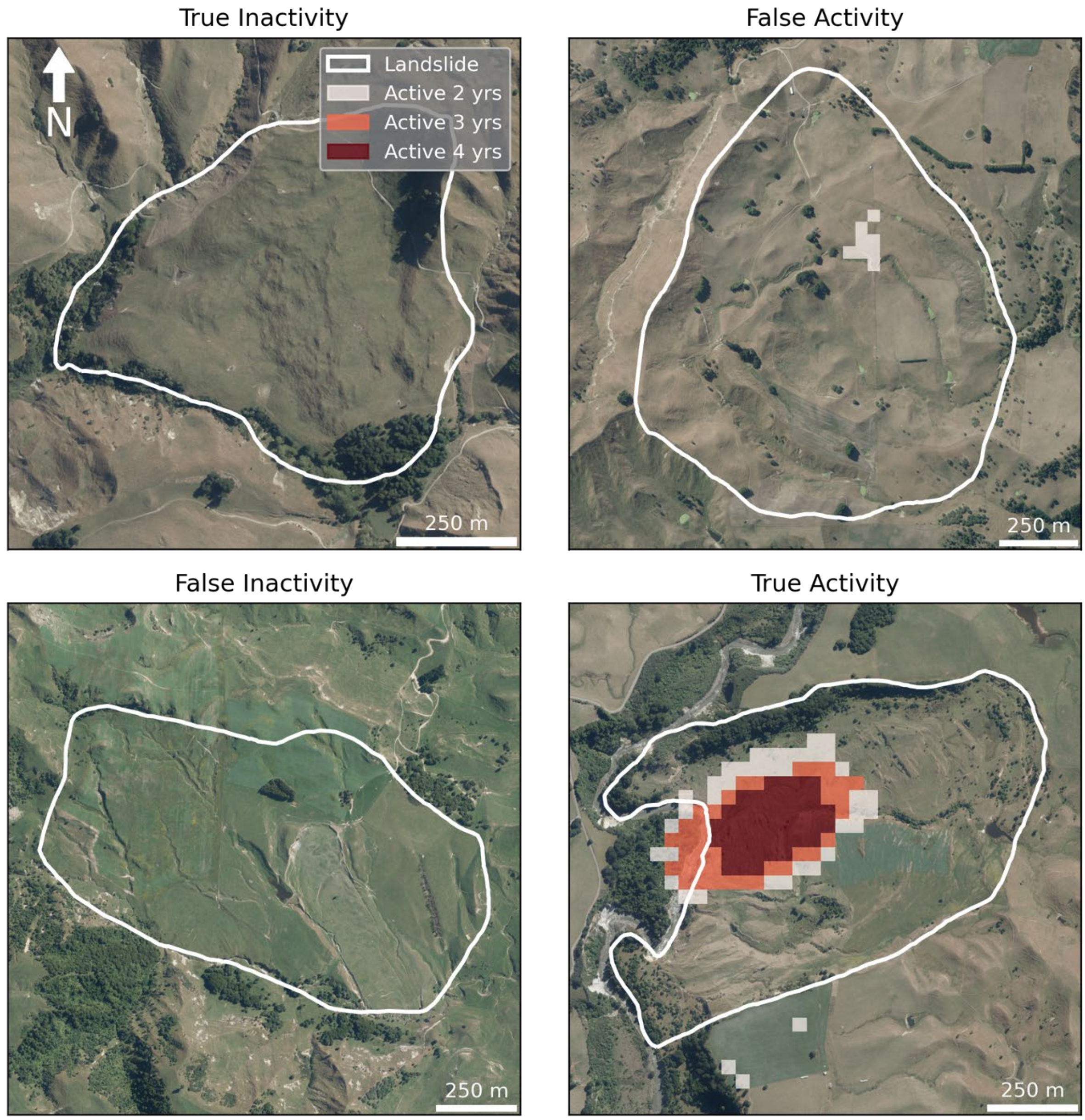


*Figure 5.5 The multi-year combined ascending and descending InSAR velocity-coherence filtered activity dataset overlaid on four landslides from the validation dataset. The top left shows an example of correctly identified inactivity, the top right shows an example of false activity, the bottom left shows an example of false inactivity, and the bottom right shows an example of true activity.*

Most of the active landslides in our activity validation dataset had a southwest downslope direction, which corresponds to the general orientation of the bedrock in this region. There is no clear relationship between landslide orientation and classification accuracy (Figure 5.6). Instead, the size of the landslide appears to have a more significant effect on the accuracy of our analysis. The smallest active landslide in the dataset (12.3 ha) was the only active landslide that was not correctly identified by the two-year activity dataset. While this analysis utilized a 40 m pixel size, the averaging within a 200 m diameter local kernel during the double-difference filter process may limit its ability to identify smaller zones of activity.

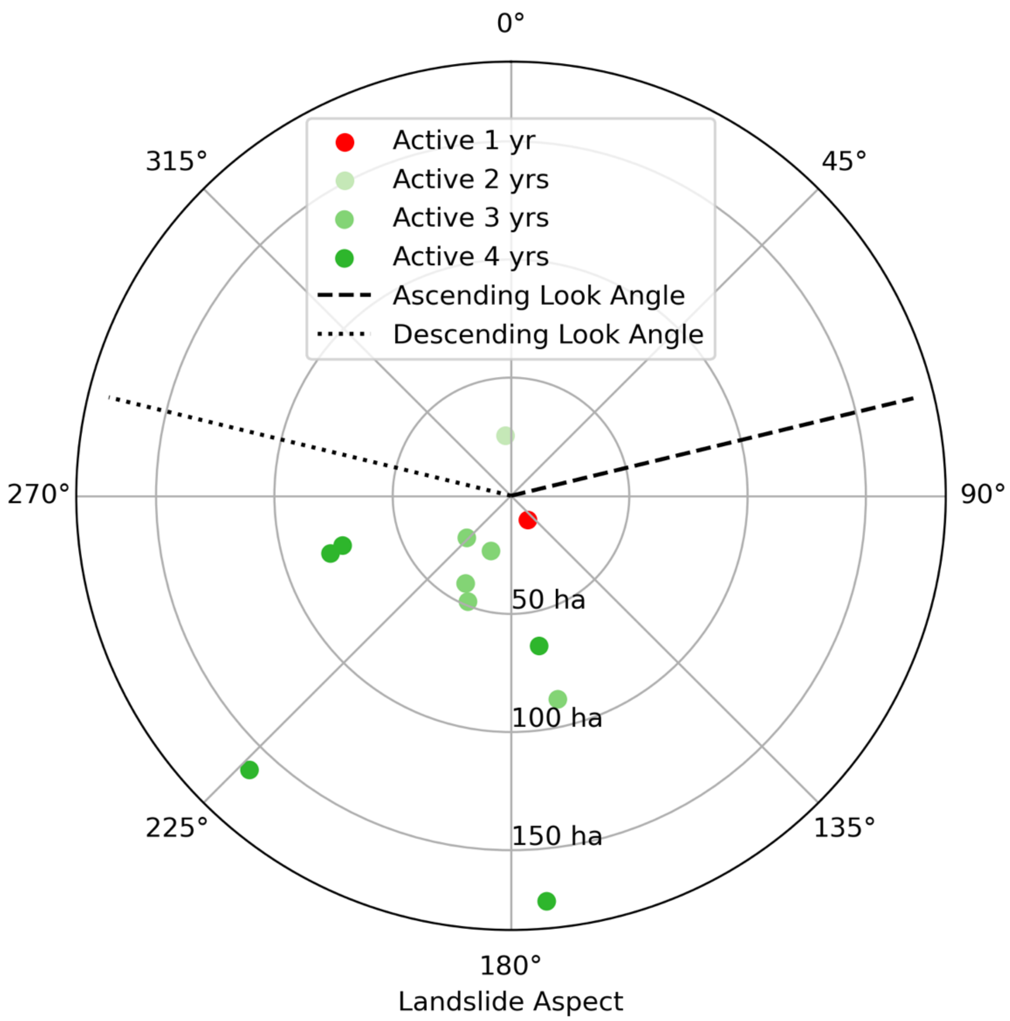


*Figure 5.6 The average aspect of each active landslide color-coded by the number of years it was identified as active within the combined activity datasets. The LOS of the Sentinel-1 satellites (in the ascending and descending orbits) within the study area are represented by the dotted lines. The distance of the points from the plot's centre represents the surface area of the active region of the landslide in hectares (ha).*

Overall, the combined filter identified 4994 zones of activity with an average size of 0.64 ha and a maximum area of 104 ha. These zones of activity represent 0.7% of the total area surveyed (for context, large deep-seated landslides represent 8%). While our activity identification procedure performed well according to our assessment, many spurious activity zones were also identified in areas where landslides are unlikely to occur, such as riverbeds and the coastal regions (Figure 5.7). The presence of these spurious activity zones highlights the importance of pairing InSAR with geomorphological and historical information on landslide occurrence. Pairing InSAR data with existing information on landslide presence results in a higher quality prediction of landslide activity and makes the activity dataset easier to interpret.

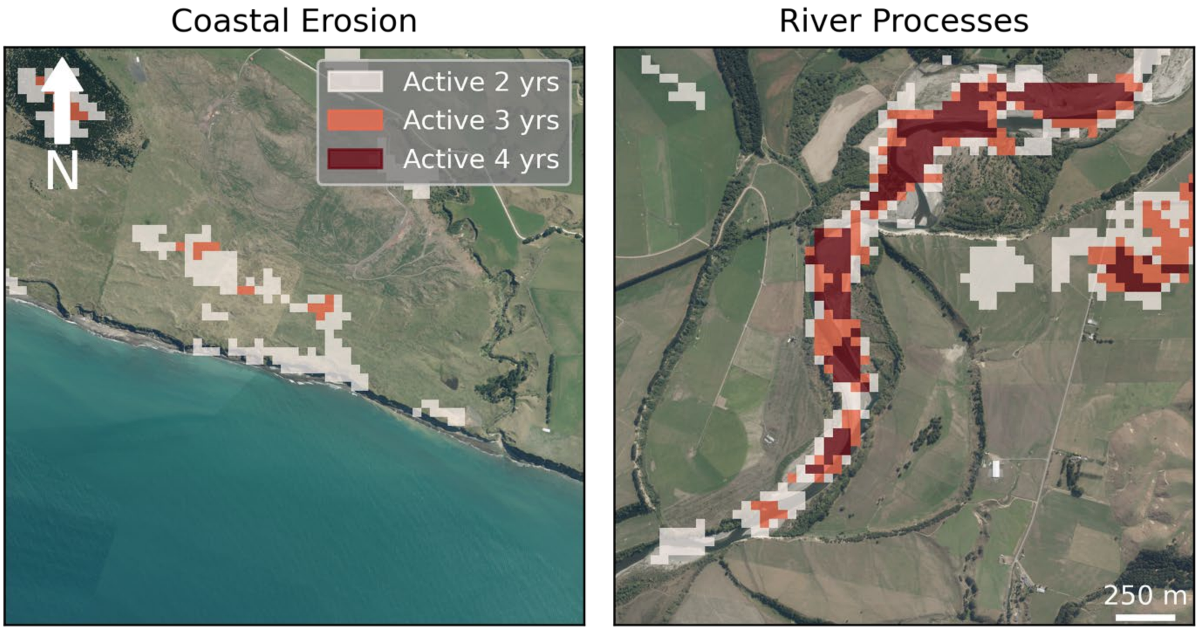


*Figure 5.7 Examples of InSAR activity false positives that may be related to other geomorphic processes. The left-hand image shows an erroneous zone of activity along the coast of New Zealand that may be related to coastal erosion or applying the double-difference filter near a large incoherent water body. The right-hand image shows another set of erroneous activity zones that may be related to river processes.*

The ascending, descending, and combined filters correctly identified activity at the Bird and Rangitikei landslides, but their estimates of movement rates were much lower than those measured by field data. When the ascending and descending InSAR data were combined and projected into the horizontal WE movement direction at Rangitikei Landslide, the maximum annual WE movement rate within the landslide body was 0.04 m/yr, and the average was -0.01 m/yr. Conversely, the maximum WE movement rate measured at Rangitikei Landslide was 3.30 m/yr, and the average was 0.17 m/yr. This trend held for the Bird Landslide. The InSAR data had a maximum WE movement rate of 0.04 m/yr and a 0.02 m/yr average movement rate, but the manual feature tracking results showed a maximum WE movement rate of 3.4 m/yr and an average rate of 1.62 m/yr. These large differences in InSAR-reported and actual movement rates are likely due to the loss of InSAR coherence in the fast-moving portions of each landslide, which tends to bias InSAR results towards lower values. In both cases, the fastest part of landslides identified by InSAR occurred in the mid-sections of the landslides where some of the slowest movement within the landslide bodies occurred, rather than at the toes where the most rapid movement rates were measured.

### *5.4.2 Sub-Pixel Offset Tracking*

As expected, sPOT was better able to measure faster landslide movement than is possible to measure via InSAR. While the sPOT datasets were generally reliable, rapid fluvial erosion of material at the toe of the Rangitikei Landslide made tracking features near the river's edges difficult. Loss of trackable features near the river's edge resulted in under-estimates of velocities within 80 m (one pixel) of the river's edge. After removing the two GNSS measurement locations within 80 m of the river's edge, we found that the average WE velocity at Rangitikei Landslide (Figure 5.8) was 0.14 m/yr, and the mean absolute error of the sPOT measurements was 0.25 m/yr. In the SN direction, the average velocity was -1.23 m/yr and the MAE was 0.75 m/yr (Table 5.3). At Bird Landslide (Figure 5.9), the average movement rate measured using manual feature-tracking in the WE direction was 1.62 m/yr, and the MAE of the sPOT measurements was 0.60 m/yr. In the SN direction, the average velocity was -2.17 m/yr, and the MAE was 0.92 m/yr (Table 5.3). When considering validation data from both sites and using the horizontal magnitude of the combined WE and SN vectors, we found that the landslide features had an average speed of 2.05 m/yr and the MAE of the sPOT measurement was 0.74 m/yr.

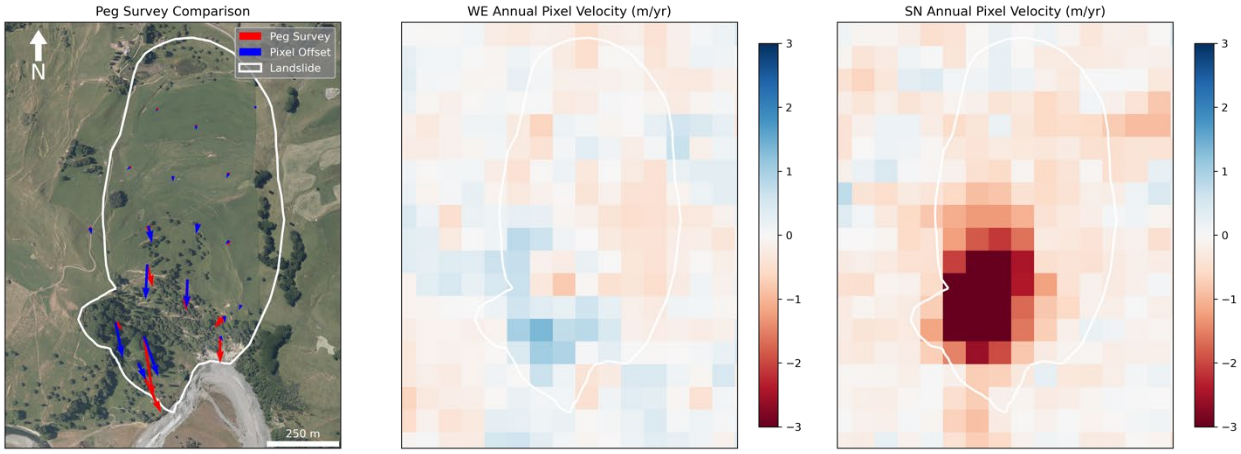


*Figure 5.8 Comparison of the annual movement rates derived from the dGNSS validation data and the sPOT analysis for the Rangitikei Landslide. The left panel shows an image of the Rangitikei Landslide with arrows representing the average annual velocity vector for both datasets at the survey points. In this panel, the length of the velocity vectors has been exaggerated by 33x to improve readability. The centre panel shows the sPOT velocity map in the WE direction (eastward movement is positive), and the right panel shows the sPOT velocity map in the SN northward movement is positive).*

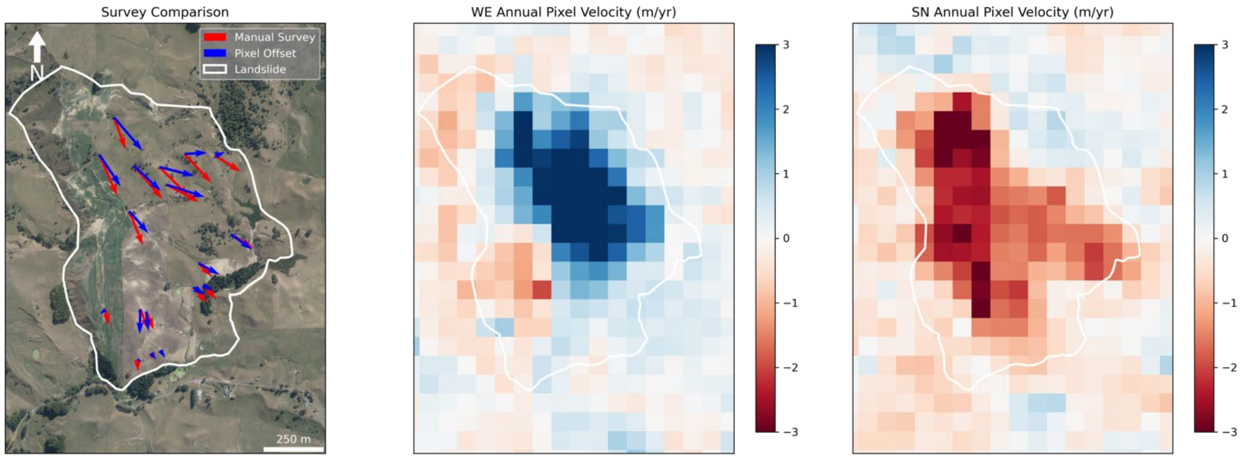


*Figure 5.9 Comparison of the annual movement rates derived from the manual pixel tracking validation data and the sPOT analysis for the Bird landslide. The left panel shows an image of the Bird Landslide with arrows representing the average annual velocity vector for both datasets at the survey points. In this panel, the length of the velocity vectors has been exaggerated by 33x to improve readability. The centre panel shows the sPOT velocity map in the WE direction (eastward movement is positive), and the right panel shows the sPOT velocity map in the SN northward movement is positive).*

*Table 5.3 Average validation dataset movement rate, average sPOT measurement bias, sPOT bias standard deviation, mean absolute error (MAE), and root mean square error (RMSE) at the Rangitikei Landslide (Rangitikei), the Bird Landslide (Bird), and both landslides combined (Both). The direction column indicates the type of velocity measured (WE, SN, or the magnitude of the combined horizontal movement vector), and the n column shows the number of samples in that group.*

| Landslide | Direction | n | Avg Rate (m/yr) | sPOT Avg Bias | sPOT Bias Std | sPOT MAE | sPOT RMSE |
|---|---|---|---|---|---|---|---|
| Rangitikei | WE | 18 | 0.14 | -0.01 | 0.44 | 0.25 | 0.43 |
| Rangitikei | SN | 18 | -1.23 | 0.13 | 1.19 | 0.75 | 1.17 |
| Rangitikei | Magnitude | 18 | 1.30 | -0.15 | 1.20 | 0.75 | 1.17 |
| Bird | WE | 18 | 1.62 | 0.01 | 0.78 | 0.60 | 0.75 |
| Bird | SN | 18 | -2.17 | 0.79 | 0.95 | 0.92 | 1.21 |
| Bird | Magnitude | 18 | 2.81 | -0.45 | 0.82 | 0.73 | 0.92 |
| Both | WE | 36 | 0.88 | 0.00 | 0.62 | 0.42 | 0.61 |
| Both | SN | 36 | -1.70 | 0.46 | 1.11 | 0.83 | 1.19 |
| Both | Magnitude | 36 | 2.05 | -0.30 | 1.02 | 0.74 | 1.05 |

Overall, our sPOT velocity measurements have a concordance correlation coefficient of 0.76 (Figure 5.10). This coefficient is similar to Pearson's correlation coefficient, and is interpreted the same way, but always measures the correlation relative to the 1:1 line (the line of concordance) and was designed to compare measurement methodologies (Lin, 1989). In general, the relative error of the sPOT analysis remained consistent as the measured velocities increased (i.e. absolute error increased as measured velocities increased). However, when the dGNSS measured velocities were below 0.5 m/yr there was an increase in the relative error (Figure 5.10). As the measured dGNSS velocity increases, the sPOT velocities tend to produced more underestimates of dGNSS velocities than overestimates (Figure 5.10). This may be due to the mismatch in resolution between the validation data and our sPOT data. Our dGNSS tracks the movement of the landslide at specific points with high accuracy, but our sPOT analysis tracks the movement of much coarser 10 m-scale features in comparison to a much larger area. Thus, our sPOT velocity residual trends may be due to over-smoothing of the velocity within the sPOT analysis.

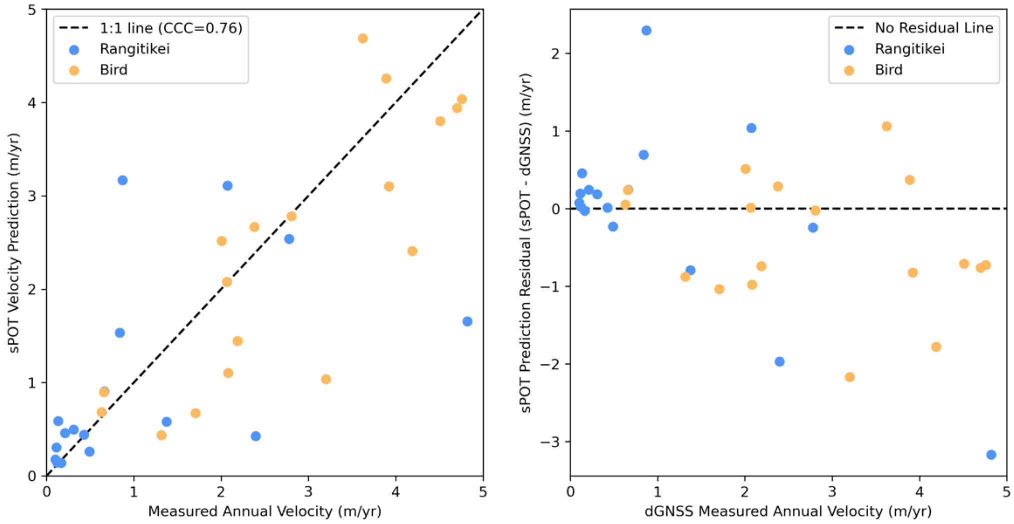


*Figure 5.10 Comparison of the sPOT-derived velocity measurements to dGNSS-measured velocities at the Rangitikei and Bird landslides. The left panel shows the two measurements plotted against each other with a 1:1 correspondence line. The CCC metric in the left panel's legend denotes the concordance correlation coefficient (Lin, 1989). The right panel shows the prediction residual of the sPOT measurement when compared to the dGNSS measurement (sPOT - dGNSS).*

The stable areas within 5 km buffers around the Rangitikei and Bird landslides had sPOT WE and SN velocities close to zero (0.01 m/yr for the Rangitikei and 0.02 m/yr for the Bird) but had standard deviations that ranged from 0.35 m/yr to 0.55 m/yr with a mean of 0.48 m/yr. Consequently, activity at landslides whose maximum velocities do not exceed 0.48 m/yr will be more difficult to distinguish from the background noise of the dataset in this sPOT analysis than in our InSAR analysis. This rate was exceeded at both the Rangitikei and Bird landslides, and we were able to identify clear movement signatures in the sPOT data for both sites (Figure 5.11).

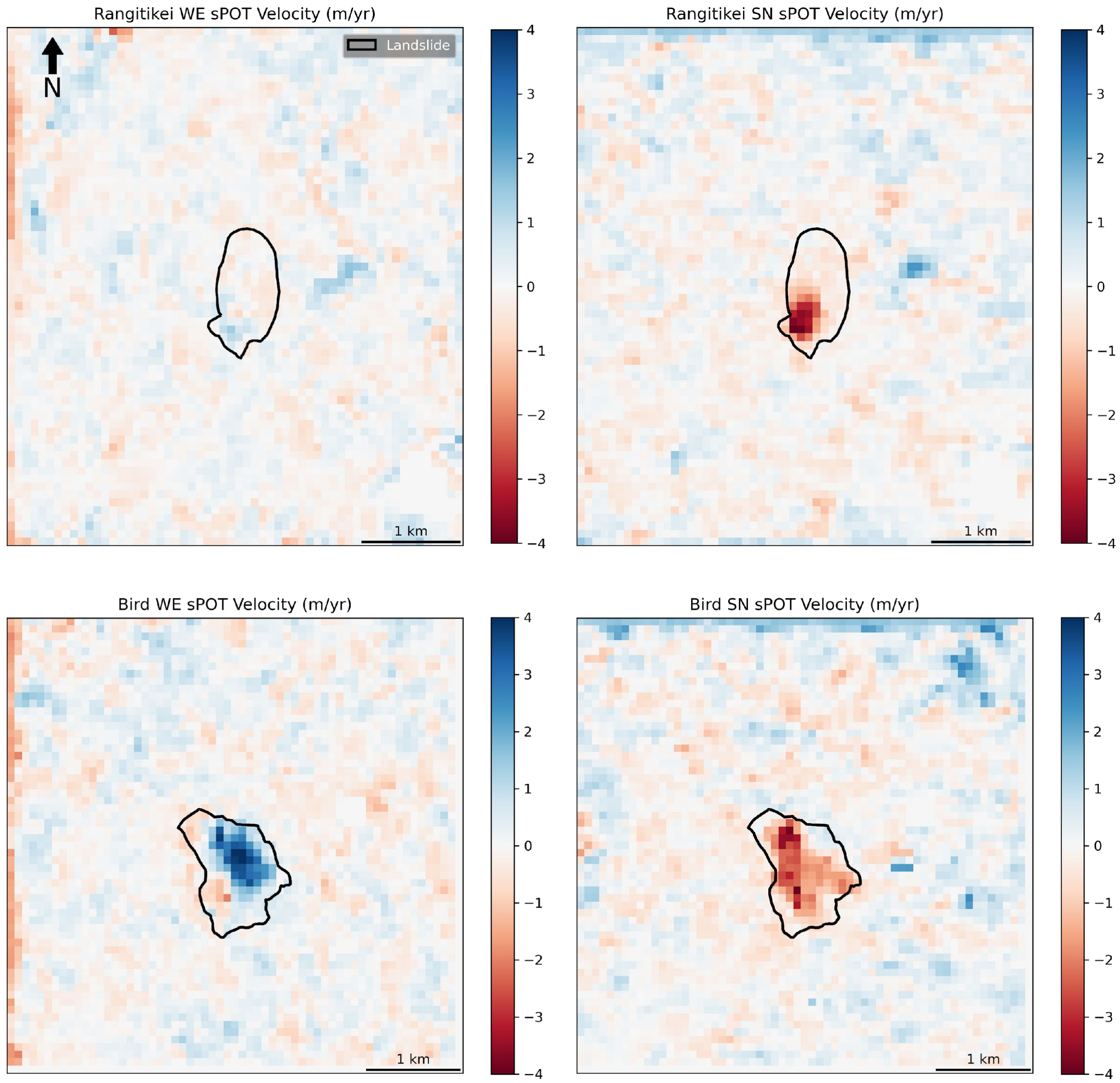


*Figure 5.11 sPOT results for the Rangitikei and Bird landslides in the WE and SN directions (aerial imagery of the landslides can be found in Figure 5.8 and Figure 5.9. There is noise in the stable areas surrounding the landslides. Still, the landslide movement can be seen in all subplots except for the WE Rangitikei Landslide plot since most movement in this location is SN-oriented.*

When the WE InSAR velocity data are paired with the WE sPOT velocity data (Figure 5.12), it becomes apparent that areas with high velocities in the InSAR data have low velocities in the sPOT data. It appears that InSAR is identifying movement in the slowest portions of the landslide, where the noise level in the sPOT data is high but losing coherence in the higher velocity areas. Conversely, our sPOT analysis appears to be less sensitive to movements below 0.5 m/yr in either the WE or SN directions but capable of identifying movement on the order of several meters per year.

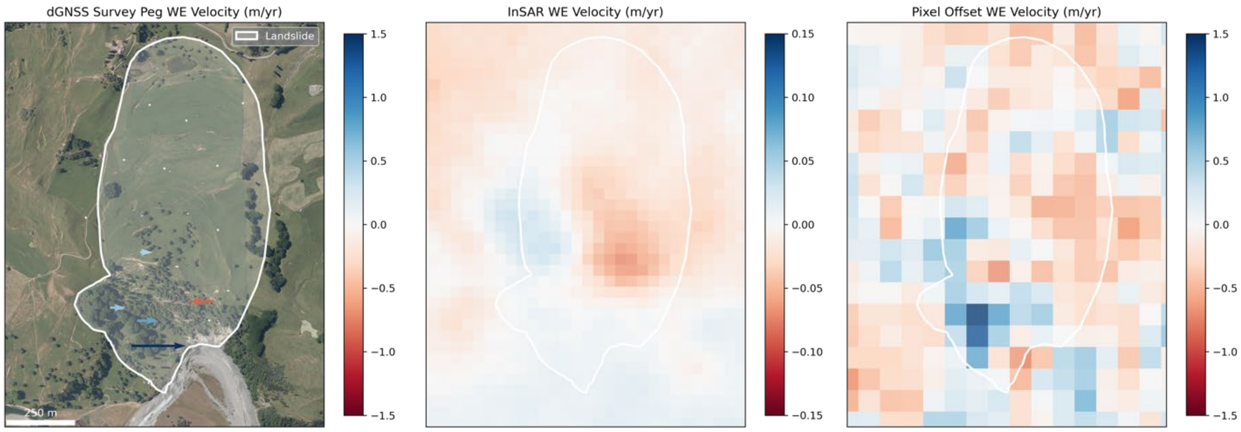


*Figure 5.12 Comparison of the InSAR and sPOT velocity data for the Rangitikei Landslide. The left panel shows an aerial image of the landslide with arrows at the location of dGNSS observations whose colour and length correspond to the measured velocity at that location. The middle panel shows the InSAR WE velocity data, and the right panel shows the sPOT WE velocity data. In all panels, positive values indicate westward motion. Note the much smaller velocity scale for the centre InSAR panel as compared to the two outer panels. It appears that the InSAR analysis identifies movement in the slower-moving central portion of the landslide but fails to identify the faster motion in the bottom portion.*

## 5.5 Discussion

### *5.5.1 InSAR*

Surprisingly, there is a large difference in the results achieved using Bekaert et al.'s standard deviation filter when comparing our work and theirs. While this filter failed to identify activity zones in our data reliably, it appears to have worked quite well in Bekaert et al.'s original study. This disparity likely resulted from differences in pre-processing of the original data and not with an inherent fault of the filter. Importantly, we applied the filter to data that had been multi-looked two pixels in range and ten in azimuth, while Bekaert et al.'s study used non-multi-looked data.

Multi-looking generally increases the signal-to-noise ratio of InSAR data and reduces computation costs at the expense of decreased resolution (Lee et al., 1994). It also enhances the temporal stability of the InSAR signal. The improved temporal stability afforded by multi-looking likely contributed to the low standard deviations found within the bootstrapped sample sets, resulting in the deviation filter being ineffective. However, we found that if the threshold was increased from two times the standard deviation to eleven times the standard deviation, we could produce classification results similar to the velocity-coherence filter results. However, this number is likely to be different for other processing frameworks. We believe that thresholding the data using the mean of the temporal coherence data (e.g. the velocity-coherence filter) will produce more consistent results and is a more transferrable method.

While the individual years of the velocity-coherence filtered InSAR dataset performed adequately in isolation, combining data from both orbits and multiple years produced better results. Combining data from both orbits allows for the detection of movement along multiple LOS vectors, and including data from different years makes it possible to detect movement at landslides that display episodic annual movement. This cycle of movement is particularly common in large deep-seated landslides that intersect erosive river systems since landslide movement can be closely tied to the patterns of river erosion (McColl et al., 2022).

We were surprised to find no clear relationship between the landslide aspect and our landslide activity classification accuracy since InSAR is typically insensitive to movement in the SN direction. This may be because movement vectors within large landslides can be complex. Even landslides that are dominantly oriented SN may have portions moving in the WE or vertical directions that are detectable by InSAR (as shown by the Rangitikei Landslide, Figure 5.12). However, a more significant limitation of our analysis is that this InSAR technique less reliably identifies activity within smaller (< 10 ha) landslides. This is likely because multi-looking and double-difference filtering significantly decreased the effective resolution of the data within our InSAR analysis. While future studies should consider reducing the double-difference filter sizes if they plan to assess the activity of smaller landslides, we found that reducing the filter size in our study area led to a sharp increase in the amount of noise present in our activity dataset. However, new SAR missions such as the upcoming NISAR mission will also produce higher quality data that may not need to be filtered to the same extent.

Even though our activity analysis performed well within the landslide boundaries, many false positives existed outside the mapped landslide areas. Further investigations revealed that some of these false positives were unmapped landslides, but most were areas of high noise or real movement associated with other geomorphic processes. InSAR can detect local movement related to centimetre-scale geomorphic processes such as soil porewater pressure changes (Cohen-Waeber et al., 2018), so it is essential to remove activity areas related to processes that are irrelevant to the study in question. In the case of active landslide identification, searching for InSAR activity within the bounds of previously mapped landslides provides a mechanism for updating existing landslide databases and filtering out InSAR-identified movement related to other processes. Overall, we believe that our results demonstrate that this InSAR framework is capable of using readily available free datasets to reliably detect landslide activity states within natural settings where quality InSAR datasets are more challenging to obtain.

We were pleased to see that even though the two landslides that we had independent movement data for were moving at rates exceeding 1 m/yr in many locations, our InSAR landslide activity map still identified both as active. However, as expected, the InSAR results were incoherent in the fastest moving portions of the landslides in both cases. This indicates that our InSAR activity analysis is likely to be effective even in cases high levels of movement decorrelation are expected. Some studies have also used InSAR decorrelation to perform this type of analysis (Jung and Yun, 2020), but this technique still needs to be adapted for landslides that do not experience catastrophic failure (i.e. do not experience full decorrelation). For our study, movement was identified by InSAR in the transition and periphery zones where movement rates were slower.

This finding has important implications for estimating landslide velocities based on InSAR data. When using Sentinel-1 C band SAR data, coherent estimates of landslide velocity are only likely to exist in areas whose movement velocities in the LOS direction do not exceed a few centimetres between image pairs. If there is faster movement at another location on the landslide, InSAR will likely not identify this movement, and the measured velocity of the landslide will be capped at a few cm/yr. Thus, it is crucial to pair InSAR analyses with other measurement techniques, such as sPOT, to identify faster movement.

### *5.5.2 Sub-Pixel Offset Tracking*

We found that our time-series sPOT methodology could measure multi-year landslide movement at a variety of different velocities, but that our ability to distinguish true movement from background noise increased when velocities were below 0.5 m/yr. At our test sites, which had an average horizontal velocity magnitude of 2.05, the MAE was 0.74 m/yr. This finding is in line with previous studies (Bickel et al., 2018; Dille et al., 2021), which have found that pixel offset tracking techniques can accurately measure movement exceeding 1/20$^{th}$ to 1/10$^{th}$ of a pixel (which equates to 0.5 to 1m for the 10 m pixel resolution of the Sentinel-2 imagery used in our study).

The random noise in our sPOT analysis made it challenging to use this technique to distinguish between activity and inactivity at landslides whose maximum movement rates were less than 0.5 m/yr. Additionally, the removal of features at the periphery of landslides via river erosion led to unreliable results within one-pixel width (80 m) of the landslide's edge. Due to these issues, we believe that our sPOT methodology is less useful for regional identification of slow-moving (0.01 – 0.1 m/yr) landslide activity and is instead best used in tandem with another technique that can identify activity at these slower movement rates (e.g. our InSAR analysis). However, this technique is likely applicable on its own within regional analyses where landslide movements rates are expected to exceed 2 m/yr. Also, since the accuracy of sPOT methodologies are directly related to the georectification accuracy and spatial resolution of the imagery used, utilizing data from proprietary high-resolution repeat image missions, such as PlanetScope, may result in improved accuracy where this is needed.

### *5.5.3 A Framework for Landslide Monitoring*

Overall, we find that by combining existing information on landslide presence, time-series InSAR, and time-series sPOT, we can create a landslide monitoring framework that is greater than the sum of its parts. Figure 5.13 shows how we propose setting up this framework. First, a dataset of landslide polygons is obtained from an existing database or from new geomorphological mapping. Second, the time-series InSAR analysis described in this paper is performed for the region, and areas of activity are identified. These areas of activity can then be intersected with the known landslide locations to identify active landslides, and areas of activity outside the mapped landslides can be discarded (after checking to ensure they are not associated with a landslide potentially missing from the initial landslide dataset). For those landslides that have been identified as active, we can then perform the times-series sPOT analysis described above to estimate movement rates in areas whose velocities exceed the threshold detectable via time-series InSAR (~ 5 cm/yr).

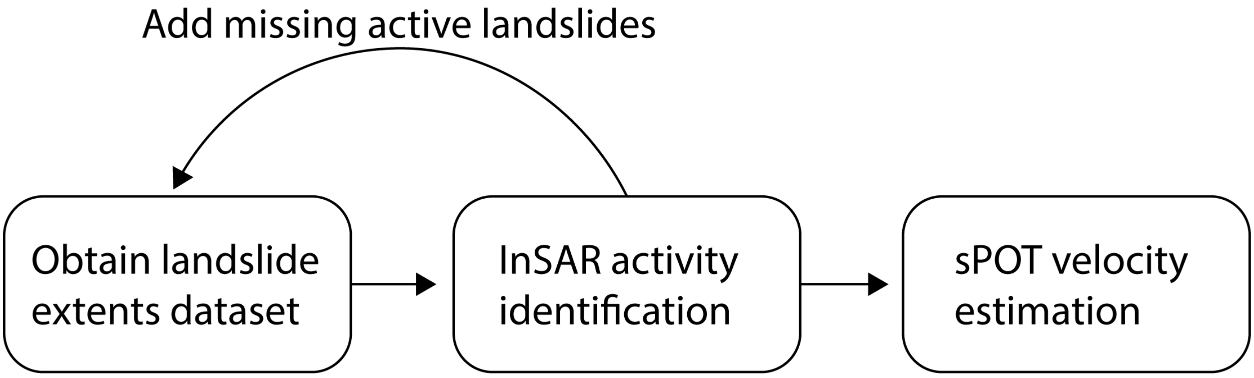


*Figure 5.13 Our proposed framework for time-series InSAR and time-series sPOT remote landslide monitoring. First, use time-series InSAR to identify activity within a previously mapped landslide dataset, optionally use the InSAR data to add new active landslides to the landslide dataset, then perform a time-series sPOT analysis within the active landslides to identify faster motion.*

We believe that this framework represents a reliable and reproducible approach for remote landslide monitoring, with a few important caveats and opportunities for improvement. First, we found increased uncertainty when using sPOT to measure landslide movement between 0.05 m/yr and 0.5 m/yr. As noted previously, satellite imagery from proprietary high-resolution (< 5 m spatial resolution) satellite imagery missions may reduce this error. Second, the resolution of the underlying SAR data and the application of the double-difference filter also limits the spatial resolution of the InSAR analysis, and our activity analysis may not produce reliable results when assessing the activity of landslides smaller than those found within our activity validation dataset (i.e., < 10 ha). However, proprietary higher-resolution SAR sensors may offer data that can detect activity at smaller landslides. Third, this workflow has not been tested in scenarios where landslide velocities exceed 10 m/yr. Still, glacier velocity studies have shown that sPOT techniques are be reliable in these settings (Gardner et al., 2018; Lei et al., 2021), so we expect the same for faster moving landslides (provided their features are still detectable, i.e. not lost into a river or with substantially disrupted ground).

In addition to the reliability of a monitoring framework, its ease of use plays a significant and often dominant role in its adoption and utility. In this context, our framework is an important step forward. The data and software needed to perform InSAR and sPOT analyses can often be fragmented between multiple desktop applications and programming languages, some of which may not be available to users without paid licenses. In contrast, our framework can utilise freely available data for the entire processing chain and is wholly contained within Python Jupyter Notebooks available for download and use (see Code and Data Availability section). Additionally, we have built our framework on existing cloud computing services and have shown that it is possible to use these services to reduce the computational cost of these analyses, especially when applied across large regions, while producing reliable results.

## 5.6 Conclusion

In this study, we presented and assessed the reliability of a framework for the remote monitoring of large, slow-moving landslides. This framework builds upon existing landslide inventories and utilizes a time-series InSAR analysis to identify landslide activity and a time-series sPOT analysis to measure the movement rate of active landslides. We found that our InSAR activity analysis was able to identify activity within existing landslide extents with an accuracy of 91% and a kappa of 0.76. Our InSAR WE dataset significantly underestimated the movement rates of the two landslides where we had independent validation of movement rates. However, our time-series sPOT analysis measured the movement of landslides that had an average velocity of 2.05 m/yr with an MAE of 0.74 m/yr. Overall, we found that InSAR and sPOT are reliable tools within their domains, but they are more useful when combined into a single framework.

Landslides are an important and widespread natural hazard, but many landslides are unmonitored because there are insufficient resources to do so. The field of remote sensing has created many tools to overcome this challenges, but, if those tools are not freely available, reliable, and computationally efficient, practitioners are unlikely to adopt them. By developing upon Python-based tools, utilizing cloud computing where possible, rigorously testing the validity of our results, and making our workflow freely available, we believe that we have created a remote landslide monitoring framework that coincides with the needs of practitioners.

## 5.7 Acknowledgements

Thank you to many scientists across the world who took the time to talk to a PhD student about how to perform quality InSAR and sPOT analyses. Also thank you to the Alaska Satellite Facility and the Microsoft Planetary Computer for offering on-demand processing of geospatial data at no cost to scientists. This research was supported by the New Zealand Ministry of Business, Innovation and Employment research program "Smarter Targeting of Erosion Control (STEC)" [Grant Number C09X1804] and by the MBIE Strategic Science Investment Funded Hazards Program at GNS Science.

## 5.8 Code and Workflow Availability

The notebooks used to perform the InSAR analysis can be found at this repository, and the notebooks used to perform the sPOT analysis can be found at this repository. The notebook used to create the figures in this study can be found at this repository.

## Thesis Synthesis of Chapter 5

In this chapter I described the development and validation of my InSAR and sPOT analyses for the screening of landslide activity and measuring movement rates (Objective 3). In this chapter I highlighted how careful selection of image networks can improve the quality of InSAR and sPOT analyses. For the InSAR analysis, I maintained connected networks by conducting the analysis separately for each year, and for the sPOT analysis I utilized pairs separated by a whole number of years that also occurred during the same time of year. While there is still a high degree of uncertainty in the validation results for both measurement techniques, I believe that the reliability of these techniques is sufficient to use them to identify soft-rock landslide activity and track soft-rock landslide motion at regional scales. These capabilities will be directly used in Chapter 6 to identify which soft-rock landslides are active within the Whanganui Basin and to estimate their movement rates. This information will then be used in Chapter 6 to complete Objective 4 and Objective 5 respectively.

# Chapter 6 The Contributions of Soft-Rock Landslides to Riverine Sediment Budgets

## Introduction to Chapter 6 of Thesis

Chapter 6 addresses Objective 4 (perform a landslide activity factor analysis to determine the factors leading present-day landslide activity in the Whanganui Basin) and Objective 5 (estimate the annual average sediment export from the soft-rock landslides in the region, and compare these results to estimates of basin-wide sediment inputs). This chapter relies on the methods developed in Chapter 5 (Objective 3) and thus there is a tight coupling between these chapters. While other studies have measured the sediment exports from a few landslides in the region, this is the first study that attempts to create a basin-wide estimate of sediment inputs from soft-rock landslides. It is also one of the first analyses that uses a time-series InSAR and sPOT analysis to estimate landslide sediment exports across an entire region. Due to the dependence of this chapter on Chapter 6, it will not be submitted for publication until Chapter 5 is published, but it is currently ready for submission. Also, for the purposes of this thesis, all references to "Williams et al., in Prep" refer to the work detailed in Chapter 5 of this thesis.

*This chapter will be submitted to Earth Surface Processes and Landforms as:*

Williams, F., McColl, S., Fuller, I., Smith, H., Neverman, A., 2022. The contributions of soft-rock landslides to riverine sediment budgets. Earth Surface Processes and Landforms.

## 6.1 Abstract

Excess suspended sediment is an environmental pollutant that can negatively impact the health of river systems. Shallow and episodic event-driven landslides are a well-known source of sediment in steepland catchments, but less is known of the contributions from slow-moving, deep-seated landslides. Few landslide inventories contain information on the activity state and movement rates for these landslides, but this information is necessary to estimate their sediment exports. In this study, we apply a recently developed time-series interferometric synthetic aperture radar (InSAR) and time-series sub-Pixel Offset Tracking (sPOT) landslide monitoring framework to catchments of the Whanganui Basin in New Zealand to: (1) identify large, actively moving landslides; (2) assess landscape factors that explain the distribution of the active landslides; (3) measure landslide velocities to calculate annual sediment contributions from each landslide, and (4) compute their total sediment contributions to local rivers with measures of uncertainty as well as sensitivity, and contextualize this within wider catchment sediment loads. We find that 66 of the 731 deep-seated landslides in the study region are currently active (within the past 4 years) and that gentle slopes, high terrain roughness, and high annual rainfall best explain the distribution of active landslides. These active landslides contribute 10±2% of the total sediment export (varying from 2±1% to 19±3% between catchments) even though these landslides occupy only 0.3% of the study area. We conclude that deep-seated, slow-moving landslides are an important, but often overlooked, sediment source in the soft-rock catchments within our study area. Consequently, if manageable, they may represent an opportunity for sediment export reduction since they are likely the largest point-source of sediment within these catchments.

## 6.2 Introduction

Excess fine sediment in rivers and streams is a significant biological impairment that reduces water clarity and increases the cost of water treatment (Collins et al., 2011; Davies-Colley and Hughes, 2020; Davies-Colley and Smith, 2001; Owens, 2020). Excess sedimentation can also lead to the mortaring of gravel-beds, in which fines clog gravel interstitial spaces, embedding coarse clasts in the substrate, resulting in a loss of habitat for riverine invertebrates and spawning for fish (Bilotta and Brazier, 2008; Jones et al., 2012). Within steepland landscapes, landslides are an important source of river sediment and can sometimes overwhelm or block river channels (Agliardi et al., 2013; Korup, 2006; Xu et al., 2009). Two important distinctions for landslide sediment export are whether the landslides are shallow or deep-seated and rapid or slow moving. Shallow landslides tend to strip regolith and are typically episodic and one-off, small (< 1000 $m^2$) failures, triggered in response to large precipitation events (Fuller et al., 2016) or earthquakes (Massey et al., 2018). Conversely, deep-seated landslides are typically larger, with failure surfaces within bedrock. Their patterns of failure usually reflect long-term (millennial and longer) changes in climate, uplift, and river incision (Kuehl et al., 2016; Larsen et al., 2010; Larsen and Montgomery, 2012), and while they can be rapid, one-time failures (e.g. triggered by earthquakes), many are long-lived and undergo sustained or episodic phases of movement (Agliardi et al., 2013; Pánek and Klimeš, 2016; Williams et al., 2021). In particular, soft-rock deep-seated landslide are particularly prone to prolonged slow movement because the weak material they're composed can easily shift between a marginally stable or unstable state (Mackey and Roering, 2011; Mountjoy, 2005; Thompson, 1982).

At millennial and longer timescales, evidence suggests that soft-rock landslides and other deep-seated landslides play a dominant role in the denudation of uplifting regions (Korup, 2006, 2004; Larsen and Montgomery, 2012). Less is known about the role soft-rock landslides play in contemporary sediment budgets, especially relative to the contributions from shallow landslides (Betts et al., 2017; Broeckx et al., 2020; Heckmann and Schwanghart, 2013; Smith et al., 2021) and multiple occurrence regional landsliding events (Crozier, 2005; Dadson et al., 2004; Page et al., 1999; Parker et al., 2011). This is likely due to several factors. First, little regional-scale (1,000 $km^2$ to 100,000 $km^2$) data exists for movement rates of active soft-rock landslides, partly due to the inhibitive costs of monitoring landslides. Second, many sediment load models track sediment export for non-point sources only, providing continuous probabilistic estimates of sediment export for all locations within a landscape (Dymond et al., 2010; Renard and service, 1997). Shallow landslides are typically incorporated into these sediment load models via the creation of landslide susceptibility maps, which provide a continuous estimation of the potential for shallow landslides based on factors such as slope, land cover, and soil properties (Reichenbach et al., 2018; Smith et al., 2021). The susceptibility map approach is less suitable for soft-rock landslides because they are larger, occur at much lower spatial densities, and are more akin to a point source of sediment.

Regional information on soft-rock landslides is often documented in landslide inventories (Guzzetti et al., 2012), which contain the location and areal extent of landslides. Such inventories can be used in statistical analyses that seek to determine which factors control the generation of landslides (Ayalew and Yamagishi, 2005; Budimir et al., 2015; Williams et al., 2021). However, these inventories tend to not include information on landslide activity state and often contain many relict (inactive) landslides. Consequently, studies performed using these inventories typically convey information about only the long-term (millennial and longer) patterns in landslide occurrence and not the factors controlling present day activity. Additionally, sediment export models need reliable activity state and movement rate data to incorporate soft-rock landslides into broader sediment budget models, but this information is often not available in these types of inventories.

To overcome this limitation, newer sediment budget model frameworks are beginning to incorporate data from discrete features by leveraging the power of GIS and remote sensing analyses (De Rose and Basher, 2011; Dymond et al., 2010). Such approaches are challenging, however, because a bespoke sediment export model is typically needed for each type of erosional process (e.g., surface erosion, gully erosion, riverbank erosion, and landslides). As an alternative to bespoke models, repeat aerial or drone surveys of the landscape using LiDAR or photogrammetry methodologies can be used to create a series of digital elevation models (DEMs) that can then be combined to create DEMs of differences (DoDs) (Day et al., 2013b; Lane et al., 2003; McColl et al., 2022; Wheaton et al., 2010). These DoDs can then measure sediment export and storage across the landscape, regardless of the erosion process.

However, high resolution elevation models are unavailable for many parts of the world. Thus, this methodology is difficult to rely on for regional studies of landslide sediment contribution.

Emerging remote sensing technologies such as interferometric synthetic aperture radar (InSAR) and sub-pixel offset tracking (sPOT) are now also being used to monitor activity at soft-rock landslides (Amitrano et al., 2019; Bekaert et al., 2020; Hu et al., 2020b; Kang et al., 2021). Some prominent examples include the work at the Slumgullion Landslide in Colorado, USA (Hu et al., 2020b), the Rangitikei and Bird landslides of New Zealand (Williams et al., in prep; McColl et al., 2022), the Ikoma Landslide in the Democratic Republic of Congo (Dille et al., 2021), and the landslides surrounding the Three Gorges Dam in China (Sun et al., 2017). These techniques are incredibly cost-effective because they can make use of publicly available remote sensing data that, in many cases, is continually collected and can produce accurate measurements of landslide motion. In theory, these methods are well suited to application over large areas (>1000 km$^2$), but to date most studies have been limited to only a few landslides. Some exceptions to this are an InSAR analysis of the Pacific Northwest, USA by Xu et al. (Xu et al., 2021b), and a manual tracking of features between successive aerial photography surveys in California, USA by Mackey and Roering (2011) as well as an inclinometer-based study that assessed the velocities and sediment export in Italy at regional scales (Simoni et al., 2013b). Still, no studies have used automated remote sensing techniques such as these to create a regional sediment export model for deep-seated landslides.

However, we have recently developed a landslide monitoring framework that combines the use of time-series InSAR and sPOT to efficiently monitor the movement of landslides at regional scales (Williams et al. in prep). This framework uses time-series InSAR to identify recently active landslides, then uses time-series sPOT to estimate their movement rates. In the present study, we apply this framework within the Lower Whanganui Basin of New Zealand, a region containing over 731 soft-rock landslides greater than 10 ha in size, to (1) identify which of these landslides are active using InSAR; (2) determine which landscape factors best predict the activity/inactivity of these landslides; (3) measure landslide velocities and create a sediment export model to calculate annual sediment contributions from each landslide; and (4) use an uncertainty analysis to estimate the sediment contribution of these landslides to their catchments.

## 6.3 Study Area

The Lower Whanganui Basin (hereafter referred to as the Whanganui Basin) of the southwest North Island, New Zealand, is bounded by axial ranges composed of greywacke to the east and the Taupo Volcanic Zone to the north (Figure 6.1). It is a back-arc basin associated with subduction along the Australian-Pacific plate boundary off the east coast of the North Island (Walcott, 1978). Pliocene to Pleistocene subsidence is driven by lithospheric loading and down warping caused by coupling between the overriding and subducting plates at the Hikurangi Subduction Zone (Armstrong et al., 1998). Migration of the Taupo Volcanic Zone to the south-southwest within the past 5 Ma has caused a migration of the basin centre and a 2°–15° rotation of the basin's bedrock in the same direction (Pulford and Stern, 2004). Currently, the Basin centre lies offshore and is actively accreting.

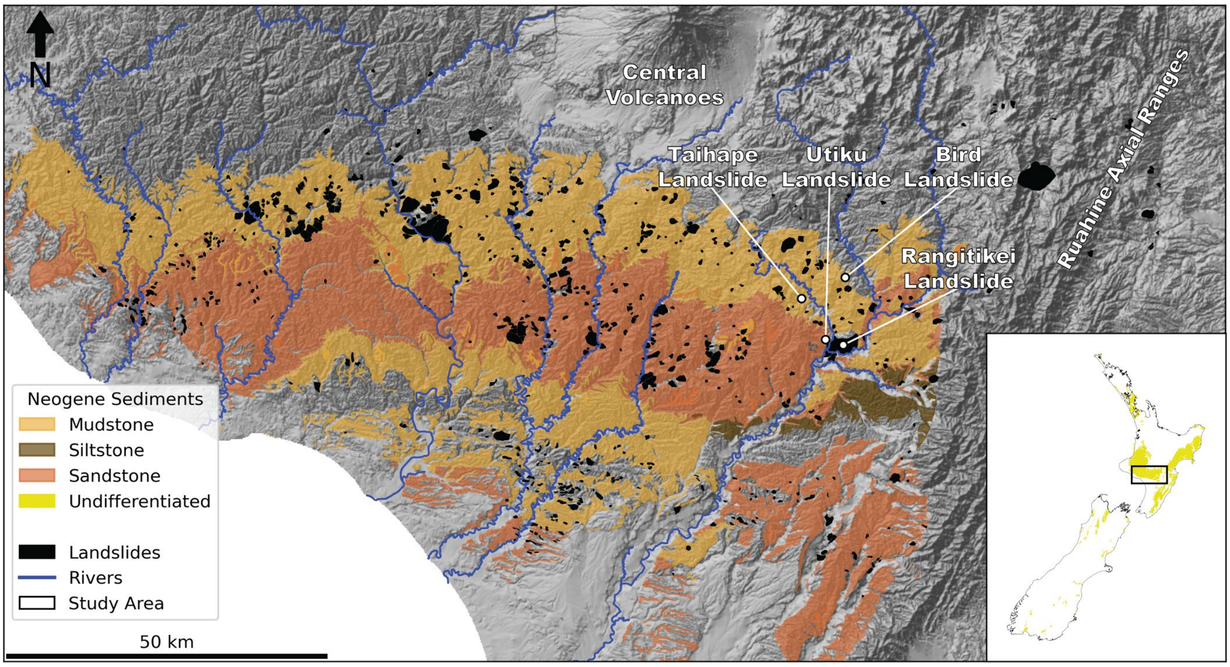


*Figure 6.1 The Whanganui Basin with deep-seated landslide extents and major river systems. The bedrock layers shown here include all units of the Whanganui Basin that are susceptible to deep-seated landslide occurrence (i.e., it excludes limestone and unconsolidated sediments). The yellow portions of the inset map indicate the parts of New Zealand that are composed of Neogene sediments that are similar to those found in the Whanganui Basin. Specific landslides that are discussed within this study are highlighted within the main portion of the map.*

The sediments of the Whanganui Basin reach a maximum thickness of 4 km and range in age from 0-5 Ma (Anderton, 1981). Similar rates of uplift and aggradation during Basin formation and the migration of the Basin centre have led to the deposition of shallow-water limestones, mudstones, and sandstones with a down-lapping geometry. Within the sandstone and mudstone units of the Basin, thin syndepositional clay layers are present (Pillans, 2017). These clays are rich in smectite (Reyes, 2007), and are formed from volcanic ash sourcing from nearby rhyolitic volcanoes. They have also been shown to be preferential failure surfaces for some deep-seated landslides in the region (Carey et al., 2019; Massey et al., 2013). The matching rates of deposition and uplift have led to stunted diagenesis of the basin sediments, which has resulted in relatively low rock strengths (i.e., soft rock). Erosion has resulted in deeply incised rivers with rectilinear slopes, and sharp drainage divides. The Whanganui Basin contains seven major catchments that drain southwest into the Tasman Sea. The catchments in the east are bounded by the central volcanoes and the Ruahine mountain ranges, but the catchments in the west, namely the Whanganui, extend farther north into the upper Whanganui basin.

Before human habitation, the basin was widely vegetated by native forest cover (McGlone, 1989). When Polynesians arrived in New Zealand in the late 13th or 14th centuries AD, they burned portions of the lowland forest (Ewers et al., 2006) and early European settlers in the late 19th century cleared much of the remaining forest in the region. By the mid-20th century, most of the land surface had been converted to cropland and pasture. Widespread increases in shallow landslide activity, gully erosion, and earthflows (Glade, 2003; Marden et al., 2012) led to conservation programs in the 1960s that resulted in the establishment of exotic forest plantations (Michelsen et al., 2014; Richardson, 2011) in some locations. However, pasture is still the dominant form of land use in the region, and according to the New Zealand Ministry of Environment's land use dataset, the basin is composed of 19% Native Forest, 8% Exotic Forest and 73% Pastureland.

Today, mapped currently active and inactive soft-rock landslides cover roughly 8% of the study area (Figure 6.1). Previous research of these landslides has included in-situ monitoring of the Utiku, Taihape, and Rangitikei landslides in the eastern portion of our study area (Figure 6.1) (Massey et al., 2016b, 2013; McColl et al., 2022), and studies of regional- or local-scale landslide distributions (Crozier et al., 1995; Rees et al., 2019; Thompson, 1982; Williams et al., 2021). These studies all conclude that low internal rock strength, low shear-strength clay layers on dip slopes, and high uplift rates (coupled with fluvial incision) contribute to the occurrence of soft-rock landslides in the region. Movement rates for the monitored landslides vary widely. The Utiku and Taihape landslide were found to move roughly 10-100 mm/yr (Massey et al., 2016b, 2013), but with some periods of very slow creep and other periods of accelerated movement of several meters per year. Average movement rates of the Rangitikei landslide zones ranged from 0.2-9.4 m/yr, with one monitoring location experiencing over 18 m/yr (McColl et al., 2022). Undercutting of the landslide toe by fluvial erosion and excess porewater pressures were found to influence movement rates of all three landslides. It is unclear how regionally representative these few studied landslides are, since the activity states of the remaining 728 deep-seated landslides within the region are unknown.

The region, and its neighbouring catchments, have also been the subject of several landslide susceptibility studies and sediment budget analyses, albeit predominantly for shallow landslides. Several shallow landslide susceptibility studies have been conducted within the Manawatū catchment to the south as well as the Whanganui catchment (Betts et al., 2017; Dymond et al., 2006; Smith et al., 2021), and in their study, Fuller et al. (2016) estimated a figure of over 350 tons/km$^2$ per year of erosion from a set of shallow landslides in the Ruahine Ranges between 1946 and 2011. The NZeem erosion model (Dymond et al., 2010) and the SedNetNZ sediment budget model (Dymond et al., 2016) have both been used to study sediment dynamics within the basin. These models offer a way to compare the sediment export rate we produce for soft-rock landslides to the rates of sediment export of other processes occurring within the basin.

## 6.4 Methods

### *6.4.1 Identifying Active Landslides*

#### *6.4.1.1 Landslide Dataset*

In this study, we applied the InSAR/sPOT landslide activity and movement rate analysis described in Williams et al. (in prep) to the landslides of the Whanganui Basin. These landslides include the landslides previously mapped by Williams et al. (2021) as well as roughly 50 that were mapped outside of the basin during the same mapping effort. We exclude landslides smaller than 10 ha, since this is the estimated lower limit of our InSAR activity analyses (Williams et al,. in prep). This excludes 5% of the total area covered by >2 ha soft-rock landslides in region, which represents 0.4% of the total study area. In total, we include 731 landslides (Figure 6.1), which likely includes a range of relict (highly degraded), dormant, and active landslides. Some of these landslides are likely to have been one-time failures (typical for rotational failures), while others are likely to experience continuous or episodic movement (typical for low-angled translational failures) for potentially hundreds to thousands of years.

*6.4.1.2 Landslide Activity Screening Using Time-series InSAR*

To detect which of the landslides in the inventory have been recently active (i.e., since 2018), we applied a time-series InSAR movement analysis, using the framework described in Williams et al. (in prep). This analysis was found to predict activity at deep-seated landslides with an accuracy of 91% and a Cohen's kappa of 0.74 when compared to a set of 60 visually-assessed active and inactive deep-seated landslides (Williams et al. in prep). We used the 2-in-range and 10-in-azimuth (40x40 m resolution) unwrapped interferograms provided by the Alaska Satellite Facility's Hybrid Plugin Processing Pipeline (HyP3). HyP3 is a cloud-based on-demand interferogram generation service available at no cost to scientists (Hogenson et al., 2016). From HyP3, we requested all possible Sentinel-1 interferograms formed between each Single Look Complex (SLC) image and the previous three images between 2017 and 2021 for both the ascending and the descending orbit directions that covered the study area shown in Figure 6.1 (Table 6.1). Due to inconsistencies in the collection of Sentinel-1 data over New Zealand, descending orbit data was not available for 2017 (Figure 6.2), so that year was excluded from our analysis.

*Table 6.1 The collection information for the Sentinel-1 Single Look Complex images (SLCs) and interferograms (Ifgs) available within the study area.*

| Orbit | Path | Frames | Start Date | End Date | # SLCs | # Ifgs |
|---:|---:|---:|---:|---:|---:|---:|
| Ascending | 81 | 1043 | Jan 2018 | Oct 2021 | 112 | 330 |
| Ascending | 81 | 1048 | Jan 2018 | Oct 2021 | 112 | 330 |
| Descending | 73 | 720 | Jun 2018 | Nov 2021 | 89 | 261 |
| Descending | 73 | 725 | Jun 2018 | Nov 2021 | 89 | 261 |

Once downloaded, we loaded the portion of the interferograms that intersected our study area into the Miami InSAR Time-series in Python (MintPy) program (Yunjun et al., 2019), where we conducted the remainder of the movement analysis. Following Williams et al. (in prep), we removed low-quality (average coherence < 0.4) interferograms then conducted the InSAR time-series analysis separately for the longest connected network within each year and orbit direction (Figure 6.2). Performing the analysis individually for each year allowed us to use only fully connected networks, which removes significant bias from the analysis and captures sporadic landslide movement (i.e., landslides that are only active in a subset of years). Before the time-series inversion was conducted, we applied Bekaert et al.'s (2020) double-difference filter, which enhances the strength of local deformation signals at the expense of obscuring regional trends. We then performed the small-baseline subset (SBAS) time-series inversion and estimated a linear velocity at each pixel by averaging the results of 100 linear velocity estimates conducted using bootstrapped samples of the time-series data.

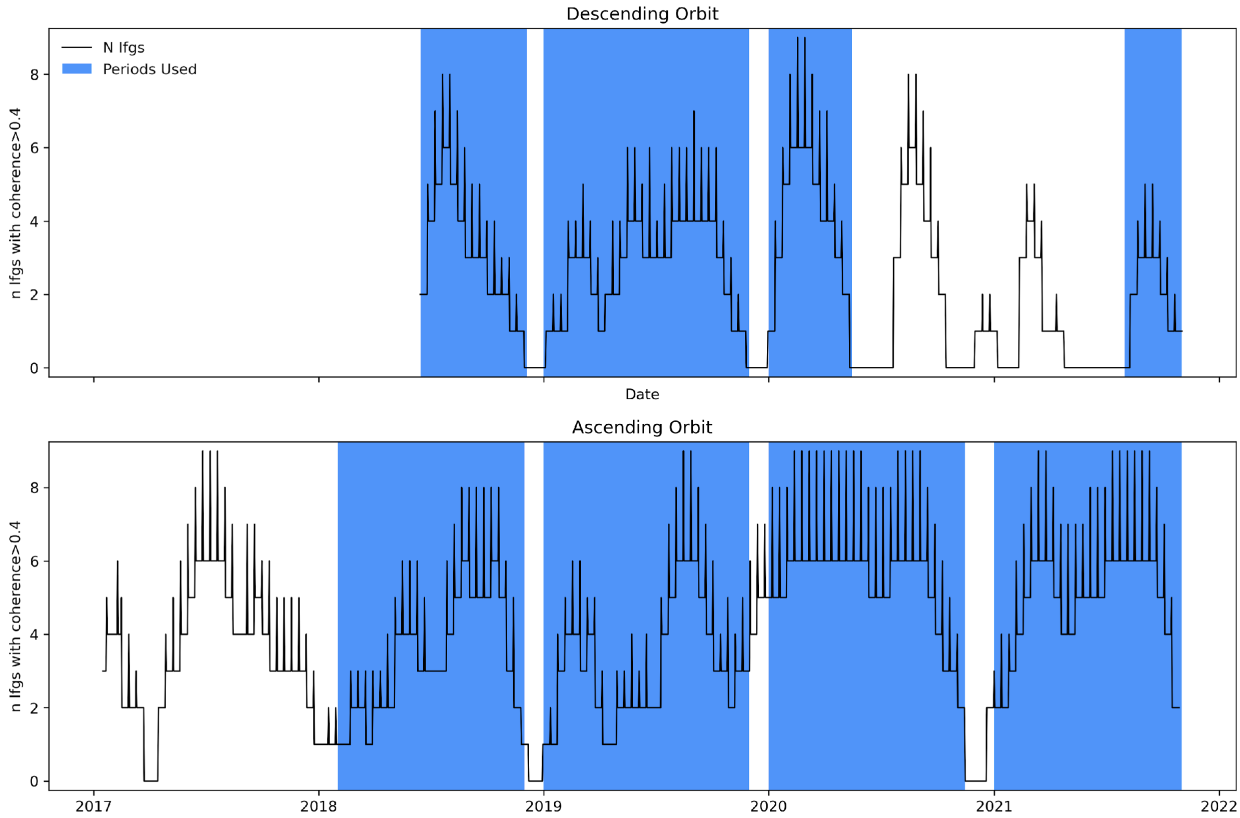


*Figure 6.2 The number of valid interferograms (with average spatial coherence > 0.4) available for our study area between 2017 and 2021. The top plot shows data availability for the descending orbit data, and the bottom plot shows the availability for the ascending orbit data. The blue regions cover the longest continuous interferogram network for each year and represent the epochs used within our study.*

To identify movement within the InSAR velocity datasets, we applied the velocity-coherence filter described in Williams et al. (in prep). This filter removes all InSAR pixel velocity values whose temporal coherence values are less than the dataset mean (0.905), then removes pixels whose absolute velocity value is less than twice the standard deviation of the velocity dataset, then finally removes all pixel clusters that include fewer than 19 pixels (a 3 ha area). We then combined the ascending and descending orbit movement datasets from each year using a logical OR operation to form annual movement datasets. We defined areas of active movement to be any location identified as moving in at least two of the four annual movement datasets.

To increase of certainty that areas of active movement in our time-series InSAR analysis were related to landslide activity, we intersected the areas of active movement with our landslide extent dataset (buffered inward by 40 m to remove edge effects). We then assumed that one or more areas of activity within landslide boundaries was indicative of landslide activity. However, before conducting our landscape factor analysis, we reviewed each area of movement within the landslide boundaries to determine if the identified movement occurred in an unreliable setting (e.g., located within areas known to produce erroneous results in C-band SAR data such as forests and waterbodies, or located along the margin of the landslide).

Areas of activity within such locations were discarded, and, if no other areas of movement existed, that landslide was classified as inactive.

### *6.4.2 Analysis of Landscape Factors Controlling Landslide Activity*

To identify the landscape factors behind the distribution of active deep-seated landslides, we performed a landslide susceptibility analysis. The method was similar to what Williams et al. (2021) used to assess regional controls on the presence of all large landslides (i.e. regardless of activity). For each of the active and inactive landslides within our study area, we associated landscape factors previously used by Williams et al. (2021) (Table 6.2) with each landslide. We then used a logistic regression analysis to assess which factors had the most influence on whether landslides were active or not. Inactive landslides were more abundant than active landslides, so we randomly sampled from the inactive landslides to achieve balanced sample sizes. We ran the logistic regression analysis ten times, each with a different sample of inactive landslides. The landscape factor values summarized at each landslide are the covariates (predictor variables) for our logistic regression analysis, and a binary activity metric (1 = active, 0 = inactive) is our response variable. To limit the covariance within our dataset, we calculated the variance inflation factor (VIF) for each covariate, then removed all covariates with a VIF score greater than 5. We also converted all covariates into their standard score following the equation below:

*Equation 6.1 Standardization of a sample member*

$$z = \frac{x - \mu}{\sigma}$$

Where $z$ is the observation's standard score, $x$ is an observation of the covariate, $\mu$ is the covariate mean, and $\sigma$ is the covariate's standard deviation. This conversion normalizes the values of the covariates, which allows the model coefficients for each covariate to be interpreted as a measure of covariate importance (Lombardo and Mai, 2018). We performed our logistic regressions using a five-fold cross-validation split of our data between training and testing (i.e., 20% of the training data was reserved in each of five iterations to test the model) and a LASSO regularization to penalize model complexity. For the regularization, we selected a weight factor of 5 because it provided an adequate balance between model simplicity and performance. We used the Area Under the receiver-operator Curve (AUC) metric to assess the model's predictive performance and assessed the importance of each covariate using the magnitude of the regression coefficients and a jackknife regression analysis (Lombardo and Mai, 2018).

*Table 6.2 The susceptibility factor datasets we used within the activity analysis portion of this study. A more in-depth discussion of these datasets can be found in Williams et al. (2021).*

| Datasets | Category | Source |
|---:|---:|---:|
| Rainfall | Climatic | NZ Ministry for the Environment |
| Soil Moisture | Climatic | NZ Ministry for the Environment |
| Uplift | Geologic | Pulford and Stern 2004 |
| Dip Angle | Geologic | Rattenbury and Isaac 2012 |
| Distance to Active Fault | Geologic | Rattenbury and Isaac 2012 |
| Distance to Fault | Geologic | Rattenbury and Isaac 2012 |
| Early Pleistocene Sediments | Geologic | Rattenbury and Isaac 2012 |
| Quaternary Sediments | Geologic | Rattenbury and Isaac 2012 |
| Predicted Peak Ground Acceleration (2475 yr return) | Geologic | Stirling et al 2012 |
| Stream Power Index | Geomorphic | GRASS GIS r.watersheds tool |
| River Incision | Geomorphic | Litchfield and Berryman 2006 |
| Maximum Elevation | Geomorphic | NZSoSDEM |
| Eastness | Geomorphic | NZSoSDEM, Horn 1981 |
| Northness | Geomorphic | NZSoSDEM, Horn 1981 |
| Slope | Geomorphic | NZSoSDEM, Horn 1981 |

Jackknife regression analyses are used to assess the importance of covariates in univariate and multivariate contexts by performing regressions for each covariate that include only the covariate in question, then performing regressions that include all covariates except this covariate. The single variable regressions measure the univariate predictive power of each covariate, while the covariate exclusion regressions highlight the contribution of covariates in a multivariate setting. In the covariate exclusion regressions, decreases in performance relative to the full model indicate increasing variable importance.

### *6.4.3 Estimation of Landslide Sediment Mass Contributions to Catchments*

To estimate the sediment mass contributions to the catchments of the Whanganui Basin, we calculated the total annual sediment mass contributions for the soft-rock landslides in our study area according to the sediment mass export formula (Mackey and Roering, 2011; Simoni et al., 2013b):

*Equation 6.2 Landslide sediment export*

$$Q_l = \sum_{i=1}^{n} w_i \times d_i \times v_i \times \rho_i$$

Where $Q_l$ is the total annual sediment mass contribution from deep-seated landslides within a given catchment, $w_i$ is the width of the $i^{\text{th}}$ landslide, $d_i$ is the average depth of the landslide, $v_i$ is the average velocity of the landslide, $\rho_i$ is the density of the landslide material, and *n* is the number of landslides in the catchment. In the case of depth and velocity, we also trialled multiple methodologies for computing these components to determine what effect varying the methodology would have on the results. Guided by the InSAR data, we also reduced the areal extent of landslide features in the database to remove areas within a landslide polygon that were deemed to be inactive. For example, some landslide polygons in our dataset represent landslide complexes made up of multiple, smaller parasitic landslides, only some of which are active. In such instances, only the active parasitic landslides were included in further analyses (e.g. Figure 6.3). Active landslides that were not directly coupled to a river or stream system were excluded from the sediment mass export estimation since their sediment is unlikely to contribute to river sediment budgets within the six-year timeframe that our sPOT analysis covers.

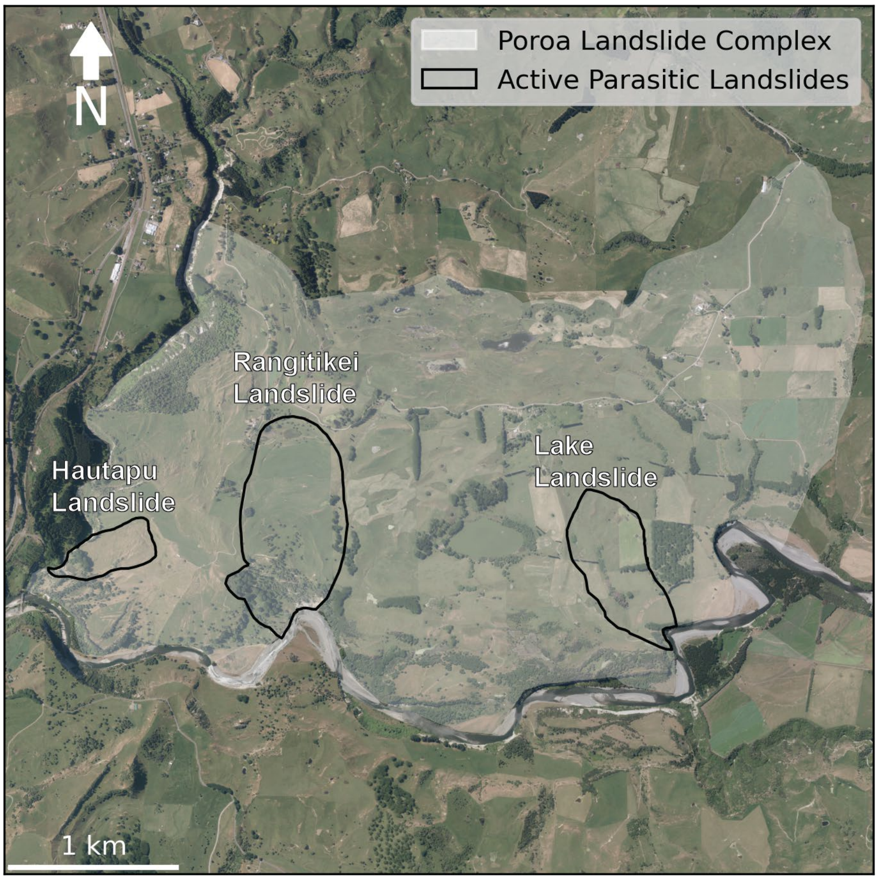


*Figure 6.3 An example of parasitic landslides within a large landslide complex. The Poroa Landslide Complex contains three active parasitic landslides, the Hautapu, Rangitikei and Lake landslides. While the broader landslide complex is inactive, all three of these parasitic landslides are active and have distinct movement directions. The names for the parasitic landslides are taken from (Thompson, 1982).*

### *6.4.3.1 Time-Series sPOT*

To determine the velocity of the active landslides for the sediment mass export estimation, we used the time-series sPOT framework described in Williams et al. (in prep). For each active landslide, we used the Microsoft Planetary Computer Hub cloud computing environment to select a set of cloud-free Sentinel-2 near-infrared (Band 8) images between 2016-2021 that fell closest to a single calendar day (i.e., all the images were taken in the same month or close to it). Using an annual image set allowed for there to be more movement at the landslides between image capture dates, which should increase the overall accuracy of the sPOT analysis. Additionally, selecting images that occurred at a similar time of year reduced differences in shadow and vegetation growth between images. These images were cropped to a 2 km buffer beyond each active landslide and downloaded to a local computer where the rest of the analysis was conducted.

We measured the displacement in the horizontal west-to-east (WE) and south-to-north (SN) directions between each possible pair of images using the Auto-Repeat Image Feature Tracking (AutoRIFT) Python program (Lei et al., 2021). For the AutoRIFT analyses, we used a minimum template window size of 32, a maximum template window size of 128, a maximum search area of 10 pixels, and an 8-pixel step. We removed the bias in each image by subtracting the median velocity within the stable areas from the WE and SN velocity datasets, then ingested these datasets into MintPy, where we conducted our time-series analysis.

We used the MintPy SBAS time-series tool to estimate time-series of deformation then used these datasets to estimate linear velocities in the WE and SN directions for each landslide. We then calculated the mean velocity for all pixels in the lower half of each active landslide polygon (Mackey and Roering, 2011; Simoni et al., 2013b) to determine each landslide's velocity. Then, we calculated the hillslope aspect for each landslide using an external DEM, and projected the velocities along each landslide's aspect vector to determine the horizontal downslope velocity for each landslide.

Since Williams et al. 2022 (in prep) found that there was increased uncertainty in the velocity measurement within areas that had WE or SN velocities less than one standard deviation (~0.5 m/yr) from the mean velocity within the stable areas, we trialled two methodologies for dealing with these low values. In the first methodology, we set the values of all WE or SN velocity pixels that had velocities less than this standard deviation cutoff to 0 m/yr. This can be seen as a conservative approach since we are unlikely to detect motion where this mask is not applied, but might underestimate the velocity in some locations. In the second methodology, we did not alter any of the velocity values and assume that any errors in the low velocity pixels will be uniformly distributed and will not bias the overall calculation. We used both techniques to perform the landslide sediment export calculation (Equation 6.2) and compared the results to determine what impact this choice has on our overall results.

#### *6.4.3.2 Landslide Metrics*

In addition to determining the downslope velocity of the landslides, we needed to determine their average depth, width, and material density to estimate their sediment export (Equation 6.2). To estimate the average depths of the landslides we also employed two different methodologies. In the first methodology, we used the area to volume power-law relationships provided by Larsen et al., (2010) for rock slides to estimate the volume of each landslide:

*Equation 6.3 Volume ~ area scaling relationship*

$$V = \alpha \times A^{\gamma}$$

Where $V$ is the landslide's predicted volume, $A$ is the landslide's surface area, and $\alpha$ and $\gamma$ are fitting parameters equal to 0.186 and 1.35, respectively. We then divided the volume estimate derived from this calculation by the landslide's area (Guzzetti et al., 2009) to determine its average depth. In cases where the active landslide is a parasitic feature within a larger stable landslide's body, we used the larger landslide's area to estimate the failure surface depth since we assume that the parasitic landslide is sliding on the failure surface of the larger landslide. Other studies that employ these techniques in areas with similar landslide (Guzzetti et al., 2009; Simoni et al., 2013b) have found that these techniques produced reasonable results.

As an alternative to this approach, other studies have used an external DEM to measure the height of the landslide toe to estimate landslide depths (Mackey and Roering, 2011). We followed this alternative approach for our second depth estimate methodology, using profiles along an external DEM to measure the toe height at three different locations along the river expression of each landslide (Figure 6.4). Each toe height value was calculated by subtracting the elevation at the bottom of toe from the elevation at the top of the toe, then the three estimated toe heights for each landslide were averaged to create the final estimate. Due to the complex geometries of the landslides we studied, we found it difficult to create objective definitions for the bottom and top of the landslide toe. However, wherever possible, we defined the bottom of the landslide toe as the location where it intersected the river system, and the top of the toe as the first shoulder slope encountered while traversing up that transect's DEM profile (Figure 6.4).

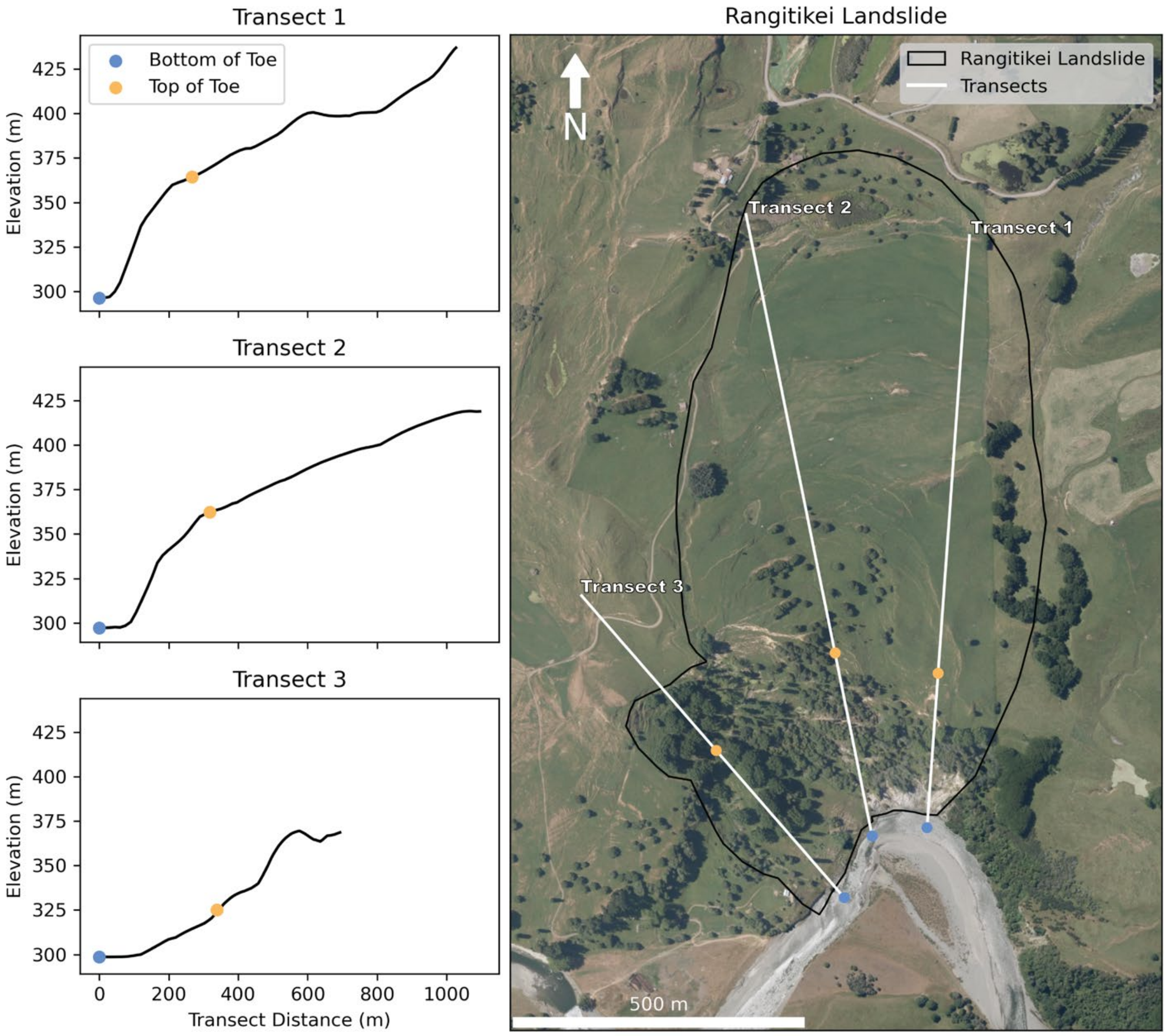


*Figure 6.4 Toe height calculation for the Rangitikei Landslide. The DEM transects for the landslide are shown in the left-hand panels, and the map on the right shows the location of the transects and the associated toe bottom/top locations. While the identification of the toe tops for transects 1 and 2 was relatively straightforward, it was difficult to select an appropriate toe top location for transect 3.*

For both depth estimation techniques, we also compared Monte-Carlo uncertainty based estimates of landslide depth (discussed further below) to in situ measurements of the depth to the failure surfaces (from drill core and inclinometers) at the Utiku and Taihape landslides (Massey, 2010) (Figure 6.1) where field data was available. At the Utiku landslide, the average measured depth was 28.1 m. At this landslide the volume-area methodology estimated a depth of 22.1 m and the DEM toe height methodology estimated a depth of 29.2 m. At the Taihape landslide, the average measured depth was 24.3. At this landslide the volume-area methodology estimated a depth of 21.8 m and the DEM toe height methodology estimated a depth of 23.2 m. Overall, there is a large variability in the field-measured landslide depths as well as both depth estimation methodologies (Figure 6.5). However, the high variability of the measured observations is due to real variation in the landslide thicknesses, not to measurement uncertainty. For example, at Taihape Landslide the dip slope is thinner at the toe and thicker at the head of the landslide, and the Utiku landslide thickness also varies across the slope, due to the underlying bedding, and therefore failure surface, dipping obliquely to the ground slope (Massey, 2010).

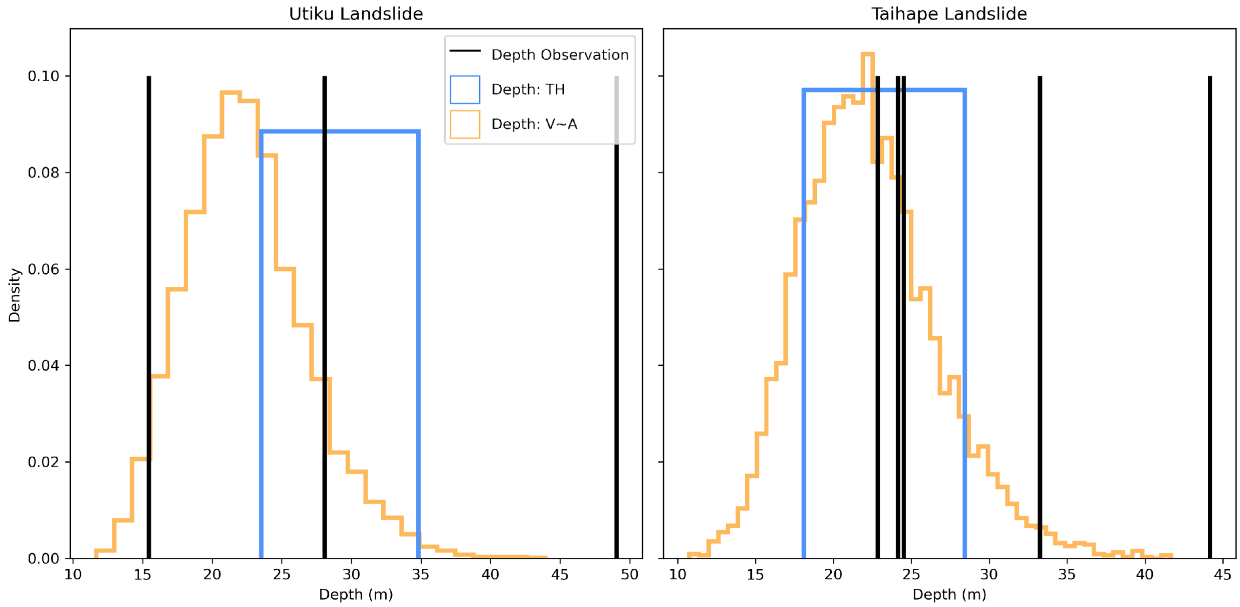


*Figure 6.5 Comparison between Monte Carlo simulations of landslide depths based on area-volume scaling relationships (V~A) (Equation 6.3) and DEM-based Toe Heights (TH) at the Utiku and Taihape landslides to in-situ depth observations (black bars). Both sites have a large distribution of measured and predicted depth values, but both estimation techniques provide an adequate estimate of landslide depth.*

We defined the width of the landslides as equal to the width of the landslide at the top of the landslide toe. This was often close to where it intersected the river system, but this was not always the case. We measured these widths using the active landslide polygons mentioned in the previous section and the imagery used to map the landslide extent. In cases where an active landslide had multiple active lobes, we measured the widths of each separately, then added these widths together.

We estimated the density of the landslide material within the study area using the rock density data provided by Tenzer et al. (2011). Their analysis combined New Zealand's 1:250,000 scale geologic map and 9256 rock density samples throughout the country to estimate rock densities for the entire nation. Since most of a soft-rock landslide's volume is sourced from bedrock, rock (rather than soil) density values are appropriate for estimating mass. The remoulding of landslide material during failure tends to reduce the density, but Massey et al.'s (2010) measurements of both intact rock (2.1 tons/m$^3$) and landslide debris (2.0 tons/m$^3$) rock density at the Taihape and Utiku landslides differed by only 5% from the national rock density dataset at these locations. The two depth estimation methodologies were combined with the two velocity estimation methodologies at each landslide along with the width, depth, and density information to create a set of four possible estimates of landslide sediment export within the study area.

#### *6.4.3.3 Sensitivity and Uncertainty Analysis*

To assess our confidence in the landslide sediment export results we produced, we investigated the sensitivity and uncertainty of our results using two approaches. As discussed above, we have implemented both the velocity estimation and depth estimation using two methodologies each. Since these components of Equation 6.2 are likely to have the largest impact on the overall results, comparing the results we obtain using different combinations of these methodologies should help us understand the extent to which upstream methodological choices affect our results. We combined each velocity methodology with each depth methodology, which produced a set of four distinct landslide sediment export calculations.

Similar to previous regional studies of landslide sediment export (Simoni et al., 2013b), we then estimated the total landslide sediment mass contributions and the uncertainty surrounding these estimates for each methodological combination using a Monte Carlo uncertainty analysis. For each of the covariates in Equation 6.2 and each methodological combination, we defined the distribution of possible values at each landslide, then sampled from these distributions to create 5,000 unique realizations of possible results. We used the median of these realizations as our final sediment export estimate and used two times the standard deviation of the realization distribution as our uncertainty metric.

For the velocity parameter realizations, we added normally distributed noise to the WE and SN velocity maps with a mean of zero and a standard deviation equal to the mean absolute error of the horizontal velocity magnitude predictions (0.74 m/yr) reported in Williams et al. (in prep). This was done separately for the EW and SN velocity datasets, then we recalculated the horizontal downslope velocity of each landslide using these values. When we used the unaltered velocity methodology, the random noise was added to all pixels. However, for the zero-filled velocity methodology, random noise was only added to the pixels that had not been set to zero.

We created the realizations for the volume-area based landslide depth measurements by varying the fitting parameters within Equation 6.3, using the error measurements provided by Larsen et al. (2010). We used a log-normal distribution with a mean of 0 and a standard deviation of 0.06 for the $\alpha$ parameter and a normal distribution with a mean of 0 and a standard deviation of 0.01 for the $\gamma$ parameter. For the toe-height based depth estimation, we created realizations by sampling from a uniform distribution of toe height values for each landslide whose minimum value was equal to the minimum measured toe height and whose maximum was equal to the maximum measured toe height.

For the density estimate we created individual normal distributions for each landslide within the dataset. Each landslide density distribution had a mean equal to that landslide's mean density value within Tenzer et al.'s (2011) rock density map of New Zealand, and a standard deviation equal to the population standard deviation for the entire landslide density dataset. The error in the width and area of the landslides are assumed to be negligible compared to the other factors in this calculation, and consequently we assume that there is no error in these measurements (Simoni et al., 2013b).

We also conducted a sensitivity analysis (within each methodology combination) by setting all but one of the parameters equal to their median realization value, then calculating the total landslide sediment mass export using the 25$^{th}$ and 75$^{th}$ percentile realization values for the parameter in question. We used the difference between the sediment mass export estimates created using the 25th and 75th percentile values to measure the model's sensitivity to this parameter. We then repeated this procedure for each parameter that we created realizations for and for each combination of methodologies.

*6.4.3.4 Comparison with DoDs*

To assess the validity of our sediment mass calculation, we used existing repeat photogrammetry-derived digital surface models (DEMs) from the Rangitikei and Bird landslides to create DODs from which we calculated the net volume losses at each (Figure 6.6). The DEMs for the Rangitikei landslide were produced by  using structure from motion (SfM) photogrammetry with photos collected by a drone in October of 2016 and October 2017. The DEMs for the Bird landslide came from a regional photogrammetry survey conducted in 2016 (Horizons Regional Council), and photos collected by drone in 2021, which were processed using SfM photogrammetry (Williams et al., in prep). While the technique used to create these DEMs does not remove the added height of vegetation from the DEMs, all areas with trees or shrubs were manually removed from the DEMs, and the remaining pastureland was dominated by short (<10 cm tall) grass.

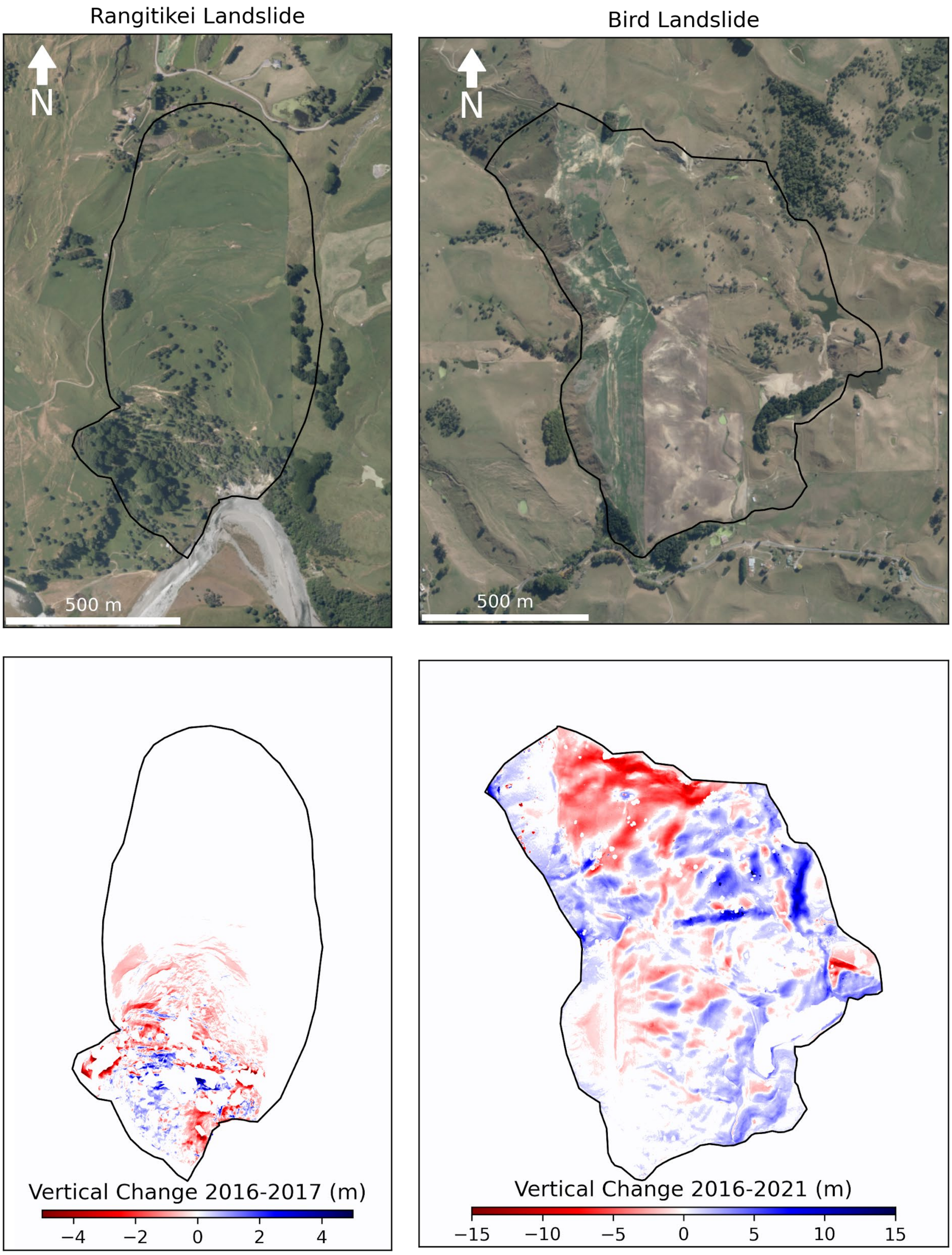


*Figure 6.6 Dems of Differences (DoDs) for the Rangitikei and Bird landslides. Rangitikei Landslide data was collected in 2016 and 2017, while Bird landslide data was collected in 2016 and 2021. Due to the slow movement rates in the upper portion of the Rangitikei landslide, DoD results are only available for the lower portion of the landslide.*

The drone imagery data were collected using a Phantom 3 Professional remotely piloted aircraft system (RPAS) with a 20 mm (35 mm format equivalent) lens and 12-megapixel sensor. A systematic flight path was flown for the surveys at the Rangitikei and Bird Landslides, ensuring a minimum of 75% forward and 65% side overlap between the images. For the Rangitikei survey, an altitude of 50-60 m was used, but due to taller obstructions at the Bird Landslide, an altitude of 90-110 m was used. Each flight path was also flown a second time with an oblique (30° off-nadir) camera angle to reduce the effects of radial distortion (James and Robson, 2014). 24-32 ground control points (GCPs) were surveyed using RTK GNSS during each drone survey. The SfM processing was conducted within the Agisoft Metashape v1.6.2 software platform, and the final DSMs were found to have a vertical root mean squared error (RMSE) of 0.16 to 0.30 m when compared to 17 independent GCPs at the Rangitikei Landslide and 15 independent GCPs at the Bird Landslide.

Aerial Surveys Inc. of New Zealand conducted the aerial SfM survey of the Bird Landslide on behalf of the Horizons Regional Council. All photography was captured using Vexcel's digital UltraCam Eagle and UltraCamLp cameras and flown at elevations between 3,500-5,769 m above sea level with a ground sample distance of 0.3 m and a sun angle minimum of 35°. Aerial Surveys Inc. also conducted the SfM DSM generation. They utilized a series of GCPs to determine that the final DSM had an average vertical error of ±0.6 m at a 68% confidence interval.

DoDs and associated error metrics were calculated using the Geomorphic Change Detection tool (Wheaton et al., 2010). The RMSE between the DEM pairs was used to create a continuous error surface, which was then propagated using standard error propagation, and used as a minimum level of detection. We then calculated the total volumetric change at both landslides, then converted these measurements to annualized sediment export so the results could be directly compared to our sediment export analysis. For the Rangitikei Landslide, the net volumetric change represents the volume of sediment delivered to the nearby Rangitikei River (i.e. surface raising minus surface lowering). However, the Bird Landslide is not connected to a river system, so the volumetric change was calculated as the average of the absolute volume of sediment lost (i.e. volume lost from surface lowering) from the head of the landslide and the sediment delivered to the lower portion and the toe (i.e. volume gained by surface raising). Consequently, the sediment export value reported for the Bird Landslide is the volume of material that has been moved from the head of the landslide to its toe.

#### *6.4.4 Comparison with Modelled Sediment Loads*

To provide context for our sediment export analysis results, we compared our results to the annual region-wide sediment export predicted by the NZeem model (Dymond et al., 2010). NZeem is a statistically based nationwide sediment export model for New Zealand that relates measurements of catchment suspended sediment loads to rainfall, land cover, and a fitted erosion coefficient for each type of 'erosion terrain' (Dymond et al., 2010). NZeem represents all sediment transported to the channel network over a multi-decadal scale (a sediment delivery ratio of one), and thus there is no intermediate storage component. For each major catchment within the study area, we compare the NZeem predicted annual sediment export with our predicted sediment export for the deep-seated landslides of the Whanganui Basin to determine the relative contribution of sediment mass from soft-rock landslides to these catchments. In the case of the Whanganui Catchment, which extends north into the Upper Whanganui Basin, we calculate the NZeem sediment export only within the portion of the catchment that falls within our study area (i.e. the Lower Whanganui Catchment).

## 6.5 Results

### *6.5.1 Activity Analysis*

Our landslide activity analysis identified 114 landslides that intersected areas of activity in at least 2 out of the past four years. Most of these landslides were self-contained, but in multiple cases, the landslides were smaller parasitic landslides on the margins of larger landslides (Figure 6.3). Of the 114 landslides identified as having areas of movement, 48 were discarded during the manual inspection process due to the location of the observed movement (e.g., located within areas known to produce erroneous results in C-band SAR data such as forests and waterbodies, or located along the margin of the landslide). The remaining 66 active landslides ranged in size from 11 – 1047 ha (median of 56 ha) and were primarily located in the northern portion of the study area within Early Pleistocene age sedimentary rocks (Figure 6.7).

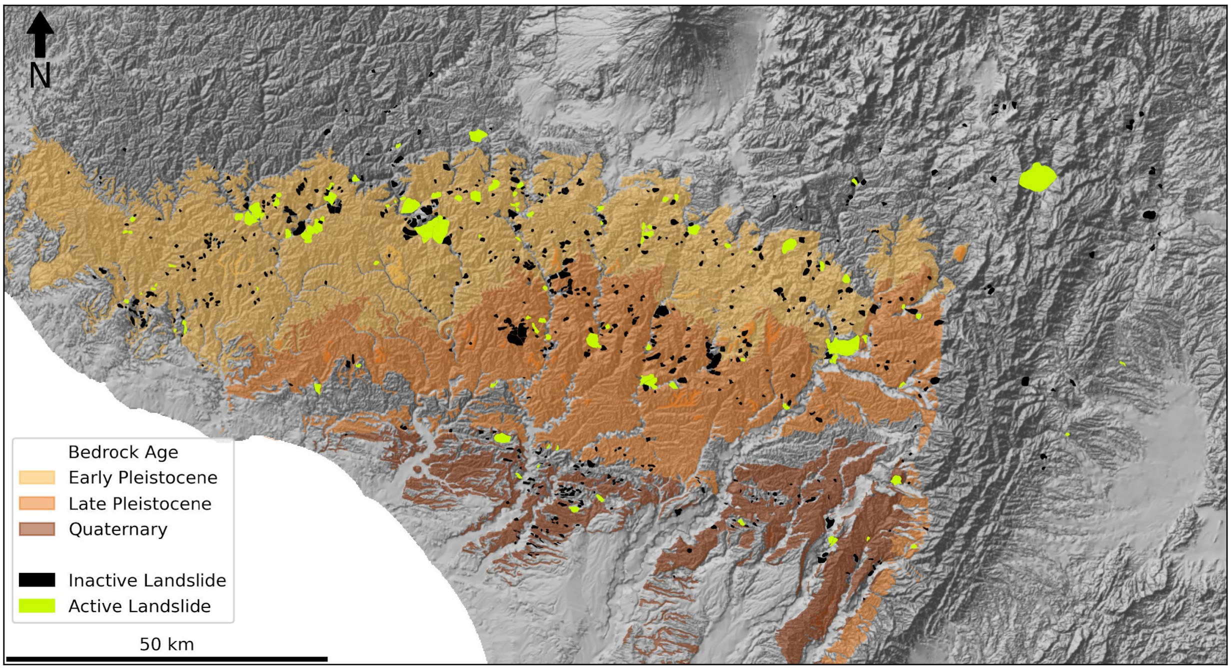


*Figure 6.7 Map of the active landslides identified within our InSAR time-series analysis. The bedrock units indicate the age of the underlying units. More active landslides occur in the Early Pleistocene basin units, but active landslides are scattered throughout the study area. Active landslides are defined here as those showing detectable movement in the timeframe of our analysis*

Our multivariate logistic regression analysis of active versus inactive landslides was able to correctly predict the activity state of the landslides within our study area most of the time. Overall, the model had a classification accuracy of 66% and an AUC of 0.75. With adequate performance in both metrics, we are confident interpreting the relative importance of covariates within these models as predictive of which factors contribute to the occurrence of active landslides. When considering the model covariates, we see that slope, the local standard deviation of the elevation (a measure of surface roughness), location within the Early Pleistocene (ePl) units (the oldest and most northern rocks of the study area (Figure 6.7), and annual average rainfall were the most influential within the model (Figure 6.8). Slope had a negative coefficient, suggesting that lower than average slopes predict current landslide activity, which was a similar finding to that of Williams et al.'s (2021) landslide occurrence analysis, which suggested that this relates to the structural control of landsliding along gently inclined weak bedding.

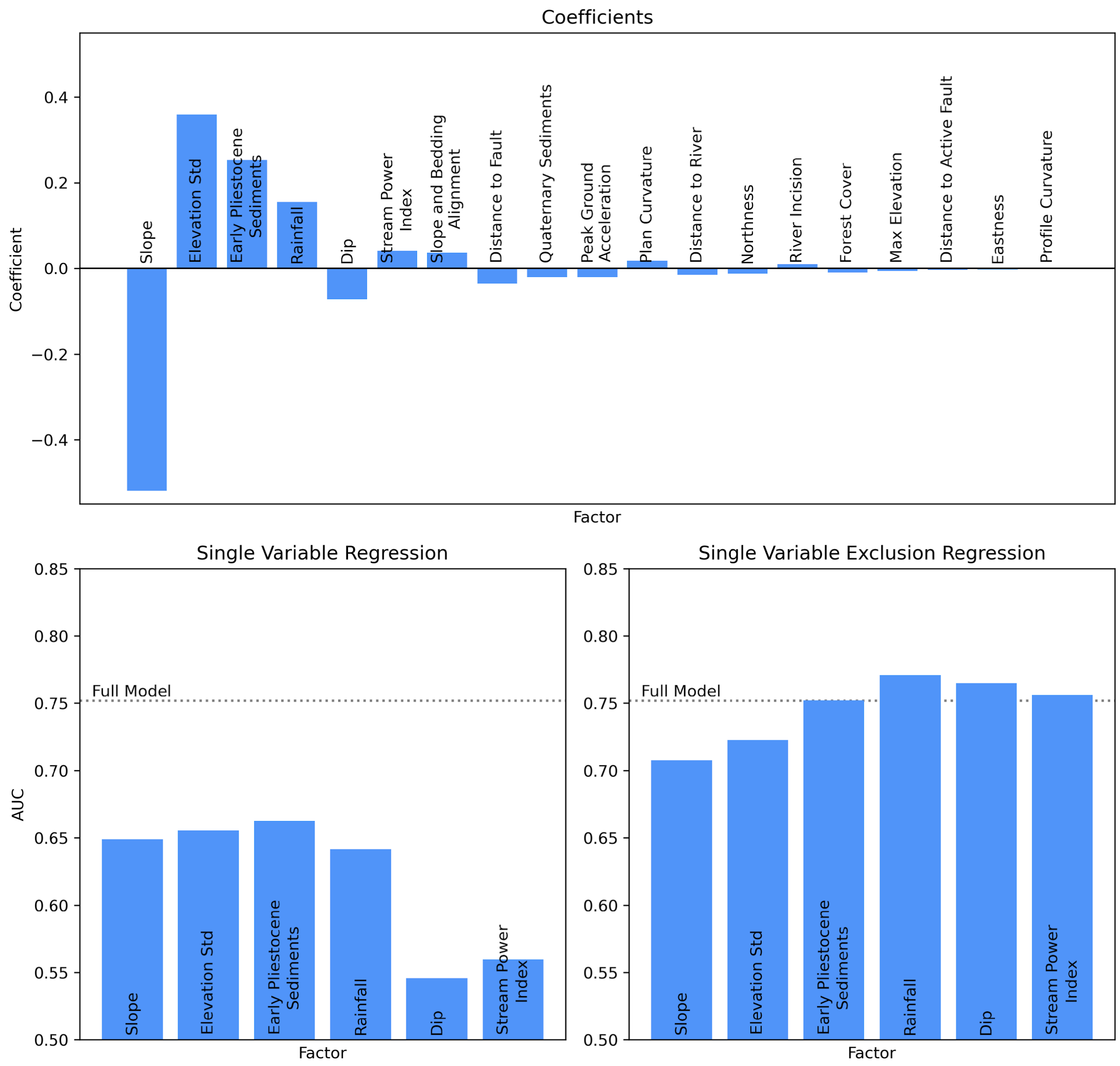


*Figure 6.8 Logistic regression susceptibility factor importance results for the landslide activity analysis. The top plot shows each factor's coefficient's standardized value within the model, and the two bottom plots show the jackknife regression results. In the top plot, negative coefficients indicate that landslide activity is more likely when the factor is lower. In the bottom right plot, lower AUCs indicate a drop in performance when a factor is excluded and thus higher variable importance.*

The jackknife logistic regression analyses (Figure 6.8) showed a similar measure of variable importance. In the univariate regressions, a location within ePl units was the most predictive of landslide activity. This was followed closely by the performances of the slope, local standard deviation, and average annual rainfall. The stream power index was a decent univariate predictor of landslide activity, but it did not have a large coefficient. When factors were excluded from a multivariate model, slope was associated with the most significant drop in performance, followed closely by the local elevation standard deviation. In contrast to the other results, removal of the annual average rainfall or ePl variable was associated with a slight increase in performance. This may be due to the correlation between these variables and others in the dataset (e.g. rainfall and river incision, or ePl and Quaternary sediments).

Similar to our previous models of landslide occurrence in this region (Williams et al., 2021), no strong relationship with seismic variables (e.g., distance to faults, distance to active faults, peak ground acceleration) was found. In contrast to the occurrence model, however, slope and bedding alignment, forest cover, and river incision were not good predictors of activity. In general, active and inactive landslides both have strong slope and bedding alignment and high river incision (Williams et al., 2021), limiting their utility in distinguishing between active and inactive landslides within the time period studied.

### *6.5.2 Landslide Sediment Contributions*

#### *6.5.2.1 Comparisons with Validation Data*

The DoD analyses of the Rangitikei Landslide and Bird Landslide showed that these landslides had annualized sediment export rates of 43,600±25,900 $m^3$/yr (McColl et al., 2022) and 48,000±15,900 $m^3$/yr, respectively. In the case of the Bird Landslide, this value represents the amount of material that was transported from the upper half of the landslide to the lower half. The annualized sediment volume export estimates produced using each methodology combination are shown in Figure 6.9. Estimates for the Rangitikei Landslide ranged from 24,000±18,400 to 34,000±16,500 $m^3$/yr and from 22,000±9,400 to 29,000±16,800 $m^3$/yr for the Bird Landslide. The Rangitikei Landslide estimates are not statistically distinguishable from its DoD-derived value but are biased towards a lower value. In addition however, McColl et al. (2022) reported a dGNSS-derived estimate of sediment export of 20,600 $m^3$/yr for the Rangitikei Landslide and our estimate of 22,000-29,000 $m^3$/yr falls in between this estimate and their DoD-based estimate of 43,600 ± 25,900 $m^3$/yr. For the Bird Landslide estimates, all estimates were also biased towards lower values, but only the error range of the estimates overlapped with the DoD estimates. This may be because a larger proportion of movement at the Bird Landslide is in the vertical direction (due to the confinement of the landslide) and sPOT analyses are insensitive to vertical motion. Overall, both the choice of depth methodology and velocity methodology contribute a comparable amount of methodological uncertainty to the resulting sediment export estimate.

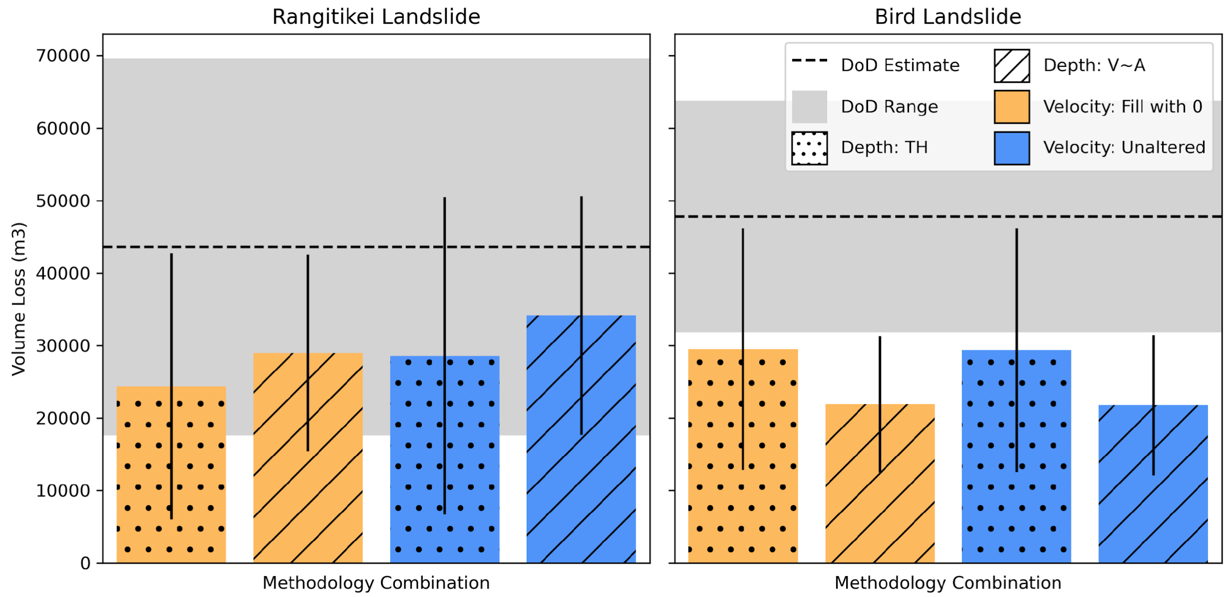


*Figure 6.9 Comparison of sediment volume exports by methodology combination for the Rangitikei and Bird landslides. The bar pattern and colour represent the methodology combination (TH: toe height depth, V~A volume-area scaling depth) used, the bar height represents the median* Monte Carlo *estimate of sediment export ($m^3$), and the error bars represent the two standard deviation range around the estimates. The horizontal dashed lines represent the DoD sediment export ($m^3$) and the grey area represents the uncertainty of the estimate.*

### *6.5.2.2 Regional Sediment Contributions*

Estimates of soft-rock landslide sediment export for the methodology combinations across the entire study area can be found in Table 6.3. Of the 66 active landslides within our study area, 54 were directly connected to major river systems and thus are a potential source of short-term sediment supply. Estimates for the total landslide sediment export ranged from 330±58 to 520±122 kT/yr with the zero-filled velocity and volume-area based depth combination providing the lowest estimate, and the unaltered velocity and toe-height based combination providing the highest estimate.

*Table 6.3 Sediment export by methodology combination for all landslides in the study area. The velocity column denotes whether low velocity values were reclassified to zero, or were left unaltered. The Depth column denotes whether the volume-area relationship or the landslide toe height was used to estimate landslide depth. The export column denotes the median total export value for landslides based on the Monte Carlo analysis, and the Proportion of Total column shows what percent of the total sediment input from the study area (based on the NZEEM model) the export value represents. In the last two columns the error values are equal to twice the standard deviation of the Monte Carlo distributions.*

| Velocity | Depth | Export (kT/yr) | Proportion of Total (%) |
|---:|---:|---:|---:|
| Zero-Filled | V~A Scaling | 330±58 | 7.3±1.3 |
| Zero-Filled | DEM Toe Height | 390±90 | 8.7±2.0 |
| Unaltered | V~A Scaling | 460±88 | 10.2±2.0 |
| Unaltered | DEM Toe Height | 520±122 | 11.5±2.7 |

While the error ranges of these estimates almost overlap, the amount of variability found in the estimates by varying the methodology was greater than the Monte Carlo-based error bounds of any single estimate. Our sensitivity analysis showed that our velocity estimation was the most significant contributor to our analysis error, followed closely by depth, regardless of the methodology used Figure 6.10). The unaltered velocities showed more variability than the zero-filled velocities, and the toe-height based depths tended to have more variability than the volume-area scaling based depths. Compared with these two factors, the density factor made a small contribution to the total variability.

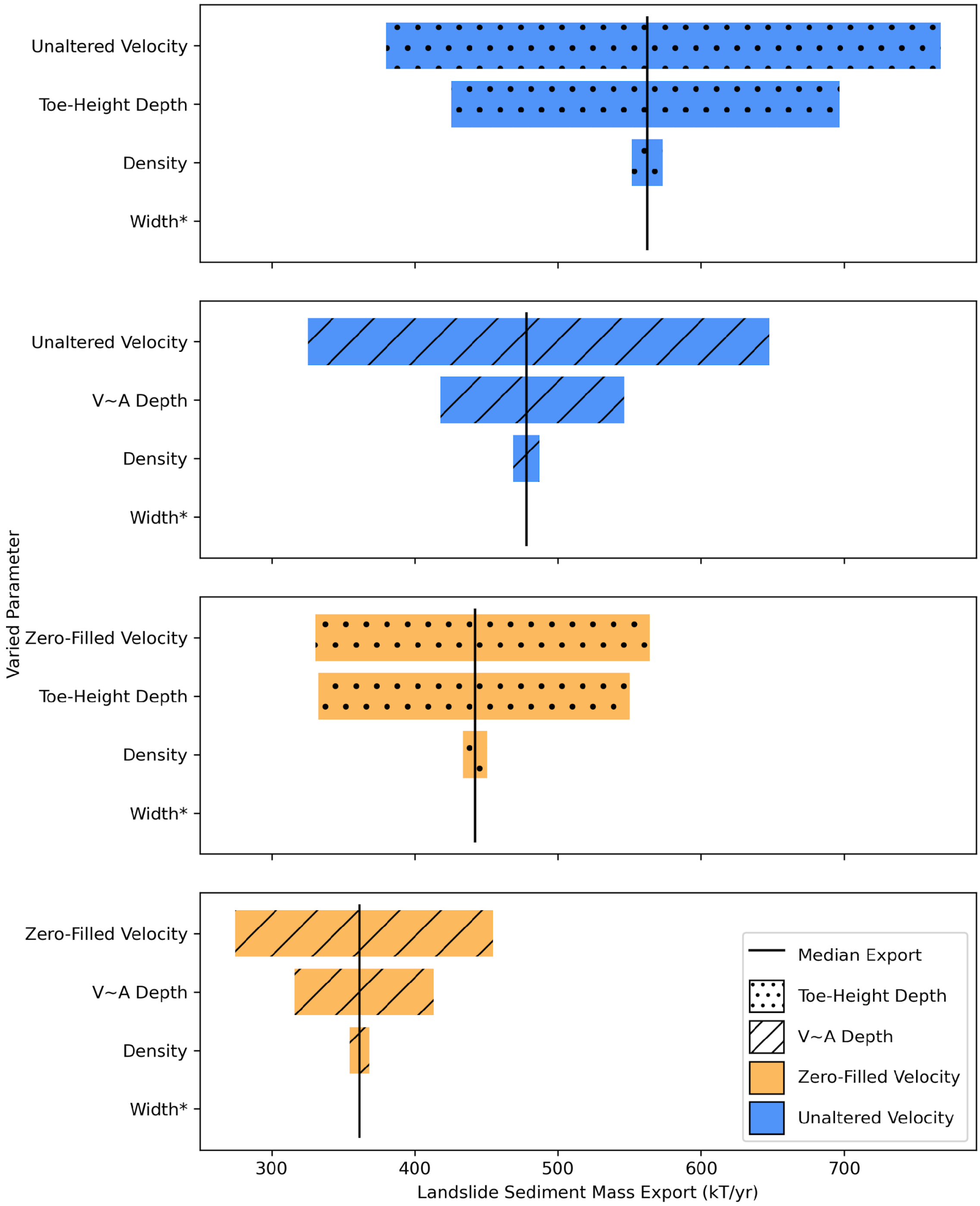


*Figure 6.10 Sensitivity results for our Monte-Carlo uncertainty analysis. Each subplot shows the results for a different methodology combination. The bar pattern and colour represent the methodology combination (V~A: volume-area scaling depth) used. The width of the bars indicates the difference between the sediment export predicted when a parameter is set to its 0.25 and 0.75 quantile values. (*) the width parameter was assumed to have a negligible error compared to the other parameters and thus is assumed to have no uncertainty.*

While all four of these methodological approaches are valid ways to estimate the sediment contribution from these landslides, we believe that the unaltered velocity methodology and volume-area scaling based combination are the most defensible. The unaltered velocity likely reflects reality more closely than the zero-filled velocity, it is more closely aligned with how the error in the sPOT data is analysed in Williams et al. (2022 in prep), and how uncertainty in sediment budgets from morphological change detection is handled using other high resolution survey methods (Neverman et al., 2016; Vericat et al., 2017; Wheaton et al., 2010). Additionally, we believe that the volume-area scaling based depth is more defensible because it is systematic and less prone to blunders, since there is no need to arbitrarily evaluate toe height. Consequently, the analyses in the rest of this study utilize export values based on this methodology combination unless stated otherwise.

For this methodology combination, average downslope velocities ranged from 0.05 to 1.5 m/yr (median of 0.15 m/yr), depths ranged from 9.3 to 52.6 m (median of 19.2 m), river exposure widths ranged from 168 to 2397 m (median of 761 m), and material densities ranged from 2.2 to 2.45 tons/$m^3$ (median of 2.3 tons/$m^3$). This resulted in an estimated total sediment mass export from these landslides of 460±88 kT/yr. Overall, a few of the most productive landslides contributed most of the landslide sediment exports within the system (e.g. the Poroa Landslide complex (Figure 6.3)). In fact, the ten most productive landslides contributed 56% of the total sediment export (Figure 6.11).

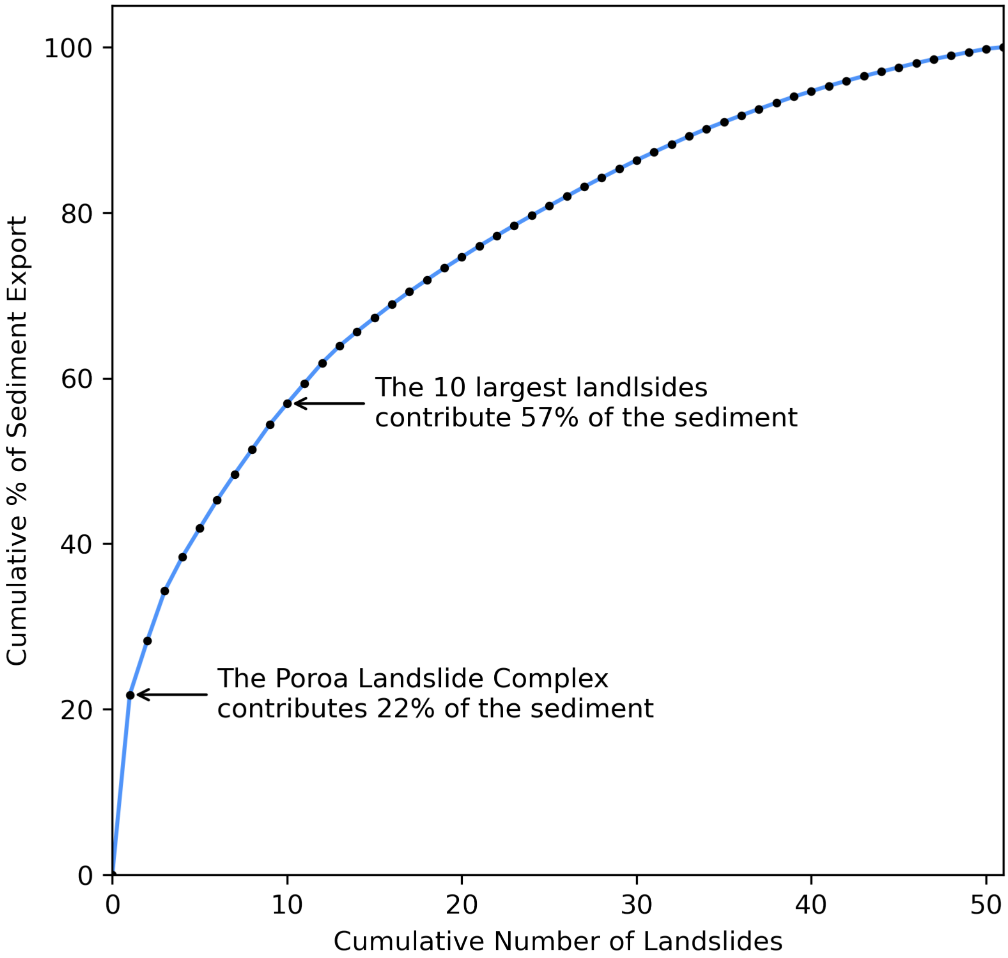


*Figure 6.11 Cumulative sediment export of the active landslides within our study area when the landslides are in decreasing order of sediment export. The Poroa Landslide Complex is the single largest contributor of sediment in the study area and contributes 22% of the total sediment. This figure uses the export estimates created using the unaltered velocity and volume-area scaling relationship depth methodologies.*

When considering soft-rock landslide sediment contributions by catchment, we see that soft-rock landslides contribute 2-19% of the total annual sediment export predicted by the NZeem model (Table 6.4) (Figure 6.12). The large variability in this estimate is mainly due to the variability in both the number of landslides within each catchment and the total catchment size. For example, the Patea catchment contains only two active soft-rock landslides that contribute 2±1% of the total sediment export (Table 6.4). In contrast, the Waitotara catchment has 16 landslides that contribute a much more significant proportion (19±3%) of the total sediment export. Thus, in catchments where they are active, soft-rock landslides contribute a considerable proportion of the sediment export. This is more significant considering that within each catchment these features make up a tiny fraction (0.08-0.94%) of the total catchment area (Table 6.4). When considering all catchments together, deep-seated landslides make up 0.3% of the total surface area but contribute 10±2% of the total sediment. Thus, deep-seated landslides are likely an important point source of sediment in catchments where they occur.

*Table 6.4 Landslide sediment export and catchment metrics for the Whanganui Basin. The landslide contribution data comes from the export estimates created using the unaltered velocity and volume-area scaling relationship depth methodologies, and the catchment export data comes from the NZeem model of* (Dymond et al., 2010)*. In this table, kT/yr stands for kilotons of sediment per year, and the Landslide Occupied Area column indicates the percent of the catchments' surface area occupied by landslides.*

| Catchment Name | # Active Landslides | Catchment Area ($km^2$) | Catchment Export (kT/yr) | Landslide Export (kT/yr) | Landslide Contribution (%) | Landslide Occupied Area (%) |
|---|---|---|---|---|---|---|
| Whenuakura | 3 | 466 | 143 | 10±6 | 7%±4% | 0.14% |
| Turakina | 5 | 955 | 568 | 37±11 | 7%±2% | 0.52% |
| Lower Whanganui | 7 | 1036 | 419 | 97±27 | 23%±7% | 0.58% |
| Patea | 2 | 1049 | 489 | 9±5 | 2%±1% | 0.05% |
| Waitotara | 16 | 1163 | 583 | 108±19 | 19%±3% | 0.94% |
| Whangaehu | 14 | 1991 | 1026 | 77±15 | 7%±1% | 0.38% |
| Rangitikei | 7 | 3925 | 1275 | 112±22 | 9%±2% | 0.08% |

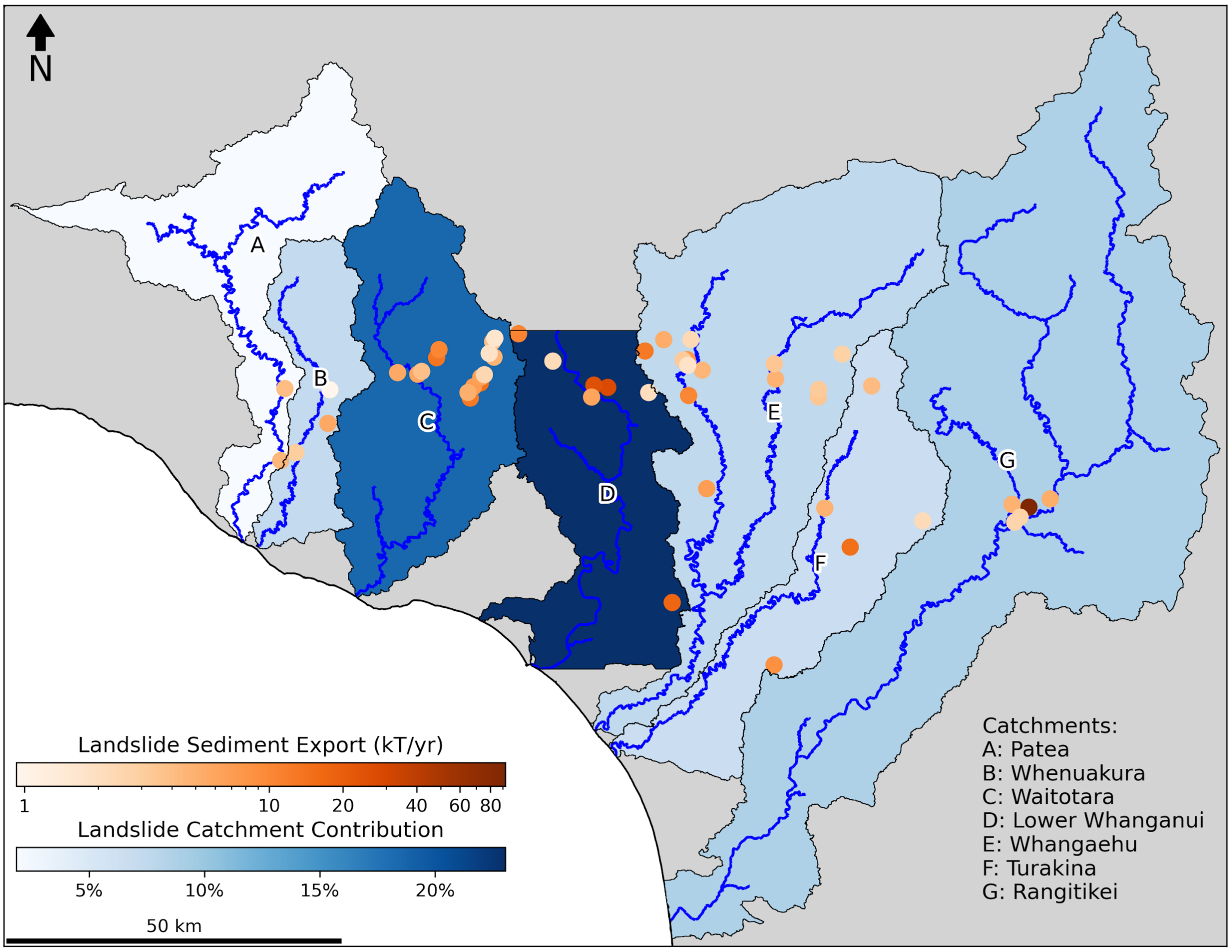


*Figure 6.12 The catchments within the Whanganui Basin color-coded by the landslide sediment contribution percent of the overall sediment budget. Overlaid on top of the catchments are the major river systems and circles indicating the location of the active landslides. The landslides are color-coded based on the log of their annual sediment contribution (in kilotons per year). This figure uses the export estimates created using the unaltered velocity and volume-area scaling relationship depth methodologies.*

## 6.6 Discussion

### *6.6.1 Activity Analysis*

Our activity results show that of the 731 deep-seated landslides mapped in the study area, only 66 are active today (i.e. between 2018 and 2022). In total active landslides represent only 9% of the total population. This result highlights the utility of remote sensing-based landslide monitoring frameworks. Performing field-based surveys at even a quarter of these landslides would be impractical, especially considering that soft-rocks landslides are prone to periods of both inactivity and reactivation, and thus require continual monitoring to determine their activity state. In contrast, InSAR analyses offer a cost-efficient way to triage the hazards associated with soft-rock as well as other large slow-moving landslides and update conventional landslide inventories with activity state information. This information can then be used to target field-based monitoring and risk-mitigation efforts at landslides where they will have the largest impact.

The landscape factor analyses conducted in this study on active landslides, and in the landslide occurrence study of Williams et al. (2021) differ in some key ways that demonstrate the temporal variations in landslide generation and stability. In Williams et al. (2021), we developed a model predictive of landslide occurrence as compared to zones of the study area where landslides had not occurred. Since many of these landslides are likely relict or dormant features, many of which may have been inactive for thousands of years (Pánek and Klimeš, 2016), this model likely predicts the factors which lead to the generation of soft-rock landslides on millennial timescales. This corresponds well with the factors identified as important within the model, such as river incision and slope and bedding alignment, which tend to develop over longer timescales (e.g. preconditioning and preparatory factors).

In contrast, our activity factor analysis determines which factors have led to, or are associated with, landslide activity within the past four years, and as expected, these differed to those landscape factors identified as important for the occurrence model. In this case, the analysis identified factors controlling landslides, or reflecting landslide morphology, at shorter timescales, such as rainfall and surface roughness (elevation standard deviation) respectively. In particular, high surface roughness is an evident characteristic of landslides that have recently failed (e.g., sharply defined scarps and landslide grabens).

An important similarity between the two models is the dominant influence of slope. Both models show landslide occurrence/activity increases where local slopes are lower. This points to the counter-intuitive relationship between these landslides and local slopes. Williams et al. (2021) argued that the lower slopes within landslide zones suggest that a high degree of slope and bedding alignment, and the consequent low threshold slope, limit the slopes attainable in these areas. Our activity factor analysis further demonstrates that this process is even more pronounced at active landslides, where the threshold slope is likely even lower than the general landslide population. It also tends to suggest that inactive landslides have not self-arrested or stabilized through slope adjustment (e.g. a reduction in slope angle towards equilibrium), or otherwise we would expect inactive landslides to have lower slopes than active landslides.

For those factors that corresponds causes of landslide instability, rainfall appeared to be the most influential. Rainfall may influence landslide activity through two different mechanisms. First, local precipitation may increase the pore-water pressure within landslides, which is known to increase movement (Massey et al., 2016b; Van Asch et al., 2009, 1999). Second, rainfall may increase the local erosive power of the rivers that intersect landslides, which can also increase movement rates (McColl et al., 2022). Our analysis, which shows little influence from the stream power index used, could suggest that local rainfall may be more important for explaining the distribution of active landslides. However, the stream power index we used (based on local stream gradient and upslope contributing area) assumes that all locations contribute equal amounts of water to the river systems, which fails to capture the true variations in stream power likely to exist as a result of uneven rainfall and runoff distributions. Thus, local variations in the erosive power of rivers may be better represented by the average annual rainfall factor data than by our stream power index variable. In the future, a stream power index factor that integrates actual flow data or runoff estimates may be able to better describe this relationship.

Our activity factor analysis also suggests that forest cover, or lack thereof, was not an important predictor of landslide activity. This contrasts with the model of Williams et al., (2021), where forest cover was an important predictor of occurrence. In Williams et al. (2021), we discussed that the importance of forest cover in the occurrence model could be explained in one of two ways. First, forest cover may help prevent soft-rock landslide occurrence. Alternatively, forest cover's high correlation with steep slopes (i.e., steep areas were not converted to pastureland) could mean that it is the presence of steep slopes that is useful for predicting the non-occurrence of landslides. However, it is difficult to use C-band SAR data to evaluate activity within forested terrain, due to high rates of decorrelation. At most, our data suggest that forest cover does not appear to be an important activity factor for landslides that are partially forested. This may suggest that the importance of forest cover within our occurrence model is due to its correlation with slope, but more work needs to be done to investigate this possibility.

### *6.6.2 Sources of Uncertainty*

While there is a high degree of uncertainty in our sediment export estimates, we believe that our approach represents a reasonable and scalable framework for estimating soft-rock landslide sediment export at region to country-wide scales. This is demonstrated by the comparison between our landslide sediment model and the DoDs at the Bird and Rangitikei landslides. While the total sediment output was underestimated at both sites, the error ranges for both measurements overlapped with error ranges of the DoD-based export estimates.

Our methodology analysis also shows that detailed methodological choices can have a significant impact on the overall results and that these variations are often not reflected in traditional uncertainty estimation procedures such as Monte Carlo simulations. Varying the methodologies used for estimating landslide velocities and depths produced total sediment export estimates that ranged from 330-520 kT/yr, and only the largest Monte Carlo uncertainty (±120 kT/yr) comes close to this range. This suggests that future landslide sediment export studies should consider alternate methodological choices when exploring the uncertainty in their results.

Our sensitivity analysis shows that the uncertainty in our velocity estimates contributes the most to our overall uncertainty. The leading cause of this uncertainty was the increase in uncertainty in our sPOT measurements when velocities were less than the standard deviation of the stable areas within the sPOT data (~0.5 m/yr) in either the WE or SN directions. However, this issue may be less apparent in other studies where the average movement rates are faster (such as the earthflow studies within California, USA (Mackey and Roering, 2011). Additionally, the sensitivity of the sPOT analyses are directly tied to the geolocation accuracy and resolution of the underlying imagery used to perform the sPOT analysis. Thus, the use of proprietary high resolution (< 5 m) imagery may also offer a way to detect slower landslide movement with reduced uncertainty.

The second most important source of error in our model is landslide depth. While area-volume scaling relationships suffer from autocorrelation, can fail to accurately predict structurally-controlled landslides, and are undoubtedly less accurate than field investigations of landslide depth, they are cost-effective and rapid to apply at a regional scale. Additionally, alternative regional scale methods, such as estimations of landslide toe height from DEM transects, also have inherent issues. In particular, toe-height estimates greatly depend on where the DEM transects are placed, and what is considered the "toe" of the landslide. Unless these issues can be resolved, it will be difficult to create reproducible measurements of landslide depth using this method. Thus, when considering the depths of a population of landslides, we believe that using a statistical approach to estimate landslide depth is an acceptable methodology, especially when the error within the area-volume scaling relationship is reported as a part of the analysis. This is further supported by the accurate estimation of landslide depth at the two landslides where we have field data on the depth of the failure surface (Figure 6.5). Alternatively, recent work has shown that it is possible to infer the three-dimensional surface geometry of a landslide's failure surface from a set of three independent sPOT/InSAR velocity measurements (Handwerger et al., 2021). Currently however, this type of data is not available outside of small test areas.

The density estimation error is small compared to the depth and velocity errors, but this is due to the relative homogeneity of the bedrock within our study area. Studies in regions with more heterogeneous bedrock may find that this component is a larger source of error than it was in our study. Overall, our estimation of landslide velocities contributes the most error and presents the best opportunity to improve the analysis without resorting to expensive field-based methodologies. Thus, future efforts to improve this model of landslide sediment contribution should focus on improving the velocity estimate.

### *6.6.3 Role of Deep-seated Landslides Within Catchment Sediment Budgets*

As noted in the introduction, landslides (including shallow and deep-seated landslides) have previously been shown to dominate sediment budgets in tectonically active regions on millennial timescales (Kuehl et al., 2016). However, it's less clear if slow-moving deep-seated landslides, such as soft-rock landslides, play an important role in contemporary sediment budgets (especially outside of major disturbance events like earthquakes). We found that the 54 landslides we considered within our sediment export model contribute 460±88 kT/yr of sediment to local river systems. This sediment export was unevenly distributed between catchments, and is largely reflective of the number of landslides present in each catchment. In catchments with a high density of active landslides, these landslides contributed up to 19±3% of the total estimated average annual sediment export. This is remarkable since these features only occupied 0.3% of the total catchment area.

In addition, soft-rock landslides may represent a larger proportion of total sediment input to rivers during baseflow periods since, when active, they contribute sediment more consistently than other processes (Massey et al., 2013; McColl et al., 2022). This is especially true when compared to rainfall-triggered multiple occurrence regional landslide events or many other event-driven erosion processes. In addition, the NZeem model is based on multi-decadal averages of annual suspended sediment loads, and thus assumes that many sources of sediment that are stored intermittently (i.e. in valley bottoms or flood plains) are transported to the river system (Dymond et al., 2010). In contrast, all landslides included within our export model are directly connected to the river systems. This means that these landslides likely contribute more sediment proportionately when there is not sufficient flow to transport sediment that is located within intermediate storage locations. Finally, these landslides are typically delivering fine grained material (sand, silt, and clay), that is easily entrained and transported by rivers, and can remain active during baseflow periods due to a lag in their response to severe precipitation events (Booth et al., 2018; Massey et al., 2013; McColl et al., 2022). Thus, even in catchments with low numbers of active landslides, these landslides likely represent an important point source of sediment.

Previous regional sediment budget models (Dymond et al., 2016) have typically excluded soft-rock landslides from their analyses because landslide locations and representative movement rates at the regional scale were unknown. Our results however suggest that deep-seated landslides should receive explicit inclusion within sediment budgets and models. This may necessitate a transition to location- and process-specific frameworks; remote sensing techniques, such as the methods used within this study, make these developments more achievable.

Recognition of the importance of deep-seated landslides for river sediment loads also helps to identify new possibilities for sediment reduction interventions. As opposed to the widespread and changing distribution of multiple shallow landslides and other surface erosion activity, soft-rock landslides have a small footprint and can be active for long periods in one location. Thus, if the goal of a conservation program is to meet suspended sediment load standards for a river while also incurring the least amount of cost, controlling erosion at soft-rock landslides may offer an opportunity to reduce sediment loads if their sediment export can be reduced cost-effectively. Other processes such as surface erosion and shallow landsliding occur diffusely at a landscape scale, and controlling these forms of highly distributed erosion can be challenging (Spiekermann et al., 2022). In part, this is because it requires conservation practices to be applied across large areas and for there to be coordination among many separate landowners. Conversely, introducing conservation practices at the most active soft-rock landslides may help to reduce sediment loads while requiring coordination among only a few landowners. Additionally, the control of soft-rock landslides is more likely to be in the economic interest of landowners than broad land-use changes, which could result in higher rates of landowner cooperation.

However, controlling soft-rock landslides is not always feasible or cost-effective. Their large sizes and deep failure surfaces make them harder to control than individual shallow landslides, and as noted in other studies (Bilderback et al., 2015; Larsen and Montgomery, 2012), soft-rock and other deep-seated landslides are part of millennial-timescale terrain denudation cycles that may not respond to most financially-viable human interventions. Nonetheless, adverse human activities can certainly worsen the stability and movement of deep-seated landslides in some cases, and thus there is evidence that anthropogenic interventions can affect their behaviour. For example, gravel-bed mining of the Rangitikei River directly downstream of the Utiku Landslide (a landslide identified as active within our analysis) is thought to have driven channel incision and removal of toe support. This, and loading of the landslide head during construction of transport infrastructure, likely led to an order-of-magnitude increase in movement rates (McSaveney and Massey, 2017). The importance of fluvial incision has also been noted by other studies (Massey et al., 2013; McColl et al., 2022), such that interventions that reduce local river erosion (such as armouring or bank protection) may help to increase stability and reduce movement (Yenes et al., 2015; Yu et al., 2010). Additionally, reducing porewater pressures within the landslides by improving surface or subsurface drainage, and introducing landcover that increases evapotranspiration may also slow movement rates (Carey et al., 2019; He et al., 2008).

While vegetation can be used to stabilize slopes via increased soil cohesion (Brown, 1991; Ghestem et al., 2011; Löbmann et al., 2020; Spiekermann et al., 2022), this is likely not an effective strategy for soft-rock and other deep-seated landslides, whose failure surfaces are usually beyond the reach of tree roots. In cases where the consequences of landslide failure are catastrophic, significant engineering works can be used to stabilize even the largest of landslides (Gillon, 1992; Hungr et al., 1999; Klimeš et al., 2012), but it is unlikely that the benefits of soil conservation and river sediment reductions alone will justify the costs of such treatments for many landslides (especially in sparsely populated steepland catchments). Still, our sediment export modelling framework gives practitioners an effective tool for triaging landslide inventories and identifying the landslides where mitigation practices have the potential to create the most significant effect. Furthermore, even if mitigation is not practical, quantifying their contributions to sediment loads at least allows us to better describe a possible minimum or background rate of sedimentation within river systems, alongside other erosion processes contributing sediment from areas deemed unmitigable. Importantly, there may be high rates of natural sedimentation in regions with soft-rock landslides, which could make meeting strict sediment water quality standards impractical.

## 6.7 Conclusions

In this study, we used a time-series InSAR and sPOT analysis to identify active deep-seated landslides and estimate their annual velocities within the Whanganui Basin region of New Zealand. Of the 731 deep-seated landslides within this region, we identified 66 as currently active, and we measured their downslope velocities to be between 0.05-1.5 m/yr. Our activity analysis showed that gentle slopes, rough surfaces, and high annual rainfall are most strongly predictive of current landslide activity. This differs from millennial time-scale landslide generation, which previous work has shown is controlled mainly by slope and bedding alignment and river incision. Additionally, we estimated the sediment contribution of the active soft-rock landslides in this region using a sediment export model and found they contribute 7±1% to 12±3% with a best estimate 10±2% of the total sediment export (varying from 2±1% to 19±3% based on the catchment) even though these active landslides occupy only 0.3% of the study area. We conclude that soft-rock landslides are an important contributor of sediment to some rivers in this region and, if cost-effective mitigation is viable, present an opportunity to reduce sediment export. If mitigation is not viable however, the sediment export from these landslides still represent an important control on the sediment load reductions that can be achieved within these catchments.

## 6.8 Acknowledgements

Thank you to Horizons Regional Council for the use of their digital surface model, and landowners for access to landslides on their properties. This research was supported by the New Zealand Ministry of Business, Innovation and Employment research program "Smarter Targeting of Erosion Control (STEC)" [Grant Number C09X1804] and by the MBIE Strategic Science Investment Funded Hazards Program at GNS Science.

## Synthesis of Chapter 6 for Thesis

In this chapter, I performed a landslide activity factor analysis (Objective 4) using the landslide dataset described in Chapter 4, and activity data produced using the time-series InSAR analysis described in Chapter 5. This analysis showed that active landslides in the region have even lower slopes than the rest of the landslide population, further supporting the concept of a slope threshold model that is dependent on site-specific factors (Chapter 4). It also showed that annual rainfall and stream power index were two of the most predictive variables in the activity model, indicating that landslide toe erosion and high pore-water pressure are likely important sustaining factors for these landslides. In this chapter I also conducted a landslide export analysis for soft-rock landslides in the Whanganui Basin (Objective 5) and found that soft-rock landslides likely represent 10±2% of the total sediment input to local river systems. While many improvements could still be made to this estimate, I did my best to explore the sources of uncertainty present in this analysis, and I believe this chapter represents an important addition to our understanding of the role these landslides play in the sediment budgets of their catchments.

# Chapter 7 Synthesis

In this chapter, I reflect upon how each thesis objective has been met, draw linkages between each chapter, and discuss the key contributions of this thesis to advancing landslide research and the understanding of soft-rock landslides.

## 7.1 Thesis Aims and Objectives Revisited

In this thesis, I attempted to analyse the factors that lead to the occurrence and contemporary activity of soft-rock landslides within the Whanganui Basin of New Zealand, develop remote sensing methodologies that could be used to monitor these landslides effectively, and quantify the sediment input of these landslides to the catchments of the regions in which they occur. In my literature review of soft-rock landslides and the techniques used to map and monitor them, I identified five key opportunities for improving our current understanding of soft-rock landslides generally, and in the Whanganui Basin specifically: (1) create an accurate map of the soft-rock landslides in the Whanganui Basin that includes information on landslide age, and type; (2) determine which regional factors are associated with the occurrence of soft-rock landslides in the basin; (3) develop a remote sensing framework to identify the activity state and measure the movement rates of soft-rock landslides and other large, slow-moving landslides; (4) identify the active soft-rock landslides in the Whanganui Basin and determine if the factors associated with contemporary activity are the same factors that are associated with landslide occurrence, and; (5) assess the sediment contribution of soft-rock landslides to contemporary Whanganui Basin sediment budgets. Addressing these knowledge gaps formed Objectives 1-5 of my thesis, and in the remainder of this chapter I discuss how these objectives were met in Chapters 4 – 6 of the thesis.

## 7.2 Factors Influencing Soft-Rock Landslide Occurrence

To analyse how susceptibility factors influence the occurrence of soft-rock landslides, I first needed to create an accurate regional map of soft-rock landslide occurrence. This mapping was done within Chapter 4. I conducted this mapping, and all other analyses, within the Lower Whanganui Basin region of New Zealand. This study area was selected because of the large number of soft-rock landslides that occur there, the previous field investigations of soft-rock landslides in the basin that allowed me to contextualize my regional-scale work, and the numerous sediment dynamics analyses that have been conducted in the area. My re-mapping of soft-rock landslides in the region identified 871 landslides, whose extents ranged from 2 ha to over 500 ha. My landslide occurrence susceptibility analysis (Chapter 4) revealed that river incision, low slopes, forest cover, slope and bedding alignment, and high annual rainfall were the most predictive of landslide occurrence.

The results of this work highlight the difficulties of applying a slope threshold model (Larsen and Montgomery, 2012) uniformly across a landscape that has different slope failure mechanisms. The importance of slope and bedding alignment within my occurrence model and the increasing likelihood of landslides in areas with low slopes indicate that this region does not have a uniform threshold slope. Instead, the threshold slope for soft-rock landslide formation is lower in areas where local slopes and bedding planes are well aligned. In these cases, the hillslope is inherently weaker because local preferential failure surfaces (e.g., the thin clay depositional layers common in the Whanganui Basin) dip downslope, which promotes landslide movement. This is supported by the fact that landslides within the study area with planar failure surfaces (e.g., translational rock slides) also have lower slopes and higher slope and bedding alignment. Previous slope threshold models, like those developed in the Himalayan Alps (Larsen and Montgomery, 2012), and the Southern Alps (Korup, 2006) have tended to ignore or average the effects of local geological controls and failure mechanisms. However, in landscapes where very weak structures commonly control slope stability and the development of landslides, slope thresholds can vary dramatically. Some parts of the landscape (e.g. anti-dip slopes) can sustain steep (> 30º) hillslopes, while in other locations (e.g. dip slopes) the hillslopes begin to fail at low (< 10º) slope angles. This is supported by Roering et al.'s (2015) work in California, which showed that the threshold slope in their study area varied based on the local lithology and erosion rates.

While slope and bedding alignment appears to be the most critical preconditioning factor, river incision and high annual rainfall are likely the most influential preparatory and triggering factors. Within the occurrence susceptibility model, river incision was the most predictive triggering factor, and rainfall was the fifth most predictive. The high importance of river incision within the model corresponds well with site investigations of soft-rock landslides within our study area (McColl et al., 2022; McSaveney and Massey, 2017) and throughout the world (Agliardi et al., 2013; Roering et al., 2005; Yenes et al., 2015). In particular, a recent study within the Whanganui Basin by McColl et al. (2022) found that river incision and toe erosion were key factors in the sustained activity at the Rangitikei Landslide. As discussed in Chapter 2, soft-rock landslides are likely not initiated by pore-water pressure increases from single storm events, but studies in the region have shown that high monthly to annual rainfall rates can increase pore-water pressure to sufficient levels to initiate landslide failure (Carey et al., 2019).

Notably, factors that corresponded to seismic activity (distance to faults and predicted peak ground accelerations from New Zealand's seismic hazard model) had little predictive power. This suggests earthquakes are likely not a dominant factor in the generation of these landslides. This contrasts with the findings of two smaller regional studies in a portion of the basin (Crozier et al., 1995; Rees et al., 2019) which both relied (wholly or in part) on the proximity of soft-rock landslides to active faults as evidence of the influence of earthquakes. However, in Chapter 4 I showed that randomly placed zones of stable land exhibit the same active fault proximity distribution as the region's soft-rock landslides, and thus proximity to active faults is likely not a good predictor of earthquake influence in this region. In addition, the non-dominance of earthquakes in the region is supported by the findings of a local case study (Massey et al., 2016a), which showed that earthquakes did not appear to explain the majority of the cumulative movement that took place at the Utiku landslide over the period of observation. A recent Mw 7.8 earthquake in the South Island of New Zealand (Massey et al., 2018) did trigger deep-seated landslides similar to those found in my study area, but it is unknown if the Whanganui Basin has experienced an earthquake of this magnitude. Consequently, earthquakes of sufficient size may still trigger the initiation of soft-rock landslides in the region, but the hillslopes where this occurs may have already been primed for failure by other processes.

## 7.3 InSAR and sPOT Landslide Monitoring Framework Development

While it is helpful to understand the distribution and causes of soft-rock landslide occurrence, this information does not provide us with all of the information on landslide behaviour that we need. Many groups also need information on which landslides are active today, why they are active, and how fast they are moving. In particular, this information can be used to quantify present-day landslide hazards and sediment contributions. To generate this information, I developed and tested a framework for remotely assessing slow-moving landslide activity and movement using a combination of InSAR and sPOT time-series analyses in Chapter 5 of this thesis.

### *7.3.1 InSAR Analysis*

In Chapter 5, I found that my InSAR analysis was able to identify activity at soft-rock landslides throughout the Whanganui Basin with an overall accuracy of 92%. Despite being based on an imprecise and subjective (i.e. remotely and visually assessed) validation set, this was a promising result given that InSAR analyses are challenging to conduct within regions dominated by natural terrain (Wang et al., 2021). In general, in-field ground truth data are sparse for InSAR activity datasets for the same reason that InSAR data are useful; in-field data are costly to obtain, particularly in the rough terrains where landslides tend to occur. This has become an important obstacle that has limited the validation of landslide InSAR analyses, and in most cases the InSAR data are compared to external data only to confirm the InSAR results (Antonielli et al., 2019; Bekaert et al., 2020) and not as a formal validation set. Thus, the InSAR activity assessment I used in Chapter 5 offers a useful and affordable alternative to in-field validation that other researchers can adopt.

Four key components of the InSAR activity contributed to its performance: (1) the use of Bekaert et al.'s (2020) double-difference filter; (2) performing the SBAS analysis using separate internally-connected annual networks; (3) using a velocity-coherence filter modified from Bekaert et al.'s (2020) original filter to identify zones of movement, and; (4) pairing the InSAR-identified zones of movement with existing landslide maps to identify motion related to landslide activity.

As discussed in Chapter 5, the double-difference filter highlights local deformation and diminishes the need to correct atmospheric phase delays. Correcting for these delays is traditionally necessary to produce a usable deformation time-series but also tends to introduce noise at the scale of landslide processes (Jolivet et al., 2011; Shi et al., 2021). Thus, not having to perform this step is a significant advantage of this filter. Furthermore, my work in Chapter 5 and Chapter 6 of this thesis is the first time that this filter has been used to monitor landslides on a large scale.

Network selection is often not discussed in detail within time-series InSAR studies, but it substantially impacts the accuracy of the final analysis. Performing my analysis using annual connected networks provided me with two key advantages. First, it is usually possible to construct a fully-connected network for at least a majority of the year, and using a fully connected network greatly reduces the noise level in the resulting deformation time-series (Lanari et al., 2004; López-Quiroz et al., 2009). Second, many studies have shown that soft-rock landslides exhibit transient motion due to reactivation cycles (Borgatti et al., 2006; Handwerger et al., 2019a; Massey et al., 2013) and using annual networks allows us to spot transient movement that may have been obscured in a multi-year time-series. Since network selection is an important (and often subjective) step of SBAS analyses that is difficult to perform well, more studies should take the time to describe their network selection approach in detail.

As discussed in Chapter 5, activity filters that utilized statistical thresholds based on temporal coherence and linear velocity data were more effective than the bootstrap velocity approach used by Bekaert et al. (2020). Pre-processing steps such as multi-looking of the input interferograms can significantly increase the resulting dataset's coherence, which can make the bootstrap velocity filter too permissive. In addition, combining data from multiple separate years greatly improved the utility of the velocity-coherence filter, and future studies should integrate data from multiple years wherever possible.

While I found that the velocity-coherence filter could identify areas of activity, this activity did not always correspond to landslide activity. Many processes can induce ground deformation at the scale of InSAR analyses (Ahmed et al., 2011; Bayer et al., 2018; Plank et al., 2012), and I found that it was challenging to use InSAR data to identify landslide activity unless they were paired with external information on landslide presence. However, this limitation could be overcome with further research. As scientists produce more datasets of InSAR-identified landslide activity, it may become possible to use deep-learning methodologies in conjunction with InSAR velocity data and terrain information to identify landslide activity without using external landslide maps. In fact, some researchers have already begun pursuing this goal (Gaddes et al., 2021; Rouet-Leduc et al., 2021; Zhang et al., 2022).

While this InSAR analysis is useful, it has some additional limitations that are worth discussing. First, while multi-looking and the double-difference filter increased the accuracy of the analysis for larger landslides, it decreased its effective resolution. Thus, this analysis can likely not detect activity at small landslides (<10 ha), which made up 5% of the total area covered by the > 2 ha landslides in the region. Second, the InSAR analysis underestimated the velocity of landslides at locations whose line-of-sight velocities exceeded a few centimetres per year. Errors and bias in interferogram unwrapping and the loss of coherence during periods of accelerated landslide motion likely led to this velocity underestimation, which at times exceed an order of magnitude or more.

Still, these limitations may be confined to the InSAR products created using Senintel-1 SAR data. SAR missions that use longer sensor wavelengths, such as the L-band ALOS-2 (Kankaku et al., 2013) and upcoming NISAR (Simons et al., 2021) missions should be able to detect landslides with faster velocities with less decorrelation, and commercial SAR constellations such as those operated by Capella Space and ICEYE could offer shorter revisit times which would effectively increase the effective maximum velocity identifiable in an InSAR dataset. For the time being though, Sentinel-1 is the only freely-available SAR dataset with the data quality and image catalogue necessary to perform this type of analysis. Consequently, I suggest that landslide InSAR investigations be paired with independent velocity estimates from sPOT analyses or other techniques to determine if InSAR-derived velocities are underestimating landslide velocities. In fact, even short revisit L-band InSAR will likely be unable to measure movement that is greater than 50 cm between images, so pairing InSAR with sPOT will still provide improvements in many cases.

### *7.3.2 sPOT Analysis*

Overall, I found that my sPOT analysis was able to reliably measure landslide velocities, but the accuracy of the sPOT analysis decreased when velocities fell below roughly half a meter per year. This finding is in line with previous sPOT studies which found that sPOT accuracies typically range from 1/20$^{th}$ to 1/10$^{th}$ of the imagery pixel size used (Bickel et al., 2018; Leprince et al., 2007). Combining velocity estimates from multiple sPOT pairs in an SBAS-like time-series and careful selection of a sPOT pair network were both essential factors in the performance of this analysis.

Unlike previous time-series sPOT analyses that utilized networks similar to the nearest-neighbour connections used by InSAR SBAS analyses, I utilized a network of annual images that fell closest to a single calendar day. Using this network increased the amount of deformation observable between images because the temporal separation of the images was at least one year. Additionally, only using images from the same time of year decreased variations in reflectance due to vegetation growth and shadow orientation which can lead to increased noise in the sPOT velocity estimate. This pair selection strategy necessarily makes it impossible to observe sub-annual movement rates, but I believe the increased accuracy this strategy affords is worth introducing this limitation. However, like the InSAR analysis, future researchers should spend more time selecting, and describing, an appropriate image network for their application since it dramatically affects the final velocity product.

With the wide availability of continuously operating remote sensing imagery missions, I believe that SBAS-based time-series sPOT, instead of single image pair analyses, should now be the analysis standard. The value of this approach has been demonstrated by several previous studies (Casu et al., 2011; Dai et al., 2020; Sun et al., 2017) and my research further supports its value. While performing this additional step does require extra processing time, the increased accuracy and the reduction of noise within the final velocity product are well worth the effort. Additionally, if an annual set of images is used to form the network, the extra computation needed is still much less than is required for an SBAS InSAR analysis.

While useful, time-series sPOT analyses still have some drawbacks worth considering. Since most publicly available satellite imagery has resolutions of 10-15 meters, most sPOT analyses will likely have increased error when movement rates are less than 0.5-1 m per year. This means that performing a sPOT analyses to identify active landslides may miss landslides moving slower than this threshold. However, pairing sPOT analyses with InSAR analyses may alleviate this concern. Currently there is still a gap in the ranges of velocities where sPOT analyses are reliable and the range where InSAR analyses are reliable. An important goal for both analysis types should be to increase their reliable velocity ranges so their ranges overlap and their results can be used to validate each other. Since the sensor platforms and analysis techniques used in both methodologies are evolving rapidly, I believe this is an achievable goal within the near future. Additionally, sPOT analyses are likely unable to detect motion when the features they are tracking are removed from the scene. In particular, the erosion of landslide toes by river systems makes it difficult to use sPOT analyses at margins of eroding landslide toes. This could be mitigated by using more frequent imagery that could track features before they are removed, but once again this also tends to result in the inclusion of poorer-quality data that reduces the overall accuracy.

Overall, time-series InSAR and sPOT work best for regional landslide monitoring when combined into a single monitoring framework. Time-series InSAR data has a higher signal to noise ratio, which allows it to reliably identify activity, but time-series sPOT analyses produce more reliable velocity estimations over a wider range of velocities. Thus, InSAR can be used to identify active landslides; then sPOT can be used to measure the velocities of landslides that are known to be active. This combination of techniques has proven to be useful in a number of case studies (Dai et al., 2020; Handwerger et al., 2019b; Hu et al., 2020a), but the application of these techniques to a broad region as in Chapter 6 is still relatively new. In addition to the reliability of a monitoring framework, its ease of use and computational expense are key factors that affect its utility. The landslide monitoring framework described in Chapter 5 uses cloud-computing services wherever possible to ease computational demands and is wholly contained within a set of freely available Jupyter Notebooks. Relying on these technologies significantly lowers the barriers to entry for other researchers who want to perform similar analyses.

## 7.4 Factors Influencing Contemporary Soft-Rock Landslide Activity

In Chapter 6, I used the framework described in Chapter 5, to identify the soft-rock landslides that have been active during the past four years (2018 to 2022) within the Whanganui Basin, then used this information to create a logistic regression model of landslide activity. In contrast to the landslide occurrence model from Chapter 4, which identified the stability factors that lead to landslide occurrence, this activity factor analysis identified the factors most strongly correlated with the distribution of active versus inactive landslides.

The correlation of terrain roughness with activity within the model was unsurprising, as active landslides are likely to have deformed the terrain more recently, which leads to higher surface roughness. Importantly however, it indicates that surface roughness may be useful in predicting how long a landslide in this region has been inactive (i.e. landslides inactive for long periods may have less surface roughness). In comparison, the high predictive power of low slopes was more surprising. The occurrence model (Chapter 4) indicated that the threshold slope for soft-rock landslide formation is lower in areas where local slopes and bedding planes are well aligned. Our activity factor analysis further demonstrates that this process is even more pronounced at active landslides, where the threshold slope is likely lower than the general landslide population. This extends the findings of Chapter 4 and indicates that the divergence from a uniform threshold slope model is even more pronounced in the currently active landslides of the region. It also suggests that inactive landslides have not self-arrested or stabilised through slope adjustment (i.e. a reduction in slope angle towards equilibrium), or otherwise we would expect active landslides to have steeper slopes than inactive landslides.

The predictive power of the average annual rainfall and stream power index factors within the activity factor analysis indicate that changes in porewater pressure and toe erosion are likely the most important factors sustaining the activity of these landslides at the regional scale. This finding is line with work at the Rangitikei (McColl et al., 2022), Utiku (McSaveney and Massey, 2017) and Taihape (Massey et al., 2016b) landslides which indicate that toe erosion is a major driver of landslide activity. However the evidence from case studies that high rainfall (and thus high pore-water pressure) is an important sustaining factor is mixed. Evidence from the Utiku Landslide shows that high pore-water pressure was well correlated with landslide motion (Carey et al., 2019), but a similar study at the Taihape landslide did not find this correlation (Massey et al., 2016b). It is likely that site-specific factors control the amount of influence pore-water pressures have on the stability of these landslides (e.g. as a function of how close ground-water levels are to preferential failure surfaces) and our regional scale models may be poorly suited to capturing these interactions.

The average annual rainfall factor was more important than stream power index within the model, but some issues with the stream power index factor limit its interpretability. The stream power index we used assumes that all locations contribute equal amounts of water to the river systems, which fails to capture the actual variations in stream power likely to exist due to uneven rainfall and runoff distributions. Thus, local variations in the erosive power of rivers may be better represented by the average annual rainfall factor than the stream power index factor. However, it may be the case that neither of these factors is dominant, and instead, both work together to sustain landslide failure. This is the case at the Utiku landslide, where toe erosion and river incision were found to initiate reactivation (McSaveney and Massey, 2017), but movement rates varied annually with variations in pore-water pressure (Carey et al., 2019). Importantly however, the strong influence of both pore-water pressure and toe erosion suggests that many of the soft-rock landslides in the region might not be exhausted and could reactivate if there is increased precipitation in the area.

As in the occurrence factor analysis, there was no indication that seismic factors were predictive of landslide activity in the activity factor analysis. This furthers the hypothesis that seismic factors do not heavily influence these landslides. In contrast to the occurrence factor analysis, the absence of forest cover was not correlated with the presence of active landslides. However, as discussed in Chapter 6, the inability of C-band SAR observations to produce reliable estimates of movement under tree cover limits the interpretability of this observation. Still, this could suggest that the correlation of forest cover with non-landslide terrain in the occurrence model was due to this factor's anti-correlation with low slopes. In other words, steep forested slopes were less commonly converted to pasture, and steep slopes that had been cleared were later more likely targeted for subsequent afforestation. Thus, the apparent importance of forest absence within the occurrence model could be due to this relationship and not to the destabilizing effect of forest clearance. Conducting a similar InSAR activity analysis that is based on L-band SAR data, which can detect motion under tree cover, could provide a way determine if this is the case.

## 7.5 Estimation of Whanganui Basin Sediment Contribution

The use of remote sensing velocity estimates to create a sediment model for soft-rock landslides in Chapter 6 is an important step forward for the field. Large, slow-moving landslide sediment contributions are often excluded from sediment budget analyses because they are both difficult to measure and to incorporate into sediment budget models. In Chapter 6 however, I described and utilized a methodology for estimating large slow-moving landslide sediment contributions that can be incorporated into a feature-based sediment budget model.

The British statistician George Box famously wrote that "All models are wrong, but some are useful" and I believe that this landslide sediment delivery model has crossed the important threshold from "wrong" to "wrong but useful". We know landslides are an important terrain regulation process over geologic timescales but hitherto we have had little information on their role within contemporary sediment budgets. My model in Chapter 6 is the only one of its kind for regional-scale contemporary sediment delivery from large slow-moving landslides anywhere in the world. While considerable uncertainty is attached to my model outputs, especially associated with the landslide velocity and depth variables, I believe the model presented in Chapter 6 represents a reasonable compromise between the accuracy and efficiency of the analysis. Still, there are exciting opportunities to further improve the model as remote sensing imagery increases in resolution and accuracy, and to apply it to other locations in NZ and beyond as well.

Estimates of the sediment contributions from soft-rock landslides in the Whanganui Basin (Chapter 6) indicate the need for their incorporation into the sediment budget models of the region. Our model indicates that soft-rock landslides contribute roughly 10±2% of the sediment export predicted by the NZeem suspended sediment load model for the region. In addition, studies of soft-rock landslides in the region have shown that while movement is often caused by storm events that induce landslide toe erosion or increased pore-water pressure, there can be a significant lag between when these storm events end and when these landslides stop moving at accelerated rates (Massey et al., 2016b; McColl et al., 2022; McSaveney and Massey, 2017). Consequently, these landslides may persist in delivering sediment even during baseflow periods, when other erosional sources are typically far less active.

Due to the sizeable sediment contributions from these landslides, they may also represent an important opportunity to reduce sediment loads. Further work needs to be done to determine if human interventions can cost-effectively reduce the movement rates of these landslides, but attempting to reduce catchment sediment loads by reducing the inputs from soft-rock landslides does have some potential benefits. For example, reducing sediment contributions from many widely distributed sources, such as shallow landslides, or diffuse soil erosion processes like soil creep, requires broad cooperation across catchments and a large number of landowners. Conversely, reducing sediment contributions from a soft-rock landslide would require coordination among a much smaller group of landowners while potentially reducing sediment loads by a large amount. Additionally, stabilizing landslides is likely to be in the immediate financial interest of landowners, which may make them more willing to cooperate.

The role of soft-rock landslides in the long-term sediment dynamics of uplifting regions, the predisposition of many hillslopes to failure due to slope and bedding alignment, and the long-term incision may make it challenging to stabilize these landslides. However, the results of our landslide occurrence and activity factor analyses (Chapters 4 & 6) provide us with information that will help us determine which interventions may be effective. These models indicate that high porewater pressures and toe erosion are the main drivers of destabilization, and interventions that seek to eliminate or reduce these factors may prove effective. This aligns with previous reports of other deep-seated landslide stabilization projects, which mainly attempt to route groundwater away from the landslide's failure surface (Grosser et al., 2020; Klimeš et al., 2012; Zapico et al., 2020). Additionally, the landslide monitoring framework described in Chapter 5 provides us with a methodology to triage the soft-rock landslides across a region to determine where conservation efforts should be targeted to reduce the most soft-rock landslide erosion as efficiently as possible.

# Chapter 8 Conclusion

## 8.1 Assessment of Objectives

Overall, this thesis has completed the objectives it sought to achieve. The aim of this thesis was to expand our understanding of the factors controlling soft-rock landslide failure, develop new methodologies for monitoring these landslides, and determine the role that these landslides play in the sediment dynamics of the Whanganui Basin. I found that river incision and slope and bedding alignment were primary factors influencing slope instability and that toe erosion and porewater pressure are far more likely to destabilize soft-rock landslides than seismic factors. I also developed a reliable remote sensing framework for monitoring soft-rock landslides, and I determined that roughly 10±2% of the sediment export within the basin is derived from soft-rock landslides. The results as they pertain to the specific objectives are:

1. In Chapter 4, I improved upon previous mapping work done by GNS Science and mapped 871 landslides within the Whanganui Basin. Many of these landslides were not included in the previous landslide map of the area or had significantly altered extents.

2. In Chapter 4, I found that river incision, low slopes, high slope and bedding alignment, and high annual rainfall were predictive of soft-rock landslide occurrence and, thus, are likely the key factors controlling landslide occurrence.

3. In Chapter 5, I developed a time-series InSAR and time-series sPOT framework for soft-rock landslide monitoring that could identify activity with 92% accuracy and measure landslide velocities that averaged 2.05 m/yr with a mean absolute error of 0.74 m/yr.

4. In Chapter 6, I used the framework from Chapter 5 to identify 66 active soft-rock landslides in the Whanganui Basin and used a landslide susceptibility model to determine that high annual rainfall and the stream power index were the most predictive of activity. This suggests that high porewater pressure and toe erosion are likely the most influential sustaining factors for these landslides.

5. In Chapter 6, I estimated the annual sediment budgets of the active soft-rock landslides in the region using site-specific width, depth, density, and velocity information to determine the total sediment export for these landslides. Overall, these landslides contribute 10±2% of the total basin sediment export, but this varies from 2%±1% to 19%±3% by catchment.

I believe that this thesis contributes to our understanding of soft-rock landslides in New Zealand and globally and provides a series of methodologies that other scientists can use to detect and monitor slow-moving reliably on regional scales.

## 8.2 General Findings

Based on the work of Chapter 4, we determined that river incision and slope and bedding alignment were important factors influencing the stability of the soft-rock landslides within the Whanganui Basin, and that seismic shaking is likely not a dominant factor controlling landslide occurrence. This analysis was extended in Chapter 6 to show that toe erosion and high pore-water pressure are likely the dominant sustaining factors in the region. These relationships are similar to those found in the soft-rock landslides of California (Roering et al., 2015) and Italy (Borgatti et al., 2006; Peruccacci et al., 2012), but diverged from those of the deep-seated landslides in the Himalayas (Korup and Weidinger, 2011; Larsen et al., 2010; Larsen and Montgomery, 2012) and the South Island of New Zealand (Korup, 2006; Massey et al., 2018). Still, all studies do point to the important role that rock strength and river incision play in the generation of deep-seated landslides.

One interesting similarity between studies in the Eel River catchment of California, USA (Handwerger et al., 2019b; Roering et al., 2015) and our study area is that both sites are closer to the soft-rock end of the deep-seated landslide continuum than to the hard-rock end and both show more heterogeneity in local threshold slope angles and a larger influence of rainfall as a sustaining factor. Thus, heterogeneity of slope threshold angles and the prevalence of rainfall as a sustaining factor may be a particularly pronounced in soft-rock landscapes.

In addition to these scientific findings, this thesis also advances the techniques used to study large, slow-moving landslides. My InSAR and sPOT analyses in Chapter 5 demonstrate that we can combine these techniques with freely available data to efficiently monitor large slow-moving landslides. Furthermore, I show that combining these data with a susceptibility factor analysis (Chapter 6) can lead to insights that might not be possible to uncover when performing susceptibility factor analyses with occurrence data alone. Consequently, it would be worth revisiting other prominent landslide occurrence factor analyses such as those performed in California, USA (Roering et al., 2015) and the Apennines, Italy (Guzzetti et al., 2005; Peruccacci et al., 2012) to see if similar trends are found.

Using the landslide sediment export analysis in Chapter 6, I was able to estimate that soft-rock landslides contribute roughly 10±2% of total sediment being exported to catchments in the region. Since this a decent proportion of the total sediment, and because these landslides may be contributing proportionately more sediment during baseflow periods, it is worth investigating if interventions at these landslides could represent a cost-effective way to reduce sediment loads in local rivers. Additionally, the susceptibility factors influencing these landslides that were identified in the analyses of Chapters 4 and 6, namely the importance of river incision, toe erosion, and pore-water pressure, offer some guidance as to how these landslides could be controlled. Soft-rock landslides are often overlooked due to their slow movement rates, but I hope this thesis has shown that they are an important part of contemporary sediment dynamics and that there are reliable, efficient ways to monitor them.

## 8.3 Future Research

While my thesis fulfilled the objectives it set out to, it also revealed new pathways for future research. The first set of new research avenues are those that improve upon the remote sensing methodologies I discussed within this thesis. In particular, the low correlation of InSAR data in natural settings was a significant impediment to the quality of the analysis. However, new satellites are being launched that may be able to overcome this limitation. As of mid-2022, the NASA-ISRO Synthetic Aperture Radar (NISAR) satellite has a planned launch year of 2023. This satellite has an L-band SAR sensor that is much more powerful and resilient to vegetation and deformation-related decorrelation than the C-band Sentinel-1 SAR data I used in this thesis. Using data from this satellite will likely improve many existing workflows and inspire the creation of many new methodologies.

Similarly, sub-meter satellite-based SAR and optical imagery are now being routinely collected and are starting to become available to researchers. Since sPOT accuracy is directly controlled by the geolocation accuracy and resolution of the input imagery, this will greatly improve the accuracy of sPOT analyses. Due to these two advancements, we may soon have an overlap between the ranges of velocities that are detectable using InSAR and sPOT techniques. This will allow us to create a continuous portrait of land surface deformation from millimetres per year to tens of meters per year. As mentioned in the synthesis, machine learning computer vision techniques are continually improving, and in almost every case where adequate training data exist, these techniques have produced useful results. Since projects like this thesis are now generating the training data needed to create these models, we may soon be able to use these techniques to create automated workflows for identifying landslide activity.

A consistent theme of my thesis is that seismic forces do not control the occurrence or activity of the landslides in the Whanganui Basin. However, research from the South Island of New Zealand has shown that large earthquakes (> $M_w$ 7) can generate landslides like those found in the Whanganui Basin (Massey et al., 2018). A comparison study between the soft-rock landslides caused by these earthquakes and those found within the Whanganui Basin would likely provide useful insights into the relationship between deep-seated landslide generation and factors like slope and bedding alignment, river incision, and earthquakes in New Zealand. Additionally, the role of earthquakes in the occurrence and activity of the Whanganui Basin soft-rock landslides may be difficult to discern because this region has not experienced many significant earthquakes (>$M_w$ 7) in the historical era. However, dating some of these landslides and comparing these dates to the paleo-seismic record could provide a way to determine if earthquakes triggered these landslides during the pre-historic era. Additionally, the susceptibility factor analyses in Chapters 4 and 6 demonstrated that conducting landslide susceptibility analyses with active landslide data instead of landslide occurrence data produces insightful results. Conducting activity susceptibility factor analyses in more regions where soft-rock landslides occur could help us better discriminate between the factors that control long-term occurrence and the factors that influence contemporary activity.

The landslide sediment export analysis in Chapter 6 provided useful insights on the role of soft-rock landslides in the sediment dynamics of the Whanganui Basin but applying this model to larger regions would help us better understand the role these landslides play on a broader scale. The Whanganui Basin was selected for this thesis because of the large number of soft-rock landslides in the region, but what are the impacts of these landslides when they are less numerous? Additionally, it would be useful to conduct the same analysis over a larger number of years to determine how correlated sediment inputs from soft-rock landslides are to decadal flood and drought cycles. Also, the soft-rock landslide sediment budget component developed in Chapter 6 still needs to be incorporated into a sediment budget model framework that includes a broader range of sediment sources. Finally, more work needs to be done to determine if conservation efforts can reduce the sediment export from soft-rock landslides. It would be useful to determine if interventions such as river re-alignment and bank stabilization could stop the conveyor belt of toe erosion that, in many cases, leads to soft-rock landslide destabilization.

# References

Agliardi, F., Crosta, G.B., Frattini, P., Malusà, M.G., 2013. Giant non-catastrophic landslides and the long-term exhumation of the European Alps. Earth and Planetary Science Letters 365, 263–274. https://doi.org/10.1016/j.epsl.2013.01.030

Ahmed, R., Siqueira, P., Hensley, S., Chapman, B., Bergen, K., 2011. A survey of temporal decorrelation from spaceborne L-Band repeat-pass InSAR. Remote Sensing of Environment, DESDynI VEG-3D Special Issue 115, 2887–2896. https://doi.org/10.1016/j.rse.2010.03.017

Alvioli, M., Marchesini, I., Reichenbach, P., Rossi, M., Ardizzone, F., Fiorucci, F., Guzzetti, F., 2016. Automatic delineation of geomorphological slope units with r.slopeunits v1.0 and their optimization for landslide susceptibility modeling. Geoscientific Model Development 9, 3975–3991. https://doi.org/10.5194/gmd-9-3975-2016

Amitrano, D., Guida, R., Dell'Aglio, D., Di Martino, G., Di Martire, D., Iodice, A., Costantini, M., Malvarosa, F., Minati, F., 2019. Long-Term Satellite Monitoring of the Slumgullion Landslide Using Space-Borne Synthetic Aperture Radar Sub-Pixel Offset Tracking. Remote Sensing 11, 369. https://doi.org/10.3390/rs11030369

Anantrasirichai, N., Biggs, J., Kelevitz, K., Sadeghi, Z., Wright, T., Thompson, J., Achim, A.M., Bull, D., 2021. Detecting Ground Deformation in the Built Environment Using Sparse Satellite InSAR Data With a Convolutional Neural Network. IEEE Transactions on Geoscience and Remote Sensing 59, 2940–2950. https://doi.org/10.1109/TGRS.2020.3018315

Anderton, P.W., 1981. Structure and evolution of the South Wanganui Basin, New Zealand. New Zealand Journal of Geology and Geophysics 24, 39–63. https://doi.org/10.1080/00288306.1981.10422697

Antonielli, B., Mazzanti, P., Rocca, A., Bozzano, F., Cas, L.D., 2019. A-DInSAR performance for updating landslide inventory in mountain areas: An example from lombardy region (Italy). Geosciences (Switzerland) 9, 364. https://doi.org/10.3390/geosciences9090364

Armstrong, P.A., Allis, R.G., Funnell, R.H., Chapman, D.S., 1998. Late Neogene exhumation patterns in Taranaki Basin (New Zealand): Evidence from offset porosity-depth trends. Journal of Geophysical Research: Solid Earth 103, 30269–30282. https://doi.org/10.1029/98JB02843

Ayalew, L., Yamagishi, H., 2005. The application of GIS-based logistic regression for landslide susceptibility mapping in the Kakuda-Yahiko Mountains, Central Japan. Geomorphology 65, 15–31. https://doi.org/10.1016/j.geomorph.2004.06.010

Bălteanu, D., Chendeş, V., Sima, M., Enciu, P., 2010. A country-wide spatial assessment of landslide susceptibility in Romania. Geomorphology 124, 102–112. https://doi.org/10.1016/j.geomorph.2010.03.005

Basher, L., Betts, H., Lynn, I., Marden, M., McNeill, S., Page, M., Rosser, B., 2018. A preliminary assessment of the impact of landslide, earthflow, and gully erosion on soil carbon stocks in New Zealand. Geomorphology 307, 93–106. https://doi.org/10.1016/j.geomorph.2017.10.006

Basher, L., Spiekermann, R., Dymond, J., Herzig, A., Hayman, E., Ausseil, A.-G., 2020. Modelling the effect of land management interventions and climate change on sediment loads in the Manawatū–Whanganui region. New Zealand Journal of Marine and Freshwater Research 1–22. https://doi.org/10.1080/00288330.2020.1730413

Bayer, B., Simoni, A., Mulas, M., Corsini, A., Schmidt, D., 2018. Deformation responses of slow moving landslides to seasonal rainfall in the Northern Apennines, measured by

InSAR. Geomorphology 308, 293–306. https://doi.org/10.1016/j.geomorph.2018.02.020
Bayer, B., Simoni, A., Schmidt, D., Bertello, L., 2017. Using advanced InSAR techniques to monitor landslide deformations induced by tunneling in the Northern Apennines, Italy. Engineering Geology 226, 20–32. https://doi.org/10.1016/j.enggeo.2017.03.026
Behling, R., Roessner, S., Kaufmann, H., Kleinschmit, B., 2014. Automated spatiotemporal landslide mapping over large areas using rapideye time series data. Remote Sensing 6, 8026–8055. https://doi.org/10.3390/rs6098026
Bekaert, D.P.S., Handwerger, A.L., Agram, P., Kirschbaum, D.B., 2020. InSAR-based detection method for mapping and monitoring slow-moving landslides in remote regions with steep and mountainous terrain: An application to Nepal. Remote Sensing of Environment 249, 111983. https://doi.org/10.1016/j.rse.2020.111983
Belgiu, M., Drăgu, L., 2016. Random forest in remote sensing: A review of applications and future directions, ISPRS Journal of Photogrammetry and Remote Sensing. https://doi.org/10.1016/j.isprsjprs.2016.01.011
Bennett, G.L., Miller, S.R., Roering, J.J., Schmidt, D.A., 2016. Landslides, threshold slopes, and the survival of relict terrain in the wake of the Mendocino Triple Junction. Geology 44, 363–366. https://doi.org/10.1130/G37530.1
Berardino, P., Fornaro, G., Lanari, R., Sansosti, E., 2002. A new algorithm for surface deformation monitoring based on small baseline differential SAR interferograms. IEEE Transactions on Geoscience and Remote Sensing 40, 2375–2383. https://doi.org/10.1109/TGRS.2002.803792
Bertolini, G., Pizziolo, M., 2008. Risk assessment strategies for the reactivation of earth flows in the Northern Apennines (Italy). Engineering Geology, Landslide Susceptibility, Hazard and Risk Zoning for Land Use Planning 102, 178–192. https://doi.org/10.1016/j.enggeo.2008.03.017
Betts, H., Basher, L., Dymond, J., Herzig, A., Marden, M., Phillips, C., 2017. Development of a landslide component for a sediment budget model. Environmental Modelling and Software 92, 28–39. https://doi.org/10.1016/j.envsoft.2017.02.003
Bickel, V.T., Manconi, A., Amann, F., 2018. Quantitative Assessment of Digital Image Correlation Methods to Detect and Monitor Surface Displacements of Large Slope Instabilities. Remote Sensing 10, 865. https://doi.org/10.3390/rs10060865
Bilderback, E.L., Pettinga, J.R., Litchfield, N.J., Quigley, M., Marden, M., Roering, J.J., Palmer, A.S., 2015. Hillslope response to climate-modulated river incision in the waipaoa catchment, East Coast North Island, New Zealand. Bulletin of the Geological Society of America 127, 131–148. https://doi.org/10.1130/B31015.1
Bilotta, G.S., Brazier, R.E., 2008. Understanding the influence of suspended solids on water quality and aquatic biota. Water Research 42, 2849–2861. https://doi.org/10.1016/j.watres.2008.03.018
Bishop, P., 2007. Long-term landscape evolution: linking tectonics and surface processes. Earth Surface Processes and Landforms 32, 329–365. https://doi.org/10.1002/esp.1493
Bitelli, G., Dubbini, M., Zanutta, A., 2004. Terrestrial laser scanning and digital photogrammetry techniques to monitor landslide bodies. International Archives of Photogrammetry, Remote Sensing and Spatial Information Sciences 35, 246–251.
Bonì, R., Bordoni, M., Colombo, A., Lanteri, L., Meisina, C., 2018. Landslide state of activity maps by combining multi-temporal A-DInSAR (LAMBDA). Remote Sensing of Environment 217, 172–190. https://doi.org/10.1016/j.rse.2018.08.013
Booth, A.M., McCarley, J., Hinkle, J., Shaw, S., Ampuero, J.-P., Lamb, M.P., 2018. Transient Reactivation of a Deep-Seated Landslide by Undrained Loading Captured

With Repeat Airborne and Terrestrial Lidar. Geophysical Research Letters 45, 4841–4850. https://doi.org/10.1029/2018GL077812
Booth, A.M., Roering, J.J., Rempel, A.W., 2013. Topographic signatures and a general transport law for deep-seated landslides in a landscape evolution model. Journal of Geophysical Research: Earth Surface 118, 603–624. https://doi.org/10.1002/jgrf.20051
Borgatti, L., Corsini, A., Barbieri, M., Sartini, G., Truffelli, G., Caputo, G., Puglisi, C., 2006. Large reactivated landslides in weak rock masses: A case study from the Northern Apennines (Italy), Landslides. https://doi.org/10.1007/s10346-005-0033-9
Bovenga, F., Refice, A., Pasquariello, G., 2012. Using corner reflectors and X-band SAR interferometry for slope instability monitoring, in: 2012 Tyrrhenian Workshop on Advances in Radar and Remote Sensing (TyWRRS). Presented at the 2012 Tyrrhenian Workshop on Advances in Radar and Remote Sensing (TyWRRS), pp. 114–120. https://doi.org/10.1109/TyWRRS.2012.6381114
Bozzano, F., Mazzanti, P., Perissin, D., Rocca, A., De Pari, P., Discenza, M.E., 2017. Basin scale assessment of landslides geomorphological setting by advanced InSAR analysis. Remote Sensing 9. https://doi.org/10.3390/rs9030267
Broeckx, J., Rossi, M., Lijnen, K., Campforts, B., Poesen, J., Vanmaercke, M., 2020. Landslide mobilization rates: A global analysis and model. Earth-Science Reviews 201, 102972. https://doi.org/10.1016/j.earscirev.2019.102972
Brown, R., 2016. Geomorphons: Landform and property predictions in a glacial moraine in Indiana landscapes. Catena 142, 66–76. https://doi.org/10.1016/j.catena.2016.01.002
Brown, W.J., 1991. Landslide Control on North Island, New Zealand. Geographical Review 81, 457–472. https://doi.org/10.2307/215611
Budimir, M.E.A., Atkinson, P.M., Lewis, H.G., 2015. A systematic review of landslide probability mapping using logistic regression. Landslides 12. https://doi.org/10.1007/s10346-014-0550-5
Bürgmann, R., Rosen, P.A., Fielding, E.J., 2000. Synthetic Aperture Radar Interferometry to Measure Earth's Surface Topography and Its Deformation. Annual Review of Earth and Planetary Sciences 28, 169–209. https://doi.org/10.1146/annurev.earth.28.1.169
Cai, J., Wang, C., Mao, X., Wang, Q., 2017. An adaptive offset tracking method with SAR images for landslide displacement monitoring. Remote Sensing 9. https://doi.org/10.3390/rs9080830
Calcaterra, D., Parise, M., 2010. Weathering in the crystalline rocks of Calabria, Italy, and relationships to landslides. Geological Society Engineering Geology Special Publication 23, 105–130. https://doi.org/10.1144/EGSP23.7
Campbell, J.b, Wynne, R.H., 2011. Introduction to Remote Sensing, Fifth Edition.
Carey, J.M., Massey, C.I., Lyndsell, B., Petley, D.N., 2019. Displacement mechanisms of slow-moving landslides in response to changes in porewater pressure and dynamic stress. Earth Surface Dynamics 7, 707–722. https://doi.org/10.5194/esurf-7-707-2019
Carter, R.M., Naish, T.R., 1998. A review of Wanganui Basin, New Zealand: global reference section for shallow marine, Plio–Pleistocene (2.5–0 Ma) cyclostratigraphy. Sedimentary Geology 122, 37–52. https://doi.org/10.1016/S0037-0738(98)00097-9
Casu, F., Manconi, A., Pepe, A., Lanari, R., 2011. Deformation Time-Series Generation in Areas Characterized by Large Displacement Dynamics: The SAR Amplitude Pixel-Offset SBAS Technique. IEEE Transactions on Geoscience and Remote Sensing 49, 2752–2763. https://doi.org/10.1109/TGRS.2010.2104325
Chandler, J., 1999. Effective application of automated digital photogrammetry for geomorphological research. Earth Surface Processes and Landforms 24, 51–63. https://doi.org/10.1002/(SICI)1096-9837(199901)24:1<51::AID-ESP948>3.0.CO;2-H

Chen, Y.-C., Chang, K.-T., Wang, S.-F., Huang, J.-C., Yu, C.-K., Tu, J.-Y., Chu, H.-J., Liu, C.-C., 2019. Controls of preferential orientation of earthquake- and rainfall-triggered landslides in Taiwan's orogenic mountain belt. Earth Surface Processes and Landforms 44, 1661–1674. https://doi.org/10.1002/esp.4601
Chittenden, H., Delunel, R., Schlunegger, F., Akçar, N., Kubik, P., 2014. The influence of bedrock orientation on the landscape evolution, surface morphology and denudation (10Be) at the Niesen, Switzerland. Earth Surface Processes and Landforms 39, 1153–1166. https://doi.org/10.1002/esp.3511
Cicchetti, D.V., Feinstien, a R., 1990. High agreement but low kappa: I. The problems of two paradoxes. Journal of Clinical Epidemiology 43, 551–558. https://doi.org/10.1016/0895-4356(90)90159-M
Cohen-Waeber, J., Bürgmann, R., Chaussard, E., Giannico, C., Ferretti, A., 2018. Spatiotemporal Patterns of Precipitation-Modulated Landslide Deformation From Independent Component Analysis of InSAR Time Series. Geophysical Research Letters 45, 1878–1887. https://doi.org/10.1002/2017GL075950
Collins, A.L., Naden, P.S., Sear, D.A., Jones, J.I., Foster, I.D.L., Morrow, K., 2011. Sediment targets for informing river catchment management: international experience and prospects. Hydrological Processes 25, 2112–2129. https://doi.org/10.1002/hyp.7965
Columbus, J., Sirguey, P., Tenzer, R., 2011. A free, fully assessed 15-m DEM for New Zealand. Survey Quarterly 16–19.
Crosetto, M., Gili, J.A., Monserrat, O., Cuevas-González, M., Corominas, J., Serral, D., 2013. Interferometric SAR monitoring of the Vallcebre landslide (Spain) using corner reflectors. Natural Hazards and Earth System Sciences 13, 923–933. https://doi.org/10.5194/nhess-13-923-2013
Crosta, G.B., Frattini, P., Agliardi, F., 2013. Deep seated gravitational slope deformations in the European Alps. Tectonophysics 605, 13–33. https://doi.org/10.1016/j.tecto.2013.04.028
Crozier, M., 1996. Runout behaviour of shallow, rapid earthflows. Zeitschrift für Geomorphologie. Supplementband 35–48.
Crozier, M.J., 2005. Multiple-occurrence regional landslide events in New Zealand: Hazard management issues. Landslides 2, 247–256. https://doi.org/10.1007/s10346-005-0019-7
Crozier, M.J., 1986. Landslides: causes, consequences and environment. Landslides: causes, consequences and environment. https://doi.org/10.1080/03036758.1988.10429158
Crozier, M.J., Deimel, M.S., Simon, J.S., 1995. Investigation of earthquake triggering for deep-seated landslides, Taranaki, New Zealand. Quaternary International 25, 65–73. https://doi.org/10.1016/1040-6182(94)00036-5
Crozier, M.J., Glade, T., 2005. The Nature of Landslide Hazard Impact, in: Landslide Hazard and Risk. pp. 43–74. https://doi.org/10.1002/9780470012659.ch2
Crozier, M.J., Pillans, B.J., 1991. Geomorphic events and landform response in south-eastern Taranaki, New Zealand. CATENA 18, 471–487. https://doi.org/10.1016/0341-8162(91)90050-8
Cruden, D., Varnes, D., 1996. Landslides: Investigation and mitigation. chapter 3 - landslide types and processes. Transportation Research Board Special Report.
Cruden, D.M., 1974. The static fatigue of brittle rock under uniaxial compression. International Journal of Rock Mechanics and Mining Sciences and 11, 67–73. https://doi.org/10.1016/0148-9062(74)92650-3
Dadson, S.J., Hovius, N., Chen, H., Dade, W.B., Lin, J.-C., Hsu, M.-L., Lin, C.-W., Horng, M.-J., Chen, T.-C., Milliman, J., Stark, C.P., 2004. Earthquake-triggered increase in

sediment delivery from an active mountain belt. Geology 32, 733–736. https://doi.org/10.1130/G20639.1
Dai, C., Higman, B., Lynett, P.J., Jacquemart, M., Howat, I.M., Liljedahl, A.K., Dufresne, A., Freymueller, J.T., Geertsema, M., Jones, M.W., Haeussler, P.J., 2020. Detection and Assessment of a Large and Potentially Tsunamigenic Periglacial Landslide in Barry Arm, Alaska. Geophysical Research Letters 47, e2020GL089800. https://doi.org/10.1029/2020GL089800
Davies-Colley, R., Hughes, A., 2020. Sediment-related water quality of small hill-country streams near Whatawhata, New Zealand. Response to integrated catchment management (ICM). New Zealand Journal of Marine and Freshwater Research 54, 329–353. https://doi.org/10.1080/00288330.2020.1761840
Davies-Colley, R.J., Smith, D.G., 2001. Turbidity, Suspended Sediment, and Water Clarity: A Review. JAWRA Journal of the American Water Resources Association 37, 1085–1101. https://doi.org/10.1111/j.1752-1688.2001.tb03624.x
Day, S.S., Gran, K.B., Belmont, P., Wawrzyniec, T., 2013a. Measuring bluff erosion part 1: terrestrial laser scanning methods for change detection. Earth Surface Processes and Landforms 38, 1055–1067. https://doi.org/10.1002/esp.3353
Day, S.S., Gran, K.B., Belmont, P., Wawrzyniec, T., 2013b. Measuring bluff erosion part 2: Pairing aerial photographs and terrestrial laser scanning to create a watershed scale sediment budget. Earth Surface Processes and Landforms 38, 1068–1082. https://doi.org/10.1002/esp.3359
De Rose, R.C., Basher, L.R., 2011. Measurement of river bank and cliff erosion from sequential LIDAR and historical aerial photography. Geomorphology 126, 132–147. https://doi.org/10.1016/j.geomorph.2010.10.037
Della Seta, M., Martino, S., Scarascia Mugnozza, G., 2013. Quaternary sea-level change and slope instability in coastal areas: Insights from the Vasto Landslide (Adriatic coast, central Italy). Geomorphology 201, 462–478. https://doi.org/10.1016/j.geomorph.2013.07.019
Dellow, S., Massey, C.I., McColl, S., Townsend, D., Villeneuve, M., 2017. Landslides caused by the 14 November 2016 Kaikoura earthquake, South Island. Proc. 20th NZGS Geotechnical Symposium 2016, 1–8.
Derron, M.H., Jaboyedoff, M., 2010. LIDAR and DEM techniques for landslides monitoring and characterization, Natural Hazards and Earth System Science. https://doi.org/10.5194/nhess-10-1877-2010
Dille, A., Kervyn, F., Handwerger, A.L., d'Oreye, N., Derauw, D., Mugaruka Bibentyo, T., Samsonov, S., Malet, J.-P., Kervyn, M., Dewitte, O., 2021. When image correlation is needed: Unravelling the complex dynamics of a slow-moving landslide in the tropics with dense radar and optical time series. Remote Sensing of Environment 258, 112402. https://doi.org/10.1016/j.rse.2021.112402
Dille, A., Kervyn, F., Mugaruka Bibentyo, T., Delvaux, D., Ganza, G.B., Ilombe Mawe, G., Kalikone Buzera, C., Safari Nakito, E., Moeyersons, J., Monsieurs, E., Nzolang, C., Smets, B., Kervyn, M., Dewitte, O., 2019. Causes and triggers of deep-seated hillslope instability in the tropics – Insights from a 60-year record of Ikoma landslide (DR Congo). Geomorphology 345, 106835. https://doi.org/10.1016/j.geomorph.2019.106835
Doi, I., Matsuura, S., Osawa, H., Shibasaki, T., Tosa, S., 2020. Effects of coastal erosion on landslide activity revealed by multi-sensor observations. Earth Surface Processes and Landforms 45, 2291–2299. https://doi.org/10.1002/esp.4880

Dymond, J.R., Ausseil, A.-G., Shepherd, J.D., Buettner, L., 2006. Validation of a region-wide model of landslide susceptibility in the Manawatu–Wanganui region of New Zealand. Geomorphology 74, 70–79. https://doi.org/10.1016/j.geomorph.2005.08.005

Dymond, J.R., Betts, H.D., Schierlitz, C.S., 2010. An erosion model for evaluating regional land-use scenarios. Environmental Modelling & Software 25, 289–298. https://doi.org/10.1016/j.envsoft.2009.09.011

Dymond, J.R., Herzig, A., Basher, L., Betts, H.D., Marden, M., Phillips, C.J., Ausseil, A.G.E., Palmer, D.J., Clark, M., Roygard, J., 2016. Development of a New Zealand SedNet model for assessment of catchment-wide soil-conservation works. Geomorphology 257, 85–93. https://doi.org/10.1016/j.geomorph.2015.12.022

Even, M., Schulz, K., 2018. InSAR deformation analysis with distributed scatterers: A review complemented by new advances, Remote Sensing. MDPI AG. https://doi.org/10.3390/rs10050744

Ewers, R.M., Kliskey, A.D., Walker, S., Rutledge, D., Harding, J.S., Didham, R.K., 2006. Past and future trajectories of forest loss in New Zealand. Biological Conservation 133, 312–325. https://doi.org/10.1016/j.biocon.2006.06.018

Fang, Z., Wang, Y., Peng, L., Hong, H., 2020. Integration of convolutional neural network and conventional machine learning classifiers for landslide susceptibility mapping. Computers & Geosciences 139, 104470. https://doi.org/10.1016/j.cageo.2020.104470

Fattahi, H., Agram, P.S., Tymofyeyeva, E., Bekaert, D.P., 2019. FRInGE; full-resolution InSAR timeseries using generalized eigenvectors, in: AGU Fall Meeting Abstracts. pp. G11B-0514.

Ferretti, A., Fumagalli, A., Novali, F., Prati, C., Rocca, F., Rucci, A., 2011. A new algorithm for processing interferometric data-stacks: SqueeSAR, in: IEEE Transactions on Geoscience and Remote Sensing. pp. 3460–3470. https://doi.org/10.1109/TGRS.2011.2124465

Ferretti, A., Prati, C., Rocca, F., 2001. Permanent scatterers in SAR interferometry. IEEE Transactions on Geoscience and Remote Sensing 39, 8–20. https://doi.org/10.1109/36.898661

Finnegan, N.J., Broudy, K.N., Nereson, A.L., Roering, J.J., Alexander, L., Bennett, G., 2019. River Channel Width Controls Blocking by Slow Landslides in California's Franciscan Mélange. Earth Surface Dynamics 7, 879–894. https://doi.org/10.5194/esurf-7-879-2019

Flanagan, D.C., Gilley, J.E., Franti, T.G., 2007. Water Erosion Prediction Project (WEPP): Development history, model capabilities, and future enhancements. Transactions of the ASABE 50, 1603–1612.

Flight, L., Julious, S.A., 2015. The disagreeable behaviour of the kappa statistic. Pharmaceutical Statistics 14, 74–78. https://doi.org/10.1002/pst.1659

Fuller, I.C., Riedler, R.A., Bell, R., Marden, M., Glade, T., 2016. Landslide-driven erosion and slope-channel coupling in steep, forested terrain, Ruahine Ranges, New Zealand, 1946-2011. Catena 142, 252–268. https://doi.org/10.1016/j.catena.2016.03.019

Gaddes, M., Hooper, A., Albino, F., 2021. Simultaneous classification and location of deformation in SAR interferograms using deep learning.

Gardner, A.S., Moholdt, G., Scambos, T., Fahnstock, M., Ligtenberg, S., van den Broeke, M., Nilsson, J., 2018. Increased West Antarctic and unchanged East Antarctic ice discharge over the last 7 years. The Cryosphere 12, 521–547. https://doi.org/10.5194/tc-12-521-2018

Ghestem, M., Sidle, R.C., Stokes, A., 2011. The Influence of Plant Root Systems on Subsurface Flow: Implications for Slope Stability. BioScience 61, 869–879. https://doi.org/10.1525/bio.2011.61.11.6

Gil, Y., David, C.H., Demir, I., Essawy, B.T., Fulweiler, R.W., Goodall, J.L., Karlstrom, L., Lee, H., Mills, H.J., Oh, J.-H., Pierce, S.A., Pope, A., Tzeng, M.W., Villamizar, S.R., Yu, X., 2016. Toward the Geoscience Paper of the Future: Best practices for documenting and sharing research from data to software to provenance. Earth and Space Science 3, 388–415. https://doi.org/10.1002/2015EA000136

Gillon, M., 1992. Landslide Stabilisation at the Clyde Power Project: A Major Geotechnical Undertaking. New Zealand Engineering 47, 27–29. https://doi.org/10.3316/informit.881042394121088

Glade, T., 2003. Landslide occurrence as a response to land use change: A review of evidence from New Zealand. Catena 51, 297–314. https://doi.org/10.1016/S0341-8162(02)00170-4

Gorelick, N., Hancher, M., Dixon, M., Ilyushchenko, S., Thau, D., Moore, R., 2017. Google Earth Engine: Planetary-scale geospatial analysis for everyone. Remote Sensing of Environment 202, 18–27. https://doi.org/10.1016/j.rse.2017.06.031

Gorsevski, P.V., Brown, M.K., Panter, K., Onasch, C.M., Simic, A., Snyder, J., 2016. Landslide detection and susceptibility mapping using LiDAR and an artificial neural network approach: a case study in the Cuyahoga Valley National Park, Ohio. Landslides 13, 467–484. https://doi.org/10.1007/s10346-015-0587-0

Grosser, A., Greenwood, J., Wong, M., Albrecht, B., Schwagler, C., Kurle, M., 2020. Stabilization of a Large Landslide Impacting Highway 73 in the Missouri River Badlands 80–95. https://doi.org/10.1061/9780784482797.009

Guzzetti, F., 2000. Landslide fatalities and the evaluation of landslide risk in Italy. Engineering Geology 58, 89–107. https://doi.org/10.1016/S0013-7952(00)00047-8

Guzzetti, F., Ardizzone, F., Cardinali, M., Rossi, M., Valigi, D., 2009. Landslide volumes and landslide mobilization rates in Umbria, central Italy. Earth and Planetary Science Letters 279, 222–229. https://doi.org/10.1016/j.epsl.2009.01.005

Guzzetti, F., Carrara, A., Cardinali, M., Reichenbach, P., 1999. Landslide hazard evaluation: A review of current techniques and their application in a multi-scale study, Central Italy, in: Geomorphology. pp. 181–216. https://doi.org/10.1016/S0169-555X(99)00078-1

Guzzetti, F., Mondini, A.C., Cardinali, M., Fiorucci, F., Santangelo, M., Chang, K.T., 2012. Landslide inventory maps: New tools for an old problem, Earth-Science Reviews. https://doi.org/10.1016/j.earscirev.2012.02.001

Guzzetti, F., Reichenbach, P., Cardinali, M., Galli, M., Ardizzone, F., 2005. Probabilistic landslide hazard assessment at the basin scale. Geomorphology 72, 272–299. https://doi.org/10.1016/j.geomorph.2005.06.002

Haghighi, M.H., Motagh, M., 2017. Sentinel-1 InSAR over Germany: Large-scale interferometry, atmospheric effects, and ground deformation mapping. ZFV - Zeitschrift fur Geodasie, Geoinformation und Landmanagement 142, 245–256. https://doi.org/10.12902/zfv-0174-2017

Hancox, G.T., 2008. The 1979 Abbotsford Landslide, Dunedin, New Zealand: a retrospective look at its nature and causes. Landslides 5, 177–188. https://doi.org/10.1007/s10346-007-0097-9

Handwerger, A.L., Booth, A.M., Huang, M.-H., Fielding, E.J., 2021. Inferring the Subsurface Geometry and Strength of Slow-Moving Landslides Using 3-D Velocity Measurements From the NASA/JPL UAVSAR. Journal of Geophysical Research: Earth Surface 126, e2020JF005898. https://doi.org/10.1029/2020JF005898

Handwerger, A.L., Fielding, E.J., Huang, M.-H., Bennett, G.L., Liang, C., Schulz, W.H., 2019a. Widespread Initiation, Reactivation, and Acceleration of Landslides in the

Northern California Coast Ranges due to Extreme Rainfall. Journal of Geophysical Research: Earth Surface 124, 1782–1797. https://doi.org/10.1029/2019JF005035
Handwerger, A.L., Huang, M.-H., Fielding, E.J., Booth, A.M., Bürgmann, R., 2019b. A shift from drought to extreme rainfall drives a stable landslide to catastrophic failure. Scientific Reports 9, 1569. https://doi.org/10.1038/s41598-018-38300-0
Handwerger, A.L., Huang, M.-H., Jones, S.Y., Amatya, P., Kerner, H.R., Kirschbaum, D.B., 2022. Generating landslide density heatmaps for rapid detection using open-access satellite radar data in Google Earth Engine. Natural Hazards and Earth System Sciences 22, 753–773. https://doi.org/10.5194/nhess-22-753-2022
Harris, C.R., Millman, K.J., van der Walt, S.J., Gommers, R., Virtanen, P., Cournapeau, D., Wieser, E., Taylor, J., Berg, S., Smith, N.J., Kern, R., Picus, M., Hoyer, S., van Kerkwijk, M.H., Brett, M., Haldane, A., del Río, J.F., Wiebe, M., Peterson, P., Gérard-Marchant, P., Sheppard, K., Reddy, T., Weckesser, W., Abbasi, H., Gohlke, C., Oliphant, T.E., 2020. Array programming with NumPy. Nature 585, 357–362. https://doi.org/10.1038/s41586-020-2649-2
Harshburger, B.J., Humes, K.S., Walden, V.P., Blandford, T.R., Moore, B.C., Dezzani, R.J., 2010. Spatial interpolation of snow water equivalency using surface observations and remotely sensed images of snow-covered area. Hydrological Processes 24, 1285–1295. https://doi.org/10.1002/hyp.7590
He, K., Li, X., Yan, X., Guo, D., 2008. The landslides in the Three Gorges Reservoir Region, China and the effects of water storage and rain on their stability. Environmental Geology 55, 55–63.
Heckmann, T., Gegg, K., Gegg, A., Becht, M., 2014. Sample size matters: Investigating the effect of sample size on a logistic regression susceptibility model for debris flows. Natural Hazards and Earth System Sciences 14, 259–278. https://doi.org/10.5194/nhess-14-259-2014
Heckmann, T., Schwanghart, W., 2013. Geomorphic coupling and sediment connectivity in an alpine catchment — Exploring sediment cascades using graph theory. Geomorphology 182, 89–103. https://doi.org/10.1016/j.geomorph.2012.10.033
Heid, T., Kääb, A., 2012. Evaluation of existing image matching methods for deriving glacier surface displacements globally from optical satellite imagery. Remote Sensing of Environment 118, 339–355. https://doi.org/10.1016/j.rse.2011.11.024
Hervás, J., Barredo, J.I., Rosin, P.L., Pasuto, A., Mantovani, F., Silvano, S., 2003. Monitoring landslides from optical remotely sensed imagery: the case history of Tessina landslide, Italy. Geomorphology, Studies on Large Volume Landslides 54, 63–75. https://doi.org/10.1016/S0169-555X(03)00056-4
Highland, L., Bobrowsky, P., 2008. USGS Circular 1325: The Landslide Handbook—A Guide to Understanding Landslides.
Hinderer, M., 2012. From gullies to mountain belts: A review of sediment budgets at various scales, Sedimentary Geology. https://doi.org/10.1016/j.sedgeo.2012.03.009
Hogenson, K., Arko, S.A., Buechler, B., Hogenson, R., Herrmann, J., Geiger, A., 2016. Hybrid Pluggable Processing Pipeline (HyP3): A cloud-based infrastructure for generic processing of SAR data 2016, IN21B-1740.
Hölbling, D., Betts, H., Spiekermann, R., Phillips, C., 2016. Identifying spatio-temporal landslide hotspots on North Island, New Zealand, by analyzing historical and recent aerial photography. Geosciences (Switzerland) 6. https://doi.org/10.3390/geosciences6040048
Hölbling, D., Füreder, P., Antolini, F., Cigna, F., Casagli, N., Lang, S., 2012. A semi-automated object-based approach for landslide detection validated by persistent

scatterer interferometry measures and landslide inventories. Remote Sensing 4, 1310–1336. https://doi.org/10.3390/rs4051310
Holdsworth, C.N., 2018. The influence of rainfall and river incision on the movement rate of a slow-moving, soft-rock landslide in the Rangitikei, New Zealand : a thesis presented in partial fulfilment of the requirements for the degree of Master of Science in Physical Geography at Massey University, Manawatu Campus, Palmerston North, New Zealand (Thesis). Massey University.
Holmgren, P., 1994. Multiple flow direction algorithms for runoff modelling in grid based elevation models: An empirical evaluation. Hydrological Processes 8, 327–334. https://doi.org/10.1002/hyp.3360080405
Hooper, A., Bekaert, D., Spaans, K., Arıkan, M., 2012. Recent advances in SAR interferometry time series analysis for measuring crustal deformation. Tectonophysics 514–517, 1–13. https://doi.org/10.1016/j.tecto.2011.10.013
Horn, B.K.P., 1981. Hill shading and the reflectance map. Proceedings of the IEEE 69, 14–47. https://doi.org/10.1109/PROC.1981.11918
Horrey, P., Punt, A., Kruas, C., Carson, D., n.d. Landslide Risk Management, Te Ore Ore Slip, State Highway 4 – New Zealand Geotechnical Society. URL https://www.nzgs.org/library/landslide-risk-management-te-ore-ore-slip-state-highway-4/ (accessed 8.14.22).
Hu, X., Bürgmann, R., Fielding, E.J., Lee, H., 2020a. Internal kinematics of the Slumgullion landslide (USA) from high-resolution UAVSAR InSAR data. Remote Sensing of Environment 251, 112057. https://doi.org/10.1016/j.rse.2020.112057
Hu, X., Bürgmann, R., Schulz, W.H., Fielding, E.J., 2020b. Four-dimensional surface motions of the Slumgullion landslide and quantification of hydrometeorological forcing. Nature Communications 11, 1–9. https://doi.org/10.1038/s41467-020-16617-7
Hua, Y., Wang, X., Li, Y., Xu, P., Xia, W., 2020. Dynamic development of landslide susceptibility based on slope unit and deep neural networks. Landslides. https://doi.org/10.1007/s10346-020-01444-0
Huang, Q., Wang, C., Meng, Y., Chen, J., Yue, A., 2019. Landslide Monitoring Using Change Detection in Multitemporal Optical Imagery. IEEE Geoscience and Remote Sensing Letters 1–5. https://doi.org/10.1109/lgrs.2019.2918254
Hungr, O., Evans, S., Hazzard, J., 1999. Magnitude and frequency of rock falls and rock slides along the main transportation corridors of southwestern British Columbia. Can. Geotech. J. 36, 224–238. https://doi.org/10.1139/t98-106
Hungr, O., Leroueil, S., Picarelli, L., 2014. The Varnes classification of landslide types, an update. Landslides 11. https://doi.org/10.1007/s10346-013-0436-y
Hutchinson, J.N., 1969. A Reconsideration of the Coastal Landslides at Folkestone Warren, Kent. Géotechnique 19, 6–38. https://doi.org/10.1680/geot.1969.19.1.6
Iverson, R.M., 2000. Landslide triggering by rain infiltration. Water Resources Research 36, 1897–1910. https://doi.org/10.1029/2000WR900090
James, L.A., Hodgson, M.E., Ghoshal, S., Latiolais, M.M., 2012. Geomorphic change detection using historic maps and DEM differencing: The temporal dimension of geospatial analysis. Geomorphology 137, 181–198. https://doi.org/10.1016/j.geomorph.2010.10.039
Johnson, B.G., Smith, J.A., Diemer, J.A., 2017. A chronology of post-glacial landslides suggests that slight increases in precipitation could trigger a disproportionate geomorphic response. Earth Surface Processes and Landforms 42, 2223–2239. https://doi.org/10.1002/esp.4168

Jolivet, R., Grandin, R., Lasserre, C., Doin, M.P., Peltzer, G., 2011. Systematic InSAR tropospheric phase delay corrections from global meteorological reanalysis data. Geophysical Research Letters 38. https://doi.org/10.1029/2011GL048757
Jomard, H., Lebourg, T., Guglielmi, Y., 2014. Morphological analysis of deep-seated gravitational slope deformation (DSGSD) in the western part of the Argentera massif. A morpho-tectonic control? Landslides 11, 107–117. https://doi.org/10.1007/s10346-013-0434-0
Jones, J.I., Murphy, J.F., Collins, A.L., Sear, D.A., Naden, P.S., Armitage, P.D., 2012. The Impact of Fine Sediment on Macro-Invertebrates. River Research and Applications 28, 1055–1071. https://doi.org/10.1002/rra.1516
Joyce, K.E., Belliss, S.E., Samsonov, S.V., McNeill, S.J., Glassey, P.J., 2009. A review of the status of satellite remote sensing and image processing techniques for mapping natural hazards and disasters. Progress in Physical Geography: Earth and Environment 33, 183–207. https://doi.org/10.1177/0309133309339563
Jung, J., Yun, S.-H., 2020. Evaluation of Coherent and Incoherent Landslide Detection Methods Based on Synthetic Aperture Radar for Rapid Response: A Case Study for the 2018 Hokkaido Landslides. Remote Sensing 12, 265. https://doi.org/10.3390/rs12020265
Kang, Y., Lu, Z., Zhao, C., Xu, Y., Kim, J., Gallegos, A.J., 2021. InSAR monitoring of creeping landslides in mountainous regions: A case study in Eldorado National Forest, California. Remote Sensing of Environment 258, 112400. https://doi.org/10.1016/j.rse.2021.112400
Kankaku, Y., Suzuki, S., Osawa, Y., 2013. ALOS-2 mission and development status, in: 2013 IEEE International Geoscience and Remote Sensing Symposium - IGARSS. Presented at the 2013 IEEE International Geoscience and Remote Sensing Symposium - IGARSS, pp. 2396–2399. https://doi.org/10.1109/IGARSS.2013.6723302
Klimeš, J., Rowberry, M.D., Blahůt, J., Briestenský, M., Hartvich, F., Košťák, B., Rybář, J., Stemberk, J., Štěpančíková, P., 2012. The monitoring of slow-moving landslides and assessment of stabilisation measures using an optical–mechanical crack gauge. Landslides 9, 407–415. https://doi.org/10.1007/s10346-011-0306-4
Kluyver, T., Ragan-Kelley, B., Pérez, F., Granger, B.E., Bussonnier, M., Frederic, J., Kelley, K., Hamrick, J.B., Grout, J., Corlay, S., 2016. Jupyter Notebooks-a publishing format for reproducible computational workflows.
Korup, O., 2008. Rock type leaves topographic signature in landslide-dominated mountain ranges. Geophysical Research Letters 35. https://doi.org/10.1029/2008GL034157
Korup, O., 2006. Rock-slope failure and the river long profile. Geology 34, 45–48. https://doi.org/10.1130/G21959.1
Korup, O., 2005. Geomorphic imprint of landslides on alpine river systems, southwest New Zealand. Earth Surface Processes and Landforms 30, 783–800. https://doi.org/10.1002/esp.1171
Korup, O., 2004. Landslide-induced river channel avulsions in mountain catchments of southwest New Zealand. Geomorphology 63, 57–80. https://doi.org/10.1016/j.geomorph.2004.03.005
Korup, O., Clague, J.J., Hermanns, R.L., Hewitt, K., Strom, A.L., Weidinger, J.T., 2007. Giant landslides, topography, and erosion. Earth and Planetary Science Letters 261, 578–589. https://doi.org/10.1016/j.epsl.2007.07.025
Korup, O., Densmore, A.L., Schlunegger, F., 2010. The role of landslides in mountain range evolution. Geomorphology, Landslide geomorphology in a changing environment 120, 77–90. https://doi.org/10.1016/j.geomorph.2009.09.017

Korup, O., Weidinger, J.T., 2011. Rock type, precipitation, and the steepness of Himalayan threshold hillslopes. Geological Society Special Publication 353, 235–249. https://doi.org/10.1144/SP353.12

Kuehl, S.A., Alexander, C.R., Blair, N.E., Harris, C.K., Marsaglia, K.M., Ogston, A.S., Orpin, A.R., Roering, J.J., Bever, A.J., Bilderback, E.L., Carter, L., Cerovski-Darriau, C., Childress, L.B., Reide Corbett, D., Hale, R.P., Leithold, E.L., Litchfield, N., Moriarty, J.M., Page, M.J., Pierce, L.E.R., Upton, P., Walsh, J.P., 2016. A source-to-sink perspective of the Waipaoa River margin. Earth-Science Reviews 153, 301–334. https://doi.org/10.1016/j.earscirev.2015.10.001

LaHusen, S.R., Duvall, A.R., Booth, A.M., Grant, A., Mishkin, B.A., Montgomery, D.R., Struble, W., Roering, J.J., Wartman, J., 2020. Rainfall triggers more deep-seated landslides than Cascadia earthquakes in the Oregon Coast Range, USA. Science Advances 6, eaba6790. https://doi.org/10.1126/sciadv.aba6790

Lanari, R., Mora, O., Manunta, M., Mallorqui, J.J., Berardino, P., Sansosti, E., 2004. A small-baseline approach for investigating deformations on full-resolution differential SAR interferograms. IEEE Transactions on Geoscience and Remote Sensing 42, 1377–1386. https://doi.org/10.1109/TGRS.2004.828196

Lane, S.N., Westaway, R.M., Murray Hicks, D., 2003. Estimation of erosion and deposition volumes in a large, gravel-bed, braided river using synoptic remote sensing. Earth Surface Processes and Landforms 28, 249–271. https://doi.org/10.1002/esp.483

Larsen, I.J., Montgomery, D.R., 2012. Landslide erosion coupled to tectonics and river incision. Nature Geoscience 5, 468–473. https://doi.org/10.1038/ngeo1479

Larsen, I.J., Montgomery, D.R., Korup, O., 2010. Landslide erosion controlled by hillslope material. Nature Geoscience 3, 247–251. https://doi.org/10.1038/ngeo776

Lee, J.-S., Hoppel, K.W., Mango, S.A., Miller, A.R., 1994. Intensity and phase statistics of multilook polarimetric and interferometric SAR imagery. IEEE Transactions on Geoscience and Remote Sensing 32, 1017–1028. https://doi.org/10.1109/36.312890

Lees, J.M., 2012. Open and Free: Software and Scientific Reproducibility. Seismological Research Letters 83, 751–752. https://doi.org/10.1785/0220120091

Lei, Y., Gardner, A., Agram, P., 2021. Autonomous Repeat Image Feature Tracking (autoRIFT) and Its Application for Tracking Ice Displacement. Remote Sensing 13, 749. https://doi.org/10.3390/rs13040749

Leprince, S., Ayoub, F., Klinger, Y., Avouac, J., 2007. Co-Registration of Optically Sensed Images and Correlation (COSI-Corr): an operational methodology for ground deformation measurements, in: 2007 IEEE International Geoscience and Remote Sensing Symposium. Presented at the 2007 IEEE International Geoscience and Remote Sensing Symposium, pp. 1943–1946. https://doi.org/10.1109/IGARSS.2007.4423207

Li, M., Zhang, L., Ding, C., Li, W., Luo, H., Liao, M., Xu, Q., 2020. Retrieval of historical surface displacements of the Baige landslide from time-series SAR observations for retrospective analysis of the collapse event. Remote Sensing of Environment 240, 111695. https://doi.org/10.1016/j.rse.2020.111695

Li, X., Cheng, X., Chen, W., Chen, G., Liu, S., 2015. Identification of forested landslides using lidar data, object-based image analysis, and machine learning algorithms. Remote Sensing 7, 9705–9726. https://doi.org/10.3390/rs70809705

Lin, L.I.-K., 1989. A Concordance Correlation Coefficient to Evaluate Reproducibility. Biometrics 45, 255–268. https://doi.org/10.2307/2532051

Litchfield, N., Berryman, K., 2006. Relations between postglacial fluvial incision rates and uplift rates in the North Island, New Zealand. Journal of Geophysical Research: Earth Surface 111. https://doi.org/10.1029/2005JF000374

Lo, C.-M., Huang, W.-K., Lin, M.-L., 2016. Earthquake-induced deep-seated landslide and landscape evolution process at Hungtsaiping, Nantou County, Taiwan. Environ Earth Sci 75, 645. https://doi.org/10.1007/s12665-016-5474-z

Löbmann, M.T., Geitner, C., Wellstein, C., Zerbe, S., 2020. The influence of herbaceous vegetation on slope stability – A review. Earth-Science Reviews 209, 103328. https://doi.org/10.1016/j.earscirev.2020.103328

Loche, M., Lombardo, L., Gorum, T., Tanyas, H., Scaringi, G., 2022. Distinct Susceptibility Patterns of Active and Relict Landslides Reveal Distinct Triggers: A Case in Northwestern Turkey. Remote Sensing 14, 1321. https://doi.org/10.3390/rs14061321

Lombardo, L., Mai, P.M., 2018. Presenting logistic regression-based landslide susceptibility results. Engineering Geology 244, 14–24. https://doi.org/10.1016/j.enggeo.2018.07.019

López-Quiroz, P., Doin, M.-P., Tupin, F., Briole, P., Nicolas, J.-M., 2009. Time series analysis of Mexico City subsidence constrained by radar interferometry. Journal of Applied Geophysics, Advances in SAR Interferometry from the 2007 Fringe Workshop 69, 1–15. https://doi.org/10.1016/j.jappgeo.2009.02.006

Lu, P., Stumpf, A., Kerle, N., Casagli, N., 2011. Object-oriented change detection for landslide rapid mapping. IEEE Geoscience and Remote Sensing Letters 8, 701–705. https://doi.org/10.1109/LGRS.2010.2101045

Lucchitta, B.K., Ferguson, H.M., 1986. Antarctica: Measuring Glacier Velocity from Satellite Images. Science 234, 1105–1108. https://doi.org/10.1126/science.234.4780.1105

MacDonald, D.D., Ingersoll, C.G., Berger, T.A., 2000. Development and Evaluation of Consensus-Based Sediment Quality Guidelines for Freshwater Ecosystems. Arch. Environ. Contam. Toxicol. 39, 20–31. https://doi.org/10.1007/s002440010075

Mackey, B.H., Roering, J.J., 2011. Sediment yield, spatial characteristics, and the long-term evolution of active earthflows determined from airborne LiDAR and historical aerial photographs, Eel River, California. Bulletin of the Geological Society of America 123, 1560–1576. https://doi.org/10.1130/B30306.1

Malamud, B.D., Turcotte, D.L., Guzzetti, F., Reichenbach, P., 2004. Landslide inventories and their statistical properties. Earth Surface Processes and Landforms 29, 687–711. https://doi.org/10.1002/esp.1064

Mantovani, M., Bossi, G., Marcato, G., Schenato, L., Tedesco, G., Titti, G., Pasuto, A., 2019. New perspectives in landslide displacement detection using Sentinel-1 datasets. Remote Sensing 11. https://doi.org/10.3390/rs11182135

Marden, M., Arnold, G., Seymour, A., Hambling, R., 2012. History and distribution of steepland gullies in response to land use change, East Coast Region, North Island, New Zealand. Geomorphology 153–154, 81–90. https://doi.org/10.1016/j.geomorph.2012.02.011

Martinis, S., Kersten, J., Twele, A., 2015. A fully automated TerraSAR-X based flood service. ISPRS Journal of Photogrammetry and Remote Sensing 104, 203–212. https://doi.org/10.1016/j.isprsjprs.2014.07.014

Massey, C., Townsend, D., Rathje, E., Allstadt, K.E., Lukovic, B., Kaneko, Y., Bradley, B., Wartman, J., Jibson, R.W., Petley, D.N., Horspool, N., Hamling, I., Carey, J., Cox, S., Davidson, J., Dellow, S., Godt, J.W., Holden, C., Jones, K., Kaiser, A., Little, M., Lyndsell, B., McColl, S., Morgenstern, R., Rengers, F.K., Rhoades, D., Rosser, B., Strong, D., Singeisen, C., Villeneuve, M., 2018. Landslides Triggered by the 14 November 2016 Mw 7.8 Kaikōura Earthquake, New Zealand. Bulletin of the Seismological Society of America 108, 1630–1648. https://doi.org/10.1785/0120170305

Massey, C.I., 2010. The dynamics of reactivated landslides : Utiku and Taihape, North Island, New Zealand (PhD Thesis). Durham University.
Massey, C.I., Abbott, E., McSaveney, M., Petley, D.N., Richards, L., 2016a. Earthquake-induced displacement is insignificant in the reactivated Utiku landslide, New Zealand, in: Landslides and Engineered Slopes. Experience, Theory and Practice. pp. 31–52. https://doi.org/10.1201/b21520-5
Massey, C.I., Petley, D.N., McSaveney, M.J., 2013. Patterns of movement in reactivated landslides. Engineering Geology 159, 1–19. https://doi.org/10.1016/j.enggeo.2013.03.011
Massey, C.I., Petley, D.N., McSaveney, M.J., Archibald, G., 2016b. Basal sliding and plastic deformation of a slow, reactivated landslide in New Zealand. Engineering Geology 208, 11–28. https://doi.org/10.1016/j.enggeo.2016.04.016
Massonnet, D., Feigl, K.L., 1998. Radar interferometry and its application to changes in the earth's surface. Reviews of Geophysics 36, 441–500. https://doi.org/10.1029/97RG03139
McColl, S., McCabe, M., 2016. The causes and agricultural impacts of large translational landslides: Case-studies from North Island, New Zealand, in: Landslides and Engineered Slopes. Experience, Theory and Practice. pp. 1401–1408. https://doi.org/10.1201/b21520-172
McColl, S.T., Holdsworth, C.N., Fuller, I.C., Todd, M., Williams, F., 2022. Disproportionate and chronic sediment delivery from a fluvially controlled, deep-seated landslide in Aotearoa New Zealand. Earth Surf Processes Landf 47, 1972–1988. https://doi.org/10.1002/esp.5358
McGlone, M.S., 1989. The Polynesian settlement of New Zealand in relation to environmental and biotic changes. New Zealand Journal of Ecology 12, 115–129.
McGovern, S., Brook, M.S., Cave, M., 2021. Geomorphology and triggering mechanism of a river-damming block slide: February 2018 Mangapoike landslide, New Zealand. Landslides 18, 1087–1095. https://doi.org/10.1007/s10346-020-01572-7
McSaveney, M.J., Massey, C.I., 2017. Inadvertent Engineered Activation of Utiku Landslide, New Zealand, in: Advancing Culture of Living with Landslides. Springer International Publishing, pp. 563–568. https://doi.org/10.1007/978-3-319-53487-9_66
Merghadi, A., Yunus, A.P., Dou, J., Whiteley, J., ThaiPham, B., Bui, D.T., Avtar, R., Abderrahmane, B., 2020. Machine learning methods for landslide susceptibility studies: A comparative overview of algorithm performance. Earth-Science Reviews 207, 103225. https://doi.org/10.1016/j.earscirev.2020.103225
Meunier, P., Hovius, N., Haines, J.A., 2008. Topographic site effects and the location of earthquake induced landslides. Earth and Planetary Science Letters 275, 221–232. https://doi.org/10.1016/j.epsl.2008.07.020
Miao, H., Wang, G., Yin, K., Kamai, T., Li, Y., 2014. Mechanism of the slow-moving landslides in Jurassic red-strata in the Three Gorges Reservoir, China. Engineering Geology 171, 59–69. https://doi.org/10.1016/j.enggeo.2013.12.017
Micheletti, N., Foresti, L., Robert, S., Leuenberger, M., Pedrazzini, A., Jaboyedoff, M., Kanevski, M., 2014. Machine Learning Feature Selection Methods for Landslide Susceptibility Mapping. Mathematical Geosciences 46, 33–57. https://doi.org/10.1007/s11004-013-9511-0
Michelsen, O., McDevitt, J.E., Coelho, C.R.V., 2014. A comparison of three methods to assess land use impacts on biodiversity in a case study of forestry plantations in New Zealand. Int J Life Cycle Assess 19, 1214–1225. https://doi.org/10.1007/s11367-014-0742-1

Ministry for the Environment, 2020. National Policy Statement for Freshwater Management 2020 (Governmental Report). Wellington, New Zealand.
Mondini, A.C., 2017. Measures of spatial autocorrelation changes in multitemporal SAR images for event landslides detection. Remote Sensing 9. https://doi.org/10.3390/rs9060554
Mountjoy, J., 2005. Rock mass defect controlled deep-seated landslides in Tertiary soft rock terrain: implications for landscape evolution.
Mountjoy, J., Pettinga, J.R., 2006. Controls on Large Deep-seated Landslides in Soft Rock Terrain: Rock Mass Defects and Seismic Triggering. Earthquakes and Urban Development : New Zealand Geotechnical Society 2006 Symposium, Nelson, February 2006 385.
Mulas, M., Ciccarese, G., Truffelli, G., Corsini, A., 2020. Integration of Digital Image Correlation of Sentinel-2 Data and Continuous GNSS for Long-Term Slope Movements Monitoring in Moderately Rapid Landslides. Remote Sensing 12, 2605. https://doi.org/10.3390/rs12162605
Neverman, A.J., Fuller, I.C., Procter, J.N., 2016. Application of Geomorphic Change Detection (GCD) to quantify morphological budgeting error in a New Zealand gravel-bed river: a case study from the Makaroro River, Hawke's Bay. Journal of Hydrology (New Zealand) 55, 45–63.
Nichol, J., Man, S.W., Shaker, A., 2009. Application of high-resolution satellite images to detailed landslide hazard assessment, in: 2009 Joint Urban Remote Sensing Event. https://doi.org/10.1109/URS.2009.5137737
Nilsen, T.H., Brabb, E.E., 1977. Slope stability studies in the San Francisco Bay region, California. Geol. Soc. Am. Rev. Eng. Geol 3, 235–243.
Nosek, B.A., Alter, G., Banks, G.C., Borsboom, D., Bowman, S.D., Breckler, S.J., Buck, S., Chambers, C.D., Chin, G., Christensen, G., Contestabile, M., Dafoe, A., Eich, E., Freese, J., Glennerster, R., Goroff, D., Green, D.P., Hesse, B., Humphreys, M., Ishiyama, J., Karlan, D., Kraut, A., Lupia, A., Mabry, P., Madon, T., Malhotra, N., Mayo-Wilson, E., McNutt, M., Miguel, E., Paluck, E.L., Simonsohn, U., Soderberg, C., Spellman, B.A., Turitto, J., VandenBos, G., Vazire, S., Wagenmakers, E.J., Wilson, R., Yarkoni, T., 2015. Promoting an open research culture. Science. https://doi.org/10.1126/science.aab2374
Notti, D., Herrera, G., Bianchini, S., Meisina, C., García-Davalillo, J.C., Zucca, F., 2014. A methodology for improving landslide PSI data analysis. International Journal of Remote Sensing 35, 2186–2214. https://doi.org/10.1080/01431161.2014.889864
Nunes, F.C., Delunel, R., Schlunegger, F., Akçar, N., Kubik, P.W., 2015. Bedrock bedding, landsliding and erosional budgets in the Central European Alps. Terra Nova 27, 370–378. https://doi.org/10.1111/ter.12169
Osmanoğlu, B., Sunar, F., Wdowinski, S., Cabral-Cano, E., 2016. Time series analysis of InSAR data: Methods and trends. ISPRS Journal of Photogrammetry and Remote Sensing 115, 90–102. https://doi.org/10.1016/j.isprsjprs.2015.10.003
Owens, P.N., 2020. Soil erosion and sediment dynamics in the Anthropocene: a review of human impacts during a period of rapid global environmental change. J Soils Sediments 20, 4115–4143. https://doi.org/10.1007/s11368-020-02815-9
Page, M.J., Reid, L.M., Lynn, I.H., 1999. Sediment production from Cyclone Bola landslides, Waipaoa catchment. Journal of Hydrology (New Zealand) 38, 289–308.
Pánek, T., 2019. Landslides and Quaternary climate changes—The state of the art. Earth-Science Reviews 196, 102871. https://doi.org/10.1016/j.earscirev.2019.05.015

Pánek, T., Klimeš, J., 2016. Temporal behavior of deep-seated gravitational slope deformations: A review, Earth-Science Reviews. Elsevier B.V. https://doi.org/10.1016/j.earscirev.2016.02.007

Parker, R.N., Densmore, A.L., Rosser, N.J., De Michele, M., Li, Y., Huang, R., Whadcoat, S., Petley, D.N., 2011. Mass wasting triggered by the 2008 Wenchuan earthquake is greater than orogenic growth. Nature Geoscience 4, 449–452. https://doi.org/10.1038/ngeo1154

Parker, R.N., Hancox, G.T., Petley, D.N., Massey, C.I., Densmore, A.L., Rosser, N.J., 2015. Spatial distributions of earthquake-induced landslides and hillslope preconditioning in the northwest South Island, New Zealand. Earth Surface Dynamics 3, 501–525. https://doi.org/10.5194/esurf-3-501-2015

Peruccacci, S., Brunetti, M.T., Luciani, S., Vennari, C., Guzzetti, F., 2012. Lithological and seasonal control on rainfall thresholds for the possible initiation of landslides in central Italy. Geomorphology 139–140, 79–90. https://doi.org/10.1016/j.geomorph.2011.10.005

Petley, D., 2011. Hillslopes, in: The SAGE Handbook of Geomorphology. SAGE Publications Inc., pp. 343–358. https://doi.org/10.4135/9781446201053.n20

Petley, D.N., Allison, R.J., 1997. The mechanics of deep-seated landslides. Earth Surface Processes and Landforms 22, 747–758. https://doi.org/10.1002/(SICI)1096-9837(199708)22:8<747::AID-ESP767>3.0.CO;2-#

Petley, D.N., Rosser, S.A.D.& N.J., 2005. The analysis of global landslide risk through the creation of a database of worldwide landslide fatalities, in: Landslide Risk Management. CRC Press.

Phillips, C., Hales, T., Smith, H., Basher, L., 2021. Shallow landslides and vegetation at the catchment scale: A perspective. Ecological Engineering 173, 106436. https://doi.org/10.1016/j.ecoleng.2021.106436

Pillans, B., 2017. Quaternary Stratigraphy of Whanganui Basin—A Globally Significant Archive, in: Shulmeister, J. (Ed.), Landscape and Quaternary Environmental Change in New Zealand, Atlantis Advances in Quaternary Science. Atlantis Press, Paris, pp. 141–170. https://doi.org/10.2991/978-94-6239-237-3_4

Plank, S., Singer, J., Minet, C., Thuro, K., 2012. Pre-survey suitability evaluation of the differential synthetic aperture radar interferometry method for landslide monitoring. International Journal of Remote Sensing 33, 6623–6637. https://doi.org/10.1080/01431161.2012.693646

Prabhu, N., Babu, R.V., 2015. Attribute-Graph: A Graph Based Approach to Image Ranking. Presented at the Proceedings of the IEEE International Conference on Computer Vision.

Prokešová, R., Medveďová, A., Tábořík, P., Snopková, Z., 2013. Towards hydrological triggering mechanisms of large deep-seated landslides. Landslides 10, 239–254. https://doi.org/10.1007/s10346-012-0330-z

Pulford, A., Stern, T., 2004. Pliocene exhumation and landscape evolution of central North Island, New Zealand: The role of the upper mantle. Journal of Geophysical Research: Earth Surface 109, 1–12. https://doi.org/10.1029/2003jf000046

Rattenbury, M.S., Isaac, M.J., 2012. The QMAP 1:250 000 Geological Map of New Zealand project. New Zealand Journal of Geology and Geophysics 55, 393–405. https://doi.org/10.1080/00288306.2012.725417

Rees, C., Palmer, A., Palmer, J., 2019. Litho-structural controls on Quaternary landslide distribution in the Rangitikei hill country, North Island, New Zealand. New Zealand Journal of Geology and Geophysics 1–20. https://doi.org/10.1080/00288306.2019.1629966

Reichenbach, P., Rossi, M., Malamud, B.D., Mihir, M., Guzzetti, F., 2018. A review of statistically-based landslide susceptibility models. Earth-Science Reviews 180. https://doi.org/10.1016/j.earscirev.2018.03.001
Ren, Z., Zhang, Z., Yin, J., 2017. Erosion associated with seismically-induced landslides in the middle longmen shan region, Eastern Tibetan Plateau, China. Remote Sensing 9. https://doi.org/10.3390/rs9080864
Renard, K.G., service, S.U. d'America *Department of *agriculture A. research, 1997. Predicting Soil Erosion by Water: A Guide to Conservation Planning with the Revised Universal Soil Loss Equation (RUSLE). U.S. Department of Agriculture, Agricultural Research Service.
Reyes, A.G., 2007. Petrological study of selected Taihape landslide rock samples. GNS Science Report 2007.
Richardson, B., 2011. Vegetation management practices in plantation forests of Australia and New Zealand. Canadian Journal of Forest Research. https://doi.org/10.1139/x93-250
Roering, J.J., Kirchner, J.W., Dietrich, W.E., 2005. Characterizing structural and lithologic controls on deep-seated landsliding: Implications for topographic relief and landscape evolution in the Oregon Coast Range, USA. Bulletin of the Geological Society of America 117, 654–668. https://doi.org/10.1130/B25567.1
Roering, J.J., Mackey, B.H., Handwerger, A.L., Booth, A.M., Schmidt, D.A., Bennett, G.L., Cerovski-Darriau, C., 2015. Beyond the angle of repose: A review and synthesis of landslide processes in response to rapid uplift, Eel River, Northern California. Geomorphology 236. https://doi.org/10.1016/j.geomorph.2015.02.013
Rosen, P.A., Gurrola, E.M., Agram, P.S., Sacco, G.F., Lavalle, M., 2015. The InSAR Scientific Computing Environment (ISCE): A Python Framework for Earth Science 2015, IN11C-1789.
Rosen, P.A., Hensley, S., Joughin, I.R., Li, F.K., Madsen, S.N., Rodriguez, E., Goldstein, R.M., 2000. Synthetic aperture radar interferometry. Proceedings of the IEEE 88, 333–382. https://doi.org/10.1109/5.838084
Rosenqvist, A., Shimada, M., Ito, N., Watanabe, M., 2007. ALOS PALSAR: A Pathfinder Mission for Global-Scale Monitoring of the Environment. IEEE Transactions on Geoscience and Remote Sensing 45, 3307–3316. https://doi.org/10.1109/TGRS.2007.901027
Rosser, B., Dellow, S., Haubrock, S., Glassey, P., 2017. New Zealand's National Landslide Database. Landslides 14, 1949–1959. https://doi.org/10.1007/s10346-017-0843-6
Rouet-Leduc, B., Jolivet, R., Dalaison, M., Johnson, P.A., Hulbert, C., 2021. Autonomous extraction of millimeter-scale deformation in InSAR time series using deep learning. Nat Commun 12, 6480. https://doi.org/10.1038/s41467-021-26254-3
Ruggeri, P., Fruzzetti, V.M.E., Vita, A., Paternesi, A., Scarpelli, G., Segato, D., 2016. Deep-seated landslide triggered by tunnel excavation, in: Landslides and Engineered Slopes. Experience, Theory and Practice. CRC Press.
Samsonov, S., Dille, A., Dewitte, O., Kervyn, F., D'Oreye, N., 2020. Satellite interferometry for mapping surface deformation time series in one, two and three dimensions: A new method illustrated on a slow-moving landslide. Engineering Geology 266, 105471. https://doi.org/10.1016/j.enggeo.2019.105471
Santangelo, M., Marchesini, I., Cardinali, M., Fiorucci, F., Rossi, M., Bucci, F., Guzzetti, F., 2015. A method for the assessment of the influence of bedding on landslide abundance and types. Landslides 12, 295–309. https://doi.org/10.1007/s10346-014-0485-x
Schaefer, L.N., Di Traglia, F., Chaussard, E., Lu, Z., Nolesini, T., Casagli, N., 2019. Monitoring volcano slope instability with Synthetic Aperture Radar: A review and

new data from Pacaya (Guatemala) and Stromboli (Italy) volcanoes. Earth-Science Reviews 192, 236–257. https://doi.org/10.1016/j.earscirev.2019.03.009
Schmitt, R.G., Tanyas, H., Nowicki Jessee, M.A., Zhu, J., Biegel, K.M., Allstadt, K.E., Jibson, R.W., Thompson, E.M., van Westen, C.J., Sato, H.P., Wald, D.J., Godt, J.W., Gorum, T., Xu, C., Rathje, E.M., Knudsen, K.L., 2017. An open repository of earthquake-triggered ground-failure inventories (USGS Numbered Series No. 1064), An open repository of earthquake-triggered ground-failure inventories, Data Series. U.S. Geological Survey, Reston, VA. https://doi.org/10.3133/ds1064
Schuster, R.L., Fleming, R.W., 1986. Economic Losses and Fatalities Due to Landslides. Environmental & Engineering Geoscience xxiii, 11–28. https://doi.org/10.2113/gseegeosci.xxiii.1.11
Schuster, R.L., Highland, L., 2001. Socioeconomic and environmental impacts of landslides in the western hemisphere. Citeseer.
Šegina, E., Peternel, T., Urbančič, T., Realini, E., Zupan, M., Jež, J., Caldera, S., Gatti, A., Tagliaferro, G., Consoli, A., González, J.R., Auflič, M.J., 2020. Monitoring Surface Displacement of a Deep-Seated Landslide by a Low-Cost and near Real-Time GNSS System. Remote Sensing 12, 3375. https://doi.org/10.3390/rs12203375
Sepúlveda, S.A., Murphy, W., Jibson, R.W., Petley, D.N., 2005. Seismically induced rock slope failures resulting from topographic amplification of strong ground motions: The case of Pacoima Canyon, California. Engineering Geology 80, 336–348. https://doi.org/10.1016/j.enggeo.2005.07.004
Serey, A., Piñero-Feliciangeli, L., Sepúlveda, S.A., Poblete, F., Petley, D.N., Murphy, W., 2019. Landslides induced by the 2010 Chile megathrust earthquake: a comprehensive inventory and correlations with geological and seismic factors. Landslides 16, 1153–1165. https://doi.org/10.1007/s10346-019-01150-6
Shahabi, H., Hashim, M., 2015. Landslide susceptibility mapping using GIS-based statistical models and Remote sensing data in tropical environment. Scientific Reports 5. https://doi.org/10.1038/srep09899
Shi, M., Peng, J., Chen, X., Zheng, Y., Yang, H., Su, Y., Wang, G., Wang, W., 2021. An Improved Method for InSAR Atmospheric Phase Correction in Mountainous Areas. IEEE Journal of Selected Topics in Applied Earth Observations and Remote Sensing 1–1. https://doi.org/10.1109/JSTARS.2021.3113619
Shi, X., Yang, C., Zhang, Lu, Jiang, H., Liao, M., Zhang, Li, Liu, X., 2019a. Mapping and characterizing displacements of active loess slopes along the upstream Yellow River with multi-temporal InSAR datasets. Science of the Total Environment 674, 200–210. https://doi.org/10.1016/j.scitotenv.2019.04.140
Shi, X., Zhang, L., Xu, Q., Zhao, K., Dong, J., Jiang, H., Liao, M., 2019b. Monitoring Slope Displacements of Loess Terrace Using Time Series InSAR Analysis Technique. Wuhan Daxue Xuebao (Xinxi Kexue Ban)/Geomatics and Information Science of Wuhan University 44, 1027–1034. https://doi.org/10.13203/j.whugis20190056
Shi, X., Zhang, Li, Zhong, Y., Zhang, Lu, Liao, M., 2020. Detection and characterization of active slope deformations with Sentinel-1 InSAR analyses in the southwest area of Shanxi, China. Remote Sensing 12. https://doi.org/10.3390/rs12030392
Simoni, A., Ponza, A., Picotti, V., Berti, M., 2013a. Landslide-Related Sediment Yield Rate in a Large Apenninic Catchment, in: Margottini, C., Canuti, P., Sassa, K. (Eds.), Landslide Science and Practice: Volume 4: Global Environmental Change. Springer, Berlin, Heidelberg, pp. 307–313. https://doi.org/10.1007/978-3-642-31337-0_39
Simoni, A., Ponza, A., Picotti, V., Berti, M., Dinelli, E., 2013b. Earthflow sediment production and Holocene sediment record in a large Apennine catchment.

Geomorphology, Sediment sources, source-to-sink fluxes and sedimentary budgets 188, 42–53. https://doi.org/10.1016/j.geomorph.2012.12.006
Simons, M., Bekaert, D., Borsa, A., Donnellan, A., Fielding, E., Jones, C., Lohman, R., Lu, Z., Meyer, F., Owen, S., Rosen, P.A., Zebker, H., 2021. Nisar Requirements and Validation Approach for Solid Earth Science, in: 2021 IEEE International Geoscience and Remote Sensing Symposium IGARSS. Presented at the 2021 IEEE International Geoscience and Remote Sensing Symposium IGARSS, pp. 543–546. https://doi.org/10.1109/IGARSS47720.2021.9554894
Skempton, A., De Lory, F., 1957. Stability of natural slopes in London clay. Thomas Telford Publishing, London, UK 15, 378–381.
Skempton, A.W., Leadbeater, A.D., Chandler, R.J., 1989. The Mam Tor landslide, North Derbyshire. Philosophical Transactions of the Royal Society of London. Series A, Mathematical and Physical Sciences 329, 503–547. https://doi.org/10.1098/rsta.1989.0088
Smith, H.G., Spiekermann, R., Betts, H., Neverman, A.J., 2021. Comparing methods of landslide data acquisition and susceptibility modelling: Examples from New Zealand. Geomorphology 381, 107660. https://doi.org/10.1016/j.geomorph.2021.107660
Solari, L., Del Soldato, M., Montalti, R., Bianchini, S., Raspini, F., Thuegaz, P., Bertolo, D., Tofani, V., Casagli, N., 2019. A Sentinel-1 based hot-spot analysis: landslide mapping in north-western Italy. International Journal of Remote Sensing 40, 7898–7921. https://doi.org/10.1080/01431161.2019.1607612
Solari, L., Del Soldato, M., Raspini, F., Barra, A., Bianchini, S., Confuorto, P., Casagli, N., Crosetto, M., 2020. Review of Satellite Interferometry for Landslide Detection in Italy. Remote Sensing 12, 1351. https://doi.org/10.3390/rs12081351
Spiekermann, R.I., Smith, H.G., McColl, S., Burkitt, L., Fuller, I.C., 2022. Quantifying effectiveness of trees for landslide erosion control. Geomorphology 396, 107993. https://doi.org/10.1016/j.geomorph.2021.107993
Stead, D., Wolter, A., 2015. A critical review of rock slope failure mechanisms: The importance of structural geology, Journal of Structural Geology. https://doi.org/10.1016/j.jsg.2015.02.002
Stirling, M., McVerry, G., Gerstenberger, M., Litchfield, N., Van Dissen, R., Berryman, K., Barnes, P., Wallace, L., Villamor, P., Langridge, R., Lamarche, G., Nodder, S., Reyners, M., Bradley, B., Rhoades, D., Smith, W., Nicol, A., Pettinga, J., Clark, K., Jacobs, K., 2012. National seismic hazard model for New Zealand: 2010 update. Bulletin of the Seismological Society of America 102, 1514–1542. https://doi.org/10.1785/0120110170
Stodden, V., McNutt, M., Bailey, D.H., Deelman, E., Gil, Y., Hanson, B., Heroux, M.A., Ioannidis, J.P.A., Taufer, M., 2016. Enhancing reproducibility for computational methods. Science. https://doi.org/10.1126/science.aah6168
Stumpf, A., Malet, J.-P., Delacourt, C., 2017. Correlation of satellite image time-series for the detection and monitoring of slow-moving landslides. Remote Sensing of Environment 189, 40–55. https://doi.org/10.1016/j.rse.2016.11.007
Sun, L., Muller, J.-P., 2016. Evaluation of the use of sub-pixel offset tracking techniques to monitor landslides in densely vegetated steeply sloped areas. Remote Sensing 8. https://doi.org/10.3390/rs8080659
Sun, L., Muller, J.-P., Chen, J., 2017. Time Series Analysis of Very Slow Landslides in the Three Gorges Region through Small Baseline SAR Offset Tracking. Remote Sensing 9, 1314. https://doi.org/10.3390/rs9121314

Suren, A.M., Martin, M.L., Smith, B.J., 2005. Short-term effects of high suspended sediments on six common New Zealand stream invertebrates. Hydrobiologia 548, 67–74. https://doi.org/10.1007/s10750-005-4167-5

Tellman, B., Sullivan, J.A., Kuhn, C., Kettner, A.J., Doyle, C.S., Brakenridge, G.R., Erickson, T.A., Slayback, D.A., 2021. Satellite imaging reveals increased proportion of population exposed to floods. Nature 596, 80–86. https://doi.org/10.1038/s41586-021-03695-w

Tenzer, R., Sirguey, P., Rattenbury, M., Nicolson, J., 2011. A digital rock density map of New Zealand. Computers & Geosciences 37, 1181–1191. https://doi.org/10.1016/j.cageo.2010.07.010

Thompson, R., 1982. Relationship of geology to slope failures in soft rocks of the Taihape-Mangaweka area, central North Island, New Zealand (PhD Thesis). University of Auckland.

Torres, R., Snoeij, P., Geudtner, D., Bibby, D., Davidson, M., Attema, E., Potin, P., Rommen, B., Floury, N., Brown, M., Traver, I.N., Deghaye, P., Duesmann, B., Rosich, B., Miranda, N., Bruno, C., L'Abbate, M., Croci, R., Pietropaolo, A., Huchler, M., Rostan, F., 2012. GMES Sentinel-1 mission. Remote Sensing of Environment, The Sentinel Missions - New Opportunities for Science 120, 9–24. https://doi.org/10.1016/j.rse.2011.05.028

Trigila, A., Iadanza, C., Spizzichino, D., 2010. Quality assessment of the Italian Landslide Inventory using GIS processing. Landslides 7, 455–470. https://doi.org/10.1007/s10346-010-0213-0

Turner, A.K., 2018. Social and environmental impacts of landslides. Innov. Infrastruct. Solut. 3, 70. https://doi.org/10.1007/s41062-018-0175-y

Van Asch, Th.W.J., Buma, J., Van Beek, L.P.H., 1999. A view on some hydrological triggering systems in landslides. Geomorphology 30, 25–32. https://doi.org/10.1016/S0169-555X(99)00042-2

Van Asch, Th.W.J., Malet, J.-P., Bogaard, T.A., 2009. The effect of groundwater fluctuations on the velocity pattern of slow-moving landslides. Nat. Hazards Earth Syst. Sci. 9, 739–749. https://doi.org/10.5194/nhess-9-739-2009

Van Den Eeckhaut, M., Poesen, J., Verstraeten, G., Vanacker, V., Moeyersons, J., Nyssen, J., van Beek, L.P.H., 2005. The effectiveness of hillshade maps and expert knowledge in mapping old deep-seated landslides. Geomorphology 67, 351–363. https://doi.org/10.1016/j.geomorph.2004.11.001

Varnes, D., 1978. Slopes Movement Types and Processes. Transportation Research Board Special Report.

Varnes, D.J., 1958. Landslide types and processes. Landslides and engineering practice 24, 20–47.

Vericat, D., Wheaton, J.M., Brasington, J., 2017. Revisiting the Morphological Approach, in: Gravel-Bed Rivers. John Wiley & Sons, Ltd, pp. 121–158. https://doi.org/10.1002/9781118971437.ch5

Villaseñor-Reyes, C.I., Dávila-Harris, P., Hernández-Madrigal, V.M., Figueroa-Miranda, S., 2018. Deep-seated gravitational slope deformations triggered by extreme rainfall and agricultural practices (eastern Michoacan, Mexico). Landslides 15, 1867–1879. https://doi.org/10.1007/s10346-018-1031-z

Villi, F., Bayer, B., Simoni, A., Schmidt, D.A., 2016. Long-term deformation of slow moving landslides in the Northern Apennines of Italy imaged by SAR interferometry. Rendiconti Online Societa Geologica Italiana 41, 263–266. https://doi.org/10.3301/ROL.2016.144

Walcott, R.I., 1978. Present tectonics and Late Cenozoic evolution of New Zealand. Geophys J Int 52, 137–164. https://doi.org/10.1111/j.1365-246X.1978.tb04225.x
Wang, Q., Yu, W., Xu, B., Wei, G., 2019. Assessing the use of gacos products for sbas-insar deformation monitoring: A case in southern california. Sensors (Switzerland) 19. https://doi.org/10.3390/s19183894
Wang, Y., Liu, D., Dong, J., Zhang, L., Guo, J., Liao, M., Gong, J., 2021. On the applicability of satellite SAR interferometry to landslide hazards detection in hilly areas: a case study of Shuicheng, Guizhou in Southwest China. Landslides. https://doi.org/10.1007/s10346-021-01648-y
Wasowski, J., Bovenga, F., 2014. Investigating landslides and unstable slopes with satellite Multi Temporal Interferometry: Current issues and future perspectives. Engineering Geology 174, 103–138. https://doi.org/10.1016/j.enggeo.2014.03.003
Weaver, C., 2010. Multidimensional data dissection using attribute relationship graphs, in: 2010 IEEE Symposium on Visual Analytics Science and Technology. Presented at the 2010 IEEE Symposium on Visual Analytics Science and Technology, pp. 75–82. https://doi.org/10.1109/VAST.2010.5652520
Westoby, M.J., Brasington, J., Glasser, N.F., Hambrey, M.J., Reynolds, J.M., 2012. "Structure-from-Motion" photogrammetry: A low-cost, effective tool for geoscience applications. Geomorphology 179, 300–314. https://doi.org/10.1016/j.geomorph.2012.08.021
Wheaton, J.M., Brasington, J., Darby, S.E., Sear, D.A., 2010. Accounting for uncertainty in DEMs from repeat topographic surveys: Improved sediment budgets. Earth Surface Processes and Landforms 35, 136–156. https://doi.org/10.1002/esp.1886
Wieczorek, G.F., Jäger, S., 1996. Triggering mechanisms and depositional rates of postglacial slope-movement processes in the Yosemite Valley, California. Geomorphology 15, 17–31. https://doi.org/10.1016/0169-555X(95)00112-I
Wilkinson, S.N., Dougall, C., Kinsey-Henderson, A.E., Searle, R.D., Ellis, R.J., Bartley, R., 2014. Development of a time-stepping sediment budget model for assessing land use impacts in large river basins. Science of The Total Environment 468–469, 1210–1224. https://doi.org/10.1016/j.scitotenv.2013.07.049
Wilkinson, S.N., Prosser, I.P., Rustomji, P., Read, A.M., 2009. Modelling and testing spatially distributed sediment budgets to relate erosion processes to sediment yields. Environmental Modelling and Software 24, 489–501. https://doi.org/10.1016/j.envsoft.2008.09.006
Williams, F., McColl, S., Fuller, I., Massey, C., Smith, H., Neverman, A., 2021. Intersection of fluvial incision and weak geologic structures cause divergence from a universal threshold slope model of landslide occurrence. Geomorphology 389, 107795. https://doi.org/10.1016/j.geomorph.2021.107795
Williams, F., Moore, P., Isenhart, T., Tomer, M., 2020. Automated measurement of eroding streambank volume from high-resolution aerial imagery and terrain analysis. Geomorphology 367, 107313. https://doi.org/10.1016/j.geomorph.2020.107313
Williams, R., 2012. DEMs of difference. Geomorphological Techniques 2.
Wylie, D., Jackson, D.L., Menzel, W.P., Bates, J.J., 2005. Trends in Global Cloud Cover in Two Decades of HIRS Observations. Journal of Climate 18, 3021–3031. https://doi.org/10.1175/JCLI3461.1
Xiao, L., Zhang, Y., Peng, G., 2018. Landslide susceptibility assessment using integrated deep learning algorithm along the china-nepal highway. Sensors (Switzerland) 18. https://doi.org/10.3390/s18124436

Xu, Q., Fan, X.-M., Huang, R.-Q., Westen, C.V., 2009. Landslide dams triggered by the Wenchuan Earthquake, Sichuan Province, south west China. Bull Eng Geol Environ 68, 373–386. https://doi.org/10.1007/s10064-009-0214-1

Xu, Y., George, D.L., Kim, J., Lu, Z., Riley, M., Griffin, T., de la Fuente, J., 2021a. Landslide monitoring and runout hazard assessment by integrating multi-source remote sensing and numerical models: an application to the Gold Basin landslide complex, northern Washington. Landslides 18, 1131–1141. https://doi.org/10.1007/s10346-020-01533-0

Xu, Y., Schulz, W.H., Lu, Z., Kim, J., Baxtrom, K., 2021b. Geologic controls of slow-moving landslides near the US West Coast. Landslides. https://doi.org/10.1007/s10346-021-01732-3

Yan, Y., Wang, Y., Zeng, Z., 2018. Study of landslide characteristics using time-series InSAR technique, in: International Geoscience and Remote Sensing Symposium (IGARSS). pp. 4885–4888. https://doi.org/10.1109/IGARSS.2018.8517450

Yenes, M., Monterrubio, S., Nespereira, J., Santos, G., Fernández-Macarro, B., 2015. Large landslides induced by fluvial incision in the Cenozoic Duero Basin (Spain). Geomorphology 246, 263–276. https://doi.org/10.1016/j.geomorph.2015.06.022

Yin, Y., Wang, F., Sun, P., 2009. Landslide hazards triggered by the 2008 Wenchuan earthquake, Sichuan, China. Landslides 6, 139–152. https://doi.org/10.1007/s10346-009-0148-5

Young, A.P., 2015. Recent deep-seated coastal landsliding at San Onofre State Beach, California. Geomorphology 228, 200–212. https://doi.org/10.1016/j.geomorph.2014.08.005

Yu, G., Wang, Z.-Y., Zhang, K., Duan, X., Chang, T.-C., 2010. Restoration of an incised mountain stream using artificial step-pool system. Journal of Hydraulic Research 48, 178–187. https://doi.org/10.1080/00221681003704186

Yu, T.-T., Wang, T.-S., Cheng, Y.-S., 2015. Analysis of Factors Triggering Shallow Failure and Deep-Seated Landslides Induced by Single Rainfall Events. Journal of Disaster Research 10, 966–972. https://doi.org/10.20965/jdr.2015.p0966

Yuan, Q., Shen, H., Li, T., Li, Z., Li, S., Jiang, Y., Xu, H., Tan, W., Yang, Q., Wang, J., Gao, J., Zhang, L., 2020. Deep learning in environmental remote sensing: Achievements and challenges. Remote Sensing of Environment 241, 111716. https://doi.org/10.1016/j.rse.2020.111716

Yunjun, Z., Fattahi, H., Amelung, F., 2019. Small baseline InSAR time series analysis: Unwrapping error correction and noise reduction. Computers & Geosciences 133, 104331. https://doi.org/10.1016/j.cageo.2019.104331

Zapico, I., Molina, A., Laronne, J.B., Sánchez Castillo, L., Martín Duque, J.F., 2020. Stabilization by geomorphic reclamation of a rotational landslide in an abandoned mine next to the Alto Tajo Natural Park. Engineering Geology 264, 105321. https://doi.org/10.1016/j.enggeo.2019.105321

Zêzere, J.L., Trigo, R.M., Trigo, I.F., 2005. Shallow and deep landslides induced by rainfall in the Lisbon region (Portugal): assessment of relationships with the North Atlantic Oscillation. Natural Hazards and Earth System Sciences 5, 331–344. https://doi.org/10.5194/nhess-5-331-2005

Zhang, T., Zhang, W., Cao, D., Yi, Y., Wu, X., 2022. A New Deep Learning Neural Network Model for the Identification of InSAR Anomalous Deformation Areas. Remote Sensing 14, 2690. https://doi.org/10.3390/rs14112690

Zhong, C., Liu, Y., Gao, P., Chen, W., Li, H., Hou, Y., Nuremanguli, T., Ma, H., 2020. Landslide mapping with remote sensing: challenges and opportunities, International Journal of Remote Sensing. https://doi.org/10.1080/01431161.2019.1672904

[intentionally blank]

# Appendix A: Open-Source Software Development

In addition to the scientific analyses detailed in Chapters 4, 5 and 6, I also engaged in a variety of open-source scientific software development efforts throughout the course of my PhD. These contributions are difficult to highlight within the context of peer-reviewed scientific publications, so I have created this appendix to detail some of the open-source scientific software development contributions I have made as part of this project. The majority of these contributions were in the form of GitHub pull requests (PRs), which integrated software I developed into existing scientific computing libraries.

My first major contribution was a bugfix to the main open-source InSAR processing program, the InSAR Scientific Computing Environment (ISCE2) (Rosen et al., 2015). My ISCE2 GitHub PR #110 fixed an "off-by-one" indexing error that caused InSAR jobs run for small areas to fail without clear error messaging.

The second contribution I made was the creation of a set of routines that allowed InSAR produced using the Full Resolution InSAR using Generalized Eigenvectors (FRInGE) (Fattahi et al., 2019) software to be ingested into the Miami InSAR Time-series in Python (MintPy) (Yunjun et al., 2019) software package. This allowed scientists to perform InSAR time-series analyses in MintPy using FRInGE-processed data. This work is encapsulated within MintPy GitHub PR #327.

The third contribution I made was similar to the previous contribution, but allowed InSAR products generated by the Alaska Satellite Facility's (ASF'S) Hybrid Plugin Processing Pipeline (HyP3) (Hogenson et al., 2016) to be ingested into MintPy. This allowed scientists to perform InSAR time-series analyses in MintPy using HyP3 InSAR products. The processing of HyP3-generated InSAR products in MintPy to create time-series InSAR products is now a standard community workflow and it would not be possible without the additions I made to MintPy in MintPy GitHub PR #542.

I also modernized the MintPy Docker container in order to run more efficiently without unnecessary packages and with faster build times. The Docker container I designed is the official MintPy docker container, and as of this writing, is the container being used to run test workflows for MintPy. In addition, this Docker container allows other scientists to install a stable version of MintPy with relatively low effort. This work is documented in MintPy GitHub PR #685.

In collaboration with the Dr. Bekaert, the original author of the study describing the double-difference filter (Bekaert et al., 2020), I also lead the implementation of the double-difference filter within MintPy (MintPy GitHub PR #552). I made many smaller contributions to MintPy as well, and the interested reader can find the full list of my authored PRs here.

In addition to my contributions to large open-source software projects, I have also created some personal repositories that other scientists and organizations have found useful. As discussed in the software availability section of Chapter 5, Jupyter Notebooks documenting executable versions of my InSAR workflow are available in this repository, and Jupyter

Notebooks containing my sPOT workflow are available in this repository. Finally, I also had the chance to work with InSAR data from the Unmanned Aerial Vehicle Synthetic Aperture Radar (UAVSAR) program during my PhD. In partnership with scientists at NASA's Jet Propulsion Laboratory (JPL) I created this repository, which contains a Jupyter Notebook workflow for performing UAVSAR InSAR time-series analyses in MintPy. This workflow is now being used as a prototype for creating validation data for the upcoming NISAR SAR mission.

# Appendix B: Statements of Contribution

This appendix contains completed "Statement of Contribution" forms, which are required by Massey University for the three scientific manuscript chapters (4, 5, & 6) within this thesis. These forms are akin to "Authors' Contributions" sections, which can be found in some scientific journal articles.

MASSEY UNIVERSITY
TE KUNENGA KI PŪREHUROA
UNIVERSITY OF NEW ZEALAND

GRADUATE RESEARCH SCHOOL

# STATEMENT OF CONTRIBUTION
# DOCTORATE WITH PUBLICATIONS/MANUSCRIPTS

We, the student and the student's Main Supervisor, certify that all co-authors have consented to their work being included in the thesis and they have accepted the student's contribution as indicated below in the Statement of Originality.

| | |
|---|---|
| Student name: | Forrest Williams |
| Name/title of main supervisor: | Ian Fuller |
| In which chapter is the manuscript/published work? | Chapter 4 |

Please select one of the following three options:

(●) The manuscript/published work is published or in press

- Please provide the full reference of the research output:

Williams, F., McColl, S., Fuller, I., Massey, C., Smith, H., Neverman, A., 2021. Intersection of fluvial incision and weak geologic structures cause divergence from a universal threshold slope model of landslide occurrence. Geomorphology 389, 107795. https://doi.org/10.1016/j.geomorph.2021.107795

( ) The manuscript is currently under review for publication – please indicate:

- The name of the journal:

- The percentage of the manuscript/published work that was contributed by the student: 95 %

- Describe the contribution that the student has made to the manuscript/published work:

Mr. Williams performed the data collection, data analysis, and wrote the manuscript. Dr. McColl and Dr. Massey provided suggestions for the initial hypothesis of this chapter. Dr. McColl, Dr. Fuller, Dr. Smith, and Dr. Nevermann provided suggestions after the manuscript was written.

( ) It is intended that the manuscript will be published, but it has not yet been submitted to a journal

| | |
|---|---|
| Student's signature: | Forrest Williams |
| Main supervisor's signature: | Prof. Ian Fuller Digitally signed by Prof. Ian Fuller Date: 2022.08.24 08:40:59 +12'00' |

*This form should appear at the end of each thesis chapter/section/appendix submitted as a manuscript/ publication or collected as an appendix at the end of the thesis.*

MASSEY UNIVERSITY
TE KUNENGA KI PŪREHUROA
UNIVERSITY OF NEW ZEALAND

GRADUATE RESEARCH SCHOOL

# STATEMENT OF CONTRIBUTION
# DOCTORATE WITH PUBLICATIONS/MANUSCRIPTS

We, the student and the student's Main Supervisor, certify that all co-authors have consented to their work being included in the thesis and they have accepted the student's contribution as indicated below in the Statement of Originality.

| | |
|---|---|
| Student name: | Forrest Williams |
| Name/title of main supervisor: | Ian Fuller |
| In which chapter is the manuscript/published work? | Chapter 5 |

Please select one of the following three options:

○ The manuscript/published work is published or in press

- Please provide the full reference of the research output:

○ The manuscript is currently under review for publication – please indicate:

- The name of the journal:
- The percentage of the manuscript/published work that was contributed by the student: 95 %
- Describe the contribution that the student has made to the manuscript/published work:

Mr. Williams performed the data collection, data analysis, and wrote the manuscript. Some data collection was conducted in partnership with Dr. McColl. Dr. McColl, Dr. Fuller, Dr. Smith, and Dr. Nevermann provided suggestions after the manuscript was written.

◉ It is intended that the manuscript will be published, but it has not yet been submitted to a journal

| | |
|---|---|
| Student's signature: | Forrest Williams |
| Main supervisor's signature: | Prof. Ian Fuller Digitally signed by Prof. Ian Fuller Date: 2022.08.24 08:41:51 +12'00' |

*This form should appear at the end of each thesis chapter/section/appendix submitted as a manuscript/ publication or collected as an appendix at the end of the thesis.*

MASSEY UNIVERSITY
TE KUNENGA KI PŪREHUROA
UNIVERSITY OF NEW ZEALAND

GRADUATE RESEARCH SCHOOL

# STATEMENT OF CONTRIBUTION
# DOCTORATE WITH PUBLICATIONS/MANUSCRIPTS

We, the student and the student's Main Supervisor, certify that all co-authors have consented to their work being included in the thesis and they have accepted the student's contribution as indicated below in the Statement of Originality.

| | |
|---|---|
| Student name: | Forrest Williams |
| Name/title of main supervisor: | Ian Fuller |
| In which chapter is the manuscript/published work? | Chapter 6 |

Please select one of the following three options:

○ The manuscript/published work is published or in press
- Please provide the full reference of the research output:

○ The manuscript is currently under review for publication – please indicate:
- The name of the journal:
- The percentage of the manuscript/published work that was contributed by the student: 97 %
- Describe the contribution that the student has made to the manuscript/published work:

Mr. Williams performed the data collection, data analysis, and wrote the manuscript. Dr. McColl, Dr. Fuller, Dr. Smith, and Dr. Nevermann provided suggestions after the manuscript was written.

◉ It is intended that the manuscript will be published, but it has not yet been submitted to a journal

| | |
|---|---|
| Student's signature: | Forrest Williams |
| Main supervisor's signature: | Prof. Ian Fuller — Digitally signed by Prof. Ian Fuller Date: 2022.08.24 08:42:44 +12'00' |

*This form should appear at the end of each thesis chapter/section/appendix submitted as a manuscript/ publication or collected as an appendix at the end of the thesis.*